Synthesis, Physical Properties And Applications Of Metal Oxide Semiconductor Nanostructures And Thin Films

Thesis submitted for the degree of

Doctor of Philosophy (Science)

In

Physics (Experimental)

By

Chandan Samanta

Department of Physics
University of Calcutta
February 2021

…….To my Ma

Acknowledgements

This thesis would not have been possible without the support and assistance of all those who have contributed directly or indirectly towards this thesis in this COVID-19 pandemic situation and that is beyond my ability to name them all. However, I would be failing in my duties if I do not put on record the following persons.

First of all, I would like to express my heartiest gratitude to my supervisor **Prof. Barnali Ghosh (Saha)** who has truly been a friend, philosopher and guide to me. She has given me the opportunity to work with her and provided me with a wonderful ambience of research in "New Nano Lab" at S. N. Bose National Centre for Basic Sciences. I have been benefited from her invaluable advice and useful discussions during these five and half years.

I am highly indebted to **Prof. A. K. Raychaudhuri**, former Director of S. N. Bose National Centre for Basic Sciences. His support, encouragement and guidance have been extremely crucial in building my mental grid, personality and maturity towards making a potential career as a researcher. In spite of his extremely busy schedule, he has always been compassionated and made himself available for any kind of scientific discussion.

I would like to acknowledge Dr. Sekhar Bhattacharya (KAUST) for providing the ALD samples to carry out the research. I pay my sincere thanks to Dr. Manik Pradhan for providing me an opportunity to access his lab.

I always enjoyed the warm and cordial atmosphere in our "New Nano Lab". It is my pleasure to acknowledge all my seniors and juniors. I am thankful to Kaustuv da, Ankita di, Jashashree di, Rajib da, Pabitra da, Rabeya di, Soumen da, Rishi Ji, Samik da, Subarna di, Shaili di, Ravi da, Arnab da, Arun da for their helps and suggestions during different experiments. I am thankful to Rishi Ji (Dr. Ghimire) who helped me for device fabrication and electrical measurement. However, my special thank is to Dr. Ankita Ghatak for always helping me out with all my queries particularly TEM and XPS data analysis whenever needed. I remember the beautiful moments spent with some of my lab-mates, batch-mates and friends Avisek da, Subhamita, Parushottam (Paru), Anirban. Vishal, Sudipta, Saikat, Snehamoyee are wonderful juniors and always happy to help. I have spent very nice time with Aviske da during journey for attending conference in many places in India and visiting KEK, Japan for the synchrotron XRD.

I acknowledge the help of all the technical cell members for their unconditional support and help whenever I needed. Special thanks to Samik da and Joy da in the operation of TEM and

Helios dual beam FIB and providing me samples which gave me interesting and crucial results for the thesis.

I would like to acknowledge my host institute SNBNCBS for providing me a peaceful and friendly environment for research and funding my research and providing me the hostel facility inside the campus. Also, I would like to acknowledge two funding agencies; the Science and Engineering Research Board (SERB), grant no. EMR/2017/001990), Government of India and a sponsored project "Technical Research Centre (TRC)" under grant All1/ 64/SNB/2014 (C) through the Department of Science and Technology, Government of India. I also would like to thank from the bottom of my heart to all the people of administration, engineering, computer, library, electrical, workshop and canteen for their help.

Last but not the least, I would like to express my deep sense of gratitude to my parents, my sister (Bon) and family members. I find it impossible to express in words the priceless love, contributions and sacrifices of my Ma and Baba for my wellbeing. My "baromama" who has been a great source of support and encouragement throughout my life during. Few words are not sufficient to express my immense gratitude to the love of my life Puja for her constant support and encouragement in this long journey. Their unconditional love and support throughout my life is immeasurable.

Lastly, I thank God for the priceless gift of grace and making my journey so charming....

Chandan Samanta
Department of Condensed Matter Physics and Material Sciences
S. N. Bose National Centre for Basic Sciences
Kolkata, India
February 2021

List of Publications and Patent applications

List of Publications in peer-review journal

1. **C. Samanta**, S. Bhattacharya, A. K. Raychaudhuri, and B. Ghosh, Broadband (Ultraviolet to Near-Infrared) Photodetector in n-ZnO/p-Si Nanowires core-shell Arrays with Ligand-Free Plasmonic Nanoparticles, *J. Phys. Chem. C*, **40**, 22235 (2020). *****
2. **C. Samanta**, A. Ghatak, A. K. Raychaudhuri, and B. Ghosh, ZnO/Si nanowires heterojunction array based nitric oxide (NO) gas sensor with noise-limited detectivity approaching 10ppb, *Nanotechnology*, **30**, 305501 (2019). *****
3. **C. Samanta**, R. R. Ghimire, and B. Ghosh, Fabrication of Amorphous Indium–Gallium–Zinc–Oxide Thin-Film Transistor on Flexible Substrate Using a Polymer Electrolyte as Gate Dielectric, *IEEE Trans. Electron Devices*, **65**, 2827 (2018). *****
4. S. Saha, A. K. Bhunia, C. Rana, **C. Samanta**, S. Guchhait, and R. Bhattacharya, Structural and Optical Characterization of CdS Nanoparticles Grown in Different Solvents, *IOSR Journal of Electrical and Electronics Engineering (IOSR-JEEE)*, **13**, 12 (2018).
5. **C. Samanta**, and B. Ghosh, A study on wavelength dependent persistence photoconduction of indium gallium zinc oxide thin film, *AIP Conference Proceedings*, **2115**, 030332 (2019).
6. **C. Samanta**, A. Ghatak, A. K. Raychaudhuri, and B. Ghosh, Engineering of defects control UV-Vis-NIR broadband optical response of ZnO/p-Si NWs nanostructures arrays, (Manuscript under review). *****
7. **C. Samanta**, A. K. Raychaudhuri, and B. Ghosh, Temperature dependence of steady-state UV-Vis-NIR broadband photoconductivity in ZnO/p-Si NWs core-shell nanostructures, (Manuscript under preparation).
8. **C. Samanta**, A. Ghatak, A. K. Raychaudhuri, and B. Ghosh, Ligands free Pd NPs decorated ZnO/n-Si NWs core-shell heterostructure based fast response hydrogen gas sensors, (Manuscript under preparation).

List of Patent application (Indian)

1. R. Ghimire, **C. Samanta**, B. Ghosh, and A. K. Raychaudhuri, Flexible thin film transistor using electric double layer as gate dielectric and a method of fabricating thereof, **Indian Patent Filed No. 201731015268 dated: 09/06/2017**, (FER submitted). *****

2. S. Maithani, **C. Samanta**, A. Maity, K. Das, M. Pradhan, B. Ghosh, and A. K. Raychaudhuri, A gas-sensing system for selective detection of (nitric oxide) NO gas and a method for fabricating the same, **Indian Patent Filed No. 201731038036A dated: 10/11/2017**, (FER submitted). *****

Present thesis is based on publications and patent marked with *****

List of Abbreviations

MOSs: Metal oxide semiconductors
ZnO: Zinc oxide
IGZO: Indium gallium zinc oxide
a-IGZO: Amorphous- IGZO
1D: One Dimensional
Si: Silicon
NWs: Nanowires
MACE: Metal Assisted Chemical Etching
EE: Electroless Etching
CSD: Chemical Solution Deposition
ALD: Atomic Layer Deposition
PLD: Pulsed Laser Deposition
PLAL: Pulsed Laser Ablation in liquid
DI: Deionized water
DEZ: Diethylzinc
PET: Polyethylene terephthalate
KrF: Krypton Fluoride
NPs: Nanoparticles
PMMA: Poly(methyl methacrylate)
PEO: Polyethylene Oxide
EDLT: Electric Double Layer Transistor
XRD: X-Ray Diffraction
ICSD: Inorganic Crystal Structure Database
SEM: Scanning Electron Microscope
SAED: Selected Area Electron Diffraction
CCD: Charged Coupled Device
EDS: Energy Dispersive X-ray Spectrometry
XTEM: Cross-sectional TEM
FIB: Focused Ion Beam
TEM: Transmission Electron Microscope
HRTEM: High Resolution TEM
STEM: Scanning TEM
HAADF: High Angle Annular Dark Field Detector
XPS: X-ray Photoelectron Spectroscopy
AFM: Atomic Force Microscopy
LFM: Lateral Force Microscopy
PL: Photoluminescence
E_g: Band gap
ρ: Resistivity
λ: Wavelength
nm: Nanometre
d: Diameter
μm: Micrometre
μA: Microampere
Pa: Pascal
I: Current
V: Applied Bias
UV: Ultraviolet
Vis: Visible
NIR: Near-infrared
$\Im$: Illumination intensity
I_{PC}: Photocurrent
R: Responsivity
D*: Specific Detectivity
μW: Microwatt
SPR: Surface Plasmon Resonance
E_F: Fermi level
τ_r: Rise time
τ_d: Decay time
Ř: Gas Response
I_0: Reverse saturation current
χ: Electron affinity
φ: Work function
NO: Nitric oxide
COPD: Chronic obstructive pulmonary disease
ppm: Parts per million
ppb: Parts per billion
HV: High vacuum
IOT: Internet of Things
FET: Field Effect Transistor
EDL: Electric Double Layer
EDLC: Electric Double Layer Capacitor
IC: Integrated Circuit
TFT: Thin Film Transistor
V_g: Gate voltage
V_{ds}: Drain-source voltage
I_d: Drain current
I_g: Gate leakage current
C_g: Specific gate capacitance
V_{th}: Threshold voltage
SS: Subthreshold swing
μ_{sat}: Saturation mobility
μ_{FE}: Field-effect mobility
g_m: Mutual conduction
$V_o s$: Oxygen vacancies
V_{Zn}: Zinc vacancy
Zn_i: Zinc interstitial
O_i: Oxygen interstitial
O_L: Lattice oxygen
FER: First Examination Report

Contents

List of figures

List of tables

Chapter 1

Introduction

In this chapter, we will discuss the physical properties of metal oxide semiconductor and underlying physics behind their specific electronic and optoelectronic properties that make it interesting in practical applications. This thesis deals with the basic physics related to electrical and optoelectronic and other areas using this metal oxide semiconductor heterojunction with 1D nanostructures that has not been explored much till date. We mainly focus on heterojunction arrays which has been formed using zinc oxide (ZnO) / doped ZnO and vertically aligned 1D Si NWs arrays in this thesis. The electrical, optoelectronics and gas sensing properties of oxides can be tuned by making heterostructures or FET type device structures or by decorating with plasmonic nanoparticles (Au). In this thesis, we will introduce how one can tune the charge carriers by using the effect of photo gating, gas injection or by field effect using electric double layer (EDL) gate and to understand the basic physics underlying the charge carrier transport. The electrical conductivity and photosensitivity of oxide semiconductors can also be engineered by tunning of surface/interface defects. Other than basic physics, the experimental observation/ understanding leads to a very good contribution to flexible electronics and also in gas sensing application with a very good application potential. The proof of concept had been patented and highlighted in this thesis work also. The literature survey on some novel and interesting optoelectronic, gas sensing and physical properties of these metal oxide semiconductors have been provided in this chapter. Lastly an outline of the thesis has been presented to highlight the main investigation of this thesis.

1.1 Introduction to metal oxide semiconductors

Metal oxide semiconductors (MOSs) are widely investigated in the field of fundamental research as well as industrial applications during last three decades since they are earth abundant, biocompatible, low cost, and in some cases, chemically stable and with suitable electrical and optical characteristics. The optical, electrical and optoelectronic properties of metal oxides can be engineered by modifying their size, structure, composition and stoichiometry, and by doping [1]. In recent years capability to grow oxide semiconductors at low processing temperature on flexible substrates has given a boost to the general area of oxide electronics [2-3]. Size reduction to nano dimension of oxide semiconductors leading to quantum confinement phenomena modify their intrinsic properties like electrical, optoelectronic and other physical properties with respect to their corresponding bulk properties [4-5]. The opto-electronic properties of metal oxide heterojunction can be engineered by modifying their surface morphology, size, shape, and composition. But metal oxides have uncontrollable charge carriers due to oxygen vacancies and other defects. So, it is very crucial to develop proper and appropriate materials with stable charge carrier density for practical application. This can be controlled by doping, exposure to band gap illumination as well as by field effect using gate [6-8]. Oxide semiconductor can also be integrated into heterojunction with 1D nanostructure that can tune the electrical and optoelectronic properties suitably. Recently, the heterostructure and core-shell structure-based devices are promising entrant for various sensing and optoelectronics application [9]. Interesting device concepts based on heterostructures have been proposed recently for high performance gas sensors that go beyond conventional chemiresistors because of enhanced surface to volume ratio, higher gas diffusion rate and enhanced reactivity [10]. The basic physics related to electrical and optoelectronic and other areas using these metal oxide semiconductor heterojunctions with 1D nanostructures has not been explored much till date, very few reports are available in this regime [11-13].

In this thesis, we have concentrated on heterojunction arrays (both p-n and n-n junction) which has been formed using zinc oxide / doped ZnO and vertically aligned 1D silicon nanowires (Si NWs) arrays. This combination furnishes very high-quality optoelectronics properties including high surface to volume ratio, high surface reaction activity, low reflection and strong absorption in UV-Vis-NIR broadband region, strong electron and phonon confinements and enhancement of charge transfer and that can be integrated with silicon integrated circuit (IC) technology. Their low-dimensional nanostructures with suitable band gap, unique conduction properties, and confined carrier conduction pathways made them suitable candidates for

sensitive materials in photoelectric and other sensing devices [14-15]. In this thesis, we have mainly investigated a selected portion of physical properties such as electrical, optoelectronics and gas sensing properties of ZnO/Si NWs nanostructures arrays and thin film of doped ZnO. The thesis work also focuses with the dealing of known challenges on fabrication processes and the electrical, optoelectronics and gas sensing properties of oxides can be tuned by making heterostructures or FET type device structures or by decorating with plasmonic nanoparticles (Au). Other than basic physics, the experimental observation/ understanding leads to a very good contribution to flexible electronics and also in gas sensing application with a very good application potential. The proof of concept has been established and patented in some areas; like, gas sensor used in exhaled breath analysis and flexible transistors for wearable and stretchable electronic devices. A brief discussion of basic crystal structure of metal oxide semiconductors, some novel and interesting electrical, optoelectronics and gas sensing properties associated with semiconductor nanostructures have been highlighted in the following sections.

1.2 Fundamental properties of metal oxide semiconductors

Metal oxide semiconductors can adopt the most distinct structure at the nanoscale which affects their electrical, optoelectronics, physical and chemical properties in practical application [16-17]. The most common examples of metal oxide semiconductors are ZnO, TiO_2, WO_3, CuO, SnO_2 etc. This thesis mainly focuses on synthesis and physical properties study on nanostructured ZnO heterojunction and doped ZnO. Hence this section provides a review of fundamental properties of ZnO and doped ZnO.

1.2.1 Zinc oxide (ZnO)

1.2.1.1 Crystal structure

At ambient temperature and pressure, ZnO appears in the hexagonal wurtzite structure. The other structures are zinc blend (with a cubic or hexagonal phases) and rocksalt (with a cubic phase) but under ambient conditions they are thermodynamically unstable. The hexagonal wurtzite structure has a unit cell with two lattice parameters a = 3.2495 Å and c = 5.2069 Å in the ratio of c/a = 1.602, corresponding to P63mc space group. This ZnO space group is characterized by presenting two interconnecting sublattices of Zn^{2+} and O^{2-} ions in which each zinc ion is surrounded by a tetrahedral of four oxygen ions [18]. A schematic representation of the ZnO hexagonal wurtzite structure is shown in Figure 1.1. The zinc and oxygen ions are arranged alternately along the c-axis and exhibit positive and negative polar planes rich in Zn^{2+} and O^{2-}, respectively. This Zn^{2+} and O^{2-}, tetrahedral coordination is the

origin of a polar symmetry along the hexagonal axis. The most common and stable ZnO crystal exhibits a wurtzite structure with four face terminations: polar Zn-terminated (0001) and O-terminated (0001) facets, and non-polar (1010) and (1120) facets which containing an equal number of Zn and O atoms [19-20]. The polar planes are in favour to crystal growth by changing Zn^{2+} terminated surface with the O^{2-}, terminated surface or vice versa. Such growth process is repeated over a time which enhance the growth along ± (0001) planes rather than other commonly observed non polar planes. Thus, the polar behaviour is responsible for a number of properties in ZnO such as piezoelectricity, crystal growth and defect generation [21-22].

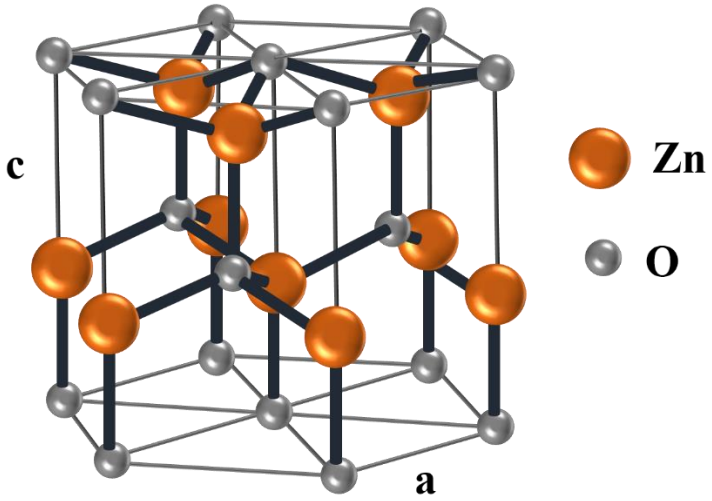

Figure 1.1 Schematic of the unit cell of the ZnO hexagonal wurtzite structure.

1.2.1.2 Electrical properties

The unique optoelectronics properties of ZnO coupled with its nontrivial electrical characteristics made it suitable candidate in photoelectric devices. As a wide band gap semiconductor, ZnO nanostructures are associated with ability to sustain large electric fields (high break down voltage), high temperature and high-power operation. The background carrier concentration of undoped ZnO varies a lot within the range of 10^{16} - 10^{19} cm^{-3} according to the quality of the samples, however the average value of carrier concentration is ~ 10^{16} cm^{-3}. All form of ZnO nanostructures usually reported to exhibit n-type conductivity with carrier mobility in the range of 0.1 – 100 cm^2/V-s. The first report claimed that the intrinsic defects such as zinc interstitials (Zn_i) or oxygen vacancies ($V_o s$) were responsible for the intrinsic n-type conductivity [23-24]. The hydrogen incorporation can cause n-type conductivity in bulk ZnO [25] and it was theoretically shown that hydrogen acts as a shallow donor [26]. Furthermore, it has been found that the group III impurities (such as Al, In, Ga) have taken into

account to increase n-type conductivity of ZnO by Zn substitution depending on the growth process [27-28]. However, the growth of p-type ZnO is still difficult. Among the p-type dopants, nitrogen acts as a promising acceptor for ZnO [29-30].

1.2.1.3 Optical properties

The semiconductor ZnO has gained substantial interest in the research community because of its direct wide band gap (E_g ~ 3.2 – 3.4 eV) with large exciton binding energy (60 meV) [31-32]. ZnO being transparent in visible region acts as a good UV absorber as well as emitter. The optical properties of ZnO are connected with both intrinsic and extrinsic effects. The interaction of light with ZnO follows various physical process such as optical absorption, transmission, reflection, photoluminescence and cathodoluminescence. The absorption of light in ZnO creates electrons in conduction band and holes in valence band by interband transition. However, these electron-hole pairs in same space point can bind as excitons due to the coulomb interaction and act as energy carriers like photons. The required condition for the exciton formation is the same group velocities of electron and hole. The extrinsic properties in ZnO are strongly dependent on dopants or defects which usually create discrete electronic states in the band gap which play the vital role for optical absorption and emission processes in this material [33].

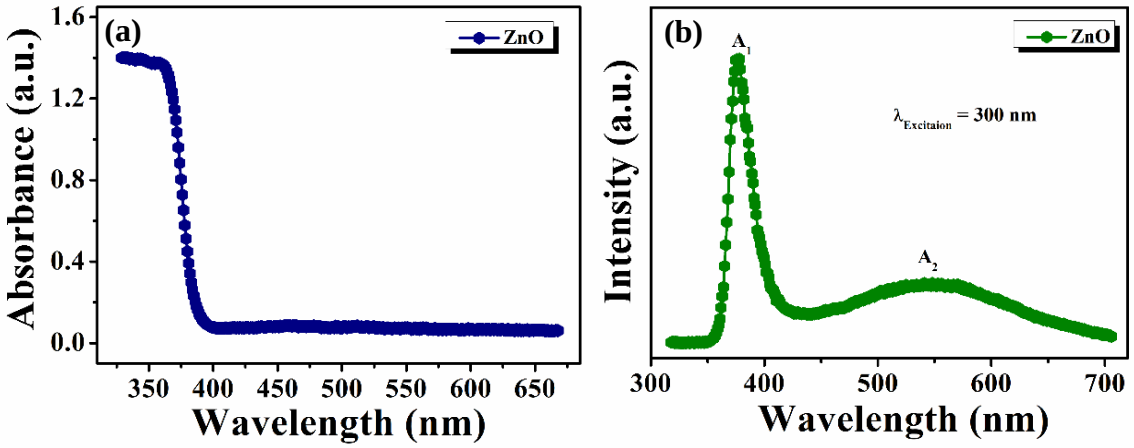

Figure 1.2 (a) UV-Visible absorption spectra of ZnO nanostructure film. (b) Photoluminescence spectra of ZnO nanostructure film. A_1 represents the excitonic emission peak where as A_2 represents the defect emission peak.

The UV-visible absorption spectra of nanostructured ZnO film exhibits the strong band gap absorption around 375 nm ($E_g \approx 3.3$ eV) in Figure 1.2 (a). From absorption spectra band gap is calculated from the extrapolation of $(\alpha h\nu)^2$ *vs* $h\nu$ graph where, α is the absorption coefficient and $h\nu$ is photon energy. The optical absorption is correlated with the transition of electrons from valence band to the conduction band or defect states. It also includes the transport of electrons from defect levels to conduction band. The optical as well as electrical

methods have been utilized to characterize the defect levels in ZnO. In optical methods, the photoluminescence (PL) spectroscopy has been used extensively to determine the crystal quality and the presence of the defects as well as exciton fine structures. This method gives the details information about charge carriers transitions from band to band through the various defect states. Figure 1.2 (b) shows the room temperature PL spectra of a nanostructured ZnO film for an excitation wavelength λ = 300 nm. The PL spectra of nanostructured ZnO exhibits the general feature of ultraviolet (UV) emission at ~ 375 nm which is corresponding to the near-band-edge (NBE) transition of wide band gap intrinsic ZnO. In addition to NBE emission there is a broad defects band emission in the visible region. The characteristics features of this emission spectra depend on the defects states available in the ZnO. Generally, the polycrystalline ZnO nanostructures having large number of grains and defect states can give rise to the weak NBE and strong broad visible/defects emission spectra. On the other hand, the highly oriented or less defective single crystal of ZnO exhibits the strong NBE and weak visible/defects emissions. The origin of defect emissions in visible region are assigned to shallow and deep level defects in nanostructured ZnO. The broad defects emission in the visible region can be readily deconvoluted into different bands named as green, yellow and red emission and these emissions are corresponding to the various type of defects present in ZnO. These defect states in ZnO are introduced at the growth time and can be controlled by growth methods and conditions, such as deposition temperature, oxygen pressure and annealing temperature [34]. The optical processes in various nanostructures of ZnO are connected with the intrinsic and extrinsic defects and the commonly reported defects in ZnO system are oxygen vacancies with different charges (V_o, V_o^+, V_o^{++}), zinc vacancies (V_{Zn}), zinc and oxygen interstitials (Zn_i and O_i). Oxygen and zinc vacancies are considered to be the most predominant defects in ZnO and these defects act as traps which exchange charge with capture of electrons/holes in the conduction band and valance band through the emission [35-36]. A schematic illustration of the excitation and emission processes of ZnO is shown in Figure 1.3 [37]. The band-to-band excitation (1) and the formation of excitons (2) have been occurred when ZnO is excited with photons of energy higher than the band gap. The excited free charge carriers are then trapped by V_o, V_{Zn} and O_i occupying in the band gap corresponding to the processes 4, 7 and 9 respectively. De-excitation process (3) and radiative recombination processes (5 and 6) give rise to the NBE and green emission bands respectively. The radiative recombination of shallowly trapped electrons with deeply trapped holes at O_i corresponding to the processes 8. The process 10 corresponds to the radiative recombination of shallowly

trapped electrons with deeply trapped holes at O_i which gives rise NIR emission. However, further investigation is required to interpret other emission bands such as yellow and red ones that we have discussed in the chapter 7.

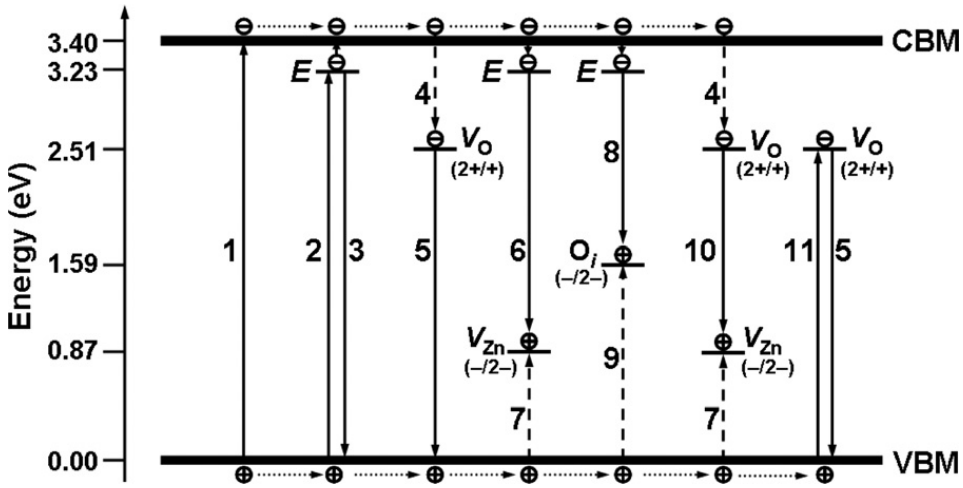

Figure 1.3 Schematic illustration of the excitation and emission processes of ZnO. (1) Band-to-band excitation, (2) and (3) adsorption and emission by excitons E; (4), (7), and (9) trapping of charge carriers by V_o, $V_{Zn}$and O_i, (5) radiative recombination of deeply trapped electrons at V_o with holes from the valence band; (6) and (8) radiative recombination of shallowly trapped electrons with deeply trapped holes at V_{Zn} and O_i; (10) donor acceptor transition involving V_o and V_{Zn}; (11) sub band excitation. Reprinted with permission from [37].

1.2.2 Doped ZnO

The doping of ZnO has attracted considerable research interest to tune optical, electrical and optoelectronics properties of ZnO suitably [38]. There are different topics of interest in doping of ZnO. Generally, doping with donor and acceptor impurities have been done to achieve high n-type and p-type conductivity of ZnO respectively. Also, doping with rare-earth elements and transition metals have been accepted to obtain desired optical and magnetic properties, respectively. It has been found that the group III impurities (such as Al, In, Ga, etc.) have taken into account to increase n-type conductivity with desire optoelectronics properties of ZnO by Zn substitution depending on the growth conditions [39]. Recently, among the state-of-the-art flexible thin film transistors (TFTs) technology, metal oxide semiconductors, especially doped ZnO, are promising candidate owing to their unique properties such as excellent carrier mobility even in amorphous state, high electrical conductivity, high optical transparency in visible as well as near-infrared region and large area uniform deposition at low temperature [2]. To increase the electrical conductivity, carrier mobility and transmittance of ZnO, In and Ga have been used as dopant because of good lattice matching with ZnO [r_{Ga}= 0.62Å, r_{In}=

0.81Å and r_{Zn} = 0.74Å] and less reactive as well as more resistant to oxidation [40]. In this section we will provide a review of fundamental properties of In and Ga doped ZnO (IGZO). The most general formula of IGZO is $InGaO_3(ZnO)_n$, where n is an integer. A homologous compound represented by the chemical formula $RMO_3(ZnO)_n$, where R=Lu, In etc. and M=In, Ga, Fe, etc. IGZO has two phases amorphous and crystalline. Amorphous phase is preferred over crystalline ones for active layers in thin film transistor (TFT) from the viewpoints of processing temperature and uniformity of device characteristics [2]. Figure 1.4 (a) illustrates the crystal structure of crystalline $InGaZnO_4$ (c-IGZO). The crystalline c-IGZO is made of the corner-sharing network between InO_6 and (Zn/GaO_6) polyhedra. Figure1.4 (b) shows a structure model of amorphous-$InGaZnO_4$ (a-IGZO) determined by extended X-ray absorption fine structures (EXAFS). It shows that the edge-sharing networks of InO_6 polyhedra are retained even in the disordered structure [41- 42]. IGZO is an n-type and direct wide band gap (3.2 – 3.6 eV) semiconductor with high transmittance (> 90 %) in visible region.

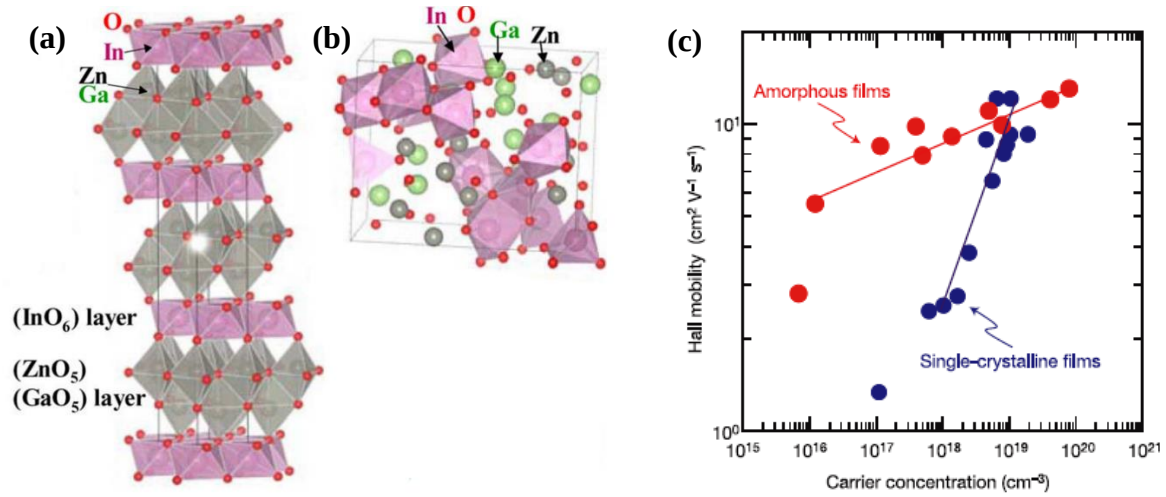

Figure 1.4 Polyhedral views of crystal structures of (a) crystalline $InGaZnO_4$ (c-IGZO) (b) amorphous $InGaZnO_4$ (a-IGZO). Red and gray polyhedra show InO_6 and (Zn/GaO_6) polyhedra. Reprinted with permission from [42]. (c) Relationship between room-temperature hall mobility and carrier concentration for a-IGZO films. Data on single-crystalline $InGaO_3(ZnO)_5$ films are shown for comparison. Reprinted with permission from [2].

IGZO exhibits the unusual carrier transport properties as sown in Figure 1.4 (c). The electron mobility of amorphous as well as crystalline IGZO increases with increasing free electron density. This phenomenon is opposite that of single crystalline covalent semiconductor like silicon, in which, the carrier mobility usually decreases with increasing carrier density due to scattering of carrier with the ionized donors or acceptors. This difference can be explained from the concept of chemical bonding [43]. The sp^3 hybridized orbitals that form the carrier transport paths in covalent semiconductor like silicon are noticeably distorted by disorder and form deep localized states (Figure 1.5 (a) and (b)). This results in the hopping conduction and

the low drift mobilities in silicon. So, both electrons and holes migrate by hopping and not by band conduction which results very low electron mobilities of < 1 cm^2/V-s. In contrast, the carrier conduction paths in metal oxide semiconductors are formed mainly by *s* orbitals of the metal cations. This spherically symmetrical *ns*-orbital provides small effective masses of electron and efficient electron transport even in the amorphous state, as a result, the electron mobilities in IGZO both in amorphous and crystalline phase easily exceed 10 cm^2/V-s [2, 42].

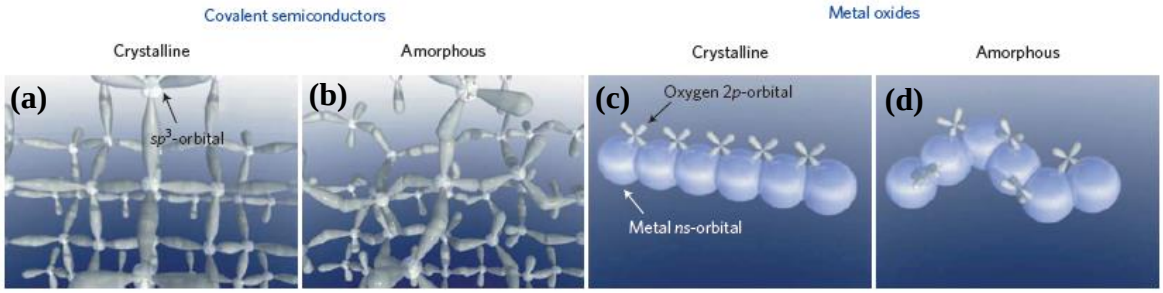

Figure 1.5 Electronic structures of Si and metal oxides. Schematic of orbital transport pathways in the conduction band of (a) crystalline and (b) amorphous covalent semiconductors; (c) crystalline and (d) amorphous metal oxides. Reprinted with permission from [2].

1.3 Optoelectronics studies on metal oxide semiconductors

Metal oxide semiconductors are widely investigated in the field of optoelectronics applications for their specific electronic and optoelectronic properties [1]. Most of the conventional photodetectors that are widely used are based on p-n junctions using elemental (Si and Ge) or binary (GaAs) and ternary (InGaAs) semiconductors. Each of these detectors have a spectral range depending on fundamental band gap of the semiconductor in which most of them lie in NIR region. Recently broadband optical detector is a fast-developing field with significant impact in various applications like UV radiation monitoring in an environment, healthcare research, secure communication, and so on. As the characteristics of the photo-generated charge carriers play an indispensable role in the photodetector operation, researchers have proposed several strategies, including modification of light absorption, design of novel heterostructures, utilization of defects engineering, and construction of specific geometries to modulate the charge-carrier behaviours and improve the photodetector performance [44]. The photo detection properties of inorganic semiconductor nanostructures such as ZnO, CdS and CdSe have been widely investigated which could pave the way of fabricating suitable photodetectors [45-46]. Among them, ZnO has received much attention as the performance of ZnO based photodetectors can be improved via tunning of surface morphology, doping with metal into ZnO, and functionalization of ZnO surface by noble metal nanoparticles [47]. However, the key issue is that these materials in their pristine form work only in ultraviolet

(UV) region. Also, a proper control over the surface/interface defect states is mandatory for practical application of ZnO nanostructures in photodetection as the modulation of defect states can be governed by the surface/interface treatment [48-49]. Most of ZnO based optoelectronic devices are either photoconductive detectors in thin film transistor (TFT) configuration or they are heterojunction between n-type ZnO and p-type semiconductor materials. The most common selection is p-type silicon due to its distinct advantages, such as abundance, stability, and ease of processing. Recently, the design and fabrication of low-dimensional semiconductor nanostructures/Si NWs composite heterostructures create a wide platform for fabrication of high-performance photodetectors which also overcome the inherent limitations of Si based photodetectors [10]. For an example, a core-shell heterostructure n-ZnO/n^+-Si NWs has been reported for NIR region with a maximum zero biased responsivity of 0.54 A/W [13]. They have claimed that the superior performance of radial junction is corresponding to the large interfacial area and efficient charge carrier collection due to the core (Si NWs)–shell (ZnO) structure. However, most of junctions based (p-n heterostructures) photodetectors have limited gain and the responsivity (mostly $\leq 1\ A/W$) and more importantly the band width of detection is governed by the band gap. But one can break the limitation of detection band width by surface plasmon resonance (SPR) using of plasmonic nanoparticles (NPs) to overcome the limitation of spectral response arising from the band gap of the channel material. In this case the photoconductive channel is not the only place where carrier generation occurs by illumination but also the plasmonic NPs contribute charge carriers into the photoconduction channel. Use of plasmonic metal NPs of aluminium (Al), silver (Ag), nickel (Ni), platinum (Pt) and gold (Au) etc can enhance response in visible region by plasmonic excitation and charge transfer to the active photoconductive channel [50-54]. There is a report of localized surface plasmon resonance (SPR) mediated by Au NPs employed to enhance the visible response of the ZnO nanowires arrays (Figure 1.6 (a)) but seen decrease in UV response (Figure 1.6 (b)). Also, both visible and UV response of this detector decreases with increasing the diameter of Au NPs [53]. There is another report of ligand free surface plasmon resonance of Au NPs implemented to improve the visible response of ZnO nanowires arrays in Figure 1.6 (c). It has been observed that Au NPs those synthesized by chemical route for attachment, need a stabilizing ligand or a dispersive media which affects the surface plasmon resonance of NPs and reduces the inter band transition which degrade the photodetector performances. Data in Figure 1.6 (c) show the responsivity (~ 0.4 A/W in UV region at a bias of 1 V) of Au NPs decorated device that is enhanced not only in the UV region but also in visible region in comparison with bare device [54]. In this report they have also shown that a relatively faster time response in decay of

photocurrent under UV illumination λ = 350 nm (Figure 1.6 (d)) has been achieved due to decoration of Au NPs. This occurs due to transfer of electrons from Au NPs to the defect states of ZnO that promotes the reconversion processes of singly charged oxygen vacancy to neutral vacancy leading to quicker relaxation of the photocurrent.

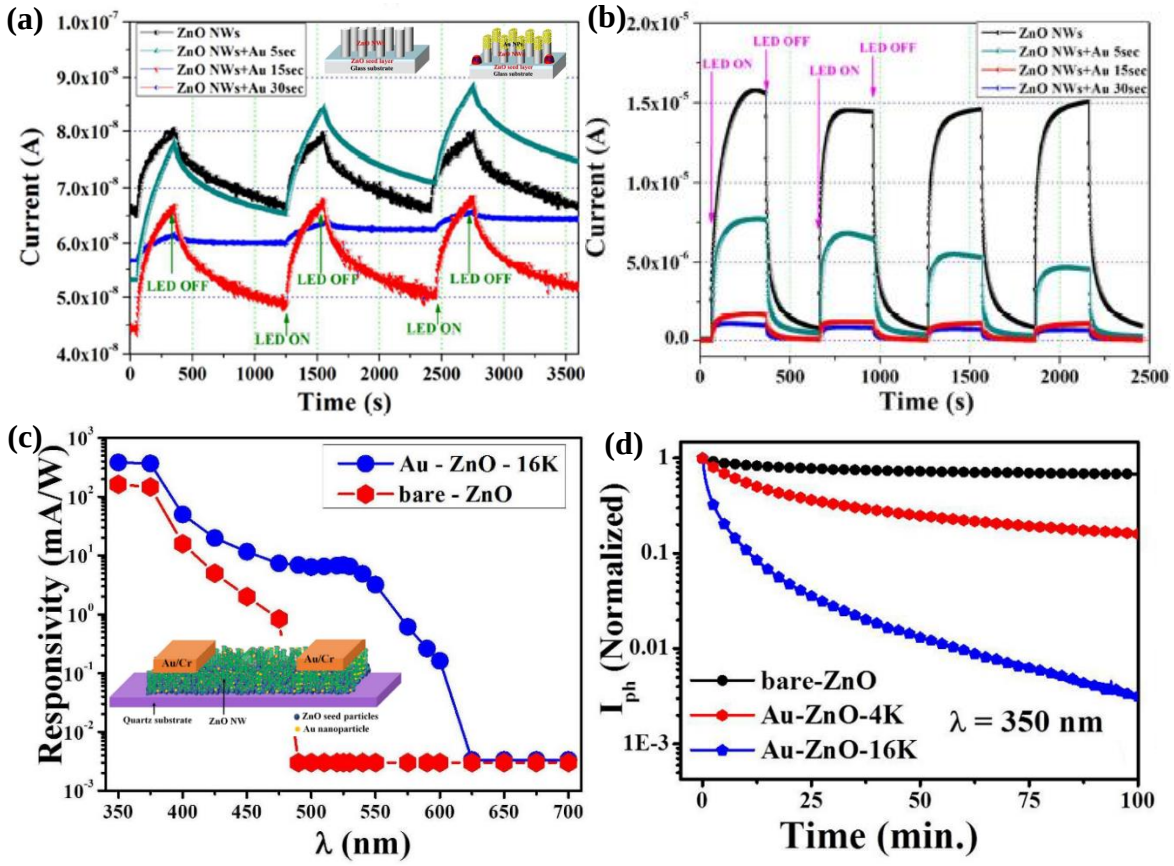

Figure 1.6 Transient photoresponse of ZnO NWs and Au NPs decorated ZnO NWs under (a) UV (b) green LED. The illumination is turned ON and OFF. Reprinted with permission from [53]. (c) Spectral responsivity of Au NPs decorated ZnO NWs device and bare ZnO NWs device, (d) decay of the normalized photocurrent of bare ZnO NWs film and Au-ZnO NWs films for wavelength λ = 350 nm. Reprinted with permission from [54].

From the above observation, we have seen that each of these detectors have a spectral range depending on fundamental band gap of the semiconductor. These photodetectors though easy to operate but certain issues need to be addressed, for instance each of photodetectors used particularly in specific wavelength region that have been working either in ultraviolet (UV) or visible (Vis) or near-infrared (NIR) region. In this thesis further investigation has been carried out to observe how one can extend the response of a ZnO based photodetector in UV to NIR broadband region beyond its fundamental band gap by exploiting the concept of surface "photo gating". The novelty of this work is, we have engineered a photodetector using oxide semiconductor nanostructure and plasmonic nanoparticles innovatively. The concept is

demonstrated in a ligand free plasmonic Au NPs decorated on n-ZnO/p-Si NWs core-shell arrays where n-ZnO is the channel of the photodetector and photo-generated carriers can be transferred to the conduction band of n-ZnO from p-Si nanowire and Au nanoparticles in NIR and visible region respectively. The responsivity of ligand free Au decorated ZnO/p-Si NWs core-shell arrays enhanced significantly not only in visible region but also in UV and NIR in broadband range (300-1100 nm) due to surface resonance coupling of Au NPs with ZnO/p-Si NWs. In addition to good responsivity over an extended wavelength range and no sizeable droop in sensitivity at wavelengths in visible range and shorter wavelength (unlike Si and Ge detectors), extremely low power consumption, the detector has added advantage of ease of fabrication which is compatible with standard semiconductor and TFT processing routes.
We have also investigated how one can tune the photoconduction and photoresponse of ZnO/p-Si NWs nanostructures arrays by modulation of surface/interface trap states.

1.4 Gas sensing properties of metal oxide semiconductors

Metal oxide semiconductors are commonly used as gas sensors in environmental monitoring and in industrial applications [55]. In recent years, in addition to hazardous gas monitoring, new vistas for application are opening up for solid-state gas sensors for use in healthcare such as exhaled breath analysis [56]. The sensor used in exhaled breath analysis would need detection capability of nitric oxide (NO) gas below 1 ppm as NO is a biologically significant molecule and can be utilized as a primary signalling molecule (present in exhaled breath) for non-invasive diagnosis of certain pulmonary diseases such as asthma, bronchitis etc [57]. While most of chemiresistors oxides gas sensors have limitations of detection capability below 10 ppm and high operating temperature. Among them, ZnO based gas sensors are widely investigated because it able to detect a great variety of gases, such as CO_2, H_2S, NO_2, NO, NH_3, and CH_4 [58-61]. The gas sensing mechanism of ZnO sensor is mainly based on the chemical or physical adsorption/desorption of the gas on the surface of ZnO that leads to variation of charge carrier concentration and the resistance [62]. The sensing response of ZnO based gas sensor is strongly affected by operating temperature. The high operating temperature of the sensor is attributed to enhance redox reaction for improving sensing performances. It has been also found that the gas sensing performances of ZnO nanostructure sensor go down due to the reduction of chemisorbed oxygen ions on the surface above optimum operating temperature [63]. Thus, the necessity for the improvement in gas response, rise and recovery time, stability, selectivity, and reproducibility at low operating temperature has paved advanced route for the modification of ZnO nanostructures. The sensing performances can be enhanced via tunning

of surface morphology of ZnO, doping with metal into ZnO, functionalization of ZnO surface by noble metal nanoparticles and UV/visible light activation [58-59, 64-67]. The most studies on ZnO based sensors focus on the influence of surface morphology on gas detection, opening new strategies to fabricate more selective and sensitive gas detectors [68]. For an example, Gupta et. al. studied the gas response for different ZnO nanostructures such as nanowires, nanobelts and tetrapods in the detection of NO and H_2S [58]. Figure 1.7 (a) and (b) show the typical gas response of ZnO nanowires thick film sensors corresponding to H_2S and NO gas respectively. They reported that the sensors based on ZnO nanobelts (Figure 1.7 (c)) are more sensitive to NO gas while tetrapods sensors are more sensitive to H_2S due to larger surface to volume ratio of nanobelts in comparison with nanowires. They claimed that the mechanism for detecting H_2S arises from changes in the only grain boundary resistance, while for the detection of NO it comes from changes in the resistances of both the grain boundary and intragrain. Recently, S. Agarwal et. al. [59] reported surface morphology dependent gas sensing properties of ZnO nanostructures, flower-like ZnO nanostructures and floral assembly of ZnO nanorods, working at high operating temperature of 150-250 ^oC. Both morphologies exhibit good sensitivity towards NO_2 at ppb level at a temperature of 250 ^oC in comparison to the other gaseous species. Figure 1.7 (d) and I show gas sensing response of flower-like ZnO and floral assembly of ZnO nanorods respectively at different NO_2 concentration and different working temperatures. Figure 1.7 (f) shows the gas response of ZnO nanoflowers at different concentration of benzene (C_6H_6) and different working temperatures. Furthermore, they analysed that nanoflowers have larger surface area and surface defects than nanorods leading to much enhance response. Another recent studies for application in nitric oxide (NO) gas sensors is based on ZnO nanospirals using glancing angle deposition technique [69]. However, the operating temperature for this sensor was high ranging from 100 to 300 ^oC. Another way to improve the gas sensing performance of ZnO is by doping with metal such as Au, Ag, Pt and Pd or functionalization of ZnO surface by noble metal nanoparticles [70-72]. There is a recent report of highly sensitive NO (order of ppb) gas sensor based on novel Ag-doped ZnO nanoflowers working at high operating temperature ranging from 100 to 300 ^oC [72]. However, the working temperature can be reduced to 150 ^oC by UV-LED illumination.

Although, the morphology tuning and surface functionalization can improve the gas sensitivity of ZnO based devices. However, combining ZnO with other materials is also a common strategy [73-75]. Furthermore, the construction heterojunctions can enhance the catalytic activity and formation of electron depletion layers and more adsorption sites improve the gas

sensing properties of the devices. However, the choice of integrated materials with ZnO for further enhancement of gas sensing performance needs to be addressed.

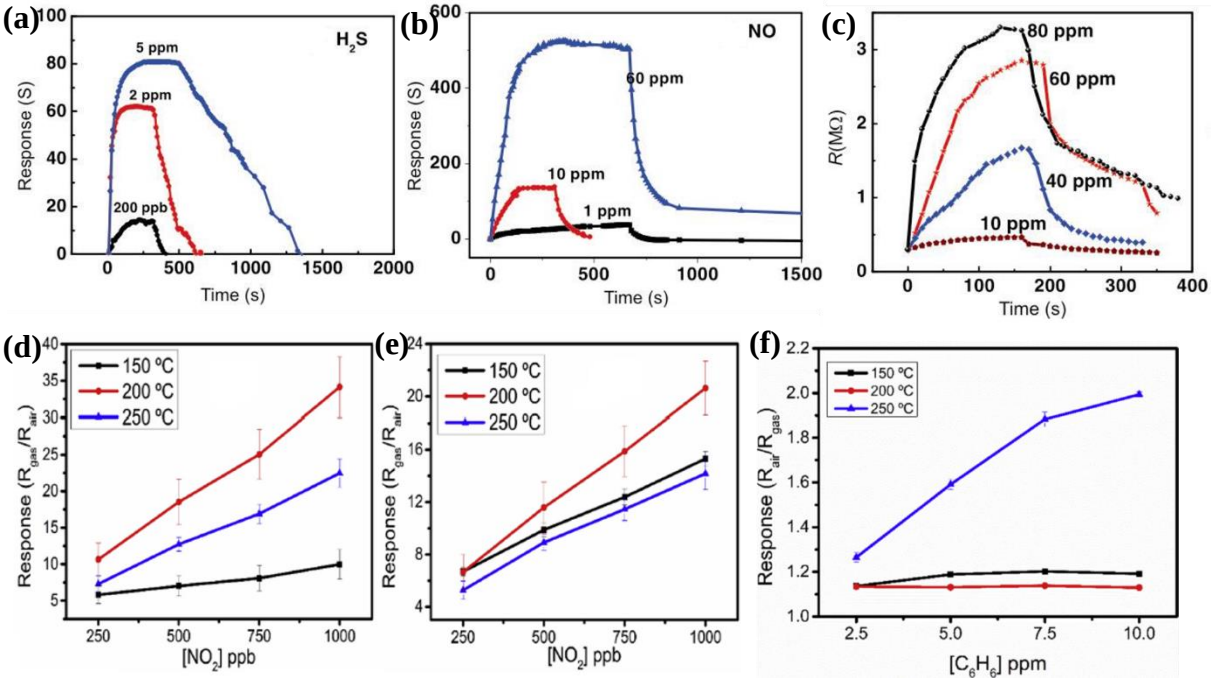

Figure 1.7 Gas response and recovery curves of ZnO nanowires thick film type sensor to different concentrations of (a) H_2S and (b) NO gas. (c) Resistance changes of ZnO nanobelts sensor on exposure to different concentrations of NO gas. Reprinted with permission from [58]. Gas response of (d) ZnO nanoflowers, (e) ZnO nanorods at different NO_2 concentration. (f) Gas response of ZnO nanoflowers at different C_6H_6 concentration and different working temperatures. Reprinted with permission from [59].

In parallel with semiconductor oxide-based gas sensors, Si nanowires (NWs) arrays and porous silicon have attracted much current attention as new generation of enabling sensor materials that can be integrated with other active materials to make heterostructures or FET type device structures that can be used for gas sensing with enhanced capability [76-79]. Recently, hybrid structures of ZnO nanorod/porous silicon nanowire n-n heterojunctions showed gas sensing performance for various NO_2 concentration at room temperature with a gas detection capability down to 5 ppm [80]. Moreover, they mentioned that the response of hybrid structure is much greater than that of individual silicon nanowire and ZnO nanorod gas sensor working individually and the distinct enhancement is mainly attributed to the faster carrier transportation after combination and the increase in gas sensing areas and the oxygen vacancy (V_o) concentration.

From the above study it is concluded that most of ZnO based gas sensor worked at high operating temperature in the range of 100 to 300 ^oC. In such sensors, there is need of heated operation thus requiring additional heater arrangements as well as enhanced power

consumption which is indeed a bottle-neck. In this thesis further investigation has been carried out to engineer ZnO into heterojunctions innovatively and how one can tune the charge carriers in ZnO heterostructure based devices by gas injection leading to room temperature operation ultra-high sensitive (~ 500 ppb) nitric oxide (NO) gas sensor. We have also proposed an in-depth gas sensing mechanism to help better understanding of the gas sensing process. The proof of concept of ultra-high sensitive nitric oxide (NO) gas sensor along with gas sensing mechanism has been patented and development of prototype is in final stage of processing which can be utilized as biomarker in exhaled breath analysis for non-invasive diagnosis of certain pulmonary diseases such as asthma, bronchitis, airflow limitation leading and chronic obstructive pulmonary disease (COPD).

1.5 Overview of electric double layer transistors (EDLTs)

The modulation of charge carriers by using electric double layer (EDL) gate dielectric in a field effect transistor (FET) device has recently emerged as a strong tool for electrostatic modulation of electronic states in solids [8, 81-82]. The key feature in electric double-layer transistor is the formation of electric double layers based on electrolytes such as ionic liquids and polymer electrolytes with mobile charges which induces an ultra-high charge carrier density on the surface of the channel [83]. Figure 1.8 shows the structure and operational mechanism of an EDL capacitor where double layer is formed between the electrodes and electrolyte under an external electric field. Moreover, the capacitance is proportional to the surface area of the electrical double layer.

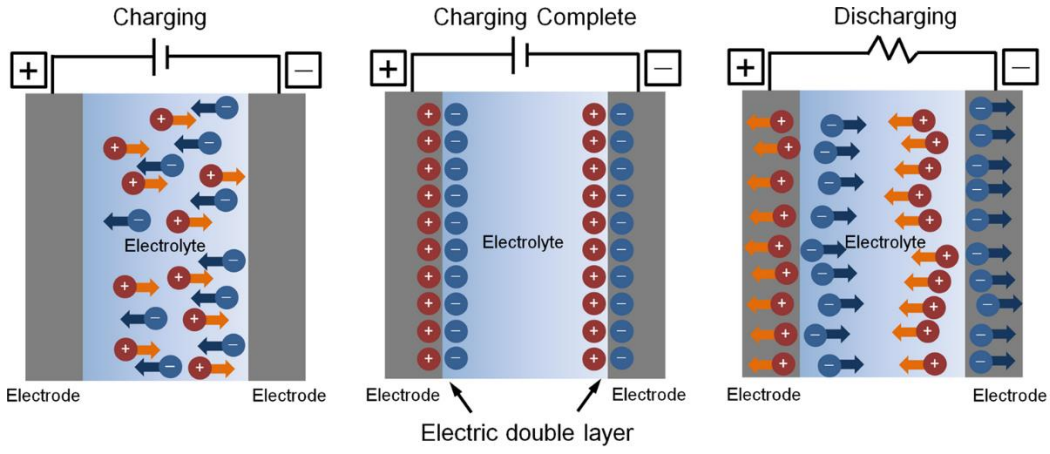

Figure 1.8 Charging and discharging of EDL capacitor. Reprinted with permission from [81].

Three fundamental models have been suggested to explain the EDL theory. The early model was proposed by von Helmholtz (Figure 1.9 (a)) where EDL is formed at the electrode/electrolyte interface separated by an atomic distance H. This model is analogous to

the conventional dielectric capacitors. Later, this Helmholtz model was further modified by Gouy and Chapman by considering a uniform distribution of ions in electrolyte (Figure 1.9 (b)). Here, the charge distribution follows the Maxwell-Boltzmann statistics and the electric potential decreases exponentially away from the surface of the electrode. However, the Gouy–Chapman model gives to an over estimation of the EDL capacitance. Later, Stern combined these two models by considering two regions of ion distribution (Figure 1.9 (c)), the inner region called the Helmholtz layer or Stern layer and the outer region called the diffused layer. The distance of the diffused layer is increasing with increasing the concentration of the ions. The total EDL capacitance (C_{EDL}) consists of the stern layer capacitance (C_H or C_{st}) and diffuse layer capacitance (C_{Diff}) in series and can be expressed by the following equation [84]:

$$\frac{1}{C_{EDL}} = \frac{1}{C_H} + \frac{1}{C_{Diff}}$$

The specific capacitance of the Helmholtz double layer denoted by C_H is given by

$$C_H = \frac{\varepsilon_0 \varepsilon_r}{H}$$

Where ε_0 and ε_r are the free space permittivity and the relative permittivity of the electrolyte solution respectively.

The diffused layer specific capacitance is given by

$$C_{Diff} = \frac{\varepsilon_0 \varepsilon_r}{\lambda_D} \left(1 + \frac{\lambda_D}{R_0}\right)$$

Here the λ_D is the Debye length for symmetric electrolytes and R_0 is the length of the diffuse layer.

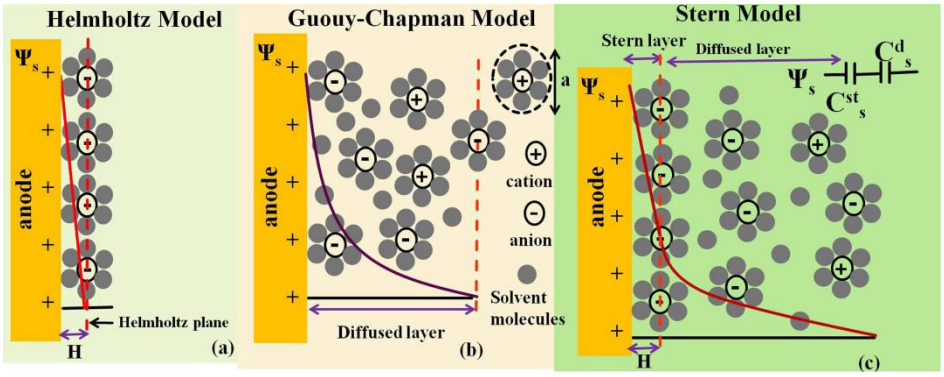

Figure 1.9 Schematic illustration of the different model of electrical double layer at a positively charged surface. (a) The Helmholtz model, (b) the Gouy–Chapman model and (c) the Stern model. Reprinted with permission from [8].

The behaviour of EDL is dependent on the several factors such as electrical field across the electrode, types of electrolyte ions, and the electrode surface that determine the value of EDL

capacitance. The distance between the ions layer in electrolyte and the charges layer in electrodes is about a nanometre range which is equivalent to thickness of the double layer. This nano gap thickness induces a huge capacitance at the interface [81]. It can modulate the charge carrier density of the semiconducting channels electrostatically at low operation voltage which has paved the way in high performance EDL transistors (EDLTs). On the other hand, metal oxide semiconductors have high value of background charge carrier density which is often in excess of $10^{19}/cm^3$. The conventional oxide gate dielectrics used in FET device have low charge accumulation capacity due to their low value of specific gate capacitances in the order of ~ nF/cm^2 and the value of gate capacitance is limited by their thickness. So, the conventional oxide gate dielectric unable to modulate such high value of charge carriers appropriately which also justify the need of the electric double layer (EDL) gate dielectric in a metal oxide FET device. Figure 1.10 shows the configuration of electric double layer transistor (EDLT) based on oxide semiconductor channel. In this configuration, double layer is formed at gate /electrolyte and semiconductor/electrolyte interface when a gate bias is applied.

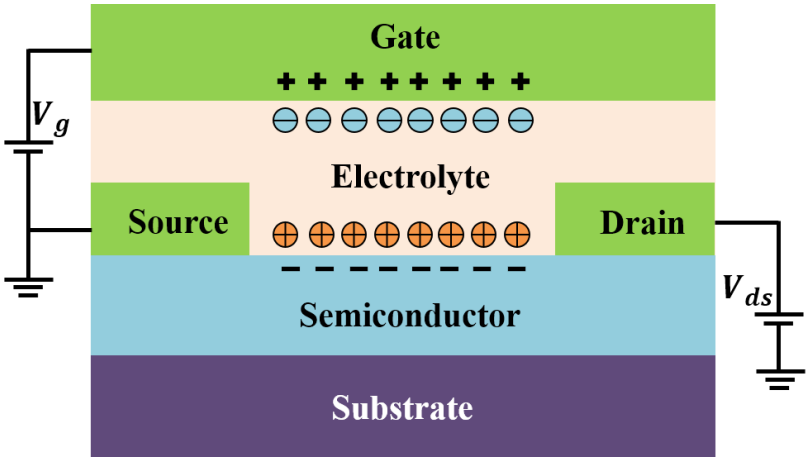

Figure 1.10 Configuration of the electric double layer transistor.

The EDL gated transistor mostly use the ionic liquids and polymer electrolytes due to their low operation voltage [85-86]. The polymer electrolyte can also be dispensed on the semiconductor oxide channel at room temperature and there is no need of vacuum, unlike conventional oxide gate dielectrics where deposition of gate dielectric requires a high vacuum and often high temperature. The low processing temperature of the EDL gate electric has natural compatibility with the flexible substrate. Thiemann et. al. [86] reported the electrical characteristics of IL gated field effects transistors (FETs) based on polycrystalline ZnO with charge accumulation capability of up to 10^{13} cm^{-2}. However, this high carrier density yielded an average field-effect mobility of ~16 cm^2/Vs and current ON/OFF ratio of 10^3-10^4. Recently use of low processing oxide semiconductors, especially amorphous one, has paved the way in future paper

electronics. Furthermore, amorphous oxides do not have grain boundaries which reduces the scattering of charge carriers resulting in remarkable progresses in high performance flexible TFTs [87]. Very recently, Ghimire and Raychaudhuri reported the electrolyte gated EDL flexible thin film transistor based on nanocrystalline ZnO [88]. They also demonstrated high density charge carrier accumulation of up to 10^{14} cm^{-2} yielding a low threshold ($V_{th} \leq 1$ V) and a high saturation mobility ~ 70 cm^2/V-s. Fujii et. al [89] and Park et. al. [90] successfully demonstrated low voltage operated amorphous oxide (indium gallium zinc oxide) (IGZO) electric double layer TFT using ionic liquids or polymeric electrolytes although these TFTs are not compatible with the flexible electronics and did not yield a field effect mobility more than 20 $cm^{2/}$Vs. Recently, Zhou et. al. [91] reported IGZO electric double layer transistor using SiO_2 based electrolyte on polyethylene terephthalate substrates, although the response is low compared to ionic liquids or polymeric electrolytes-based dielectric and there is no report of polymer electrolyte or ionic liquid gated amorphous-IGZO TFT on flexible substrates. Hence, materials with a high dielectric constant (high- κ) are preferable because this increased capacitance induces high charge carrier density, decreasing the subthreshold swing (SS) and threshold voltage (V_{th}). But most of the high- κ dielectrics can degrade the performance and stability of oxide TFTs because of their polycrystalline structure, since grain boundaries act as favourable paths for impurities diffusion and leakage current and degraded interface properties. In this thesis further investigation has been carried out to observe how one can tune charge carrier in doped ZnO (i.e., amorphous-IGZO oxide channel) grown on flexible substrate by using electric double layer (EDL) gate dielectric formed the EDL gate capacitance at oxide/electrolyte interface with large specific gate capacitance (≈ 31 μF/cm^2). This induces an ultra-high charge carrier density on the surface of the channel and device can operated with low threshold voltage. This understanding of charge carrier induction in oxide semiconductor by field effect using electric double layer (EDL) gate has been studied trough several experiments in this thesis work. The understanding and invention lead good contribution to flexible electronics. This proof of concept has been patented and activities related to packaging of prototype/product are in the final stage of processing.

1.6 Motivation of the present work

On the basis of the above discussions the main aim of this thesis is given below:

- Size reduction to nano dimension of oxide semiconductors leading to quantum confinement phenomena that modify their intrinsic properties with respect to their corresponding bulk properties. Among the several physical parameters like doping, temperature, strain etc. The

innovative integration of oxide semiconductor into heterojunction with 1D nanostructure can also be an interesting concept to tune the electrical, optical and other physical properties of oxide semiconductors in practical application to electronic and other sensing devices. These application prospects depend on the successful integration of oxide semiconductor with 1D nanostructure into heterojunction of very good quality (so that one can get definite results) and pure phase material with proper chemical composition and controllable size, shape and morphology. The basic physics as well as application potential related to electrical, optoelectronic and other areas using this metal oxide semiconductor heterojunction with 1D nanostructures has not been explored much till date, very few reports are available in this regime [11-13].

- The basic physical idea that has been utilized in this thesis is the effect of growth techniques and standardization of growth parameters that can tailor size, shape, morphology and homogeneity of semiconductor oxide nanostructures. One of the pertinent questions is that how the device structure and growth process can be modified to increase the device performances and also provide substantiable results. Spatially resolved tools for developing cross sectional sample and in-depth microstructural as well as chemical compositional analysis of the cross-section of the device enables us to make a proper physical model and that can be utilized to make a model-based simulation of the devices. One of our aim of the present work is to study the above issues and also to standardize the different growth methods to materialize semiconductor nanostructures of very good quality with controlled electronic and optoelectronic properties for use in practical applications.

  Control of the electrical and optical properties of oxide semiconductors is a key requirement for practical applications in optoelectronic and other sensing devices. Metal oxides have uncontrollable charge carriers due to oxygen vacancies and other defects. The control of carriers has been achieved generally by doping or surface treatment by annealing. But tunning of charge carrier can also be done by exposure to band gap illumination as well as by field effect using gate. No detailed study is available on this aspect till date to the best of our knowledge. So, the primary objective in this thesis focuses on the tuning of charge carriers by using the following; i) photo-gating, ii) gas injection or by iii) field effect using electric double layer (EDL) gate and to understand the basic physics underlying the charge carrier transport phenomena in oxide semiconductors.

- One of novelty of the thesis work is the tuning of charge carriers by **photo-gating** in semiconductor oxide nanostructure arrays. Most of oxide semiconductors based MSM

photodetector, the response is generally limited by its fundamental absorption edge. So, the main purpose of this work is how to extend the response of a photodetector beyond its fundamental band gap by exploiting the concept of surface "photo-gating" where photo generated carriers created in materials with different band gaps can be transferred to the conduction band of the photo-detector material. This can give rise to a broadband detector that work over an extended range from UV to NIR.

In our work, the concept is demonstrated in Au nanoparticles decorated on n-ZnO/p-Si NWs core-shell arrays where n-ZnO is the channel of the detector and photo-generated carriers from p-Si nanowire and Au nanoparticles in NIR and visible wavelength ranges respectively can be transferred to the conduction band of n-ZnO using a favorable band alignment leading to a UV-VIS-NIR (broadband, 300-1100 nm) photo detector, which has a very good application potential.

- Another novelty of the thesis work is tuning of charge of carriers in the oxide semiconductor heterostructure devices by **gas injection** leading to ultra-high sensitive (~ 500 ppb) nitric oxide (NO) gas sensor. Our aim of the present work is to engineer oxide semiconductor heterojunctions innovatively to improve the gas sensing performance of oxide semiconductors by increasing the gas adsorption sites which gives rise to more oxygen vacancies and increasing the surface activity to catalyse the reaction. The heterostructure based devices have been proposed recently that go beyond conventional chemiresistors due to their enhanced surface to volume ratio, higher gas diffusion rate and enhanced reactivity. So, it is necessary to propose an in-depth gas sensing mechanism to help us better understanding of the gas sensing process. However, no detailed gas sensing study has been done on oxide heterostructures arrays to the best of our knowledge. In this particular ZnO/p-Si NWs based device, the enhanced sensitivity of heterojunction comes from enhancement of charge carrier density through the ingenious use of heterojunction of ZnO and Si NWs on gas exposure. It can be noted that this hetero structure builds a synergy that leads to much enhanced sensitivity compare to either of the constituent material (like only ZnO or only Si NWs).
- **Field effect using electric double layer (EDL) gate** is also another proposition to tune charge carrier in the proposed oxide semiconductor device under study. The carrier mobility is the dynamic factor of metal oxide FET devices and it depends on the areal capacitance of the gate dielectric as well as the characteristics of oxide semiconductors. In the TFTs making of devices with the higher carrier density and lower threshold voltage is

challenging. The spherically symmetrical *ns*-orbital of metal oxide even in the amorphous state provides the small effective masses of electron and the efficient electron transport which reduce the charge carrier scattering and improve the device performance. It has been observed that specific gate capacitances of a conventional dielectrics used in FET device are in the order of ≈ nF/cm^2 and it can be controlled by thinning dielectric layer but give rise a large gate leakage current. Hence, materials with a high dielectric constant are indeed highly preferable because this increased capacitance can compensate the higher density of interface traps, decreasing subthreshold swing (SS) and the operating voltage.

- The electrical conductivity and photosensitivity of oxide semiconductors are strongly dependent upon the concentration of surface-interface defects and the photoconduction of oxides can be improved by tuning surface-interface defect suitably. The carrier recombination emission, in particular, if it is associated with impurity or defect states emission then one can interrelate the inter dependence between the defects and photo-conduction of oxide nanostructures with different growth methods. These defects can act as preferential sites for physical/chemical adsorption of environmental species that can introduce additional scattering/capturing of the photo-generated charge carriers that could hamper the performances of photodetector. So, our interest is to control the surface/interface defects of the heterojunction for utilization of oxide semiconductors in device applications.

1.7 Structure of the thesis

This thesis is framed on the following works: (1) growth of semiconductor oxide nanostructures (ZnO/Si NWs nanostructure arrays) and thin film of doped ZnO; indium gallium zinc oxide (IGZO) and their structural characterizations, (2) description of experimental methods and study of interface along with physical structure of the devices using advance tools and techniques, (3) effects of photo-gating in broadband photoresponse of plasmonic nanoparticles decorated core-shell arrays of oxide nanostructure, (4) investigation of electrical properties of oxide heterostructures through the injection of charge carrier by gas, (5) electrical characteristics of electric double layer thin film transistor with amorphous oxide channel on flexible substrate, and (6) defects control broadband photoconduction in oxide nanostructures arrays. Control of the electrical and optical properties of oxide semiconductors is a key requirement for practical applications in optoelectronic and other sensing devices. In this thesis the tuning of charge carriers has been done by using photo gating, gas injection or by field effect using electric double layer (EDL) gate and to understand the basic physics underlying

the charge carrier transport phenomena in oxide semiconductors. **The novelty of this thesis work is the integration of oxide semiconductor into heterojunction (both p-n and n-n junction) with silicon nanowires (Si NWs arrays) innovatively and tunning of the optoelectronics and gas sensing properties by making (a) heterostructures, (b) FET type device structures and (c) by decorating with plasmonic nanoparticles (Au) with metal oxide nanostructures.** In this thesis, we have concentrated on heterojunction arrays of ZnO/Si NWs and thin film of doped ZnO; indium gallium zinc oxide (IGZO). The basic physics and technological aspects related to electrical and optoelectronic and other areas using this metal oxide semiconductor heterojunction with 1D nanostructures has not been explored much till date, very few reports are available in this regime [11-13].

This thesis is divided into eight main chapters along with summary and one appendix chapter listed below:

1. In this present introduction chapter, we presented a brief overview of basic physical properties of metal oxide semiconductors. This chapter also includes the necessary literature survey of earlier work of oxide semiconductors in the field of optoelectronics, gas sensing and field effect devices followed by motivation and objective of the present work.
2. The 2^{nd} chapter gives a description of controlled and optimized growth of oxide semiconductors nanostructures and thin film by different growth methods (physical and chemical) and details characterization along with development of experimental set-up.
3. The 3^{rd} chapter describes fabrication of two/three terminal nano devices and experimental techniques for electrical, optoelectronic and gas sensing measurements. This chapter also provides details about the study of interface along with physical structure of the devices using spatially resolved advance tools and techniques like cross-sectional TEM (XTEM), focused ion beam based lithography etc.
4. The 4^{th} chapter describes, how the tuning of charge carriers is done using photo gating in plasmonic (Au) nanoparticle decorated oxide semiconductor (ZnO/doped ZnO) heterojunction with silicon nanowires (Si NWs arrays). The details experimental study and also photo conduction mechanism has been described in this chapter to show how the device engineering makes it very good broadband (300-1100nm) photo detector. The main purpose of this work is to extend the response of a photodetector beyond its fundamental band gap by exploiting the concept of surface "photo-gating". The optical detector combines the visible and NIR detectability of Si NWs with the UV detectivity of ZnO through the core-shell structure and enhanced broadband detectivity in the visible range has been achieved by decorating core-shell arrays with ligand-free Au NPs. The significant

enhancement of optical response and photoconductive gain in visible region can also be correlated with enhancement of absorption in visible region due to surface plasmon resonance (SPR) coupling of Au NPs with ZnO. Novelty of our work is; we have engineered the oxide semiconductor nanostructure device with plasmonic nanoparticles innovatively to make very good broadband photodetector.

5. The 5th chapter explains, how the injection of charge carrier by gas through the interface of ZnO and Si NWs leading to ultra-high sensitive (~ 500 ppb) nitric oxide (NO) gas sensor even at room temperature. These heterostructures devices go beyond the conventional chemiresistors based gas sensor. In the previous chapter (chapter 4), we have discussed how photo-gating effects tuned the charge carriers in broadband photoconduction of Au NPs decorated ZnO/p-Si NWs arrays. In this chapter, we would like to explore that charge carriers can also be induced by gas injection innovatively in ZnO/Si NWs heterojunction devices. Here the hetero-structure builds a synergy that leads to much enhanced sensitivity that can be obtained from either of the materials. In this particular ZnO/p-Si NWs based device, the enhanced sensitivity of heterojunction comes from enhancement of charge carrier density through the interface of ZnO and p-Si NWs on gas exposure. A mechanism has been proposed for operation of the sensor and been validated by numerical simulation. The simulation shows the essentiality of the heterojunction in the enhancement of sensitivity over that expected from chemiresistor mechanism. The Proof of concept on ultra-high sensitive NO gas sensor has been patented (patent application no: *201731038036*) and a prototype has been fabricated.
6. The 6th chapter demonstrates the electrical characteristics of electric double layer thin film transistor with doped ZnO (amorphous indium gallium zinc oxide) channel on flexible substrate. A details description has been done in chapter 4 and 5 on tuning of charge carriers by the effects of photo-gating in optoelectronic studies and by gas injection in the heterojunction to understand the charge carrier transport phenomena in oxide semiconductors respectively. In this chapter, we have shown the charge carrier induction through EDL as a gate dielectric (a solid polymer electrolyte) formed the EDL gate capacitance at oxide/electrolyte interface with large specific gate capacitance ($\approx \mu F/cm^2$). This induces an ultra-high charge carrier density on the surface of the channel and this high value of EDL gate capacitance easily modulated the carrier density of oxide semiconductors and device can operated with low threshold voltage. These issues have been explained in great detail through experimental observations in this chapter. The Proof of concept has been patented and a prototype has been fabricated. The present finding using

EDL gate has been applied for patent filing (patent application no: *201731015268*) and a prototype is under final stage of processing.

7. The 7th chapter explains the role of surface-interface defects on photoconduction mechanism of ZnO/p-Si NWs nanostructures arrays. In chapter 4, we have discussed how photo-gating effects tunned the charge carriers in broadband photoconduction of ZnO/p-Si NWs arrays decorated with plasmonic Au NPs. Here we have demonstrated how the optical response of ZnO/p-Si NWs photodetectors can be tuned by changing the surface-interface defects and transport of charge carriers is strongly dependent on the different concentration of defects with processing conditions experimentally. We have also shown that the photodetection performances of ZnO/p-Si NWs nanostructures are strongly dependent on the functionality of surface-interface state where existence of undesired recombination sites can hamper the carrier transport as well as photoconduction.

Last chapter is the summary and conclusions of this thesis. It also describes the main achievements of the thesis and scope for future works and challenges.

Finally, this thesis ends up with appendix describing wavelength dependent persistence photoconductivity and the behaviour of photo response properties of doped ZnO; indium gallium zinc oxide (IGZO) thin film grown by pulsed laser deposited on quartz.

Bibliography

1. D. Nunes, A. Pimentel, A. Gonçalves, S Pereira, R. Branquinho, P. Barquinha, E. Fortunato and R. Martins, *Semicond. Sci. Technol*., **34**, 043001 (2019).
2. K. Nomura, H. Ohta, A. Takagi, T. Kamiya, M. Hiranoand H. Hosono, *Nature*, **432**, 488 (2004).
3. R. Martins, I. Ferreira and E. Fortunato, *Phys. Status Solidi RRL*., **5**, 332 (2011).
4. L. S. Mende and J. L. Driscoll, *Mater. Today*, **10**, 40 (2007).
5. T. Zhai, X. Fang, M. Liao, X. Xu, H. Zeng, B. Yoshio and D. Golberg, *Sensors*, **9**, 6504 (2009).
6. S. Mondal and A. K. Raychaudhuri, *Appl. Phys. Lett*., **98**, 023501 (2011).
7. J. Nomoto, H. Makino, T. Yamamoto, *J. Appl. Phys*., **117**, 045304 (2015).
8. R. R. Ghimire "Investigation Of Opto-Electronic Phenomena In Nanostructured ZnO With Electric Double Layer Gate", Ph.D. Thesis (2016), University of Calcutta, Kolkata, India.
9. W. Tian, H. Sun, L.Chen, P. Wangyang, X. Chen, J. Xiong, and L. Li, *InfoMat*., **1**, 140 (2019).
10. J. Kim, A. Mirzaei, J. H. Bang, H. W. Kim, and S. S. Kim, *Sens. Actuators B*, **300**, 126981 (2019).
11. H. Kang, J. Park, T. Choi, H. Jung, K. H. Lee, S. Im, and H. Kim, *Appl. Phys. Lett.* **100**, 041117 (2012).
12. D. Liu, X. Shen, T. Song, J. Hu, and B. Sun, *Phys. Chem. Chem. Phys*., **15**, 4970 (2013).
13. O. Graniel, et. al., *Mater. Sci. and Eng.: B*, **236**, 139 (2018).
14. H. Y. Chen, H. Liu, Z. Zhang, K. Hu, and X. S. Fang, *Adv. Mater.*, **28**, 403 (2016).
15. T. Okino, S. Yamahira, S. Yamada, Y. Hirose, A. Odagawa, Y. Kato, and T. Tanaka, *Sensors*, **18**, 314 (2018).
16. U. Ozgur, Ya. I. Alivov, C. Liu, A. Teke, M. A. Reshchikov, S. Dogan, V. Avrutin, S. J. Cho, and H. Morkoc, *J. Appl. Phys*., **98**, 041301 (2005).
17. M. H. Huang, S. Mao, H. Feick,H. Yan, Y. Wu, H. Kind, E. Weber, R. Russo, and P. Yang, *Science*, **292**, 1897 (2001).
18. R. Kumar, A. Umar, G. Kumar, H.S. Nalwa, A. Kumar, and M.S. Akhtar, *J. Mater. Sci*., **52**, 4743 (2017).
19. B. Wen, Y. Huang, and J. J. Boland, *J. Phys. Chem. C*, **112**, 106 (2008).
20. M. R. Alenezi, A. S. Alshammari, K. D. G. I. Jayawardena, M. J. Beliatis, S. J. Henley, and S. R. P. Silva, *J. Phys. Chem. C*, **117,** 17850 (2013).
21. S. Xu and Z. L. Wang, *Nano Res*., **4**, 1013 (2011).
22. Y. Dong, Z. Q. Fang, D. C. Look, D. R. Doutt, G. Cantwell, J. Zhang, J. J. Song, and L. J. Brillson, *J. Appl. Phys*., **108**, 103718 (2010).
23. D.C Look, *Mater. Sci. Eng. B*, **80**, 383 (2001).
24. F. A. Selim, M. H. Weber, D. Solodovnikov, and K. G. Lynn, *Phys. Rev. Lett.*, **99**, 085502 (2007).
25. D. G. Thomas, and J. J. Lander, *J. Chem. Phys*., **25**, 1136 (1956).
26. C. G. Van de Walle, *Phys. Rev. Lett*., **85**, 1012 (2000).
27. B. M. Ataev, A. M. Bagamadova, A. M. Djabrailov, V. V. Mamedov, and R. A. Rabadanov, *Thin Solid Films*, **260**, 19 (1995).

28. M. Caglar, Y. Caglar, and S. Ilican, *Phys. Status Solidi C*, **4**, 1337 (2007).
29. A. Tsukazaki, A. Ohtomo, T. Onuma, M. Ohtani, T. Makino, M. Sumiya, K. Ohtani, S. F. Chichibu, S. Fuke, Y. Segawa, H. Ohno, H. Koinuma, and M. Kawasaki, *Nat. Mater*., **4**, 42 (2005).
30. O. Schmidt, A. Geis, P. Kiesel, C. G. Van de Walle, N. M. Johnson, A. Bakin, A. Waag, and G. H. Dohler, *Superlattice and Microstructure*, **39**, 8 (2006).
31. M. A. Borysiewicz, *Crystals*, **9**, 505 (2019).
32. A. B. Djurisic, and Y. H. Leung, *small*, **2**, 944 (2006).
33. J. Grabowska, A. Meaney, K. K. Nanda, J.-P. Mosnier, M. O. Henry, J.-R. DuclQre, and E. McGlynn, *Phys. Rev. B*, **71**, 115439 (2005).
34. J. Jie, G. Wang, Y. Chen, X. Han, Q. Wang, B. Xu, and J. G. Hou, *Appl. Phys. Lett*., **86**, 031909 (2005).
35. M. D. McCluskeyand S. J. Jokela, *J. Appl. Phys*., **106**, 071101 (2009).
36. M. D. McCluskey, Defects in ZnO, Defects in Advanced Electronic Materials and Novel Low Dimensional Structures, *Woodhead Publishing Series in Electronic and Optical Materials*, 2018.
37. M. Wang,Y. Zhou, Y. Zhang, E. J. Kim,S. H. Hahn,and S. G. Seong,*Appl. Phys. Lett*., **100**, 101906 (2012).
38. P. Nunesa, E. Fortunatoa, P. Tonelloa, F. B. Fernandesa, P. Vilarinhob, and R. Martinsa, *Vacuum*, **64**, 281 (2002).
39. X. Yu, T. J. Marks, and A. Facchetti1, *Nat. Mater*., **15**, 383 (2016).
40. N. Kimizuka, M. Isobe, and M. Nakamura, *J. Solid State Chem*., **116**, 170 (1995).
41. K. Nomura, T. Kamiya, H. Ohta, T. Uruga, M. Hirano, and H. Hosono, *Phys. Rev. B*, **75**, 035212 (2007).
42. T. Kamiya, K. Nomura, and H. Hosono, *J. Disp. Technol*., **5**, 468 (2009).
43. T. Kamiya and H. Hosono, *NPG Asia Mater.*, **2**, 1522 (2010).
44. W. Ouyang, F. Teng, J. H. He, X. Fang, *Adv. Funct. Mater*., **29**,1807672 (2019).
45. W. Jin and L. Hu, *Nanomaterials*, **9**, 1359 (2019).
46. P. Giraud, B. Hou, S. Pak, J. I. Sohn, S. Morris, S. N. Cha, and J. M. Kim, *Nanotechnology*, **29**, 075202 (2018).
47. B. D. Boruah, *Nanoscale Adv*., **1**, 2059 (2019).
48. S. Mondal and D. Basak, *Appl. Surf. Sci*., **427**, 814 (2018).
49. J. Jiang, C. Ling, T. Xu, W. Wang, X. Niu, A. Zafar, Z. Yan, X. Wang, Y. You, L. Sun, J. Lu, J. Wang, Z. Ni, *Adv. Mater.* **2018**, *30*, 1804332.
50. J. Lu, C. Xu, J. Dai, J. Li, Y. Wang, Y. Lin, and P. Li, *Nanoscale*, **7**, 3396 (2015).
51. P. Biswas, S. R. Cho, J. W. Kim, S. D. Baek, and J. M. Myoung, *Nanotechnology*, **28**, 225502 (2017).
52. G. Jayalakshmi, K. Saravanan, *J. Mater. Sci.: Mater. Electron.*, **31**, 5710 (2020).
53. C. L. Hsu, L. F. Changa, and T. J. Hsueh, *RSC Adv.*, **6**,74201 (2016).
54. R. R. Ghimire, R. Nath, R. K. Neogy, and A. K. Raychaudhuri, *Nanotechnology*, **28**, 295703 (2017).
55. M. M Arafat, B Dinan, S. A. Akbar, and A. S. M. A. Haseeb, *Sensors*, **12**, 7207 (2012).
56. M. Righettoni, A. Tricoli, and S. E. Pratsinis, *Anal. Chem*., **82**, 3581 (2010).

57. A. Rydosz, *Sensors*, **18**, 2298 (2018).
58. S. K. Gupta, A. Joshi, and M. Kaur, *J. Chem. Sci*., **122**, 57 (2010).
59. S. Agarwal, P. Rai, E.N. Gatell, E. Llobet, F. Güell, M. Kumar, and K. Awasthi, *Sens. Actuators B*, **292**, 24 (2019).
60. M. A. Basyooni, M. Shaban, and A. M. Sayed, *Sci. Rep*., **7**, 41716 (2017).
61. K. J. Iversen, and M. J. S. Spencer, *J. Phys. Chem. C*., **117**, 26106 (2013).
62. A. Dey, *Mater. Sci. Eng. B*, **229**, 206 (2018).
63. Z. Jing, and J. Zhan, *Adv. Mater*., **20**, 4547 (2008).
64. V. Postica et. al., *Adv.Funct. Mater*., **27**, 1604676(2017).
65. S. G. R, N. Mi, V.L. Patil, P. S, M. C, S. Kawasaki, P.S. Patil, and Y. Hayakawa, *Sens. Actuators B*, **255**, 672 (2018).
66. L. D. Bastatas, P. Wagle, E. Echeverria, A.J. Austin, and D.N. McIlroy, *Materials*, **12**, 302 (2019).
67. Q. Zhang, G. Xie, M. Xu, Y. Su, H. Tai, H. Du, and Y. Jiang, *Sens. Actuators B*, **259**, 269 (2018).
68. V. S. Bhati, M. Hojamberdiev, and M. Kumar, *Energy Rep*., **6**, 46 (2020).
69. P. Luo, M. Xie, J. Luo, H.Kanb, and Q. Wei, *RSC Adv*., **10**, 14877 (2020).
70. M.W. Maswanganye, K.E. Rammutla, T.E. Mosuang, and B.W. Mwakikunga, *Sens. Actuators B*, **247**, 228 (2017).
71. J. H. Kim, A. Mirzaei, H. W. Kim, P. Wu, and S.S. Kim, *Sens. Actuators B*, **293**, 210 (2019).
72. Y. T. Tsai, S. J. Chang, L. W. Ji, Y. J. Hsiao, I. Tang,H. Y. Lu,and Y. L. Chu, *ACS Omega*, **3**, 13798 (2018).
73. H. Naderi, S. Hajati, M. Ghaedi, and J.P. Espinos, *Sens. Actuators B*, **297**, 126774 (2019).
74. S. Tata, L. Chabane, N. Zebbar, M. Trari, M. Kechouane, and A. Rahal, *Mater. Sci. Semicond. Process*., **109**, 104926 (2020).
75. P. Srinivasan and B.G. Jeyaprakash, *J. Alloys Compd*., **768**, 1016 (2018).
76. L. Boarino, C. Baratto, F. Geobaldo, G. Amato, E. Comini, A. M. Rossi, G. Faglia, G. Lerondel, and G. Sberveglieri,*Mater. Sci. Eng. B*, **69**, 210 (2010).
77. M. Cuscuna, A. Convertino, E. Zampetti, A. Macagnano, A. Pecora, G. Fortunato, L. Felisari, G. Nicotra, C. Spinella, and F.Martelli, *Appl. Phys. Lett.*, **101**, 103101 (2012).
78. H. H. Li, C. E. Yang, C. C. Kei, C. Y. Su, W. S. Dai, J. K. Tseng, P. O. Yang, J. C. Chou, and H. C. Cheng, *Thin Solid Films*, **529**, 173 (2013).
79. D. Liu, L. Lin, Q. Chen, H. Zhou, and J. Wu, *ACS Sens*., **2** 1491 (2017).
80. J. Liao, Z. Li, G. Wang, C. Chen, S. Lv, and M. Li, *Phys.Chem.Chem.Phys*., **18**, 4835 (2016).
81. H. Du, X. Lin, Z. Xu, and D. Chu, *J. Mater. Sci*., **50**, 5641 (2015).
82. R. R. Ghimire, S. Mondal, and A. K. Raychaudhuri, *J. Appl. Phys*., **117**, 105705 (2015).
83. L. L. Zhang and X. S. Zhao, *Chem. Soc. Rev*., **38**, 2520 (2009).
84. H. Wang and L. Pilon, *J. Phys. Chem. C*, **115**, 16711 (2011).
85. H. Yuan, H. Shimotani, A. Tsukazaki, A. Ohtomo, M. Kawasaki, and Y. Iwasa, *Adv. Funct. Mater*., **19**, 1046 (2009).
86. S. Thiemann, S. Sachnov, S. Porscha, P. Wasserscheid, and J. Zaumseil, *J. Phys. Chem. C*, **116**, 13536 (2012).

87. E. Fortunato, P. Barquinha, and R. Martins, *Adv. Mater*., **24**, 2945 (2012).
88. R. R. Ghimire and A. K. Raychaudhuri, *Appl. Phys. Lett*., **110**, 052105 (2017).
89. M. N. Fujii, Y. Ishikawa, K. Miwa, H. Okada, Y. Uraoka, and S. Ono, *Sci. Rep*., **5**, 18168 (2016).
90. S. Park, S. Lee, C. Kim, I. Lee, W. J. Lee, S. Kim, B. G. Lee, J. H. Jang, and M. H. Yoon, *Sci. Rep*., **5**, 13088 (2015).
91. J. Zhou, N. Liu, L. Zhu, Y. Shi, and Q. Wan, *IEEE Electron Device Lett*., **36**, 198 (2015).

Chapter 2

Synthesis and characterization

In this chapter, we have described the synthesis methods of materials under investigation; like: metal oxide semiconductor heterojunction with 1D nanostructures of zinc oxide and silicon nanowire (ZnO/Si NWs nanostructures arrays) and thin film of doped zinc oxide (indium gallium zinc oxide (IGZO)). The different forms of oxide nanostructures (ZnO and doped ZnO) were synthesized by mainly two different growth methods: (i) chemical methods and (ii) physical methods. The grown nanostructures are characterised by using different characterization tools like; X-ray diffraction (XRD), scanning electron microscopy (SEM), atomic force microscopy (AFM), and high-resolution transmission electron microscopy (HRTEM) for structural and morphological characterization. The defect states of the samples were characterised by using X-ray photoelectron spectroscopy (XPS) and Photoluminescence spectroscopy (PL). Other than growth, we have demonstrated the brief description of characterization tools, device fabrication along with experimental outcomes in this chapter.

2.1 Introduction

In the field of experimental condensed mater physics, growth of oxide nanostructures are crucial steps and the quality of materials are strongly dependent on the growth parameters. The optical, electrical and electronic properties of metal oxides can be engineered by modifying their size, shape, structure, composition and stoichiometry [1]. Size reduction to nano dimension of oxide semiconductors leading to quantum confinement phenomena modify their intrinsic properties like electrical optoelectronic and other physical properties with respect to their corresponding bulk properties [2]. In particular, many works have been devoted to the fabrication of heterostructures based on compound semiconductors (i.e., group II–VI, III–V etc), that find widespread applications in optoelectronics, photonics, sensors etc [3]. Recently, one-dimensional (1D) nanostructures or their specified arrays such as silicon nanowires (Si NWs) are of great interest due to their high abundance and quantum size effects. Si NWs are considered to be the fundamental blocks of future nanoelectronics [4]. The motion of electrons in the confined dimension contributes to an enhancement in electrical and optical properties of their devices. Moreover, due to narrow band gap and tuneable physical characteristics, they have potential applications in various fields like microelectronics, optoelectronics, photonics, photovoltaic, sensors. Meanwhile, ZnO based hierarchical nanostructures play a key role for functional nano-devoices due to their excellent electrical and optoelectronics properties [5-6]. So, the realization of three-dimensional (3D) ZnO structures based on these 1D structures has been paid much attention due to its unique properties for novel applications in advanced catalysts or gas sensors or photodetectors. Oxide semiconductor can also be integrated into heterojunction with 1D nanostructure that can tune the electrical and optoelectronic properties suitably. The heterostructures devices often exhibit efficient and improved performance in comparison to the bare NW counterpart [7]. In this thesis work, we have integrated the oxide semiconductor nanostructures ZnO/doped ZnO into heterojunction (both p-n and n-n junction) with silicon nanowires (Si NWs) arrays innovatively and the optoelectronic properties can be tuned by making heterostructures or field effect transistor (FET) type device structures or by decorating with plasmonic nanoparticles (Au) with metal oxide nanostructures. This combination of ZnO/Si NWs nanostructure arrays furnishes very high-quality optoelectronic properties including high surface to volume ratio, low reflection and strong absorption in UV-Vis-NIR broadband region, and enhancement of charge transfer and that can be integrated with silicon IC technology. This type of heterostructures offer direct hetero-epitaxial nanoscale integration of materials with different properties, which often leads to function integration or

novel applications. Moreover, such hierarchical nanostructures offer greatly enhanced surface areas, which has attracted intensive research interest towards optoelectronic, photo-catalysis, and photovoltaic applications. There are various roots to synthesise the oxide nanostructure like chemical solution deposition (CSD), atomic layer deposition (ALD), metal assisted chemical etching (MACE), pulsed laser deposition (PLD), pulsed laser ablation in liquid (PLAL), thermal evaporation and so forth [8-14]. However, each method has their own advantages and disadvantages and favourable for a particular class of materials. In CSD method, a chemical solution of desired material is deposited on a preferred substrate by drop cast and spin coating technique with repeated coating followed by thermal annealing for getting suitable crystalline structure [8]. ALD is a chemical vapour deposition technique that allows to grow thin, uniform and conformal coating on a 3D structure in a precisely controlled way by using a self-limiting surface reaction steps with the repeated cycle of pulse and purge of precursors of desired material [9]. MACE is the process of wet chemical etching of semiconductor (mainly silicon) in a chemical etching solution of HF and $AgNO_3$ for the rapid production of large-area, aligned and well controlled silicon nanostructures including silicon nanowires (Si NWs) and silicon microstructures [10]. In addition, Si NWs formed by the electroless chemical etching method have exactly the same properties as the starting substrate (i.e. doping type and density). In PLD a high energetic pulsed laser (excimer laser) is focussed inside a high vacuum chamber or in the presence of background gas such as oxygen or mixture of argon and oxygen gases to ablate the target of desired material which condensed onto a given substrate where thin film is nucleated and growth takes place [11]. In PLAL method, a laser beam is focussed on the surface of solid target placed in liquid medium in ambient temperature and pressure. The interaction of laser with the solid target causes the surface to vaporise in the form an ablation plume and the reaction products are typically nanoparticles (NPs) composed of atoms from both the target and the liquid, which form a suspension in the liquid [13]. Thermal evaporation uses a resistive heat source to evaporate a solid material in a vacuum to form a thin film. The material is heated in a high vacuum chamber until vapor pressure is produced [14].

2.2 Synthesis of metal oxide nanostructures and thin films

We have synthesized functional oxide semiconductor nanostructures using zinc oxide (ZnO) and vertically aligned 1D silicon nanowires (Si NWs) arrays and thin film of doped ZnO. Growth methods of oxide nanostructures can be divided by either purely physical or chemical process. In this thesis work, we have employed both chemical and physical process for synthesis

of metal oxide nanostructures and thin film. Basically, for fabrication ZnO/Si NWs heterostructure arrays, the Si NWs has been grown using chemical method (electroless etching), finally, the hetero structure was made by deposition of ZnO (film/nano structures) on Si NWs by using various methods: (i) Chemical method and (ii) Physical method. (i) Chemical process includes: (a) metal assisted chemical etching (MACE) (b) chemical solution deposition (CSD), (c) atomic layer deposition (ALD) and ii) Physical process; like: pulsed laser deposition (PLD) and pulsed laser ablation in liquid (PLAL). In chemical methods material can be grown at low temperature with high throughput and chemical solution deposition is a viable, low-cost and non-vacuum process for synthesis of polycrystalline, textured and epitaxial oxide thin films. Whereas the physical process; like PLD has numerous advantages including deposition of large variety of materials and mixtures and able to maintain proper stochiometric transformation of target material.

2.2.1 Chemical process

Chemical method is one of important routes for synthesis of functional oxide nanostructures. There are many chemical methods for synthesis of ZnO nanostructures such as solgel, spin coating, chemical solution deposition (CSD), atomic layer deposition (ALD), hydrothermal, solvothermal, and spray pyrolysis etc [8, 15-18]. In this thesis, we opted the electroless etching (EE) method for synthesis of vertically aligned Si NWs arrays and we have used CSD, ALD and hydrothermal method for synthesis of ZnO to construct ZnO/Si NWs heterostructures.

2.2.1.1 Electroless etching (EE)

The properties of Si NWs are strongly dependent on the fabrication methods. For achieving high-performance devices, the production of a large-area, highly oriented arrays of crystalline Si NWs with tuneable properties are extremely important. There are various methods for fabrication of Si NWs and these methods have their own advantages and disadvantages. The commonly used methods are top down and bottom-up approach. The most commonly used bottom-up method is by vapor-liquid-solid (VLS) method [19-20]. There are various other methods also like thermal evaporation [21], molecular beam epitaxial [22], direct reactive ion etching (DRIE) [23]. However, bottom-up techniques usually require complex equipment, high temperature, high vacuum, all of which drastically increase the cost of process. However, a simple method, namely metal assisted chemical etching (MACE) or electroless etching (EE), a top-down approach, has recently emerged as a promising and a significant tool for the rapid production of large-area, aligned and well controlled Si NWs and has some great advantages

such as doping type and density of Si NWs fabricated by EE method remain same as starting substrate [24-26]. EE method requires a galvanic displacement of metal nanoparticles as a catalyst on the surface of the crystalline Si substrate. However, the shape and size, length, diameter, density, crystallinity and properties of the Si NWs strongly depend on several important factors, such as the (i) nature of the noble metal, (ii) the shape and size of the noble metal and the intermediate distance between them, (iii) the etching solution and (iv) its concentration, (v) the doping type, (vi) resistivity and the (vii) orientation of the starting Si wafer, (viii) the etching temperature and (ix) the etching duration. We have used p-type (100) silicon substrates with resistivity of 1-10 Ω-cm and n-type undoped silicon substrates with resistivity of > 1000 Ω-cm for preparation of p-type and n-type Si NWs for making of p-n and n-n junction-based devices respectively [27]. The complete fabrication processes of Si NWs arrays are shown in the flow chart below in Figure 2.1 (a). At first, the silicon wafers were cut and ultrasonically cleaned in acetone, ethanol and deionised (DI) water successively for 5 min each, and then boiled in DI water/NH_4OH/H_2O_2 (5:1:1) and DI water/HCl/H_2O_2 (5:1:1) solution for 10 min successively each to remove any organic residue and ionic parts respectively. The wafers were finally immersed into dilute HF solution to remove any oxide layer on the surface. After that, Si substrates were immersed in EE solution containing 0.02 M $AgNO_3$ (99.5%) and 4.6 M HF (38 – 40%) for 1 hr at temperature of 30 ^oC. After etching, the silver dendrites on the top of Si NWs arrays were removed completely; otherwise, they act as a barrier and influence the electrical and optical properties. So, to remove the silver dendrites, the samples were rinsed with deionized water (DI water) and placed in a solution of 1:3 mixtures of 65% nitric acid (HNO_3) and DI water for 30 mins. At the final stage of the process, samples were rinsed in deionised water and dried with nitrogen gun.

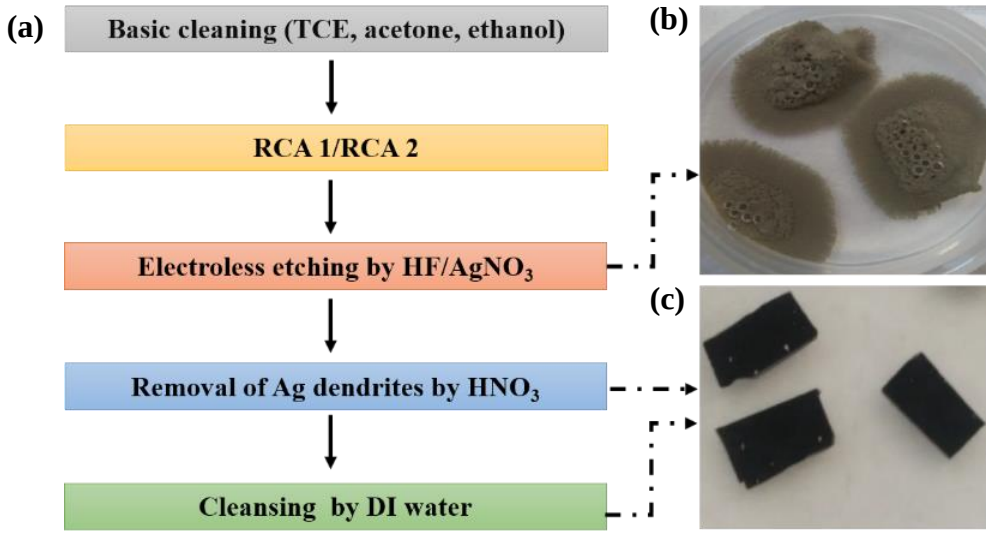

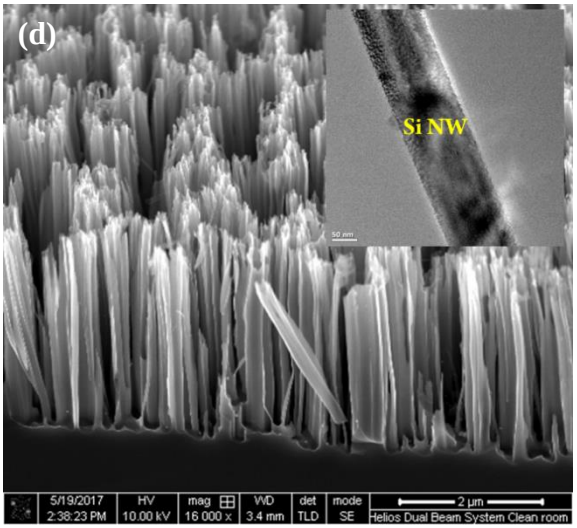

Figure 2.1 (a) Flow chart of chemical etching of Si NWs. (b) Camera image of Ag dendrites on Si NWs substrates during etching. (c) Camera image of Si NWs substrates after etching. (d) Cross-sectional SEM image of vertically aligned Si NWs. Inset shows TEM image of a single Si NW.

Mechanism of chemical etching: This process of metal assisted chemical etching is a one step process, i.e., deposition of silver (Ag) nanoparticles on Si substrate and etching of silicon takes place simultaneously. Since the silver is in its ionic form in EE solution (Ag^+), the concept of electronegativity which is the aptitude of an element to attract the shared pair of electrons rather than the work function has been employed for understanding the mechanism of metal assisted chemical etching. Since the electronegativity of silver ion (1.93 eV) is greater than that of silicon (1.90 eV), there is a transfer of electron from silicon to silver ions where the silver is deposited on Si substrate. Therefore, the silicon underneath the silver ions becomes more positively doped than the silicon around silver and oxidation will start to take place from the surface of Si around the Ag particles rather than the Si underneath it and as a result, silicon is lost into the solution as H_2SiF_6 and the remaining structure becomes vertically aligned arrays of Si NWs covered with silver (Ag) dendrites. Thus, the etching of oxidized sites of Si around silver nanoparticles starts leading to the formation of Si NWs. A schematic of Si NW etching mechanism is shown in Figure 2.2, processes a-c. The etching of Si NWs occurs by the following oxidation-reduction reaction [31]:

$$Ag^+ + e^- \rightarrow Ag(s)$$
$$Si(s) + H_2O \rightarrow SiO_2 + 4H^+ + 4e^-$$
$$SiO_2 + 6HF \rightarrow H_2SiF_6 + 2H_2O$$

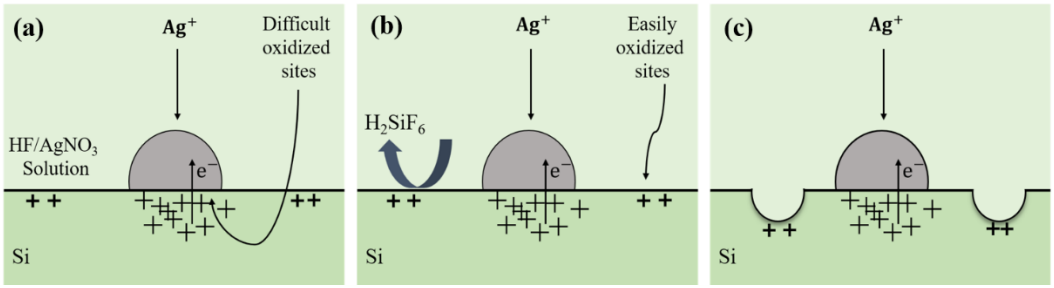

Figure 2.2 A schematic diagram of Si NW etching mechanism.

2.2.1.2 Chemical solution deposition (CSD)

Chemical solution deposition (CSD) is one of the viable, low-cost non vacuum process for the fabrication of polycrystalline, textured and epitaxial oxide thin films [8]. The quality and functional properties of thin film can be improved by understanding of precursor solution chemistry, film forming aspects and the nucleation and growth of crystalline thin films. The basic fabrication processes of CSD method are shown in Figure 2.3. In a typical chemical solution deposition (CSD) method the growth process is composed of four steps: (i) preparation of a chemical solution, (ii) deposition of solution onto a substrate, (iii) drying for removing the solvent and (iv) thermal annealing. Therefore, chemical solution-based methods encompass a broad range of techniques including sol-gel techniques, chelation, metal-organic decomposition.

(i) Preparation of chemical solution: In the first step of CSD method, a homogeneous and stable precursor solution has been prepared using inorganic or metalorganic metal salts which are dissolved in either organic or water in a proper stoichiometric ratio.

(ii) Deposition of solution onto a substrate: In the second step of CSD process the precursor solution is deposited onto a substrate either through spin coating, dip coating, or spray coating. In this case the spin coating technique is used to prepare uniform thin films because of its simplicity, the relatively inexpensive equipment used, and the good results that can be obtained. In details a typical spin coating is performed in four basic stages such as deposition, spin up, spin off and evaporation. In the first stage a small amount of precursor solution is deposited by pipette on the top of substrate which is fixed to a plate by an aspirator and by rotating the plate, the precursor solution is made to spread uniformly across the whole surface of the substrate due to centrifugal force i.e. spin up and spin off occur in sequence and the evaporation stage occurs throughout the process simultaneously and due to evaporation high volatile components are eliminated from the substrate and low volatile components of the precursor solution remain on the surface of the substrate. The spinning speed (typically 500-1000 rpm) is set at a specific value depending on the desired film thickness and thickness of the deposited layer is also controlled by the viscosity of the coating solution.

(iii) Drying for removing the solvent: In this step, a low temperature thermal treatment (typically 120 to 300 ^{o}C) has been done to form an amorphous film by removing the solvent and most of the organic components. This step is also called as "pyrolysis" because a large part of organic components is eliminated from the film due to the thermal (pyro) decomposition (lysis).

(iv) Thermal annealing: Finally, a high temperature thermal annealing (typically 450 to 800 ^{o}C, although it is material dependent) has been done at a particular time (typically 3 to 10 hours) for densification and crystallization of the amorphous film into the desired phase. The step (ii) and (iii) are repeated for obtaining desired thickness of film before crystallization. A flow chart of the basic step of CSD method has shown in Figure 2.3.

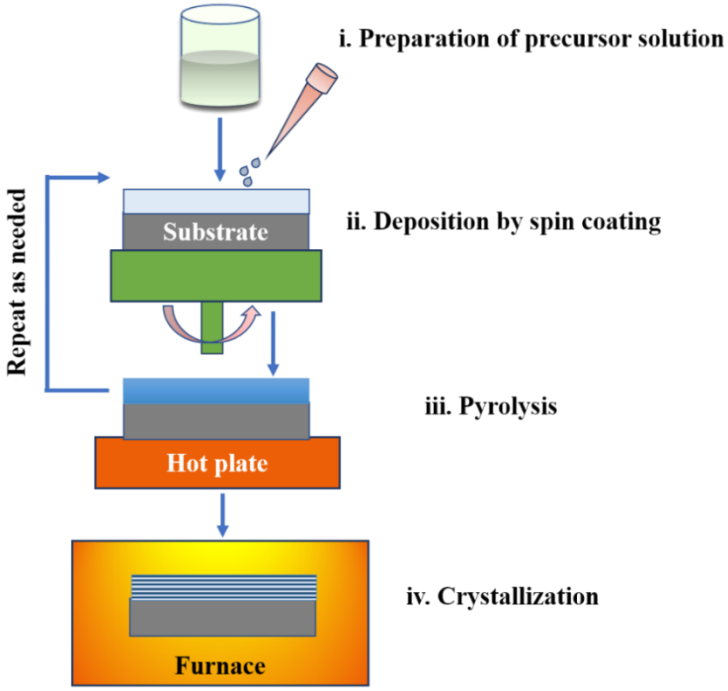

Figure 2.3 Flowchart of a typical chemical solution deposition (CSD) process.

In this thesis, for fabrication of ZnO/Si NWs heterostructure by CSD method, at first, silicon nanowires (Si NWs) were fabricated by Ag-assisted electroless etching (EE) methods from p-type/n-type silicon substrates to form both p-n and n-n junction of n-type oxide semiconductor. Then, ZnO precursor solution was synthesised by dissolving metal salt precursor, 0.1 M of Zinc acetate dehydrates ($Zn(CH_3CO_2)_2.2H_2O$), in a solvent of ethanol at 70 ^{o}C. Diethanolamine ($HN(CH_2CH_2OH)_2$) was additionally incorporated as stabilizer [27]. After continuous stirring of 2 hours, the solution is kept under 24 hours for stabilization. Then the ZnO precursor solution was deposited on prefabricated Si NWs substrates by spin coating. The solution was spin coated repeatedly to obtain desired thickness of ZnO of ≈ 300 nm with post deposition drying and

heating at 120 °C in each interval. The ZnO coated Si NWs arrays were finally annealed for 4 hours at 450 °C to get proper crystalline phase of ZnO. The overall fabrication process of ZnO/Si NWs heterostructure along with synthesis of ZnO precursor solution is shown schematically in Figure 2.4.

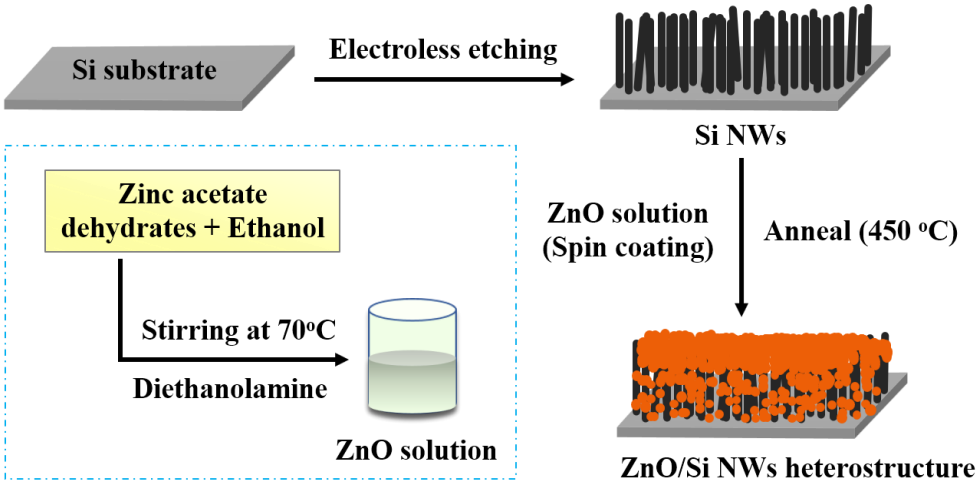

Figure 2.4 A schematic diagram of fabrication steps of ZnO/Si NWs heterostructure by CSD method.

Reaction mechanism: ZnO is formed by the following chemical reactions [28]:

$$Zn(CH_3COO)_2.2H_2O \xrightarrow{heat} Zn(CH_3COO)_2 + 2H_2O \uparrow$$

$$4Zn(CH3COO)2 + 2H2O \xrightarrow{heat} Zn_4O(CH3COO)6 + 2CH3COOH \uparrow$$

$$Zn4O(CH3COO)6 + 3H2O \xrightarrow{heat} 4ZnO + 6CH3COOH \uparrow$$

$$Zn4O(CH3COO)6 \xrightarrow{heat} 4ZnO + 3CH3COOH \uparrow + 3CO2 \uparrow$$

2.2.1.3 Atomic layer deposition (ALD)

Atomic layer deposition (ALD) is a chemical vapour deposition (CVD) based technique especially suited for growing high quality conformal thin films on three dimensional substrates with high precision [29]. A variety of materials include oxides, nitrides, sulphides, and metals have been deposited with ALD. Originally ALD technique is based on physically adsorbed precursors (two or more) that occurs through chemisorption saturation process and sequential surface chemical reaction. The net precursor adsorption rate approaches zero due to surface saturation as a result, ALD precursor cannot react with itself and after saturation the amount of precursor adsorption will not be increased due to additional exposure time of precursor. Thereby growth rates per cycle (GPC) of about 1 Å/cycle are obtained. The decomposition of physically adsorbed precursors is taken place upon chemical oxidation by water (or O_2, O_3). The majority of ALD surface reactions i.e., adsorption of precursor to the surface are driven by thermal

energy. The range of temperature (typically 50 to 350 ^{o}C) in which the process can occur is called ALD temperature window and it depends on the precursor involved on the deposition. An alternative to thermal ALD is plasma-assisted or plasma-enhanced ALD where highly reactive plasma species are required for surface reaction which reduces the thermal energy [30].

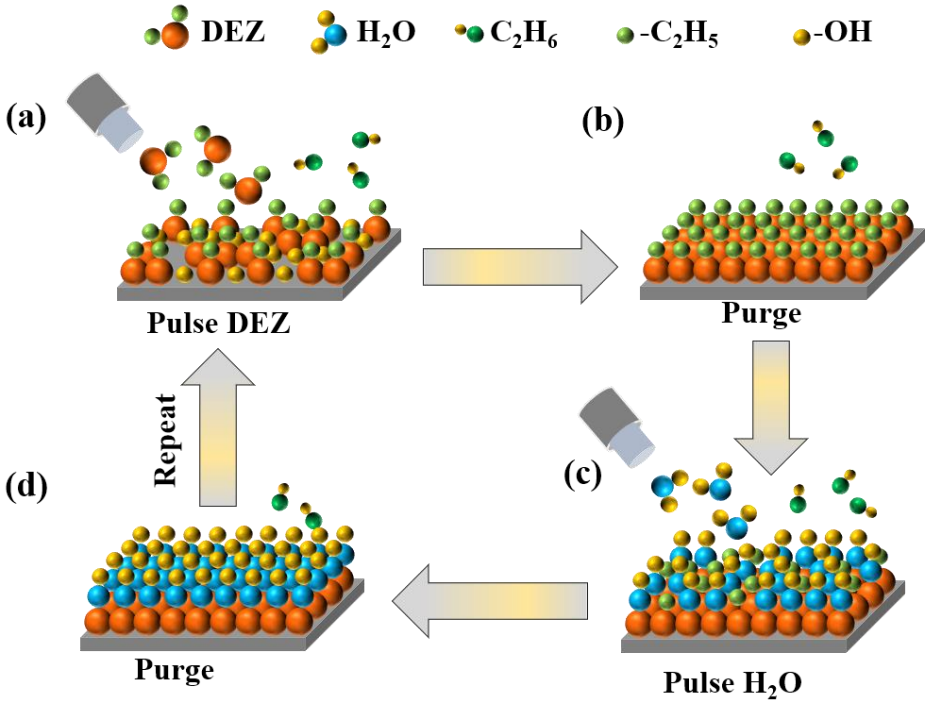

Figure 2.5 A schematic representation of growth of ALD-ZnO in one cycle. (a) Pulse of DEZ. (b) Purging with argon (Ar) to remove any excess reactants. (c) Pulse of H_2O. (d) Purging with argon (Ar) to remove any excess reactants.

A schematic representation of growth of ALD-ZnO in one cycle is shown in Figure 2.5. The overall growth of ALD cycle can be divided into four steps: (a) exposure of metal precursor (b) evacuation or purging of excess precursor and reaction by-products (c) exposure of co-reactants (non-metal precursor) (d) evacuation or purging of excess precursor and reaction by-products. The initial step in ALD process may last in several cycle which is called nucleation. Nucleation is dependent on the interaction of the precursors with the substate as well as type of surface sites accessible for growth and often is controlled by substrate surface treatment [31]. Nucleation is often improved by substrate surface treatment such as cleaning of surface by ultraviolet ozone in order to remove organics and provide a hydroxyl ($-OH$) based surface that enhanced the reaction of ALD precursors with the substrate surface. The quality of film is dependent upon processing conditions i.e., precursor choice, temperature, substrate etc.

Growth mechanism of ALD ZnO:

A schematic in Figure 2.5 shows the step of an ALD cycle for growth of ZnO with diethylzinc/DEZ ($(C_2H_5)_2Zn$) and DI water (H_2O). The growth of ZnO ALD from DEZ and H_2O is occurred due to the two self-terminating reaction as follows [32-33]:

$$S - OH + Zn(C_2H_5)_2 \rightarrow S - O - Zn(C_2H_5) + C_2H_6 \qquad (2.1)$$

$$S - O - Zn(C_2H_5) + H_2O \rightarrow S - OZn - (OH) + C_2H_6 \qquad (2.2)$$

Where, S denotes the substrate surface. The growth of ZnO thin films is started by the sequential adsorption of DEZ and H_2O as shown in Figure 2.5. In the first step, a dose of DEZ is pulsed into the reaction chamber and immediately it reacts with the hydroxyl ($-OH$) group on the substrate surface and then bind to the surface and produces gaseous by-product ethane (C_2H_6). In the second step, the excess unreacted DEZ and reaction by product ethane molecules are purged from the chamber with argon (Ar). In the third step, second precursor H_2O is pulsed into the chamber then the $-OH$ substituted with the surface ethyl ($-C_2H_5$) in another self-limiting reaction and a partial layer of the ZnO is formed. Finally, residual water molecules and excess ethane (C_2H_6) by-products molecules are purged with argon (Ar) before the next cycle and the thickness can be controlled very accurately by varying the number of cycles.

In this thesis, for formation of ZnO/Si NWs core-shell arrays, first, p-Si NWs arrays were fabricated by Ag-assisted electroless etching (EE) methods from p-type silicon substrates. Then a thin layer of Zinc oxide (ZnO) of thickness ~ 50 nm is deposited on the prefabricated p-type silicon nanowires (p-Si NWs) arrays by thermal atomic layer deposition (ALD) at a temperature of 200 ^oC by using Diethylzinc (DEZ) and H_2O as precursors [34]. Four steps of an ALD cycle were DEZ pulse of 50 milliseconds, purge with Ar for 5 sec, H_2O pulse of 1 sec and purge with Ar 8 sec. A schematic diagram of overall fabrication processes of ZnO/p-Si NWs core-shell structure is shown in Figure 2.6. The deposition rate was about 1.6 Å /cycle. The ALD deposition is done in a way that there is a core-shell structure with p-Si NW as core and ZnO as shell with a top layer of ZnO that forms the channel in the device.

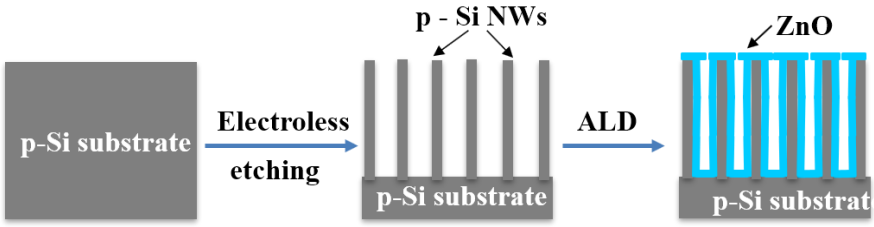

Figure 2.6 A schematic diagram of fabrication process of ZnO/p-Si NWs core-shell arrays.

A cross-sectional SEM image of the ZnO nanostructured film deposited on that vertically aligned Si NWs by chemical solution deposition (CSD) is shown in the Figure 2.7 (a). The image shows a thick top layer of the ZnO nanostructure film (thickness ≈ 350 nm) on the Si NWs and length of ZnO/Si NWs arrays is ~ 2.5-3 μm. Figure 2.7 (b) shows cross sectional SEM image of ALD grown ZnO/Si NWs core-shell arrays. Figure shows a uniform and conformal layer of ZnO on Si NWs arrays.

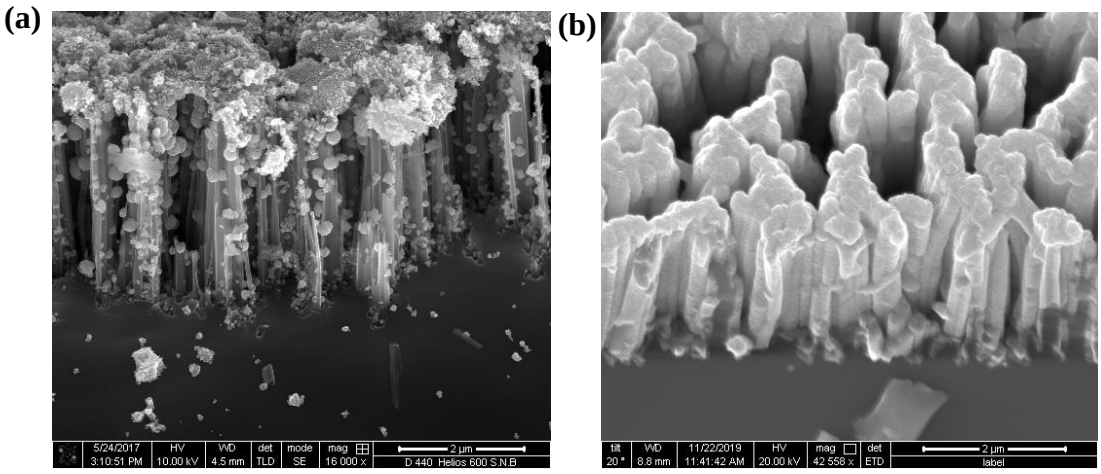

Figure 2.7 Cross-sectional SEM image of (a) CSD grown ZnO/Si NWs nanostructures arrays. (b) ALD grown ZnO/Si NWs core-shell arrays.

2.2.2 Physical process

In physical methods materials are synthesised by applying mechanical pressure, high energy radiations or thermal energy to cause material melting, evaporation or condensation. In physical methods sputtering, thermal evaporation, pulsed laser deposition (PLD) and laser ablation are the most regularly used techniques [35-36]. The main advantage of physical method is to obtain contamination free nanomaterials with better crystallinity. In this thesis, we have used PLD technique for deposition of ZnO nanostructures on Si NWs substrates and doped ZnO (IGZO) (indium gallium zinc oxide) on flexible substrate (kapton tape). We have opted solid-state synthesis for preparation of PLD targets. We have also used laser ablation method for preparation of plasmonic nanoparticles.

2.2.2.1 Solid-state synthesis

The traditional solid-state synthesis method is used to obtain polycrystalline material by mixing of two (or more) solid reagents. It involves chemical decomposition reaction at a very high temperature to allow inter diffusion of the cations [37]. Usually, several annealing steps with intermediated milling steps are needed in this process which increases the homogeneity of the mixture and to decrease the particle size of the powder. In this thesis, we have made two targets

ZnO and IGZO by conventional solid-state synthesis route. To prepare ZnO target, firstly commercially available ZnO powder is grinded in Agate mortar and pestle followed by annealing at 600 ^{o}C for six hours. Afterwards the powder is again grinded and pelletized using a pelletizer under high pressure (about 50 megapascal) followed by sintering at 1200 ^{o}C for ten hours under constant oxygen flow to get compact and large grain size. For preparation of indium gallium zinc oxide; IGZO ($InGaZn_2O_5$) target, at first, the In_2O_3, Ga_2O_3 and ZnO powders are mixed in a molar ratio of 1:1:4 and then properly grinding in Agate mortar and pestle followed by annealing at 600 ^{o}C for six hours. Then mixture is again grinded and pelletized using a pelletizer under high pressure (about 50 Mpa) followed by sintering at 1400 ^{o}C for twelve hours under constant oxygen flow to get compact and large grain size. We have characterized the pellets using XRD to conform the crystalline structure. Figure 2.8 (a) and (b) shows the XRD pattern of ZnO and IGZO pellets respectively matches well with the ICSD peaks. The surface morphology of the target is characterised by using SEM shown in Figure 2.8 (c) and (d) for ZnO and IGZO pellet respectively.

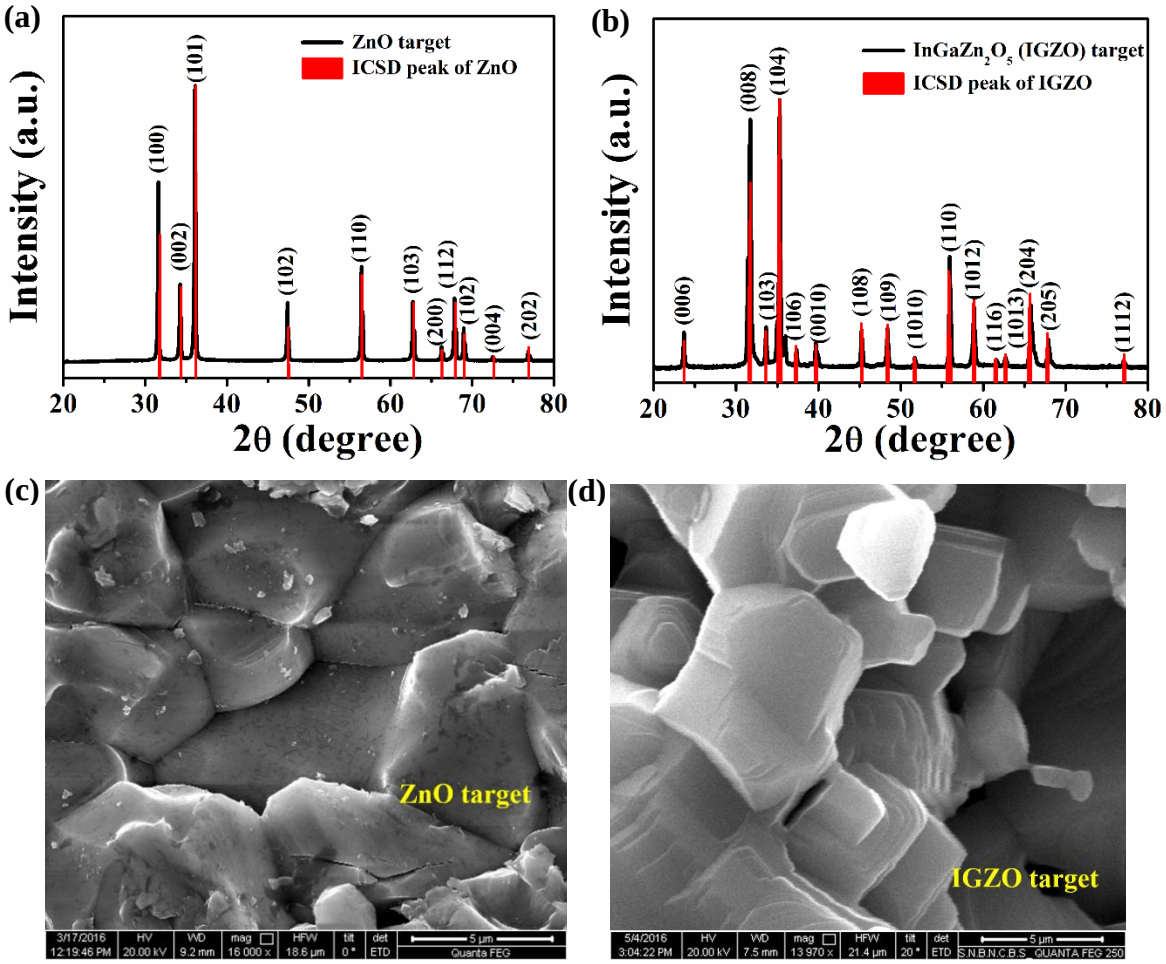

Figure 2.8 XRD of (a) ZnO and (b) IGZO pellets matches well with the ICSD peaks. SEM image of (c) ZnO and (d) IGZO target.

2.2.2.2 Pulsed laser deposition (PLD)

Pulsed laser deposition (PLD) is a class of physical vapour deposition (PVD) technique where a high energetic pulsed laser is used to melt, evaporate and ionize the material from the surface of a target. PLD has numerous advantages including deposition of large variety of materials and mixtures, able to maintain proper stochiometric transformation of target material, good adhesion between films and substrate and also deposition can be done at room temperature. A schematic diagram of the PLD setup is shown in Figure 2.9. The impact of the laser energy vaporized the target material (pellet) in the form of high luminous plasma plume that expands rapidly away from the target surface. The ablated material is deposited on a properly placed substrate upon which it condenses in the presence of a background gas, such as oxygen and growth of thin film occurs. The characteristics of the thin films can be controlled by laser intensity, substrate temperature, buffer gas pressure, and incident angle of the plasma plume.

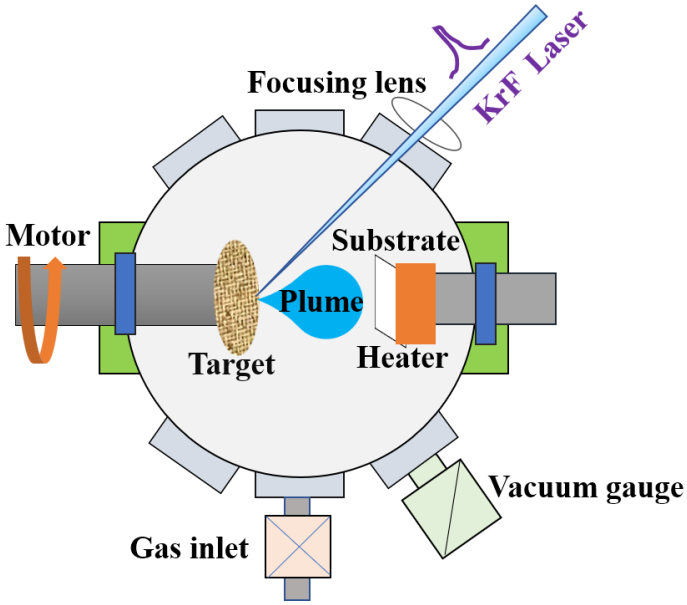

Figure 2.9 A schematic diagram of PLD set-up.

The thin film growth process in PLD can be divided generally into four stages. Each of these steps is crucial for the crystallinity, uniformity and stoichiometry of the resulting film. The steps are explained below:

1. In the first stage, when a high energetic laser pulsed is interacted with target material, the surface of the target is then heated up locally and the material is melted and this melted surface of the target gets vaporized. The vaporized material, containing neutrals, ions, electrons called as plasma plume.
2. In the next stage, this plasma plume expands rapidly away from the target surface and moves towards the substrate. The spatial distribution of the plume is dependent on the background

pressure inside the PLD chamber which influences the deposition rate and further can change the stoichiometry of the film.

3. In the third stage, the high energetic ablated plasma plume is deposited on the substrate and deposition rate depends on some factors like target material, energy of laser pulse, distance from target to substrate and type of background gases (oxygen, argon) and pressure in chamber which influences the quality of film.

4. In the final stage nucleation and growth of the film takes place on the substrate surface which determines the quality of the deposited film. The process of nucleation and growth kinetics of the film depends on following parameters including:

a. *Laser parameters*: The quality and stoichiometry of films depend on several laser parameters like laser fluence (J/cm^2) and laser energy which affects the deposition flux. Generally, the nucleation density increases with increasing the deposition flux.

b. *Surface temperature*: The nucleation density is strongly dependent on substrate temperature and with increasing the surface temperature decreases the nucleation density.

c. *Substrate surface*: The nucleation and growth of the film can be affected by the surface roughness of the substrates.

d. *Background gases*: Generally, for deposition of oxide, an oxygen background is required for maintaining the proper stoichiometry of the film.

Figure 2.10 PLD set-up in our laboratory. Reprinted with permission from [38].

In our lab a KrF excimer laser (wavelength λ = 248 nm) which is a combination of a noble gas (argon, krypton, xenon) and reactive gas (fluorine, chlorine), has been used for the deposition of ZnO and IGZO nanostructures film. The PLD set up in our lab is shown in Figure 2.10. In this thesis, we have deposited nanostructured ZnO film (thickness ≈ 300 nm) on pre-fabricated p-type Si NWs substrate by ablation of ZnO target to get ZnO/p-Si NWs core-shell arrays. The

cross-sectional SEM image of PLD grown ZnO/Si NWs core-shell arrays is shown in Figure 2.11 (a). The length and diameter of the core-shell arrays are 2.5-3 μm and 150-200 nm respectively. We have optimized laser fluences and pulses and have used the laser fluence ~1.85 J/cm^2 and repletion rate was 2 Hz. The temperature and the oxygen partial pressure were 450 ^{o}C and 10 mT respectively during deposition.

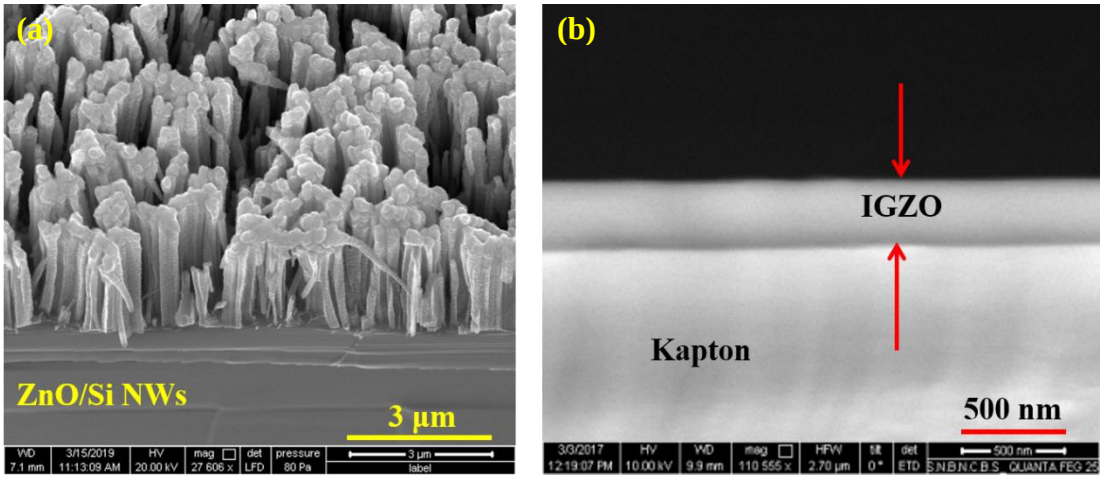

Figure 2.11 Cross-sectional SEM image of (a) PLD grown ZnO coated Si NWs core-shell arrays. (b) Amorphous-IGZO channel on Kapton substrate.

We have also deposited amorphous IGZO film on flexible Kapton substrate by ablation of IGZO target with an energy fluence of 1.38 J/cm^2 for investigation of charge carrier induction in oxide semiconductor by field effect using electric double layer (EDL) gate as discussed later in chapter 7. The temperature and the oxygen partial pressure were in the range of (100-120) ^{o}C and 10 mT respectively during deposition and the repetition rate was 2 Hz. The condensation of the ablated target species on flexible substrate gives a carbon free amorphous metal oxide channel at low temperature of growth [39]. Figure 2.11 (b) shows the cross-sectional SEM images of the amorphous IGZO film on Kapton substrate. The thickness of the film used is around 295 nm as determined from ellipsometry as well as cross sectional scanning electron microscopy (SEM).

2.2.2.3 Pulsed laser ablation in liquid (PLAL)

Most of junctions based (p-n heterostructures) photodetectors have limited gain and the responsivity (mostly $\leq 1\ A/W$) and more importantly the band width of detection is governed by the band gap [40]. But one can break the limitation of detection band width by surface plasmon resonance (SPR) by using of plasmonic nanoparticles (NPs) to overcome the limitation of spectral response arising from the band gap of the channel material [41-42]. It has been observed that plasmonic NPs those synthesized by chemical route for attachment, need a

stabilizing ligand or a dispersive media which affects the surface plasmon resonance of NPs and reduces the inter band transition which degrade the photodetector performances. Recently pulsed laser ablation in liquid (PLAL) method have received much attention for synthesis of nanoparticles (NPs) including noble metal, semiconductors and alloys [13]. In PLAL method, we are able to get uniform, mono-dispersed and stable ligands free NPs in a pure solvent (i.e., DI water) without introducing any ligands or stabilizing molecules intentionally. The absence of ligands on the particle surface enhances the charge transfer and the possibility of their functionalization with biomolecules, making them very effective as biomarkers. Furthermore, the bare surface of NPs is also attractive for catalysis purposes. This encouraged many research groups to focus their attention on the PLAL synthesis of those NPs. A custom-made experimental set up for PLAL method is shown in Figure 2.12 that needs no vacuum. In PLAL technique a high energetic pulsed laser is focused on a target material that immersed in a liquid in an ambient temperature and pressure. In this process laser induced plasma plume containing atom, electrons and ions are generated by irradiation of laser on the target immersed in liquid, followed by an interaction with the liquid medium to form NPs via nucleation and growth steps. The size, shape and crystallinity of NPs in PLAL techniques are not only dependent on laser parameters such as, laser fluence and laser pulse but also it is strongly dependent on the liquid environment such as solvent type, pH values, and temperatures.

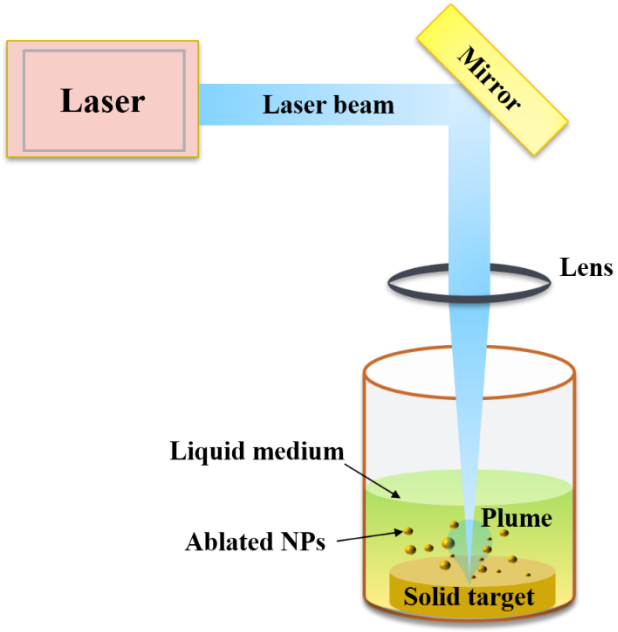

Figure 2.12 Schematic illustration of nanoparticles (NPs) synthesis via PLAL process.

In this thesis work, the plasmonic gold nanoparticles (Au NPs) have been prepared in DI water environment by pulsed laser ablation in liquid (PLAL) technique. In this method, a KrF pulsed excimer laser of wavelength 248 nm was focused on a pure Au metal target immerged in DI

water at room temperate and was pulsed with repetition rate of 5 Hz with an energy fluence ~ 2 J/cm^2. Figure 2.13 (a) shows the TEM image of Au NPs prepared by PLAL method. The average diameters of the Au NPs are ~ 10 nm. One can control the diameter of the nanoparticles by tuning laser parameters such as, laser fluence and laser pulse [43]. In this technique, we have been also prepared the plasmonic palladium nanoparticle (Pd NPs). The energy fluence was ~ 2.5 J/cm^2 and repetition rate was 5 Hz. Figure 2.13 (b) shows the TEM image of Pd NPs prepared by PLAL method and the average diameters of the Pd NPs are ~ 6 nm.

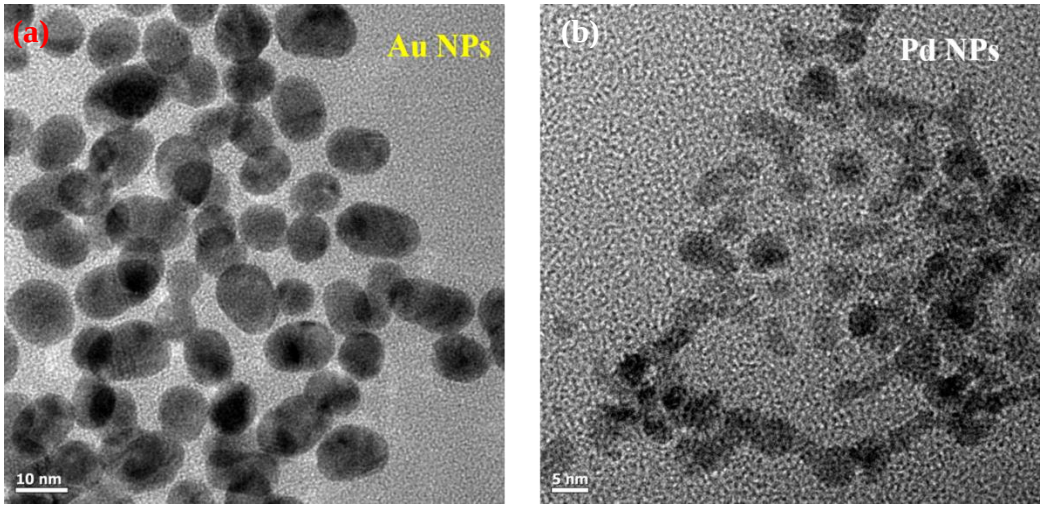

Figure 2.13 TEM image (a) Au nanoparticles and (b) Pd nanoparticles.

The PLAL process is distinctly different from chemical attachments through ligands; it gives a ligand-free growth of Au NPs. After that these plasmonic Au NPs are deposited on prefabricated ZnO/p-Si NWs core-shell arrays (Step-3 in Figure 2.14). The overall synthesis processes of different growth method are depicted schematically in Figure 2.14.

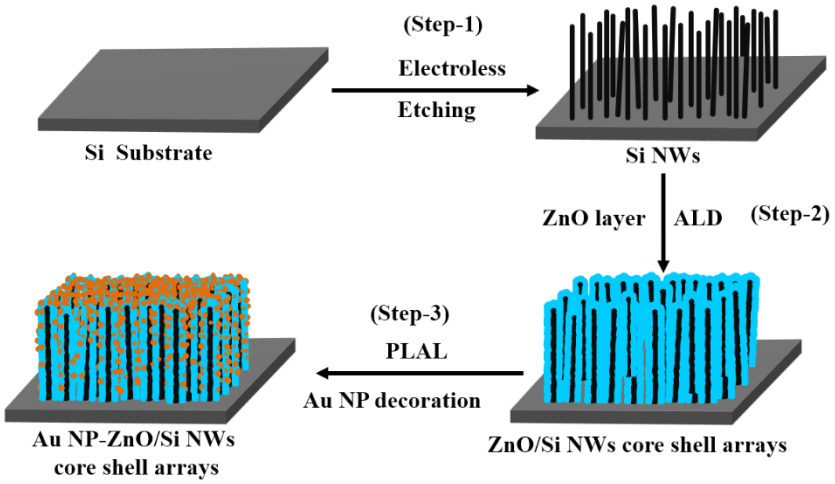

Figure 2.14 A schematic diagram of fabrication process of Au NPs decorated ZnO/p-Si NWs core-shell arrays.

Firstly, vertically aligned Si NWs were synthesised by electroless etching method from a p-type silicon substrate (Step-1). Then a thin conformal layer of ZnO is deposited on Si NWs substrate to form ZnO/p-Si NWs core-shell arrays (Step- 2 in Figure 2.14). Finally, plasmonic Au NPs prepared by PLAL method were spin coated on ZnO/p-Si NWs core-shell arrays (Step-3). The presence of ligands between ZnO and Au NPs inhibits charge transfer. Since the photoresponse of the device depends on the efficiency of the charge transfer, a ligand-free attachment is preferred as discussed later in chapter 4.

2.3 Characterization tools and techniques

The synthesised nanostructures samples are characterised using high-end characterization tools and techniques which allows us to probe into the details of nanostructures. The structural and morphological characterization has been performed through X-ray diffraction (XRD), Scanning Electron Microscopy (SEM), Atomic Force Microscopy (AFM) and Transmission Electron Microscopy (TEM). The elemental composition of the material has been determined by Energy-dispersive X-Ray Spectroscopy (EDS). The nanostructured complete device is also characterized in TEM using cross sectional lamella preparation technique which enables us to make a proper physical model of the device. The optical properties of the samples are characterised using UV-visible spectroscopy and Photoluminescence spectroscopy (PL). We have also used X-ray Photoelectron Spectroscopy (XPS) to quantify the chemical and spatial composition as well as the defects of the oxide nanostructures, which is essential for a better understanding of its physical properties.

2.3.1 Structural characterization

2.3.1.1 X-Ray diffraction (XRD)

X-Ray diffraction is a first level of characterization technique to determine the crystal structure of a material. It provides insight on structures, phase purity and other structural parameters, such as average grain size, crystallinity and crystal defects. The interaction between material and a monochromatic X-rays (Generally, Cu $K_{\alpha 1}$ (λ = 1.54 Å)) beam produces the constructive interference which satisfying the well-known Bragg's Law by the following equation [44]:

$$n\lambda = 2d \sin\theta \qquad (2.3)$$

Where θ is angle of incidence of the X-ray beam, d is the distance between two layer of atoms and λ is wavelength of the X-ray and n is an integer. On interaction with the sample, diffracted X-rays are detected by a detector and XRD peaks are produced by constructive interference of scattered X-rays from each set of lattice planes of the sample. The experimentally obtained peaks are correlated with standard reference of International Centre for Diffraction Data

(ICDD)/Inorganic Crystal Structure Database (ICSD), which provides the identification of crystallographic plane indices (h, k, l) of that sample. In this thesis work PANalytical X'Pert Pro having Cu $K_{\alpha 1}$ source with wavelength of 1.5405 Å with an accelerating voltage of 45 kV and 40 mA current has been used for performing X-rays diffraction. This system follows the Bragg-Brentano geometry (θ-θ) where the sample holding stage is fixed and the X-ray tube rotates at - θ °/min and the detector rotates at a + θ °/min. In this geometry the detector and source are located at the intersection points of the goniometer circle (fixed radius) and the focusing circle, whose radius varies with the goniometer angle.

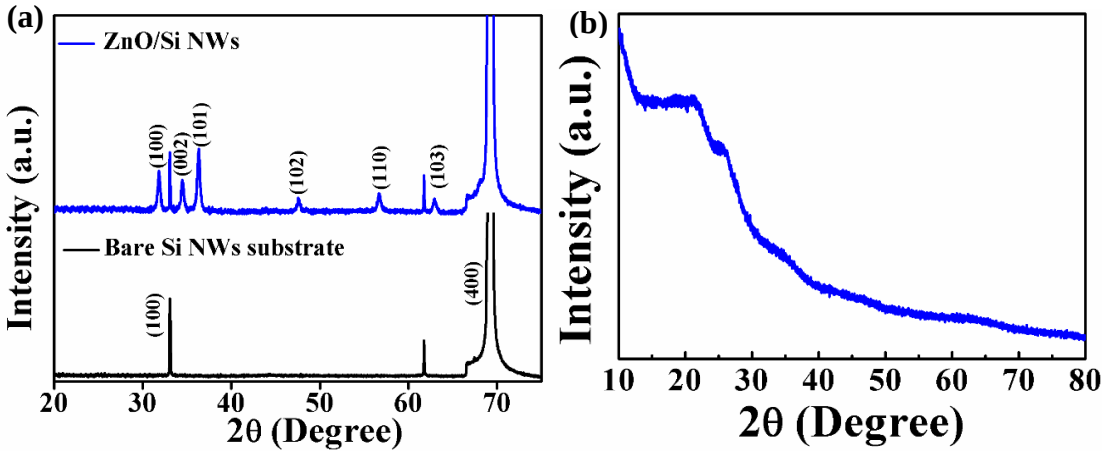

Figure 2.15 XRD of (a) ZnO/Si NWs nanostructure arrays. (b) a- IGZO channel deposited on Kapton which confirms the amorphous phase.

The X-ray diffraction (XRD) pattern of the ZnO/Si NWs nanostructure arrays grown by chemical deposition is shown in Figure 2.15 (a) and it is shown that the orientation of Si NWs is along the (100) plane same as Si substrate. The nanostructured ZnO film shows polycrystalline in nature. We have also prepared amorphous indium gallium zinc oxide (a-IGZO) film used as channel in thin film transistor (TFT). Figure 2.15 (b) shows the XRD data that establishes the amorphous nature of the IGZO film grown on the Kapton tape.

2.3.1.2 Scanning electron microscopy (SEM)

It is one of the multipurpose state-of-the-art instruments that usually provided an important information about the surface morphology, topography, composition chemistry, orientation of grains, crystallographic information, etc. of a material [45]. It is a type of electron microscope that produces images of a sample by scanning the surface with a focused beam of electrons. Generally, a beam of electrons generated from tungsten filament lamps or a field emission gun, is focused through an accelerating grid, condenser lens, objective aperture and scanning coils and finally through an objective lens and then scanned the surface of sample in a raster pattern inside an ultrahigh vacuum chamber. The interaction of the electron beam with the sample

produces different signals including secondary electrons, back-scattered electrons, auger electrons and X-rays. Among which secondary and backscattered electron are used to produce an image. Usually for the detection of the secondary electrons in SEM, an Everhart-Thornley Detector (ETD) is used. The secondary electrons play the important role for detecting the morphology and topography of the sample whereas the backscattered electron show the contrast in the composition of the elements causes the black and white images of the sample. One of the reasons that SEM is preferred for imaging of large amount of sample at once due to its large depth of filed (few mm) and also it has a very high resolution of 1-10 nm depending on the source used and the pixel size of CCD. In this thesis work, we have used FEI Quanta 200, Quanta 250FEG, Versa 3D Field emission SEM (FESEM) for sample analysis. A SEM side-view of vertically aligned Si NWs arrays synthesized by electroless etching method is shown in Figure 2.16 (a). The lengths of nanowires as depicted from SEM are about ~ 2.5-3 μm. A cross sectional SEM image of Au NPs (diameter ≈ 10 nm) decorated ZnO/p-Si NWs core-shell arrays is shown in Figure 2.16 (b) that shows the top ZnO layer and the core-shell structure of the vertically aligned ZnO/p-Si NWs arrays.

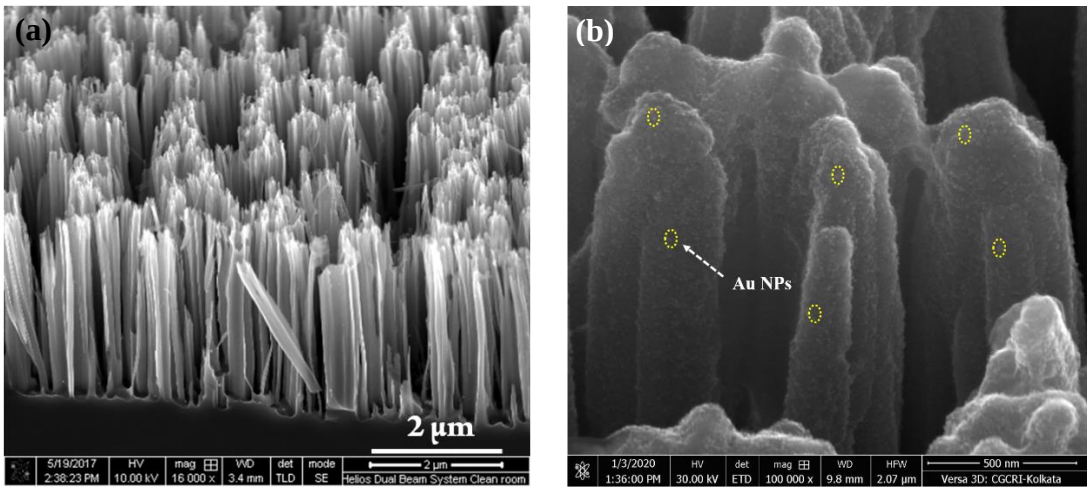

Figure 2.16 Cross-sectional SEM image of (a) vertically aligned Si NWs arrays and (b) Au NPs decorated ZnO/p-Si NWs core-shell arrays.

2.3.1.3 Energy-dispersive X-ray spectroscopy (EDS)

This method is used for identifying and quantifying the elemental composition of a nanomaterial. In a properly equipped SEM, the interaction of electron beam with the atoms on the solid surface causes the emission of specific wavelength of X-rays and the energy of each X-ray is characteristic of the atomic structure of the elements. The emitted X-rays are represented as K, L and M lines depending on the transition to the definite shell of K, L or M and Greek letter α and β subscripted to an X-ray line (K or L or M) to differentiate the transition from different high energy levels to particular low energy levels. Then, these emitted X-rays

are detected by an energy dispersive detector which analysed the energy of these X-rays emission and the specific energy of the X-ray peak has to be identified for each element via comparison with reference spectra. In this thesis, EDS is used to check the localized information about the elemental composition of the samples. Figure 2.17 shows the EDS data of ZnO coated Si NWs core-shell arrays and data confirmed that all the compositional element of ZnO/Si NWs are present without having any impurity elements. We also found that the atomic percentage ratio of Zn:O is approximately 1: 1 which is the desired composition in ZnO. EDS technique is also used in Scanning Transmission Electron Microscope (STEM) to figure out the elemental mapping which reveals the distribution of elements in a specific area of a sample.

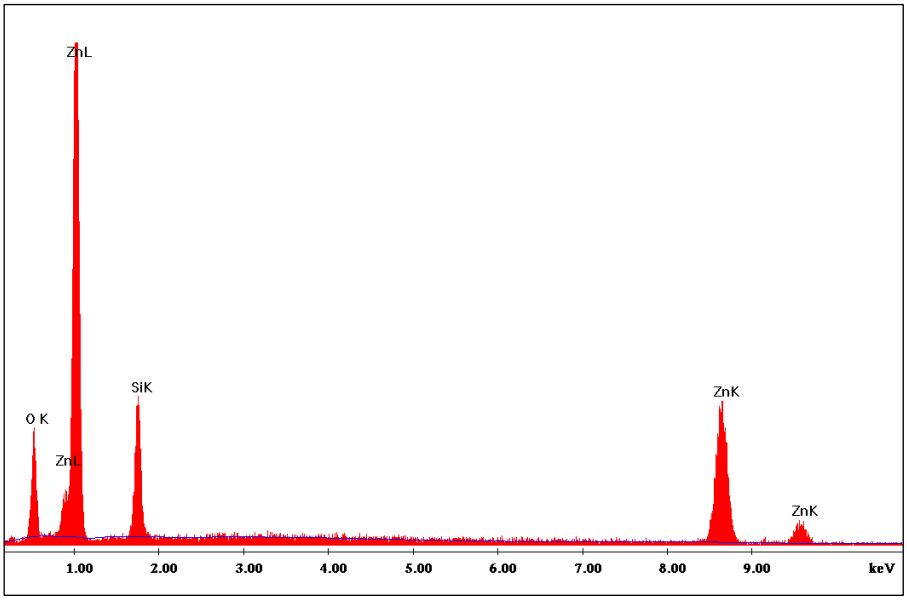

Figure 2.17 EDS data of ZnO coated Si NWs core-shell arrays.

2.3.1.4 High resolution transmission electron microscope (HRTEM)

This is a powerful electron microscope where a high energetic electron beam is transmitted through a thin specimen of sample to collect the information about the size, morphology, crystallographic structure and chemical composition of the material as well as produces 2D images of the nanomaterials [46]. It provides a much higher spatial resolution than SEM because of much higher energetic beam of electrons (100-300 KV, as compared to 5-20 kV in SEM). As the name suggests in TEM, the sample used must be thin (< 200 nm) enough to pass the electron for formation of image. The transmitted electron beam is recorded using a charge couple device camera through stage lens and objective aperture and finally the image is projected on to the fluorescent screen using projector and intermediate lenses. The transmitted beam is used for bright field imaging where the diffracted beam is used for dark field imaging

during collision with the specimen. The TEM dark field and bright field image can be used to characterize the size and morphology as well as crystal structure of the material.

According to Bragg's law the beam suffers diffraction due to interaction of electron beam with specimen. This diffracted beam forms an electron diffraction pattern which can give the information about the atoms and crystal plane and formed a high resolution TEM **(HRTEM)** image at a very a high magnification. HRTEM image gives information about the inter-planer/interatomic spacing (d) which corresponds to specific indices (h, k, l).

The selected area electron diffraction **(SAED)** pattern is obtained in reciprocal space by taking this electron diffraction pattern over a selected specific area of the sample using diffraction aperture which gives information about the indices (h, k, l). Also, the pattern informs us about the structure, orientation, lattice spacing, atomic position and crystallinity or defects.

In the Scanning TEM **(STEM)** mode, the highly diffracted transmitted beam is also collected using a High Angle Annular Dark Field Detector (HAADF) and **HAADF-STEM** image is obtained. The HAADF detector receives inelastically scattered electrons at high angles after passing through the specimen. The contrast in **HAADF-STEM** image is generated by the scattering of electrons which depends on the thickness of the sample as well as atomic number of the element. Therefore, brighter areas correspond to a heavier element while darker areas correspond to a lighter one and thus provides an elemental contrast image.

Along with this, TEM/STEM is equipped with an **EDS** with spatial resolution down to 0.1 nm (depending on the size of the beam spot). This gives an opportunity to figure out the chemical composition or elemental distribution in a specific area of a sample using **EDS line scan** or **EDS mapping**.

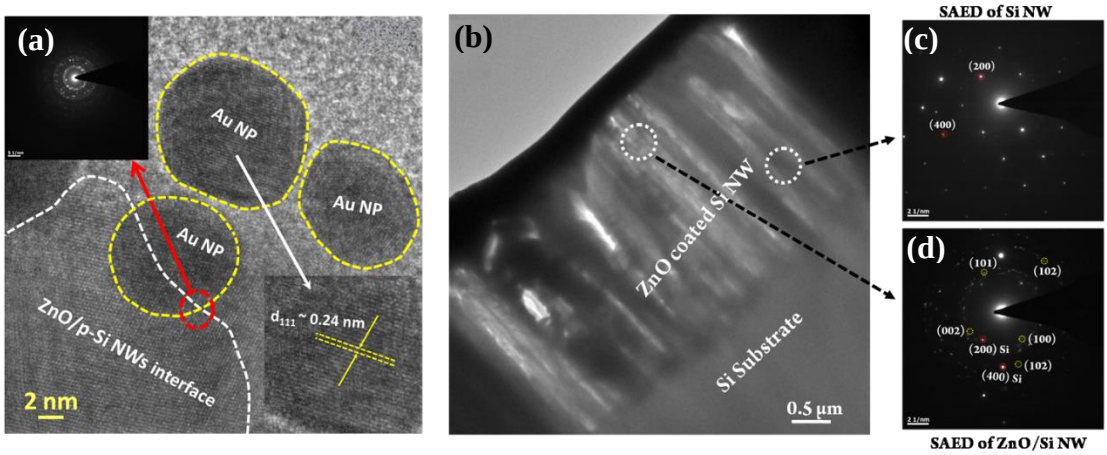

Figure 2.18 (a) HRTEM image ZnO/p-Si NWs decorated with Au NPs. (b) STEM-HAADF image of ZnO/Si NWs cross-sectional lamella. (c) SAED pattern corresponding to crystalline plane of Si and (d) SAED pattern corresponding to both ZnO and Si in ZnO/Si NWs cross-sectional lamella.

In this thesis, TEM images were taken using 200 kV Tecnai G2 TF-20 ST instrument. The conventional method using Gatan PIPS precision ion-polishing system and Focused Ion Beam (FIB) technique has been used for X- TEM sample preparation. The high resolution TEM (HRTEM) image in Figure 2.18 (a) shows the presence of Au NPs on the ZnO of the ZnO/p-Si NWs array. The average diameters of the Au NPs are ~ 10 nm. The lattice spacing of Au NP is ~ 0.24 nm for (111) planes and there are cross-linked fringes of ZnO/p-Si NWs with Au NPs interface. Inset of Figure 2.18 (b) shows the selected area electron diffraction (SAED) pattern of nano crystalline ZnO/p-Si NWs nanostructure arrays decorated with Au NPs. The STEM-HAADF imaging of ZnO/Si NWs cross-section lamellar is shown in Figure 2.18 (b). The electron diffraction patterns are shown in Figure 2.18 (c) and (d). Data in Figure 2.18 (c) shows the SAED pattern corresponding to crystalline plane of Si and Figure 2.18 (d) shows the diffraction planes corresponding to both ZnO and Si. The electron diffraction patterns show that the Si NWs retain their crystallinity whereas, nanostructured ZnO exhibits in polycrystalline phase.

2.3.1.5 X-ray photoelectron spectroscopy (XPS)

It is a very powerful surface analysis technique which gives information on the elemental composition, empirical formula, chemical state, and electronic state of the elements within a material. When a beam of X-rays interacts a solid surface of a material, the electron emission takes place and the kinetic energy of the emitted electron is dependent on the binding energy of the atomic orbital from which the electron originates. It is inherently surface sensitive technique because the low energy (<1500 eV) X-rays is used in XPS and as a result, electrons are emitted from the top 1-10 nm of the material that are being analysed. In XPS, a photoelectron is detected by counting the ejected electrons over a range of electron kinetic energies and the peaks in the spectrum appear from atoms emitting electrons of a particular characteristic energy. As the different elements have a different value of binding energy and that is to be used to identify the elements as well as their concentration in the surface.

In a XPS system, the major components are an X-Ray source, X-Ray monochromator, energy analyzer, ion-gun for sputter etching and charge neutralizer. A monochromatic X-ray (Al K_α line of energy 1486.6 eV) is incident on sample at an angel of 45^o inside a chamber with base vacuum ~ 10^{-8} Pa. The XPS spectrum is a plot of number of electrons detected i.e., intensity versus the electron binding energy in a small energy interval and the variation in the elemental binding energy arises due to the shifts in the chemical potential of the compound. For surface cleaning and depth profiling, the sample surface of an area of ~100μm x 100μm has been etched with Ar^+ ion at 2 keV with a grid voltage of 120 V with rate of sputtering ~1 nm/min for

different time intervals to sputter out the films over an area. In this thesis work, chemical states as well as defects concentration of zinc (Zn), oxygen (O) and silicon (Si) of ZnO/p-Si NWs nanostructures grown by different methods have been characterised through XPS analysis to understand the defects control photoconduction in oxide nanostructures as discussed details in chapter 7. We have also used X-ray Photoelectron Spectroscopy (XPS) through depth profiling to quantify the defects and also to probe the vertical compositions of the oxide nanostructures, which is essential for a better understanding of its optoelectronics properties.

2.3.1.6 Atomic force microscopy (AFM)

It is a kind of scanning probe microscopy to generate the topographical surface maps with unique resolution and to visualize lattices in atomic scale resolution of crystalline samples. The working principle of AFM is originated from scanning tunnelling microscopy (STM) which is based on the principle of quantum mechanical tunnelling. In AFM, a short range coulombic or van der wall's force between the interaction of probe tip and the surface is used for investigation of surface features like morphology, size, surface roughness, and texture. The probe tip is mounted at the end of a cantilever and when the tip approaches the sample surface, deflection of cantilever occurs due to a short-range van der wall's force between the interaction of probe tip and the surface. This deflection is measured by a laser beam which is reflected back of the cantilever to a position sensitive detector and a feedback is used to move the tip up and down in order to maintain a constant force between the tip and the sample surface. This deflection of the tip generates the surface topography represented by contrasted imaging on the screen. In AFM, several scanning modes such as contact mode, non-contact mode, tapping mode, and dynamic mode and intermittent contact mode have been employed for mapping the surface of a sample. In this thesis, we have used AFM in lateral force microscopy (LMF) mode which determines the accurate compactness of the film also the roughness the a-IGZO channel used in TFT (chapter 6).

2.3.2 Optical characterization

Optical characterization techniques are usually non-destructive, fast, and of simple technique for understanding the various fundamental and functional properties of the nanomaterials. The noncontact and non-invasive nature makes these techniques one of the best ideal and practical tools to investigate the physical properties of nanomaterials. The common optical characterization methods are absorption spectroscopy, photoluminescence spectroscopy, and Raman spectroscopy. In this work we have used UV-visible spectroscopy to determine the

absorbance and optical band gap and photoluminescence spectroscopy to investigate the excitonic emission and defect emission of ZnO/Si NWs nanostructures arrays.

2.3.2.1 UV-Visible spectroscopy

It is one of the most simplified and basic technique to determine the absorption of light through liquid or solid sample. It is based on the principle of Beer-lambert law where the absorbance is directly proportional to the concentration of the absorbing species and the path length of the medium. When the light interacts with materials, if the energy of the photon is greater than the band gap of semiconductor, then it can be absorbed and transferring their energy to an electron. When the energy of photon is less than the band gap energy, it cannot be absorbed and will pass through the sample. The photon energy at which the transition between absorbing and non-absorbing behaviour takes place will correspond to the band gap energy. The transition between absorption and transmission provides insight into some of the details of the electron inter-band transitions. This transition region is called absorption edge. When material absorbs light, electrons present in it undergoes excitation and deexcitation and forms absorption spectra which gives an insight into the optical response and band gap of the material. In order to measure the absorption correctly, we must include the process of reflection, transmittance or scattering by the sample. In an UV-Visible spectroscopy, the absorption of a liquid/transparent sample has been measured by recording the transmitted light using a photodetector while the reflected light has been recorded with an integrating sphere at diffuse reflection mode to measure the absorption of a solid/light opaque sample. In this thesis, the optical band gap of nanostructured ZnO is determined using Tauc plot of absorption data. The strength of absorption depends on the difference between photon energy and optical band gap as follows

$$\alpha h\nu = k\,(h\nu - E_g)^n \qquad (2.4)$$

Where h is the Planck constant and ν is the photon's frequency. α is absorption coefficient, k is a proportionality constant and E_g is the band gap of ZnO. The value of n is ½ for direct band gap semiconductor. Figure 2.19 (a) shows the Tauc plot of nanostructured ZnO film for determination of band gap. The value of the intercept due to the extrapolation of this linear region gives the band gap ($E_g \approx 3.3$ eV). As the optical response of a photo-detector depends on the light being absorbed. Thus, a broadband detector should have a broadband absorption. In this thesis, we have also measured the absorption spectra of ZnO/p-Si NWs nanostructures with an integrating sphere at diffuse reflection mode for solid sample in an UV-Visible spectrophotometer in the wavelength range of 300-900 nm. The optical absorption (α) of the ZnO/p-Si NWs core-shell arrays is shown in Figure 2.19 (b) in the wavelength range of 300-

900 nm. There is a strong absorption edge nearly at 375 nm that correspond to band gap absorption of ZnO. In addition, even in the bare n-ZnO/Si NWs array there is a hump like feature around ~ 450 nm. This arises due to absorption of Si NWs that increases at shorter wavelength and also the absorption length becoming comparable to diameter of Si NWs that contributes to decreasing absorption discussed details in chapter 4.

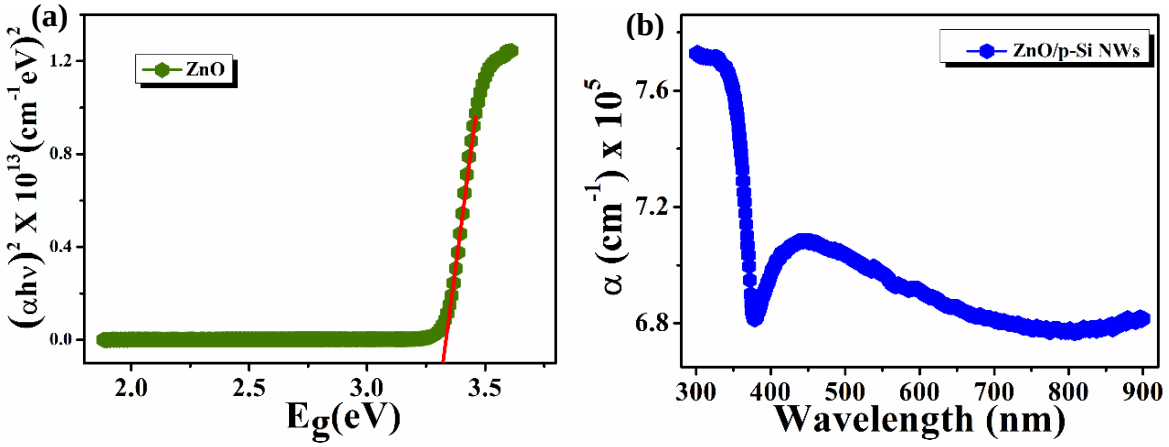

Figure 2.19 (a) Tauc plot of UV-Vis absorption spectra for determination of band gap. (b) Absorption spectra of ZnO/p-Si NWs core-shell arrays.

2.3.2.2 Photoluminescence (PL) spectroscopy

It is an extremely fast spatially resolved characterization technique which provides an important information on the optical properties, electronic structure, and also impurity levels and defects of the materials. In this process, photoexcitation of a semiconductor material elevates the electron from the valence band to the conduction band and leaving a hole in the valence band. Then this excited electron recombines with the hole either radiatively by emitting a photon or non-radiatively via impurities or defects states (Shockley–Read–Hall recombination) or by passing the energy to another electron or hole (Auger recombination). Therefore, PL spectra gives insight into the direct measurement of the band gap energy, determination of impurities, dopant concentrations, and structural defects, and understanding of the electron–hole recombination mechanisms and It has the highest potential to identify the extremely low concentration of intentionally or unintentionally created defect states which strongly affect material quality. The PL spectra of samples are recorded at room temperature at an excitation wavelength of 300 nm by using Fluorolog (Horiba) spectrometer in the wavelength range of 300-900 nm. In this thesis, photoluminescence (PL) measurement has been carried out to investigate the type of defects and their impact on photoconduction of ZnO/p- Si NWs nanostructures arrays. The electrical conductivity and photosensitivity of oxide

semiconductors are strongly dependent upon the concentration of surface/interface defects discussed details in chapter 7.

2.4 Conclusion

In this thesis chapter, we have demonstrated the different growth methods for synthesis of metal oxide nanostructures and thin film. We have also synthesised the ligand-free plasmonic NPs (Au, Pd) by novel pulsed laser ablation in liquid (PLAL) method. We have focussed with the dealing of known challenges on fabrication processes which gives the proper materials with stable charge carriers and defects state and its revival in the field of opto-electronics and other sensing applications. All the samples have been characterised by using advance characterization techniques which gives the necessary information about the phase purity, homogeneity, crystallinity and surface morphology of the samples. The detailed analysis of cross-sectional transmission electron microscopy (X-TEM) as well as energy dispersive X-ray spectroscopy (EDS) of nanostructured complete device gives an insight of high-quality device fabrication. Each of these specialized equipments gives specific information that plays an important role in this thesis.

Bibliography

1. A. K. Radzimska, and T. Jesionowski, *Materials*, **7**, 2833 (2014).
2. M. A. Borysiewicz, *Crystals*, **9**, 505 (2019).
3. D. Nunes, A. Pimentel, A. Goncalves, S Pereira, R. Branquinho, P. Barquinha, E. Fortunato and R. Martins, *Semicond. Sci. Technol*., **34**, 043001 (2019).
4. P. C. McIntyre, H. Adhikari, I. A. Goldthorpe, S. Hu, P. W. Leu, A. F. Marshall, and C. E. D. Chidsey, *Semicond. Sci. Technol.* **25**, 024016 (2010).
5. W. Li, Y. Sun, and J. Xu, *Nano-Micro Lett*., **4**, 98 (2012).
6. S. Huang, Q. Yang, B. Yu, D. Li, R. Zhao, S. Li and J. Kang, *Nanoscale Res. Lett*., **9**, 328 (2014).
7. W. Tian, H. Sun, L.Chen, P. Wangyang, X. Chen, J. Xiong, and L. Li, *InfoMat*., **1**, 140 (2019).
8. J. E. Elshof, Chemical solution deposition techniques for epitaxial growth of complex oxides, Woodhead Publishing Series in Electronic and Optical Materials, edited by G. Koster, M. Huijben, and G. Rijnders, Woodhead Publishing, 2015.
9. L. Xie, D. Abliz, and D. Li, Thin Film Coating for Polymeric Micro Parts, vol. 7 of edited by S. Hashmi, G. F. Batalha, C. J. Tyne, and B. Yilbas, Comprehensive Materials Processing, Elsevier, 2014.
10. Z. Huang, N. Geyer, P. Werner, J. Boor, and U. Gosele, *Adv. Mater*., **23**, 285 (2011).
11. Z. L. Wang, *Mater. Today*, **7**, 26 (2004).
12. P. P. Patil, D. M. Phase, S. A. Kulkarnai, S. V. Ghaisas, S. K. Kulkarni, S. M. Kanetkar, S. B. Ogale, and V. G. Bhide, *Phys. Rev. Lett*., **58**, 238 (1987).
13. M. Kim, S. One, T. Kim, H. Higashi, and T. Seto, *KONA Powder Part. J*., 34, 80 (2017).
14. C. W. Hollars and R. C. Dunn, *Rev. Sci. Instrum*., **69**, 1747 (1998).
15. J. L. Gomez and O.Tigli, *J. Mater. Sci.*, **48**, 612 (2013).
16. S. Yue, Z. Yan, Y. Shi, and G. Ran, *Mater. Lett*., **98**, 246 (2013).
17. L. Xiao, E. Li, J. Yi, W. Meng, S. Wang, B. Deng, and J. Liu, *J. Alloys Compd*., **764**, 545 (2018).
18. S. Lu, H. Wang, J. Zhou, X. Wu, and W. Qin, *Nanoscale*, **9**, 1184 (2017).
19. R. S. Wagner and W. C. Ellis, *Appl. Phys. Lett.*, **4**, 89 (1964).
20. J. Westwater, D. P. Gosain, S. Tomiya, S. Usui, and S. Ruda, *J. Vac. Sci. Technol.* B, **15**, 554 (1997).
21. D. P. Yu, Z. G. Bai, Y. Ding, Q. L. Hang, H. Z. Zhang, J. J. Wang, Y. H. Zou, W. Qian, G. C. Xiong, H. T. Zhou, and S. Q. Feng, *Appl. Phys. Lett*., **72**, 3458 (1998).
22. C. C. Buttner, N. D. Zakharov, E. Pippel, U. Gosele, and P. Werner, *Semicond. Sci. Technol.*, **23**, 075040 (2008).
23. Y. Q. Fu, A. Colli, A. Fasoli, J. K. Luo, A. J. Flewitt, A. C. Ferrari, and W. I. Milne, *J. Vac. Sci. Technol.* B, **27**, 1520 (2009).
24. J. de Boor, N. Geyer, J. V. Wittemann, U. Gosele, V. Schmidt, *Nanotechnology*, **21**, 095302 (2010).
25. B. Ozdemir, M. Kulakci, R. Turan, and H. E. Unalan, *Nanotechnology*, **22**, 155606 (2011).
26. M. A. Lachiheb, N. Nafie, and M. Bouaicha, *Nanoscale Res. Lett*., **7**, 455 (2012).

27. C. Samanta, A. Ghatak, A. K. Raychaudhuri, and B. Ghosh, *Nanotechnology*, **30**, 305501 (2019).
28. P. Uthirakumar, B. Karunagaran, S. Nagarajan, E. K Suh, and C. H. Hong, *J. Cryst. Growth*, **304**, 150 (2007).
29. Z. Gao, and P. Banerjee, *J. Vac. Sci. Technol. A*, **37**, 050802 (2019).
30. A. Afshar and K. C. Cadien, *Appl. Phys. Lett*., **103**, 251906 (2013).
31. J. T. Tanskanen, C. Hägglund, and S. F. Bent, *Chem. Mater*., **26**, 2795 (2014).
32. J. Cai, Z. Ma, U. Wejinya, M. Zou, Y. Liu, H. Zhou, and X. Meng, *J. Mater. Sci*., **54**, 5236 (2019).
33. T. Weckman and K. Laasonen, *J. Phys. Chem. C*, **122**, 7685 (2018).
34. C. Samanta, S. Bhattacharya, A. K. Raychaudhuri, and B. Ghosh, *J. Phys. Chem. C*, **40**, 22235 (2020).
35. M. A. Borysiewicz, E. Dynowska, V. Kolkovsky, J. Dyczewski, M. Wielgus, E. Kami, and A. Piotrowska, *Phys. Status Solidi A*, **209**, 2463 (2012).
36. S. Y. Bae, C. W. Na, J. H. Kang, and J. Park, *J. Phys. Chem. B*, **109**, 2526 (2005).
37. A. R. West, Solid State Chemistry and Its Applications, *Wiley and Sons*, 2005.
38. R. Nath, "Investigation of novel electrical and magnetic properties of perovskite oxides", Ph.D. Thesis (2015), University of Calcutta, Kolkata, India.
39. C. Samanta, R. R. Ghimire, and B. Ghosh, *IEEE Trans. Electron Devices*, **65**, 2827 (2018).
40. W. Ouyang, F. Teng, J. H. He, and X. Fang, *Adv. Funct. Mater*., **29**, 1807672 (2019).
41. H. Atwater, and A. Polman, *Nature Mater*., **9,** 205 (2010).
42. M. Valenti, M. P. Jonsson, G. Biskos, A. S. Ott, and W. A. Smith, *J. Mater. Chem. A*, **4**, 17891 (2016).
43. R. K. Neogy and R. Nath, *Micro and Nanosystems*, **3**, 319 (2011).
44. B. D. Cullity and S. R. Stock, "Elements of X-ray Diffraction", Prentice Hall, 2001.
45. R. F. Egerton, "Physical Principles of Electron Microscopy: An Introduction to TEM, SEM and AEM", Springer, 2005.
46. D. B. Williams, C. B. Carter "Transmission Electron Microscopy A Textbook for Materials Science", Springer, 2009.

Chapter 3

Description of experimental techniques

In this chapter, we have discussed the different experimental techniques along with the details of fabrication of different devices like photodetector, gas sensors and thin film transistors, used for electrical and optoelectronic measurements of two terminals and three terminal field effect semiconductor devices depending upon the nature of the measurements. We have also discussed about the preparation techniques of cross sectional TEM (XTEM) sample (lamella) which helps us to establish the physical structure of the devices and also to study the surface-interface physics of oxide nanostructures. We have fabricated devices (photodetector, gas sensor and thin film transistor) based on ZnO/Si NWs nanostructures arrays and amorphous IGZO thin film through hard mask lithography technique. The measurement setups are automated by General Purpose Interface Bus (GPIB) interfacing with LabVIEW/C++ programming for data acquisition.

3.1 Introduction

Along with growth of pure phase good quality sample preparation, the fabrication of high-quality nanostructure devices are also the key components that have an important role for understanding of the basic physics related to electrical, optoelectronic and other physical properties of oxide nanostructures. The interfacing of nanodevices with the micro electronic system has been done through various nanofabrication techniques for realization of physical behaviour in nanoscale. The formation of electronics devices has been done by contacting two or more dissimilar materials (semiconductor, metal, insulator) together. The optoelectronics and electrical measurement can be done by making the electrical contacts (metal contacts) on both ends of oxide nanostructures arrays and thin film devices. The interface between metal and semiconductor becomes crucial because it affects the optoelectronics and electrical properties of the devices as utilizing the fine control of charge carriers, which are injected into the semiconducting material through electrical contacts. Spatially resolved tools for developing cross sectional sample and microstructural as well as chemical compositional analysis of the cross-section of the device enables us to make a proper physical model and that can be utilized to make a model-based simulation of the devices using COMSOL Multiphysics software. The preparation and characterization of cross-sectional (X-TEM lamella) samples have been done through conventional method and also using Focused Ion Beam (FIB) milling technique enables us to make a proper physical model of the devices and study the surface/interface physics of oxide nanostructures. In this thesis our goal is to tune the electrical and the optoelectronic properties of oxide semiconductor by making heterostructures or FET type device structures. So, the various nanodevices have been fabricated depending upon the nature of experiments. We will also discuss the experimental techniques developed and used for measurement.

3.2 Device fabrication

Electronic and optoelectronic measurements are convenient technique for investigation of charge carrier characteristics in nanostructured materials. The resistivity, carrier mobility, carrier concentration, etc., can be determined using electronic measurement technique. The optoelectronic measurement technique includes the interaction of light with material which gives the information about the transport properties of photo generated charge carriers and carrier recombination process. In this thesis work we have fabricated the devices such as photodetector, gas sensor and thin film transistor (TFT) based on ZnO/Si NWs nanostructures and amorphous IGZO thin film. Experimental techniques for electrical, optoelectronics and gas

sensing measurements have also been discussed. These are two terminals and three terminal field effect devices depending upon the nature of the measurements. For electrical and optoelectronic measurements, two Au/Cr contact pads are deposited by thermal evaporation on ZnO/Si NWs core-shell arrays in metal-semiconductor-metal (MSM) configuration through a hard mask. The interface/junction between metal and semiconductor becomes crucial because it affects the optoelectronics and electrical properties of the devices as utilizing the fine control of charge carriers, which are injected into the semiconducting material through electrical contacts.

A schematic diagram of photodetector based on Au NP decorated ZnO/p-Si NWs core-shell arrays is shown in Figure 3.1 (a). A top gated TFT device structure is shown in Figure 3.1 (b) where the a-IGZO serve as channel material and Au/Cr contact pads act as source (S) and drain (D) as well as gate (G) is deposited by thermal evaporation method and the polymer electrolyte ($PEO+LiClO_4$) serve as gate dielectric layer [1]. The W/L ratio of the a-IGZO device is 1:3. The gate dielectric was prepared from a gel containing 10:1 weight ratio of polyethylene oxide (PEO) and $LiClO_4$, which was deposited on the a-IGZO channel at room temperature by spin coating / drop casting. The S and D metal electrodes were protected from the electrolytes by a layer of poly(methyl methacrylate) (PMMA). This protection by PMMA reduced the gate leakage current significantly and the ratio of drain to gate current > 10^3.

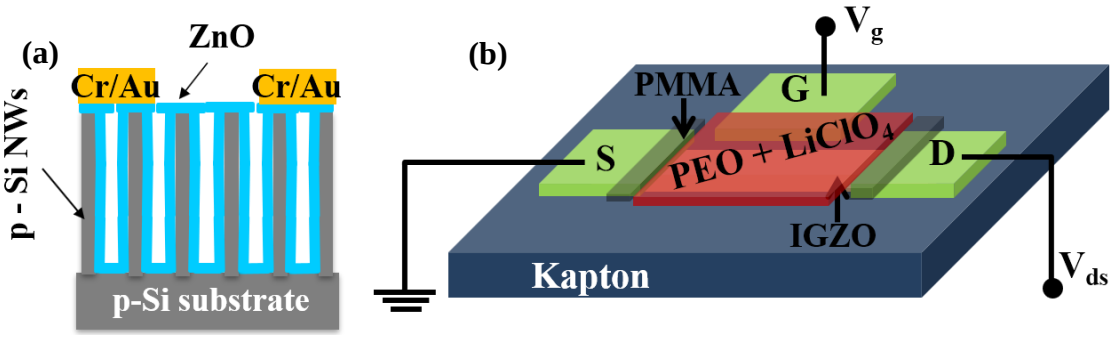

Figure 3.1 (a) Schematic diagram of ZnO/p-Si NWs core-shell arrays based photodetector. (b) A schematic of Flexible TFT composed of a kapton substrate, source, drain and gate Cr/Au electrode patterns, an amorphous IGZO semiconducting channel and polymer electrolyte (PEO + $LiClO_4$) as gate dielectric and PMMA layer for electrical isolation.

Electrical connections to the devices are made on the macroscopic (~2mm x 2mm) metal contact pads (Figure 3.1 (b)). An enamelled Cu wire (Gauge number: 39) is dipped partially in ortho-phosphoric acid and the two ends etched out. One end of Cu wire is attached to the metal electrodes through a conducting silver epoxy paste (sheet resistance ~ 0.02Ω/sq.). The sample is dried for 6-8 hrs before any measurements. The other end of the Cu wire is soldered onto a

printed circuit board. From here, banana or BNC connectors are used to connect to the required instrument.

3.3 Experimental techniques

3.3.1 Optoelectronics measurement

The optical response has been measured in ambient conditions with a Xenon lamp and a monochromator working in the wavelength (λ) range 300 nm to 1100 nm. A schematic of the experimental set-up is given in Figure 3.2. The power density of the incident light was calibrated in the wavelength range up to 1100 nm using a Si detector with calibration traceable to National Institute of Standards and Technology (NIST).

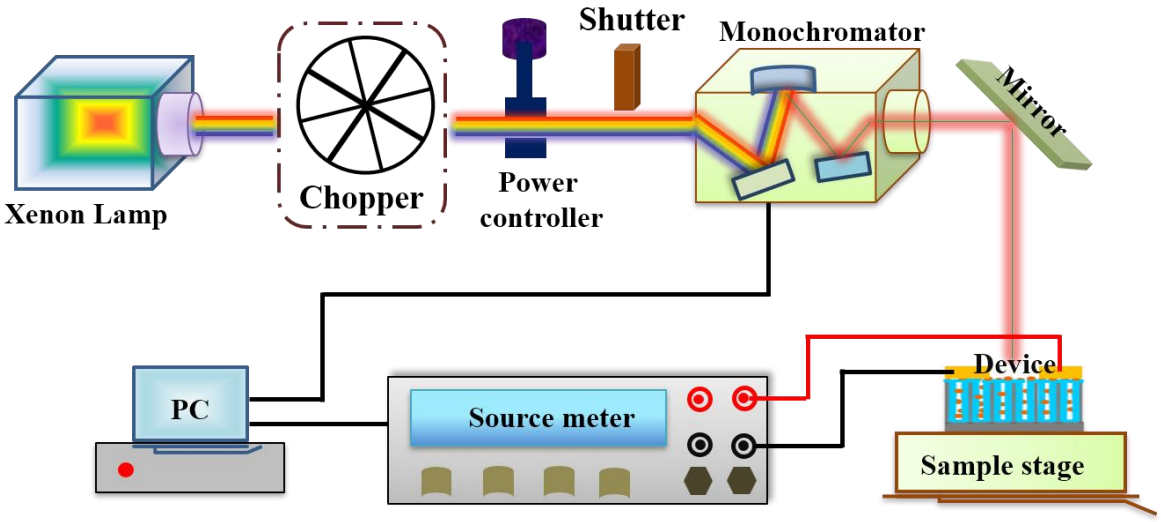

Figure 3.2 A schematic of photoresponse measurement set-up.

The sample is placed on an adjustable XYZ stage inside a dark chamber with electrical leads connecting to a Source Meter with a current resolution of 10 pA. The illumination is turned 'ON' and 'OFF' mechanically by a shutter when data (shown in chapter 4 in the section of broadband photoresponse of Au NPs decorated n-ZnO/p-Si NWs core-shell arrays) has been taken. The optical responses, such as device current vs. wavelength $(I-\lambda)$ and the current-voltage $(I-V)$ characteristics in dark as well as under illumination of different power intensity are measured using a Source Meter. For these measurements we have used LabView program to collect the data using a GPIB interface. All measurements were taken at room temperature and under ambient atmospheric conditions. The main experiments consist of measuring the followings:

- Device current (I) as a function of bias (V) at a fixed wavelength (λ) with different illumination intensities ($\Im$) by turning illumination ON and OFF referred to as $I-t$ curves.

● The $I - V$ curves in dark and under illumination of variable intensities ($\Im$)

● Spectral dependence of photocurrent (I_{PC}) in the spectral range 300-1100 nm for a fixed bias. Photocurrent is defined $I_{PC} \equiv I - I_d$ for a given bias, illumination intensity and wavelength where I is the total device current under illumination and I_d is the dark current.

From the observed data following opto-electronic parameters have been obtained that are used to quantitatively evaluate the photodetector characteristics:

(a) The responsivity $R \equiv \frac{I_{PC}}{P}$ (in units of A/Watt) is the ratio of the photocurrent I_{PC} to incident power (P), P is obtained from the illumination intensity $\Im$ (in Watt/cm^2) measured with the Si standard photo diode, so that $P = \Im \times A$.

(b) The current gain $G \equiv \left(\frac{I_{PC}}{e}\right)\left(\frac{h\frac{c}{\lambda}}{P}\right)$, the first term in bracket is the charge generated per unit time and $\left(\frac{P}{h\frac{c}{\lambda}}\right)$ being the number of photons of wavelength λ absorbed by the device per unit time.

3.3.2 Gas sensing measurement

The gas sensing properties are measured in a high vacuum (HV) custom-made chamber at room temperature. A schematic of the experimental set-up is given in Figure 3.3. The chamber was initially pumped down to a base pressure 10^{-6} mbar by a Turbomolecular pump and flashed by dry nitrogen (N_2) a number of times. After initial cleaning, a fixed number of moles of dry N_2 was admitted to the chamber.

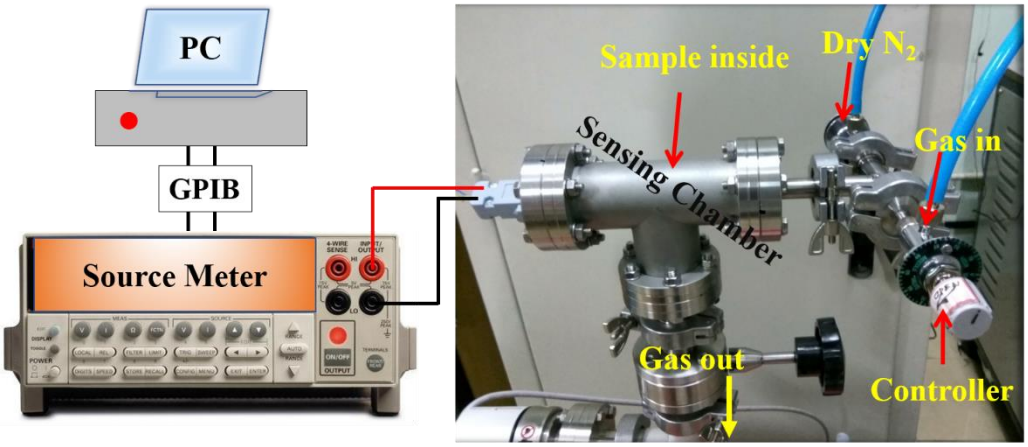

Figure 3.3 Gas sensing measurement set-up.

The sensor is biased with 0.5 V and the current and resistance of the sensor are recorded over time till it is stable. The current-voltage ($I - V$) curve is also measured. After getting stable

values of device current at a given bias a known moles of nitric oxide (NO) gas are injected into the chamber and the changed device current was measured. The $I-V$ curves after gas exposure were also measured. The measurements were done using a source- meter. By repeating the measurements for several times, the changes of current/resistance with time under different concentrations of NO were recorded. Data were taken in controlled NO concentration range of 0.5 – 200 ppm (in dry N_2 ambience). We have tested a number gas sensing devices made in similar fashion to establish the reproducibility of the sensors. The sensor is also stable under dry air. NO gas is known to react with oxygen to form NO_2. Due to this instability of NO in air, we did all the measurements in dry N_2. From the device current I (at a given bias V), the device resistance was obtained. The performance of gas sensor device is quantified by the normalized response Ř defined as:

$$\check{R}(\%) = \frac{R_g - R_0}{R_0} \times 100\% \qquad (3.1)$$

Where, R_0 and R_g are the measured electrical resistances of gas sensing devices in dry nitrogen environment and on exposure to nitric oxide (NO) respectively. In this definition when the device resistance increases (decreases) on gas exposure Ř is positive (negative).

3.3.3 Electrical characteristic of FET device

The transistor characteristics such as transfer characteristic (drain current vs. gate voltage), output characteristic (drain current vs. drain voltage) and transient gate response (gate current vs. time) are measured at room temperature using Keithley 2400 source meter [2]. The measurement setup is shown in Figure 3.4 where the source meter is connected to the computer using GPIB cable. Data Acquisition process is done using C^{++} code (In some cases $LabVIEW$ programs also used). To calculate field effect mobility, the specific gate capacitance (C_g) of electric double layer (EDL) capacitor has been calculated from the time constant of charging of gate dielectric when a step change in the gate bias (V_g) is applied to the gate dielectric. The capacitance of the EDL gate dielectric has been also measured separately with (metal/electrolyte/metal) configuration using a precision LCR-meter (HIOKI) in C_P mode. The saturation mobility (μ_{sat}) is commonly evaluated from the slope of the square root of the drain current ($\sqrt{I_d}$) against the gate voltage (V_g) and threshold voltage (V_{th}) is measured from the intercept of linear fitting of $\sqrt{I_d}$ vs. V_g curve using the following conventional equations [3]:

$$I_{ds}^{1/2} = \left(\frac{C_g W \mu_{sat}}{2L}\right)^{\frac{1}{2}} (V_{gs} - V_{th}) \qquad (3.2)$$

$$\mu_{FE} = \frac{g_m}{C_g \frac{W}{L} V_d} \quad (3.3)$$

Where L and W are the length and width of the device respectively, C_g is the specific gate capacitance and $g_m = \frac{\partial I_d}{\partial V_g}$, is the mutual conduction or transfer conduction that depends on gate voltage (V_g). There is yet another effective mobility (μ_{sat}) that depends on V_g which can be obtained from output characteristics and defined as:

$$\mu_{eff} = \frac{g_D}{C_g \frac{W}{L}(V_g - V_{th})} \quad (3.4)$$

Where conduction, $g_D (= \frac{\partial I_d}{\partial V_{ds}})$ obtained from the output characteristics curve with low V_{ds} at a fixed gate voltage (V_g).

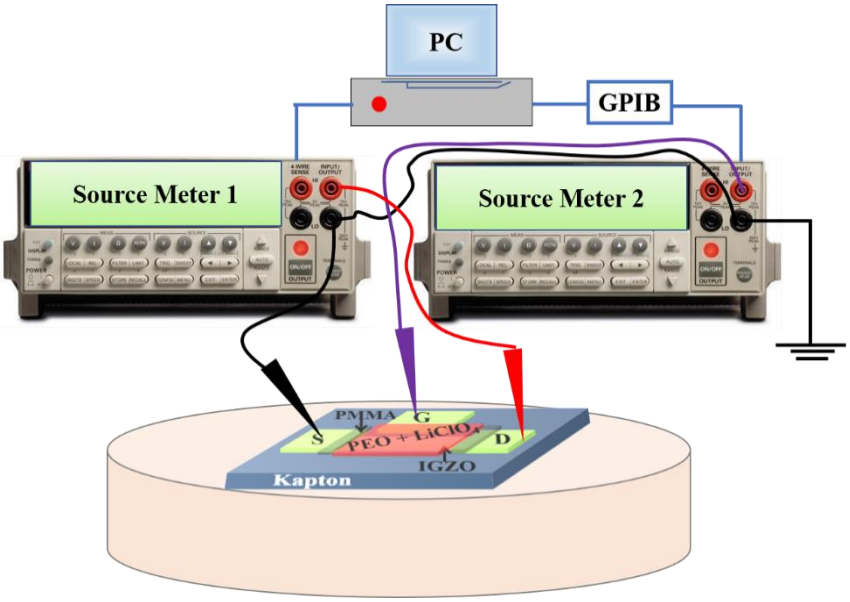

Figure 3.4 Measurement set-up for transistor characteristics.

3.4 Fabrication of cross-sectional sample (XTEM lamella) for high resolution TEM analysis

In recent, the requirements for X-TEM samples have been increasing through the years for study of micro structure, composition and interfaces (such as semiconductor devices, thin film layers, etc.) by transmission electron microscopy (TEM) and preparation technique is one of the most crucial stage to reach the ultimate quality of TEM samples. Ideally, the sample shall be flat and smooth and thin enough (under 50 nm) to be electron transparent. The goal in TEM sample preparation is simple in principle: the sample must have a defined geometry and thickness (to fit in the electron microscope sample holder and be electron transparent) with a large area of equal thickness. Artefacts should not be introduced during the preparation steps

and it should be mechanically strong enough to withstand handling and the process should be fast and reproducible. We have prepared the X-TEM samples by two standard methods: (i) the conventional mechanical method with Gatan PIPS (GATAN Inc., Pleasanton, CA) precision ion-polishing system and also (ii) ion beam lithography using a focused ion beam (FIB) set-up with Ga^+ ions. The procedure for lamella preparation has been described in below.

3.4.1 Mechanical method with ion milling

This TEM sample preparation method consists of mechanical cutting (ultrasonic cutting), grinding, polishing, and dimpling. After that ion milling technique has been employed for additional thinning of the sample and that can be electron transparent [4]. A short overview of ion milling technique is shown schematically in Figure 3.5.

(a) First, two rectangular pieces of sample (ZnO/Si NWs nanostructures arrays) with the interesting surfaces face-to-face are sandwiched with $Gatan\ G1$ epoxy and mounting inside a brass tube of 3 mm diameter. Then a disk of ~200 um thickness is obtained by sectioning this brass tube using a Buehler ISOMET (Buehler Inc., Lake Bluff, IL) low speed diamond saw [5].

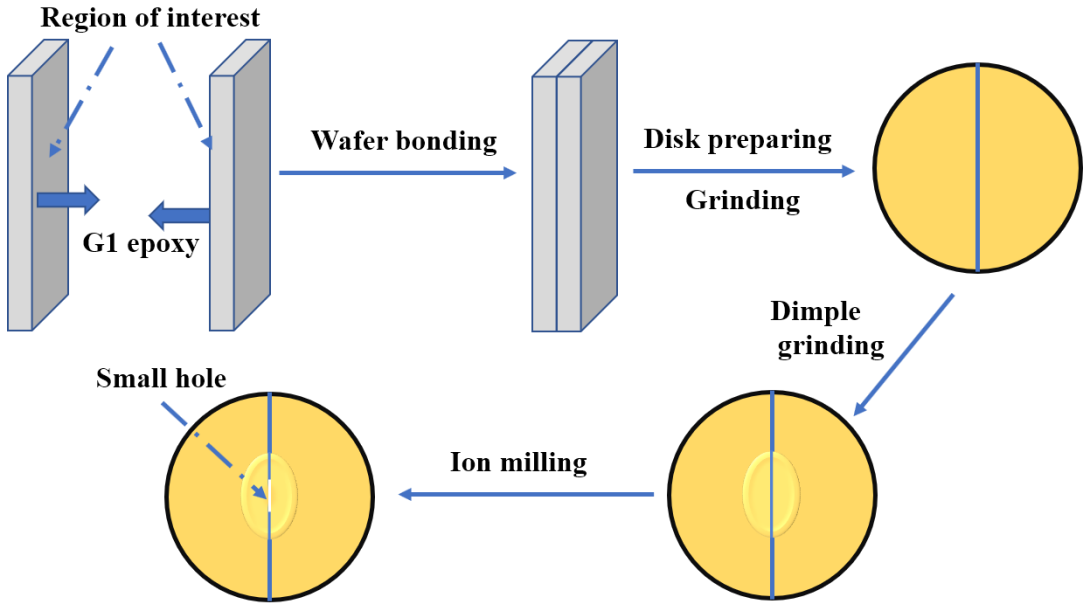

Figure 3.5 Schematic diagram of XTEM sample preparation technique by mechanical method with ion milling process.

(b) The thickness of the sectioned disk is further reduced to ~ 80-100 um in thickness by grinding and polishing with a series of diamond abrasive papers with decreasing grain sizes. Each step removes the scratches from the previous one.

(c) After that dimpling is performed on the disk center using a $Gatan\ 656$ dimple grinder. In the next stage, dimple-polishing wheel with cloth has been utilized to obtain a smooth surface. The dimpling can be done only one or both side of the disk and the nominal thickness after dimpling is ~20-25 μm.

(d) Now the dimpled disk is ready for ion milling. Ion milling is performed with 4 keV Ar^+ ions at an incident angle of 4° and ~ 55 -60 μA of beam current to obtain the electron transparency in the film-substrate cross-section using a Gatan precision ion polishing (PIPS) system. The process of thinning has been completed by opening a small hole in the middle of the disk which is monitored by the optical microscope during the ion-milling process.

In this technique we have prepared a cross sectional lamella of ZnO/Si NWs core-shell arrays which enables us to make a proper physical model of the devices and study the surface/interface physics of oxide heterostructures.

3.4.2 Focused ion beam (FIB) method

Focused Ion Beam is a fabrication tool used for industrial and research applications for decades. The precision and sensitivity required for fabrication the devices like sensors, actuators and interconnects inspires researchers to push their limits on systems like FIB. FIB uses liquid metal ion source (LMIS) as a primary component of the system. The instrument used here is a dual beam FIB-FESEM which consists of ion source (LMIS) as well as electron beam (e^- beam) source and both can be used as imaging like SEM [6]. Apart from imaging, dual beam system mainly utilized for lithography for nano device fabrication and sample preparation (cross sectional lamella) for High Resolution TEM analysis with the help of other additional accessories. The primary part of FIB consists of liquid metal ion source (LMIS), e^- beam source, electrostatic lenses, gas injection system (GIS) and Omni Probe needle used for in-situ sample lifting. Figure 3.6 (a) shows FEI Dual Beam Helios 600 FIB-SEM instrument with a separation angle of 52^o between ion beam and electron beam at our nanofabrication lab and Figure 3.6 (b) shows the inside view of the sample chamber of that FIB-FESEM. The ion beam is aligned at an angle of 52^o with the electron beam as shown schematically in Figure 3.7 (a). Primarily, the ion source (here Ga^+) is used to deposit metal and cutting/milling. The details of FIB ion milling, deposition and in-situ sample lifting techniques have been discussed below.

FIB milling: FIB milling is a process to remove (sputter) the target material using a beam of positively charged ions emitted from liquid metal ion source (LMIS) [6]. Ga is the most

commonly used ion source for FIB instruments for its low melting points, volatility, vapor pressure and excellent mechanical, electrical, properties. A schematic diagram of Ga^+ ion source is shown in Figure 3.7 (b).

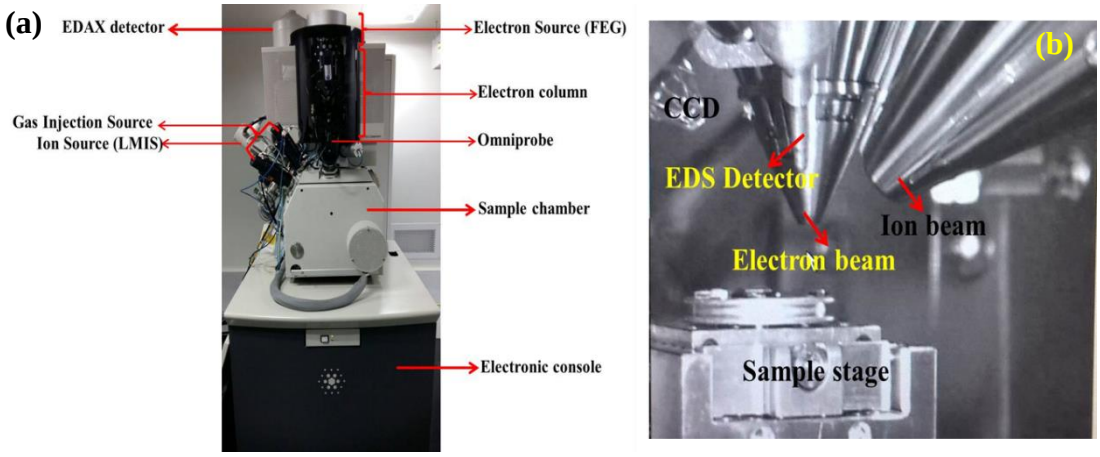

Figure 3.6 (a) Helios 600 Dual beam FIB-FESEM System (lab set up). (b) Image of all the probes inside the FIB-FESEM sample chamber. Reprinted with permission from [7].

This ion beams are accelerated, collimated and focused by a series of apertures and electrostatic lenses on to the sample. The milling rate is dependent on the angle of the incident beam and the mass of the targeted material atoms as well as the ion energy. The cutting/milling of the ZnO/Si NWs nanostructure sample during the lamella preparation has been done using this Ga^+ LMIS FIB.

FIB metal deposition: In FIB system both electron and ion beam are used according to the requirement of deposition of metals like platinum (Pt) or insulators like silicon dioxide (SiO_2) thin film with the assistance of gas injection system (GIS). The Pt deposition is achieved by the electron/ion beam assisted decomposition of methylcyclopentadienyl platinumtrimethyl $(CH_3)_3(CH_3C_5H_4)Pt$, which is a metal-organic gas precursor for Pt metal [8]. Figure 3.7 I shows the schematic of platinum deposition using FIB. It is one of the crucial steps during cross sectional lamella preparation as it has been used for depositing a protective layer and welding purpose. Ion beam deposition has been done with accelerating voltage of 15 kV and beam current of 43 pA.

In-situ sample lift out: An Omni Probe needle (OmniProbe) has been used to lift out the cross-sectional lamella from the bulk substrate. It is made of stainless-steel material and the tip has to be sharpened using ion beam milling as per the requirement during lamella lift off [6]. It is specially used along with the GIS to lift off the lamella from the bulk ZnO/Si NWs substrate and attaching it to the TEM-grid.

In this thesis, the lamella preparation of ZnO/Si NWs nanostructure is carried out using the FIB system. First, we have been chosen the region of interest (ROI) before starting the lamella preparation and then sample is placed at a eucentric height (focal plane of electron and ion source), so that it remains focused for both ion beam and e^- beam during lamella preparation. Also, we have standardized the process parameters (i.e., ion energy, beam current) to avoid possible damage during cross section.

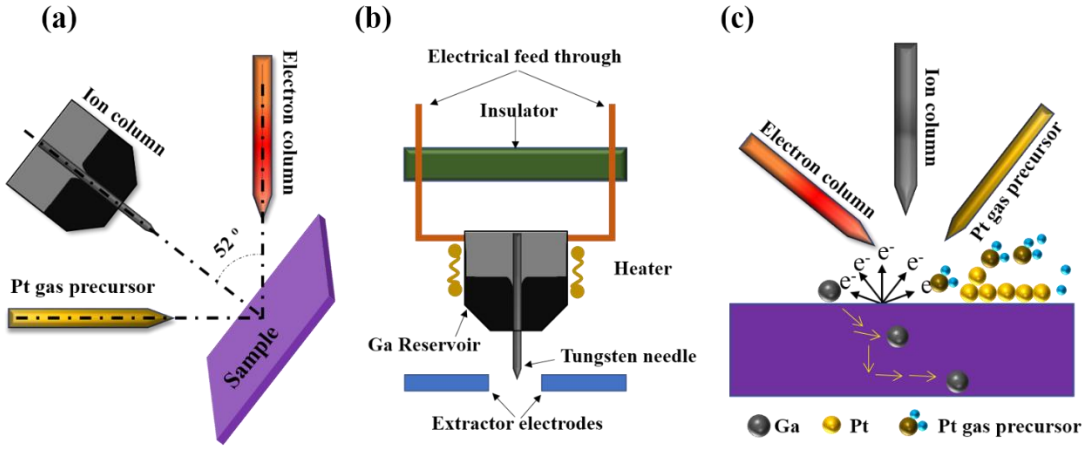

Figure 3.7 Schematic of (a) typical dual-beam column configuration, a vertical electron column with a tilted ion column, (b) Gallium ion source and (c) Platinum deposition using FEB. Sample is tilted at 52º to make the sample surface normal to ion column.

The procedure for lamella preparation has been described as follows:

3.4.2.1 Protective layer deposition

In the first step, a platinum layer is deposited to protect the ROI of sample using FIB and GIS the ROI. The typical dimension (X × Y ×Z) of the protective layer made on sample is (15µm ×2 µm ×2 µm) shown in Figure 3.8 (a).

3.4.2.2 Bulk milling, Intermediate milling and U-Shape cut

Milling and cross sectional cutting of lamella from the sample is carried out after the deposition of the protective layer. In this process standardization has been made to minimize Ga^+ deposition and the lamella is prepared for X-TEM analysis. The steps involved in this process are:

(a) Bulk milling

In this step the FIB regular cross-sectional cut has been performed. The milling with dimension of (15µm ×10µm ×5µm) has been performed with accelerating voltage of 20 kV and beam current of ~ 10-20 nA. just below the lamella with Pt-layer on both side of the ZnO/Si NWs

sample. The stage is tilted at 52^{o} to face of the ion beam directly during this process. The lamella after the bulk or regular milling has been shown in Figure 3.8 (b) and it is standing like a nano wall inside the ZnO/Si NWs hetero structure sample.

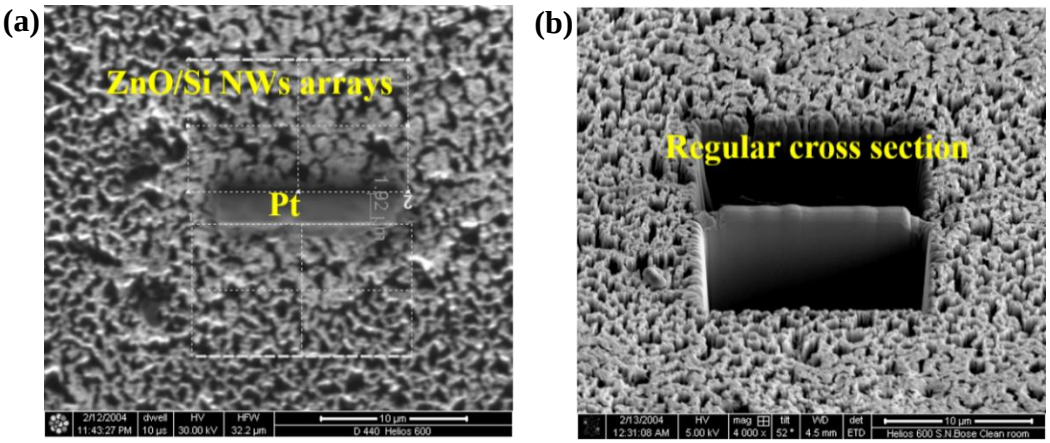

Figure 3.8 (a) Protective Pt layer deposited on top of the ZnO/Si NWs arrays. (b) After regular cross-sectional cut in lamella of ZnO/Si NWs arrays by FIB.

(b) Intermediate milling

This process reduces the lamella thickness from few micrometres (~5-10 μm) to hundreds of nanometres (~ 800 nm) with low beam current of ~ 2.5 nA using cleaning cross section (CCS) mode at half depth of the bulk mill to clean the lower and upper exposed portion of the lamella (Figure 3.9 (a)).

(c) U-shape cut

In U-Shape cut, regular cutting has been carried out at low ion current (2.4nA) at three side of the lamella and one side was half cut to keep the lamella hanging from the bulk ZnO/Si NWs and it is welded with Omni Probe for lifting out. Figure 3.9 (b) shows the lamella hanging from one end of ZnO/Si NWs sample.

3.4.2.3 Lamella lift out

This is the most difficult and sensitive part of cross-sectional sample preparation. The OmniProbe and GIS are inserted at very low magnification and 0° stage tilt of the FIB-FESEM. Omni Probe is used to lift out the lamella from the bulk ZnO/Si NWs sample and attaching it to the TEM grid. Initially it is moved and welded with the lamella surface using Pt-deposition. Afterwards the attached left portion of the lamella is cut from the bulk sample and OmniProbe needle is lifted away from the sample position shown in Figure 3.10 (a).

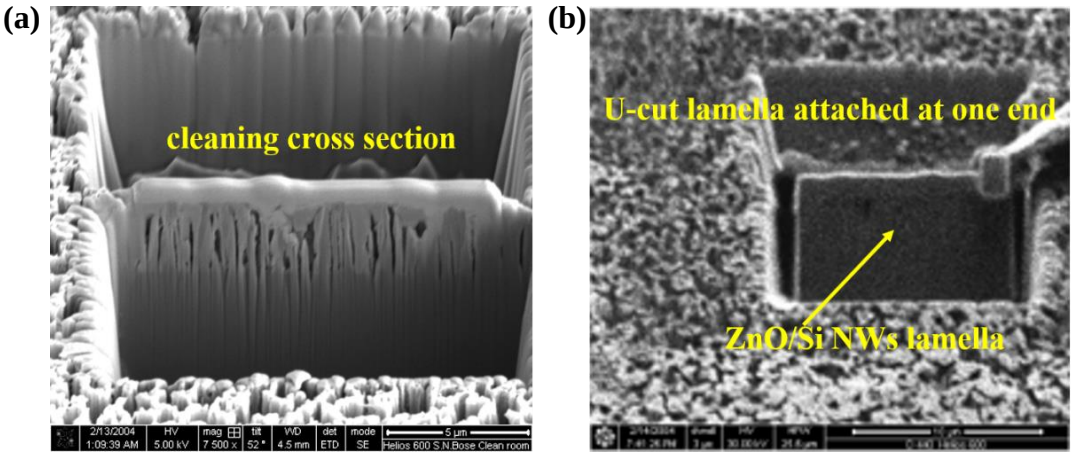

Figure 3.9 (a) Cross-sectional cut in lamella of ZnO/Si NWs after cleaning. (b) U-Shape cut of lamella before lifting.

3.4.2.4 Transfer and welding of lamella to TEM grid

The lamella of ZnO/Si NWs needs to be attached to the specially designed OmniProbe TEM grid (inset of Figure 3.10 (a)) to perform microscopic analysis. Initially the position of the TEM grid is chosen and the lamella surface placed close to TEM grid followed by welding using GIS-Pt deposition. Then, the lamella is attached to OmniProbe and TEM grid shown in Figure 3.10 (b). Afterwards OmniProbe is detached from the lamella using FIB milling.

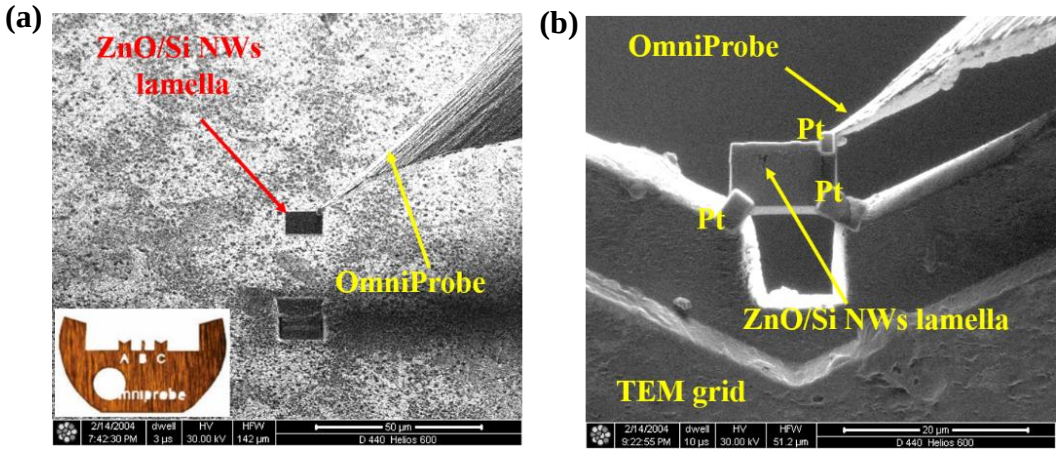

Figure 3.10 (a) Lamella attached to OmniProbe needle (Inset: OmniProbe TEM grid). (b) Lamella attached on TEM grid and with OmniProbe needle.

3.4.2.5 Final thinning of the lamella

The last and most crucial part of cross-sectional sample preparation is final thinning of the ZnO/Si NWs lamella. In this step, a special care has been taken for avoiding the damage in thin lamella. The FIB parameters for final thinning are provided in Table 3.1.

Table 3.1 FIB parameters for lamella final thinning.

Initial lamella thickness	kV	FIB Current	Final lamella thickness
1µm-800nm	10-20 kV	2.4 nA	300-200 nm
300-200nm	2-5 kV	0.24 nA	<100 nm

The final thinning is performed at low kV and low beam current to avoid possible damage of the thin lamella. Afterwards fast scan imaging with electron beam was performed to remove remittent residue material/ions on the surface of the thin lamella. Figure 3.11 (a) shows the cross-sectional SEM image of ZnO/Si NWs lamella after thinning down to 200-300 nm and Figure 3.11 (b) shows the thin (<100nm) portion of the ZnO/Si NWs lamella which is ready for HRTEM analysis [9].

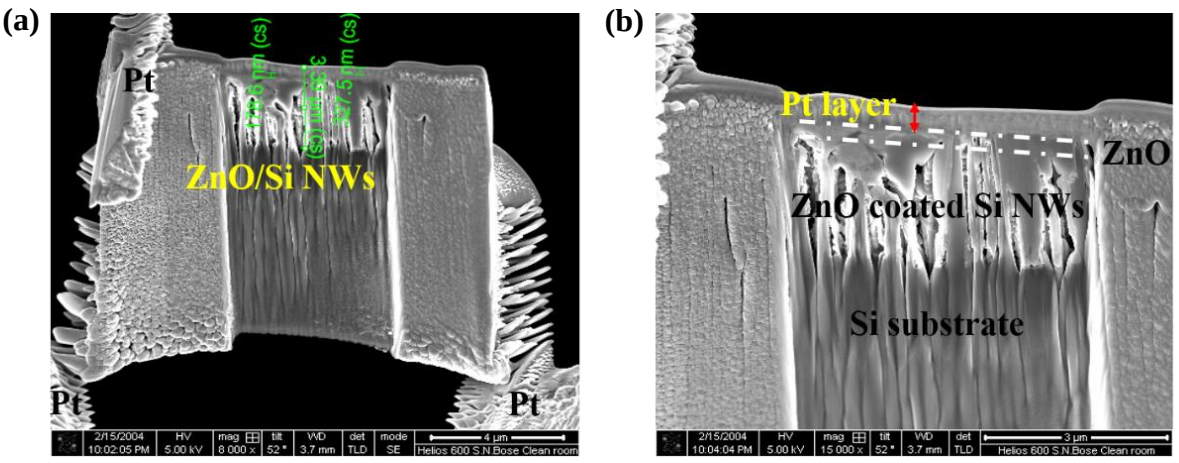

Figure 3.11 (a) Lamella after initial thinning. (b) Lamella after final thinning.

3.5 Conclusion

In summary, we have discussed the fabrication method of different devices such as photodetector, gas sensor and thin film transistor (TFT) based on ZnO/Si NWs nanostructures arrays and amorphous IGZO thin film. Experimental techniques for electrical, optoelectronics and gas sensing measurements have also been discussed. We have discussed the fabrication processes of cross-sectional (X-TEM lamella) samples through conventional method and also using Focused Ion Beam (FIB) milling technique for high resolution TEM analysis that enables us to make a proper physical model of the devices.

Bibliography

1. C. Samanta, R. R. Ghimire, and B. Ghosh, *IEEE Trans. Electron Devices*, **65**, 2827 (2018).
2. http://www.keithley.com
3. E. Fortunato, P. Barquinha, and R. Martins, *Adv. Mater*., **24**, 2945 (2012).
4. Y. Liao, Practical Electron Microscopy and Database, 2007 (www.globalsino.com/EM/).
5. A. Bose, M. Sreemany, and S. Bysakh, *J. Am. Ceram. Soc*., **94**, 4066 (2011).
6. Operation manual Helios nanolab 600 dual beam FESEM (www.fei.com).
7. S. R. Moulik, "Synthesis And Study Of Physical Properties Of Binary Oxide Nanostructures", Thin Films And Devices", Ph.D. Thesis (2018), University of Calcutta, Kolkata, India.
8. A. R. Vaz, M. M. da Silva, J. Leon, S. A. Moshkalev, and J. W. Swart, *J. Mater. Sci*., **43**, 3429 (2008).
9. C. Samanta, A. Ghatak, A. K. Raychaudhuri, and B. Ghosh, *Nanotechnology*, **30**, 305501 (2019).

Chapter 4

Effects of photo-gating in broadband photoresponse of Au NPs-ZnO/p-Si NWs core-shell arrays

In this chapter, we have described how the tuning of charge carriers is done using photo gating in ZnO/p-Si NWs core-shell arrays decorated with plasmonic Au nanoparticles (NPs) by using pulsed laser ablation in liquid (PLAL) method that works efficiently in the broad frequency range from UV (300 nm) to NIR (1100 nm) and consumes low power (few μW). The main purpose of this work is to extend the response of a photo-detector beyond its fundamental band gap by exploiting the concept of surface "photo gating". The optical detector combines the visible and NIR detectability of Si NWs with the UV detectivity of ZnO through the core- shell structure and enhanced broadband detectivity in the visible range has been achieved by decorating core -shell arrays with ligand-free Au NPs. The significant enhancement of optical response and photoconductive gain in visible region can be correlated with enhancement of absorption in visible region due to surface plasmon resonance (SPR) coupling of Au NPs with ZnO. We observed significant enhancement of responsivity R not only in visible range but also in UV and NIR region with a high detectivity of 10^{11} *(*$cmHz^{1/2}W^{-1}$*). The responsivity of the detector ~ 1 A/W from 700nm to longer wavelength (at bias of 1V) and in the visible region the responsivity of the photo detector with Au NPs is > 0.5 A/W and increases to ~2 A/W at UV region.*

4.1 Introduction

In recent broadband optical detectors is a fast-developing field with significant impact in various applications like UV radiation monitoring in an environment and healthcare research, secure communication, sensing, fire detection, portable electronic equipment, and so on [1-4]. However, due to lack of energy it is very crucial to develop low-power and even zero-power optoelectronics devices [5]. In addition to low power consumption, the focus on development of an optical -detector sensor working in a broad spectral range is attractive proposition as that would avoid use of multiple detectors to cover the same range. Most of the conventional photodetectors that are widely used are based on p-n junctions using elemental (Si and Ge) or binary (GaAs) and ternary (InGaAs) semiconductors [6-8]. Crystalline silicon photodetectors are routinely used in the range of visible to near-infrared photo imaging and that can be easily integrated with the silicon integrated circuit technology. Each of these detectors have a spectral range depending on fundamental band gap of the semiconductor in which most of them lie in NIR region. They show peak responsivity at wavelengths shorter than but close to their band edge and the responsivity is < 0.7 A/W, barring InGaAs where higher responsivity has been reported [8]. In these semiconductors where the band edge is in NIR, the responsivity of device falls remarkably in UV/Visible region due to various optical losses such as reflection, thermal effects, incomplete absorption and recombination of photo induced carriers.

Among photoconductive detectors, ZnO is useful in UV range while CdSe and PbS can be used in visible and NIR range [9-11]. Most of ZnO based optoelectronic devices are either photoconductive detectors in thin film transistor (TFT) configuration or they are heterojunction between n-type ZnO and p-type semiconductor materials. The most common choice is p-type silicon due to its distinct advantages, such as abundance, stability, and ease of processing. But the uses of silicon nanowires (Si NWs) based photo devices have potential advantages mainly in visible to NIR region due to their low reflection and small photo response time [6, 12-13]. Especially, vertically aligned Si NWs are promising building blocks for a range of vertical devices, including surround-gate field-effect transistors, solar cells, and thermoelectric modules. Recently nanostructured materials such as heterostructure and core-shell arrays based devices have shown greater advantages for improving the photon capture and collection of photo generated charge carriers. There is report of n-ZnO/p-Si NWs core-shell heterostructure type photodetector working in UV to visible region with a maximum responsivity of 0.98 A/W at a bias voltage of 5 V [14]. A core-shell heterostructure n-ZnO/n^+-Si NWs has been reported

for NIR region with a maximum zero biased responsivity of 0.54 A/W [15]. These photo-detectors though easy to fabricate but certain issues need to be addressed, for instance each of photodetectors used particularly in specific wavelength region that have been working either in ultraviolet (UV) or visible (Vis) or near-infrared (NIR) region. The photoconductive detectors like TFT are mostly based on planar metal-semiconductor-metal (MSM) configuration. In this configuration, the active material surface being exposed, it allows innovative ways to induct carriers in the active channel in addition to those created by photo-excitation on illumination. The photo-conductive detectors suffer from mobility of carriers and the finite recombination length but gated photo-conductive detectors (mostly TFT type) show better performance. A report of ZnO based photodetector shows a large enhancement of responsivity in UV region by synergy of illumination and gate voltage [16], where the charge has been induced through an electric double layer gate dielectric. In this case the detector has enhanced sensitivity but the spectral range of response has not been widened. In the case of 1D single semiconductor photoconductive detectors as M-S-M configuration, the surface states play an important role and play the role of photo transistor thus separating out the electrons and holes and inhibiting recombination. The photo-conductive detectors can use the surface to do gating to enhance the performance. An example of utilizing the surface oxide and band bending as an active agent of inhibiting carrier recombination has been done for single Ge NW based broadband (300-1100 nm) photodetector, where a peak responsivity of 10^7 A/W in NIR region at a low power consumption has been achieved [17-18]. Broadband high responsivity in single Si NW and Si NWs arrays based detectors have been achieved using similar concepts [19-20]. These single NW detectors can function as self-biased (zero applied bias) detectors with high responsivity of the order of 10^4 A/W with Si NW [19] and 10^5A/W with Ge NW [21]. Inspite of ultra-high responsivity over a broad spectral range and extremely low power dissipation, these detectors suffer from the disadvantage due to difficulty in fabrication technique, the fabrication process is lithography intensive and needs availability of nano-lithography facilities and expertise.

Whereas, the most junctions based (p-n heterostructures) photodetectors have limited gain and the responsivity (mostly $\leq 1\ A/W$) and more importantly the band width of detection is governed by the band gap. It has also been shown that one can break the limitation of band width by example of photo-gating to circumvent the limitation of spectral range of response arising from the band gap of the channel material by using of plasmonic metal nanoparticles (NPs). In this case the photoconductive channel is not the only place where carrier generation

occurs by illumination. Use of plasmonic metal NPs of aluminium (Al), silver (Ag), nickel (Ni), platinum (Pt) and gold (Au) etc can enhance response in visible region by plasmonic excitation and charge transfer to the active photoconductive channel [22-27]. There are few reports of localized surface plasmon resonance (SPR) mediated by plasmonic NPs like, Al, Ag, Ni, etc. to enhance the UV response of the ZnO nanostructures devices [22-24]. Another report of ligand free surface plasmon resonance of Au NPs is implemented to improve the visible response of ZnO nanowires arrays with a maximum responsivity of 0.4 A/W in UV region W at a bias of 1 V [26]. The decoration of Au NPs on ZnO NWs arrays with a maximum responsivity of 1.9 A/W in UV region at bias of 5 V has also been reported but seen decrease in responsivity due to Au NPs from bare ZnO NWs arrays [27]. These reports have been summarized for comparison in Table 4.3 later in this chapter.

Novelty of our report is; in this work, we have engineered a photodetector using oxide semiconductor nanostructure innovatively. Here we make a core-shell structure of Si NW surrounded by ZnO that makes the channel which in turn has been decorated with ligand free plasmonic Au NPs. The transfer of photo generated carriers from p-Si NWs array into n-ZnO were done using a core-shell structure where the n-ZnO shell that makes the photoconductive channel and surrounds the shell of p type Si NWs arrays. This core-shell structure then is decorated by ligand-free Au NPs made using pulsed laser ablation in liquid (PLAL) method in aqueous medium (DI water). This structure may be contrasted with n-ZnO/p-Si NWs heterostructure p-n junctions used before by others [14-15]. It has been observed that plasmonic NPs used by others, synthesized by chemical route for attachment, need a stabilizing ligand or a dispersive media which affects the surface plasmon resonance of NPs and reduces the inter band transition which degrade the photodetector performances. It is very crucial to have a synthesise technique that would enhance the optical absorption as well as photoresponse utilizing the plasmonic resonance of Au NPs mainly in visible range as well over the broadband range without interfering effects of ligands. We have employed an improved technique, in our thesis work. In PLAL method (discussed in chapter 2), we are able to get uniform, mono-dispersed and stable ligands free NPs in a pure solvent (i.e., DI water) without introducing any ligands or stabilizing molecules intentionally. The PLAL process is distinctly different from chemical attachments through ligands; it gives a ligand-free growth of Au NPs. The presence of ligands between ZnO and Au NPs inhibits charge transfer. Since the photoresponse of the device as discussed later on shows dependence on the efficiency of the charge transfer, a ligand-free attachment is preferred [26]. Here in this work, we show how the photodetection ability of

the ZnO/p-Si NWs core-shell arrays can be tuned from UV to NIR region with the decoration of the ligand free Au NPs. The work reported here has the novelty that the responsivity of ligand-free Au decorated ZnO/p-Si NWs core-shell arrays enhanced significantly not only in visible region but also in UV and NIR in broadband range due to surface resonance coupling of Au NPs with ZnO/p-Si NWs. We further develop the concept of using photo- gating to circumvent the band width limitation by using photo generated carrier infusion in the conduction band of the photoconductive channel n-ZnO using a tandem effect where Visible-NIR range the carriers are generated in Si NWs and in Visible as well as in UV carriers are generated in Au NPs. Favorable band alignments enable both the materials to transfer there photo-generated carriers (electrons) to the conduction band of n-ZnO. This leads to a substantially flat photoresponse of 1 A/W in the wavelength range 650 nm to 1100nm and somewhat reduced response in the range down to 375 nm (but the responsivity minima > 0.5 A/W) and enhanced response reaching 2 A/W in the UV.

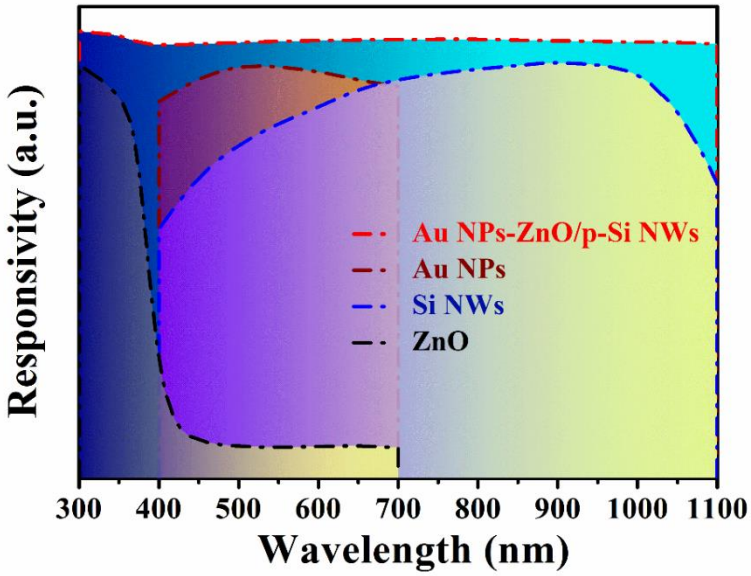

Figure 4.1 Schematic of variation of spectral responsivities of individual components (ZnO, Si NWs and Au NPs) and that of the Au NPs decorated core-shell arrays.

The high responsivity is reached at a low applied bias of 1V with total power consumption ≤ 2 μW, thus making them operable with batteries for very long periods (e.g, Li batteries with 3200 mAh rating). The schematic of the device photoresponse and the response of the underlying component parts are shown in Figure 4.1 which in a nutshell explains the ideas utilized in this thesis work. In addition to good responsivity over an extended wavelength range and no sizeable droop in sensitivity at wavelengths in visible range and shorter wavelength (unlike Si and Ge detectors), extremely low power consumption, the detector has added

advantage of ease of fabrication that is compatible with standard semiconductor and TFT processing routes.

4.2 Experimental details

The device has been fabricated from p-type Si wafer in three steps firstly the Si nanowires array had been synthesized by chemical process as reported elsewhere [28] and then core-shell structure is made by deposition of ZnO by atomic layer deposition (ALD) and finally ligand-free Au NPs is decorated on ZnO/p-Si NWs core-shell arrays by using pulsed laser ablation in liquid (PLAL) method. The details of fabrication processes have been given in chapter 2. The Au NPs-ZnO/p-Si NWs core-shell arrays have been characterised by X-ray diffraction (XRD). The nanostructured complete device has been also characterised by high resolution transmission electron microscopy (HRTEM) as well as energy dispersive X-ray spectroscopy (TEM-EDS) by using Cross-sectional TEM (XTEM) sample preparation technique for understanding of the physical structure of the devices. The optical absorption of Au NPs decorated ZnO/p-Si NWs core-shell device has been recorded with an integrating sphere at diffuse reflection mode for solid sample in an UV-Visible spectrophotometer in the wavelength range of 300-900 nm. For photo conductivity measurement two Cr/Au contact pads are deposited by thermal evaporation on the n-ZnO top layer of the Au NPs-ZnO/p-Si NWs core-shell arrays through a hard mask in MSM configuration with a channel length and width of 1.5 x 1 mm. The details of experimental work have been given in chapter 3. All measurements were taken at room temperature and under ambient atmospheric conditions.

4.3 Experimental Results

4.3.1 Electron microscopy and structural analysis

The cross-sectional view of the device in Figure 4.2 (a) shows the scanning transmission electron microscopy high angle annular dark field (STEM-HAADF) image. Figure 4.2 (a) shows the top ZnO layer and the core-shell structure of the vertically aligned ZnO/p-Si NWs arrays. The figure also shows the ligand-free Au nanoparticles (Au NPs) that decorate the ZnO. The average diameters of the Au NPs are ~ 10 nm. The crystalline structure as well as phase formation and phase purity of the sample is identified through X-ray diffraction (XRD) shown in Figure 4.2 (b). The diamonds, asterisks and squares show peak belonging to Au NPs, ZnO and p-Si NWs respectively.

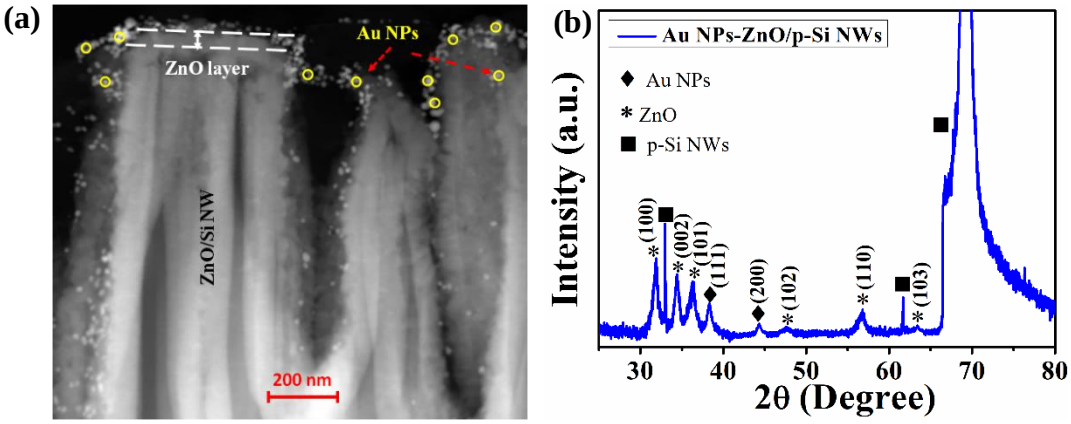

Figure 4.2 (a) STEM-HAADF image of Au NPs decorated on ZnO/p-Si NWs arrays. (b) XRD of Au NPs decorated ZnO/p-Si NWs core-shell arrays.

Scanning tunnelling electron microscopy high angle annular dark-field (STEM-HAADF) imaging of the cross-section lamellar is shown in Figure 4.3 (a). A composition profile of the device was obtained by EDS line scan marked by yellow arrow and the data are shown in Figure 4.3 (b). The line scan of the ZnO/Si NWs shows the contents of Au, Zn, Si and O. There is a clear top ZnO layer on the NWs array, which is followed by the conformal coating of ZnO through the Si NWs array and the concentration of Au NPs layer with thickness of about 30 nm is maximum on the top of ZnO/Si NWs and then concentration is uniform throughout the core-shell structure.

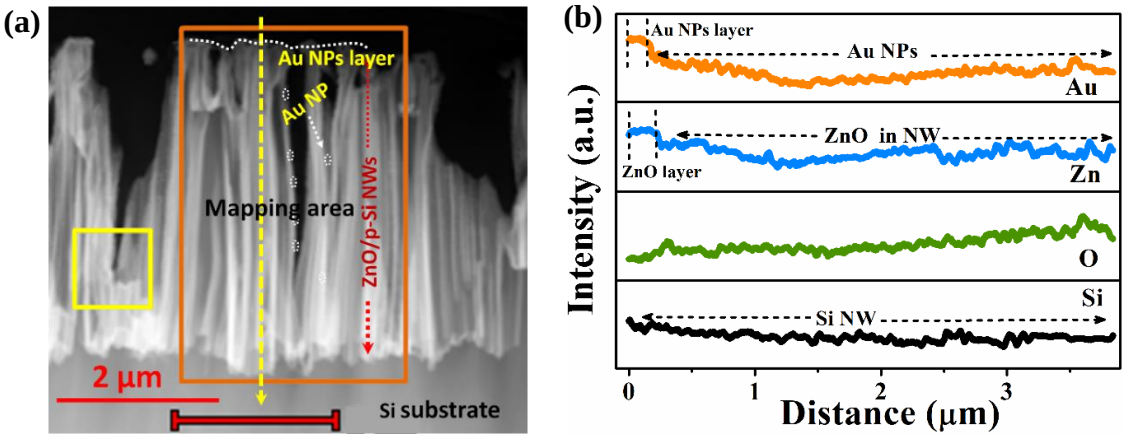

Figure 4.3 (a) The cross-sectional scanning tunnelling electron microscopy high angle annular dark field (STEM-HAADF) image. (b) Elemental composition of Au NPs on ZnO/Si NWs arrays taken by EDS line scan showing the chemical composition.

The STEM-EDS mapping for the Au M shell, Zn L shell, O K shell and Si K shell are given in Figure 4.4 (a) – (d) respectively. STEM-EDS mapping on a portion of Au NPs decorated ZnO/p-Si NWs arrays (marked by orange box in Figure 4.3 (a)) shows a conformal layer of ZnO throughout the Si NWs arrays and Au M shell mapping shows that concentrations of Au NPs are fairly uniform and homogeneous throughout the surface of the ZnO/p-Si NWs arrays.

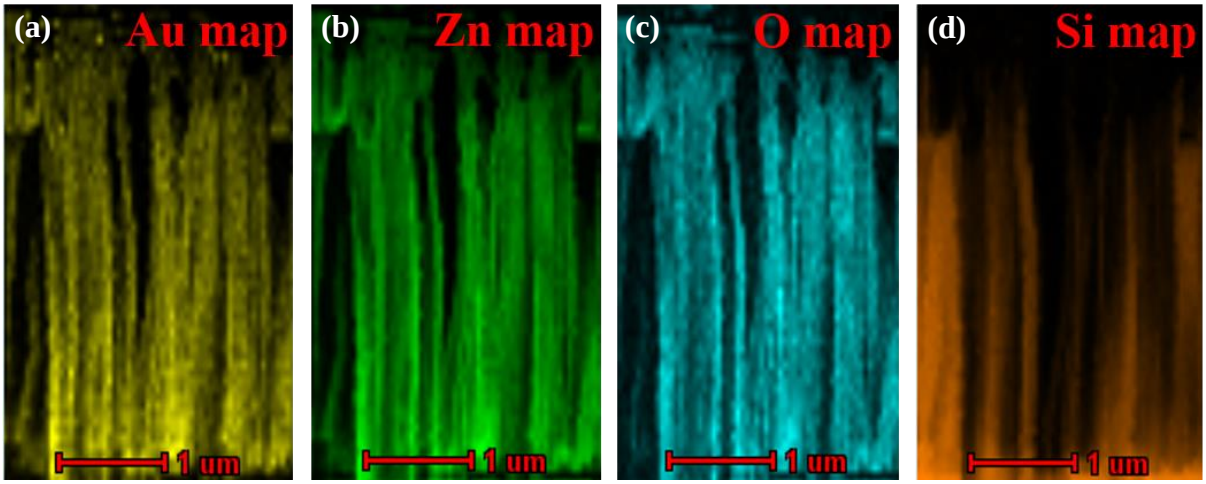

Figure 4.4 STEM-EDS mapping of (a) Au (M shell), (b) Zn (L shell), (c) O (K shell) and (d) Si (K shell) of Au NPs decorated ZnO/p-Si NWs core-shell arrays.

4.3.2 Broadband photoresponse in Au NPs-ZnO/p-Si NWs

Figure 4.5 (a) shows the current-voltage data of ZnO/p-Si NWs core-shell arrays and Au NPs decorated ZnO/p-Si NWs core-shell arrays under dark condition in metal semiconductor metal (MSM) configuration. Data in Figure 4.5 (a) shows that the dark current (I_d) of Au NPs decorated device has been lowered at least two order of magnitude in comparison with bare device due to decoration of Au NPs. Generally, the intrinsic defects such as oxygen vacancies in the surface layer of ZnO act as adsorption sites for O_2 molecules act as electron acceptors to form O_2^-, which deplete the surface electron states and consequently reduce the channel conductivity in the dark. After decoration of Au NPs, since the work function of ZnO ($\varphi_{ZnO} \approx 4.1\ eV$) is smaller than that of Au ($\varphi_{Au} \approx 5.1\ eV$), the electrons flow from ZnO to Au sites due to alignment of Fermi levels (E_F) at interface which also enhances the existing depletion layer and further reduces the channel conductivity. Figure 4.6 (a) shows the variation of photocurrent with time (photocurrent I_{PC} vs. t) of the photo-detector when it is illuminated by lights of different wavelengths (λ) for a fixed power ≈ 1.5 μW (Illumination intensity ($\Im$) ≈ 100 μW/cm^2). The data have been taken at a bias of 1V. The data were taken with illumination ON and OFF. Data in Figure 4.6 (a) shows a sharp and distinct ON/OFF states in the photodetector with rise and decay time constants of < 1 s when the illumination is turned ON/OFF. From the Figure 4.6 (a), it is shown that with decoration of Au NPs, the I_{PC} of n-ZnO/p-Si NWs core -shell device is enhanced considerably over the whole spectral range. The dark current being low (~10^{-6} A) the power dissipation even at 1V is < $2\mu W$.

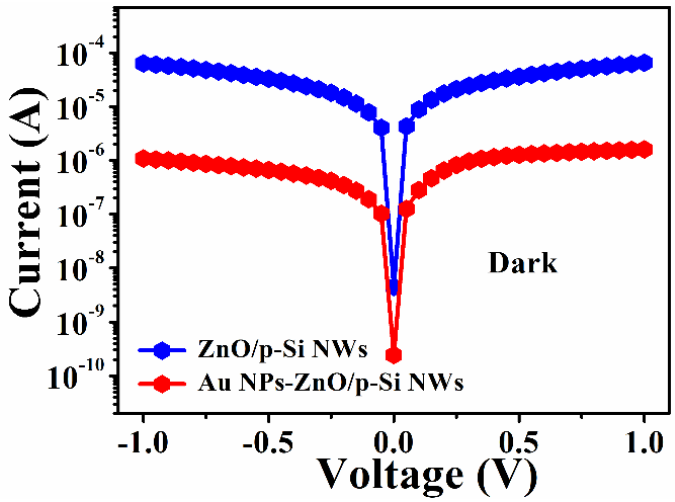

Figure 4.5 $I-V$ characteristic of ZnO/p-Si NWs core-shell arrays and Au NPs decorated ZnO/p-Si NWs core-shell arrays in dark condition.

In Figure 4.6 (b) shows the photo-current I_{PC} at selected wavelengths (UV-Vis-NIR) for the bare device and that with Au NPs decorated device. In case of UV region (λ = 300 nm), data shows the rapid raise in photocurrent is followed by a slower component, which follows to an exponential relation. When the illumination is turned OFF, the decay of the photocurrent for both bare and that of Au NPs decorated devices exhibit a long tail generally known as persistent photoconductivity. Data in Figure 4.6 (b) shows that in UV region (λ = 300 nm), a relatively fast response of photocurrent has been achieved for Au NPs decorated device in comparison with bare device discussed details in later section of Role of Au NPs in transient photoconductivity.

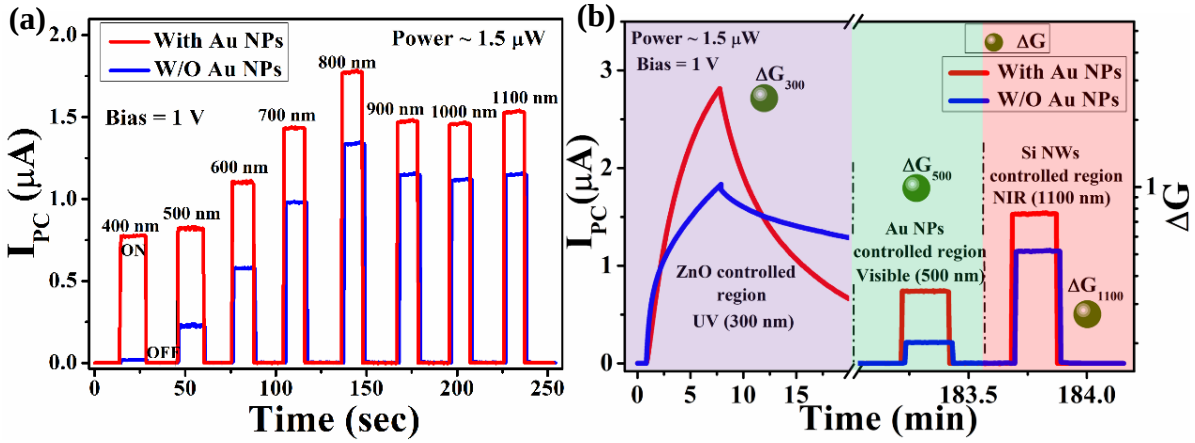

Figure 4.6 (a) Photocurrent (I_{PC}) under different illumination of light of wavelength ranging from 400-1100 nm at a fixed power of 1.5 μW. The illumination was turned ON and OFF. (b) Plot of I_{PC} at different wavelengths for the n-ZnO/p-Si NWs core-shell arrays with and without Au NPs. The right-hand scale shows the change in gain (ΔG) on decoration by ligand-free Au NPs.

In case of visible and NIR region, we observed a sharp and distinct ON/OFF states in the photodetector with rise and decay time constants of < 1 s when the illumination is turned

ON/OFF. The right-hand scale in the same graph shows the gain (G) as obtained from the data. The enhancement of G on addition of the Au NPs (marked as ΔG) for all wavelength region can be observed. However, the photo current gain (G) is comparatively higher in visible region than that in NIR region of the Au NPs decorated photo-detector. This data establishes the broad claim of the paper that innovative engineering of the device; by integration with plasmonic NPs (Au) in n-ZnO/p-Si core-shell arrays leads to significant enhancement of the photoresponse in broadband (300-1100 nm) region. Figure 4.7 shows the spectral responsivity R of n-ZnO/p-Si NWs core-shell arrays with and without Au NPs at a bias voltage of 1 V measured at illumination power P = 1.5 μW. Compared with bare n-ZnO/p-Si NWs core-shell array the responsivity of Au decorated core-shell arrays is enhanced significantly not only in visible range but also in UV and NIR regions. Presence of the Au NPs thus makes the detector broadband with substantial R over the whole frequency range. Data in Figure 4.7 shows that at bias 1 V the average value of R ~ 1 A/W for the wavelength range 700 nm-1100 nm. It decreases to below 1 A/W and in the visible range and shows minima of $R \approx 0.5$ A/W for $\lambda \approx$ 450 nm. The contribution of the plasmonic Au NPs can be best appreciated in this range. In the bare array without the Au NPs, R drops rapidly in the visible range of the spectrum and goes down even as low as 10^{-2} A/W as compared to 0.5 A/W for the Au NPs decorated detector. In UV region ($\lambda \leq 375$ nm) R ~ 2 A/W for Au NPs decorated photo-detector. It is noted that this performance is much improved over a typical Si detector available commercially (Table 4.1).

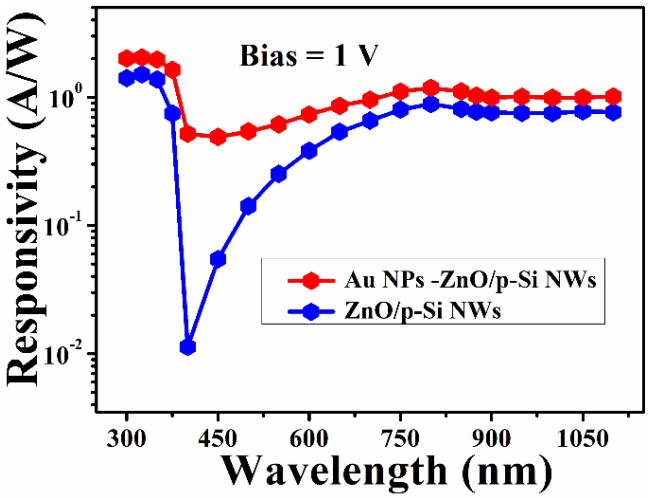

Figure 4.7 Spectral responsivity (R) of ZnO/p-Si NWs core-shell arrays with Au NPs and without Au NPs under different wavelength.

Responsivity (R) is function of bias voltage and increases as the bias V increases and is also dependent on the illumination power P and it decreases as P is increased. The dependence of

R on these two parameters for bare n-ZnO/p-Si NWs and Au NPs decorated n-ZnO/p-Si NWs core-shell arrays are shown in the contour plot in Figure 4.8 (a) and (b) respectively. It can be seen from Figure 4.8 (b) that at a small bias of 1V and up to 3 μW illumination power it is possible to get responsivity $R \geq 1$ A/W.

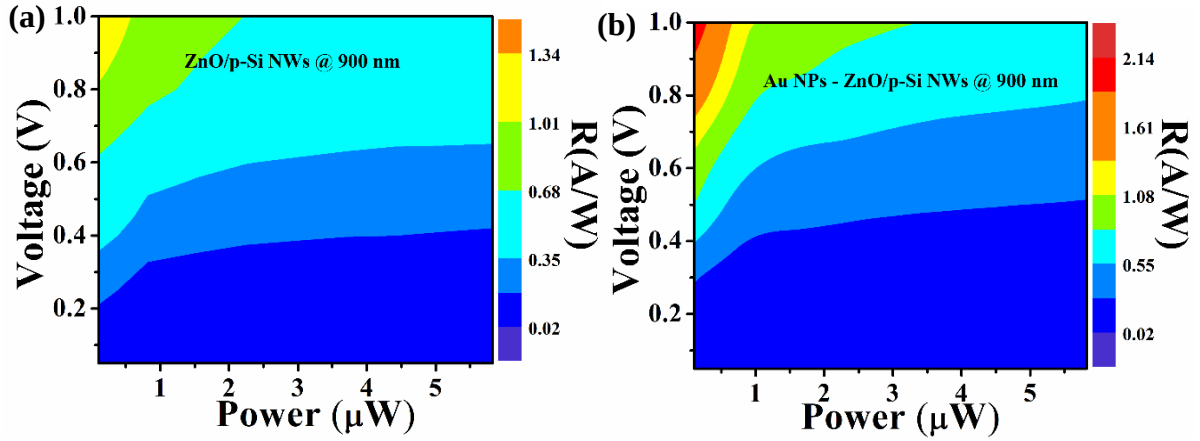

Figure 4.8 Contour plot of responsivity R as a function of bias voltage (V) and illumination power (P) of (a) n-ZnO/p-Si NWs and (b) Au NPs decorated n-ZnO/p-Si NWs core-shell arrays.

Table 4.1 Comparison of device characteristics value with commercial Si photodetector.

Detectors	Wavelength range (nm)	Peak wavelength	Responsivity I	Power dissipation
Si commercial detector	400-1100	970 nm	0.65 A/W	100 mW
Au NPs-ZnO/p-Si NWs (Present work)	**300-1100**	**800 nm**	**1.2 A/W**	**< 2 μW**

Thin film and heterostructures based photo-detectors have a wide dynamic range where the photo-current I_{PC} has dependence on the incident power P which is generally expressed by the relation$I_{PC} \propto P^{\beta}$, where typically the power exponent $\beta < 1$. The value β depends on the existence of localized traps near the band edges that controls the process of recombination and the energy distribution of the localized states near the conduction band edge [29]. Since the responsivity $R = \frac{I_{PC}}{P}$, variation of R with incident power P is given by the relation $R \propto P^{-(1-\beta)}$. β being < 1, R decreases as the incident power P on the device increases. This is shown in the contour plot of Figure 4.8 (a) and (b) as well as in Figure 4.9 (a) and (b). Figure 4.9 (a) shows the P dependence of value of responsivity R for illumination with light of λ = 500 nm for without and with Au NPs decorated devices and Figure 4.9 (b) shows the corresponding data for illumination at λ = 900 nm. For λ = 500 nm $\beta \approx$ 0.78-0.90 for the devices and are significantly higher than those seen at λ = 900 nm where $\beta \approx$ 0.66-0.70. In general, β depends

on the distribution of trap states around the Fermi Level E_F and band edges. For a more uniform distribution $\rightarrow 1$. Since β does not change much when Au NPs is added to the device, these traps that control this exponent, are likely to lie within ZnO shell or Si NW core or at their interface. β being smaller at longer wavelength (900 nm), where the excitation and carrier generation by illumination is controlled by Si NW, it is expected that there are non-uniform trap distribution within Si NW. Small value of β has been seen in Si single NW photo-detectors before where the Si NW had been grown by same method [19].

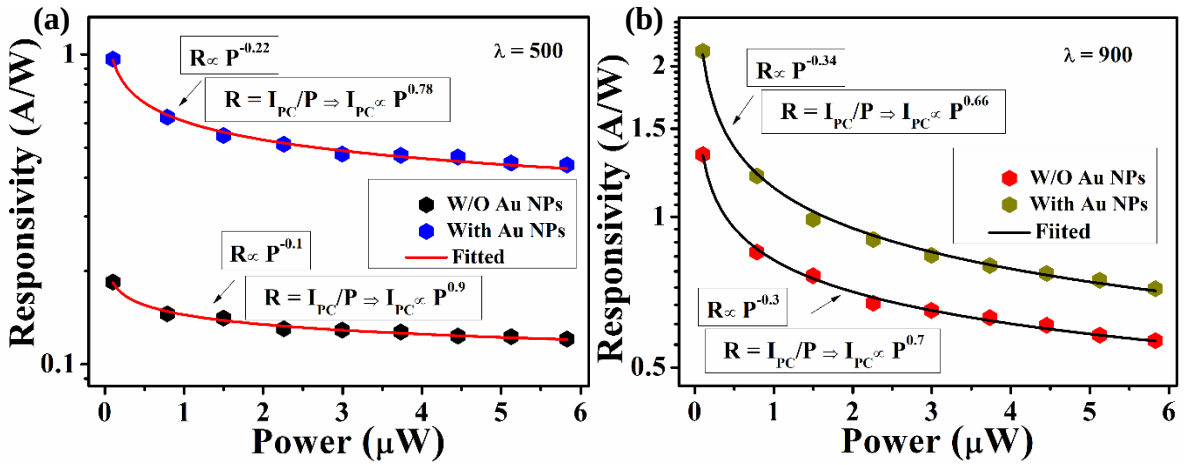

Figure 4.9 (a) Variation of responsivity with incident power before and after Au NPs decoration on ZnO/p-Si NWs for λ = 500 nm and (b) λ = 900 nm of wavelength. Values of exponent β are shown in inset boxes.

4.3.3 Photodetection limit and stability of the devices

The sensitivity of a photo detector is determined by estimating the detectivity which is related to the noise equivalent power, the minimum incident power at which signal to noise ratio reaches unity i.e., a detector can differentiate from the noise. The detectivity is related to NEP by the following equation [17]:

$$D^* = \frac{\sqrt{A.\Delta f}}{NEP} \qquad (4.1)$$

Where A is the effective area in cm^2 of photodetectors and Δf is band width of the signal in Hz and D^* is the specific detectivity measured in cm $Hz^{1/2}$ W^{-1} (or Jones). The detectivity is limited mainly by the three types of noise including shot noise from dark current, Johnson noise and flicker noise from thermal fluctuation. The contribution of Jhonson noise as well as the flicker noise is lower than that contributed by the shot noise. For estimation, we may thus consider that the shot noise is the dominant source of the noise. The rms value of shot noise current $S_n(i_n) = \sqrt{2eI_d\Delta f}$, where I_d is the dark current and noise equivalent power, $NEP = \frac{\sqrt{\langle i_n 2\rangle}}{R}$. So, the sensitivity of the photodetector and the limit of detection sensitivity are important

factors which are often measured and parameterized by the spectral dependence of the specific detectivity as [30]:

$$D^*(\lambda) = \frac{\mathrm{R}(\lambda)}{(2\mathrm{e}\mathrm{J_d})^{1/2}} \qquad (4.2)$$

Where J_d is cark dark density, R(λ) is the spectral dependence of responsivity. Briefly, one can find the minimum power that can be detected by a photodetector, from the observed value of responsivity and the detectivity. For a detection band width of 1.66 Hz (integration time ~ 0.3 s) the observed value of R ~ 1 A/W at 900 nm, for Au NPs decorated ZnO/p-Si NWs can detect ≈ 1.5×10^{-12} W. The value of detectivity limits ($D^*(\lambda)$) for the wavelength of 500 nm and 900 nm at the bias voltage of 1 V of the n-ZnO/p-Si NWs core-shell arrays without and with Au NPs are tabulated in Table 4.2. The detectivity of ZnO/p-Si NWs with Au NPs is found to be higher as compared to that for the bare n-ZnO/p-Si NWs arrays.

Table 4.2 The details of devices characteristics value measured at wavelength of 500 nm and 900 nm at 1 V bias.

Devices (n-ZnO/p-Si NWs)	**Responsivity I at 1 V bias (A/W)**		**Detectivity (D^*) at 1 V bias ($cmHz^{1/2}W^{-1}$)**	
	λ= 500 nm	λ= 900 nm	λ= 500 nm	λ= 900 nm
W/O Au NPs	0.14	0.75	~ 5×10^9	~ 6×10^{10}
With Au NPs	0.55	1.0	~ 3×10^{10}	~ 2×10^{11}

To check the stability and reproducibility of bare and Au NPs decorated devices, we have tested total twelves devices for bare ZnO/p-Si NWs and Au NPs decorated ZnO/p-Si NWs core-shell arrays which shows excellent reproducibility in broadband (UV-visible-NIR) region and deviation of responsivity (R) in photodetectors is less than ± 5 %. We have monitored the photoresponse of the devices at an interval of 30 days for a period of six months. The data are shown in Figure 4.10. The decrease in responsivity of photodetector is < 10 % over a period of 180 days which shows good stability and a good self-life of detectors.

A comparison of the devices in our work with others reported photodetectors have been summarized in Table 4.3. As seen in Table 4.3 the performance of the device reported in the present investigation can be seen to be comparable or even better than the performances of devices reported in literatures.

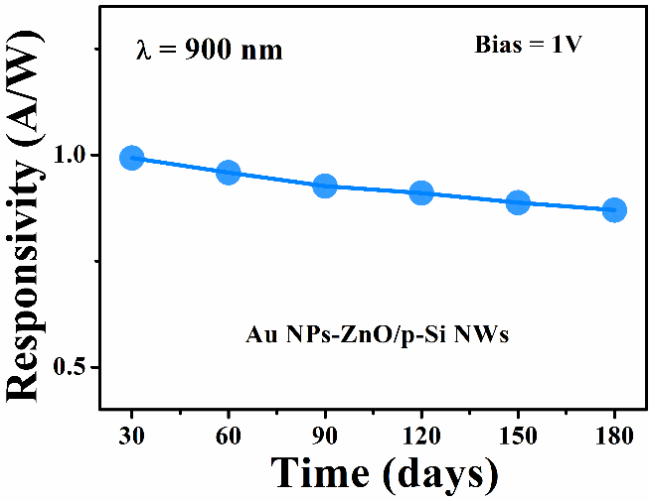

Figure 4.10 Stability study of photodetector during six months of time span.

Table 4.3 Comparison of present photodetector characteristics value with previous reported values in literatures.

Photodetectors	**Wavelength range (nm)**	**Power dissipation (μW)**	**Bias voltage (V)**	**Peak Responsivity I in A/W**	**Ref.**
ZnO/p-Si NWs	**300 – 1100**	**1.5**	**1**	**1.4**	**Present work**
Au NPs-ZnO/p-Si NWs	**300 – 1100**	**2.8**	**1**	**2**	**Present work**
n-ZnO/p-Si NWs	325 – 660	$> 10^5$	5	0.98	7
n-ZnO/n+-Si NWs	400-1100	-	0	0.54	8
Al NPs- ZnO NRs	300 – 400	150	5	1.59	15
Ag NPs- ZnO NTs	320 – 400	400	2	-	16
Ni NPs-ZnO NRs	325	210	1	0.124	17
ZnO/Pt NPs/ZnO	220 – 400	-	60	0.4	18
Au NPs- ZnO NWs	350 – 625	1	1	0.4	19
Au NPs- ZnO NWs	300 – 600	-	5	1.9	20

4.4 Discussions

4.4.1 Absorption and Responsivity: Role of plasmonic Au NPs

The optical response of a photodetector depends on the light being absorbed. Thus, a broadband detector should have a broadband absorption. The optical absorptions (α) of the n-ZnO/p-Si NWs core-shell arrays (with and without Au NPs) are shown in Figure 4.11 (a) in the wavelength range of 300 – 900 nm. Over the whole range α for the Au NPs decorated sample is much larger than that of the bare n-ZnO/p-Si NW array and the enhancement of α is largest in the visible range of the spectrum (400 – 700 nm) with a prominent peak at λ = 510 nm (high lighted). This excess visible absorption of Au NPs decorated device is due to the Au NPs

plasmon resonance which can be confirmed by direct comparison of the absorption of bare Au NPs in colloidal suspension (inset of Figure 4.11 (a)) which are also synthesised by pulse laser ablation in liquid (PLAL) method. (Note: The absorption of Au NPs extends over an extended range of measurement). In addition to the peak at 510 nm due to plasmon resonance, there is absorption in Au NPs for $\lambda \leq 650$ nm due to transition from d band to hybridized sp orbitals that extends to shorter wavelengths to UV.

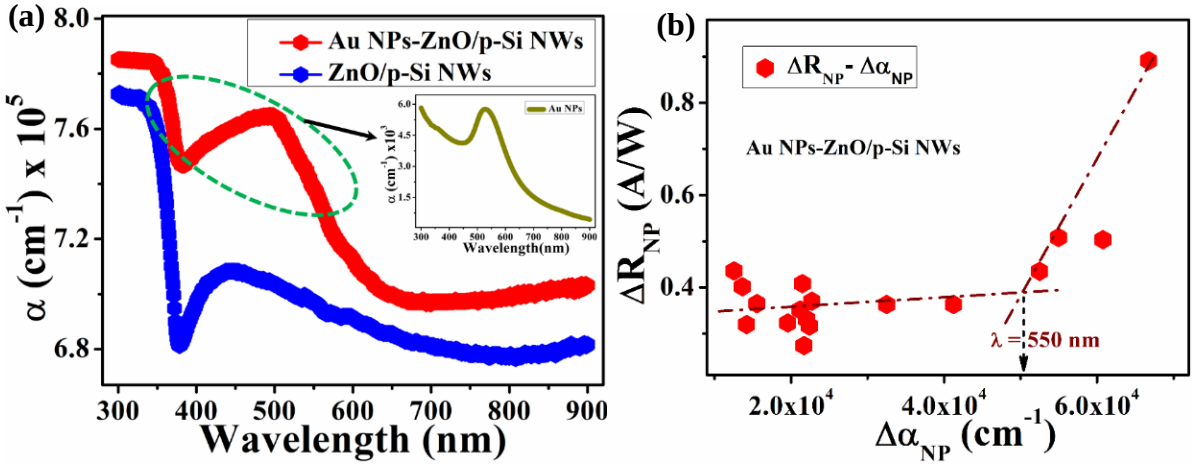

Figure 4.11 (a) Absorption spectra of ZnO/p-Si NWs core-shell arrays and Au decorated core-shell arrays. Inset is the absorption Au NPs alone synthesised by PLAL method. (b) Variation of enhanced responsivity (ΔR_{NP}) with the enhanced absorption ($\Delta\alpha_{NP}$) of n-ZnO/p-Si NWs due to decoration of Au NPs.

It can be seen from the Figure 4.11 (a), that the absorption of bare n-ZnO/p-Si NWs (without Au NPs) has a dependence on the wavelength illumination that has characteristics of both the components namely p-Si NWs and ZnO. In the shorter wavelength side, there is a strong absorption edge nearly at 375 nm. This can be seen for both the samples. This strong absorption edge corresponds the band gap absorption of ZnO which is established by different researchers [31]. At longer wavelengths in the region 400 nm and up, the absorption is dominated by the Si NW. The Si NW like bulk Si absorbs at all wavelength $\lambda < \lambda_{edge}$, where λ_{edge} corresponds to the band edge. For Si NW arrays the absorption increases at shorter wavelength as in bulk Si due to primary absorption process leading to electron-hole creation [32-33]. In NW array the absorption is more due to reduction in reflectivity. We also see the rise in absorption in p-Si NWs at shorter wavelength through measurements as shown in Figure 4.11 (a). There is a small broad maximum in absorption at 450 nm in NW array [33]. This small broad maximum exists in both bulk and film at 510 nm. The small hump seen by us in the absorption spectra of n-ZnO/p-Si NWs as shown in Figure 4.11 (a), arises from this. It has been shown that this is due to additional absorption process like inter-band Auger effect and emission of phonons

directly connected with the generation of additional electron-hole pairs [34]. Decoration of the bare core-shell arrays by Au NPs enhances the absorption α and also enhances the responsivity R. To establish a direct connection between α and R due to the Au NPs decoration we plot in Figure 4.11 (b), the excess absorption $\Delta\alpha_{NP}$ due to the Au NPs, obtained by subtracting out the absorption of the bare device from that of the Au NPs decorated device (see Figure 4.11 (a)), and the excess responsivity ΔR_{NP} obtained by subtracting out R of the bare device from that of the Au NPs decorated device (see Figure 4.7). The large enhancement of the responsivity occurs for $\lambda \leq 550$ nm, when the absorption gets enhanced and is dominated by the surface plasmon resonance of the Au-NPs. There is also enhancement of R when the wavelength is in the UV region due to tandem effect of ZnO fundamental edge absorption along with the enhanced absorption due to Au NPs (see inset of Figure 4.11 (a)).

4.4.2 Photo-gating effects in the Au NPs decorated device

The device presented in this thesis work is innovated around an n-ZnO photoconductive channel which shows response for wavelengths shorter than its fundamental absorption edge of ZnO at ~ 375 nm. The core-shell structure with Si NW array as the core and Au NPs decoration, led to the broadband response of the optical device extending from UV to NIR region. In a photoconductive type detector, which has a metal-semiconductor-metal (MSM) configuration, the response is generally controlled by electron-hole pair generation in the active channel and thus its fundamental absorption edge will determine the longest wavelength of response. In a gated photodetector, carriers are introduced into the channel by induction of charge carrier through the gate when a voltage is applied [16]. In photo-gating the carrier are introduced through "gate" materials that can be photoexcited and can introduce the photoexcited carriers into the channel without any gate bias being applied. This ensures that the response of the detector will not be limited by the fundamental absorption edge of the channel and it will be enabled for response in other wavelength regions as well that will be decided by the opto-electronic properties of these "gate" materials that are being excited by illumination introduce carriers into the channel [35]. In the specific context of this work the n-ZnO channel receives photo-excited carriers from the core of Si NWs as well as AuNPs when they are illuminated. This is illustrated through a schematic in Figure 4.12. In the wavelength range 1100 nm to 450 nm the illumination creates electron-hole pair in p-Si and the electrons transfer to n-ZnO from p-Si which increases the conductivity in ZnO. In the wavelength range 600nm to 400nm additional electrons come from Au NPs which are excited by plasmonic excitation. For wavelength < 400 nm it is usual ZnO photoconductivity.

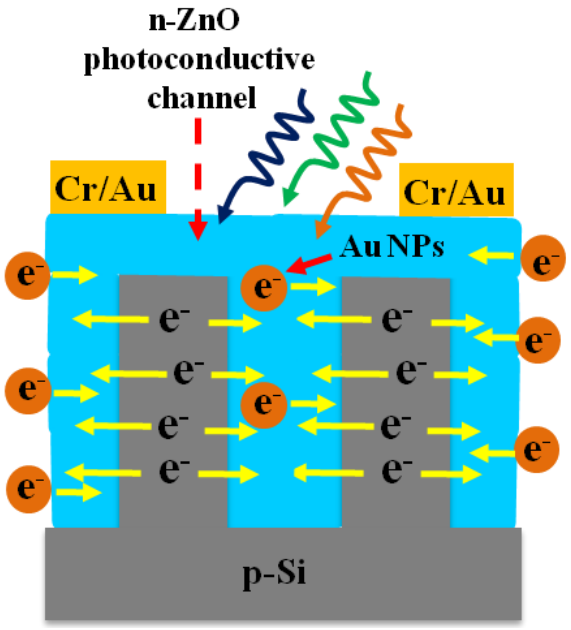

Figure 4.12 A schematic illustration of photo-gated device where the n-ZnO channel receives carriers from the core of Si NWs as well as Au NPs when they are illuminated.

4.4.3 Role of Au NPs in transient photoconductivity

In case of UV region, a relative quickening of photoresponse of Au NPs decorated ZnO/p-Si NWs core-shell arrays have been observed. Figure 4.13 (a) and (b) shows the photocurrent rise and decay response respectively for Au NPs decorated device and bare device under UV illumination λ = 300 nm. The shaded area represents the time period of illumination of excitation source. We show that photocurrent rise edges and recovery edges consists of two components, a fast response components and slow response components. Generally, the fast response components can be ascribed to the rapid changes of carrier concentration when the light is ON/OFF, while the slow response is corresponding to adsorption and desorption of O_2 and/or H_2O on the surface of photodetectors causes the carrier trapping/releasing at defects sites available in the semiconductor. For a more detailed comparison of response time of Au NPs decorated device and bare device, we have estimated the time constants quantitatively by the fitting of dynamic response of photocurrent with a biexponential equation. According to this model, the raising part of the photoresponse curve in presence of illumination follows the equation as [36]:

$$I = I_0 - A_1 e^{-t/\tau_{r1}} - A_2 e^{-t/\tau_{r2}} \qquad (4.3)$$

Where I_0 is the steady state photocurrent, t is the time, A_1 and A_2 are positive constant, τ_{r1} and τ_{r2} are the fast and slow components of rise time constant respectively. When illumination is turned off, the photocurrent decay follows the other equation, which is given by

$$I = I_0 + B_1 e^{-t/\tau_{d1}} + B_2 e^{-t/\tau_{d2}} \qquad (4.4)$$

Where I_0 is the steady state photocurrent, t is the time, B_1 and B_2 are positive constant, τ_{d1} and τ_{d2} are the fast and slow decay time constants respectively.

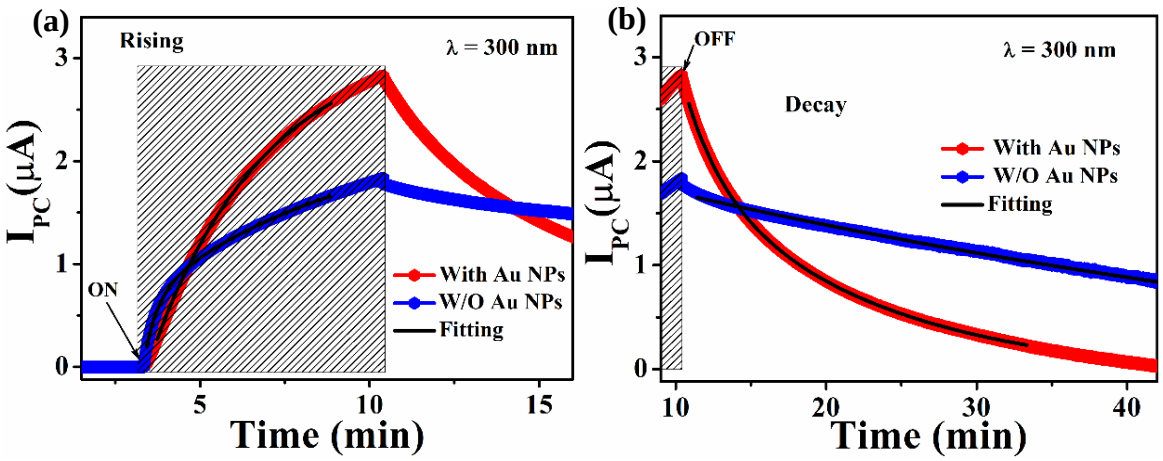

Figure 4.13 (a) Photocurrent rise response and (b) photocurrent decay response of ZnO/p-Si NWs core-shell arrays with Au NPs and without Au NPs for λ = 300 nm illumination and the corresponding fittings. The shaded area represents the period of illumination.

We have fitted the dynamic response (Figure 4.13 (a) and (b)) with the equation (1) and (2) to estimate the rise (τ_{r1} and τ_{r2}) and decay (τ_{d1} and τ_{d2}) time constants (Table 4.4). A relatively faster time response in photocurrent decay achieved on decoration of Au NPs under UV illumination λ = 300 nm can be seen in Figure 4.13 (b). The decay time constant of the slower component (τ_{d2}) decreases from 700s in the bare device to 250 s in the Au NPs decorated device (Table 4.4). Therefore, a significant enhancement of photodetector performance has been realized due to decoration of Au NPs. The kinetics of transient photocurrent in ZnO is controlled by the trapping/releasing of charge carrier in the defects state within the semiconductor. So, the population of defects levels (surface as well as bulk) will thus control the photocurrent decay. Generally, slow kinetics of photocurrent is due to gradual accumulation of negative charge at the surface by simultaneous oxygen adsorption and desorption processes which is linked to the slow relaxation of singly charged oxygen vacancy (V_O^+) to neutral vacancy (V_O). In case of Au NPs decorated device, electrons can populate the conduction band of ZnO, being transferred of electrons from SPR band of Au NP to semiconductor (ZnO) because of plasmon enhanced optical absorption in the visible as well as UV region [26]. As a result, these generated charge carriers indeed neutralize some of charge defects state (V_O^+) that also take part in emission. The filling of charged defects on illumination will also lead to reduction of the emission in the visible which arises from these charged defect states. To confirm this proposed hypothesis, we have compared the defects state emission for bare device

and Au NPs decorated device in photoluminescence measurement at an excitation wavelength λ = 450 nm, which being of lower energy than the fundamental edge will not lead to near-band-edge (NBE) emission in Figure 4.14. A strong reduction of defect emission around 507 nm has been observed due to decoration of Au NPs. This observation is in good agreement with the proposed model stated earlier. The filling of the charged defect states on illumination reduced scattering and increased the photocurrent significantly and the transfer of electrons from the Au NPs to ZnO facilitates the process of charge neutralization of defects states leading to faster relaxation of the photocurrent for Au NPs decorated ZnO/p-Si NWs core-shell device.

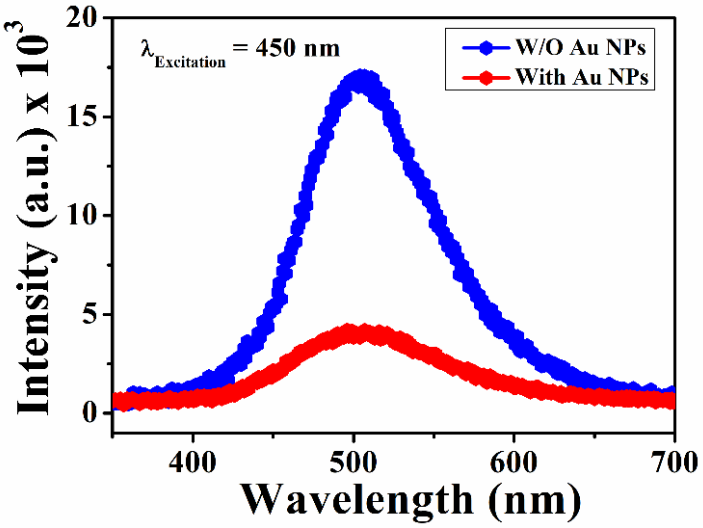

Figure 4.14 Room temperature PL spectra at an excitation wavelength λ = 450 nm for bare and Au NPs decorated ZnO/p-Si NWs core-shell arrays.

Table 4.4 Comparison of saturation photocurrent, rise and decay time constant for bare and Au NPs decorated ZnO/p-Si NWs photodetectors under λ = 300 nm illumination.

Photodetectors	**Saturation I_{PC} (μA) for λ = 300 nm**	**Rise time constant (s)**	**Decay time constant (s)**
ZnO/p-Si NWs	1.88	τ_{r1} ~ 20, τ_{r2} ~ 225	τ_{d1} ~ 50, τ_{d2} ~ 700
Au NPs-ZnO/p-Si NWs	2.52	τ_{r1} ~ 18, τ_{r2} ~ 150	τ_{d1} ~ 20, τ_{d2} ~ 250

4.4.4 Proposed model for charge transfer

Enhanced photoresponse is based on transfer of photo excited carriers from Si NW and Au NPs to the n-ZnO. The transfers of carriers are proposed to be explained on the basis a model shown schematically in Figure 4.15. The model shows the band alignments. The electron affinities of ZnO (χ_{ZnO}) and Si (χ_{Si}) are taken as 4.35 and 4.05 eV, respectively [37]. While the band gaps of ZnO and Si are taken as 3.3 and 1.12 eV, respectively. The band gap discontinuity at

conduction band and valence band is therefore equal to $\Delta E_c = \chi_{ZnO} - \chi_{Si} = 0.3$ eV and $\Delta E_V = E_{gZnO} - E_{gSi} + \Delta E_c = 1.88$ eV. At the n-ZnO and p-Si interface, which is an interface of a p-type and an n-type material, the conduction and valence bands in the p-type material bend- down and those in n-type material bend-up. This allows transfer of electrons from the conduction band of p-type Si NW to the conduction band of n-ZnO and transfer of holes from valence band of ZnO to valence band of Si without application of any bias.

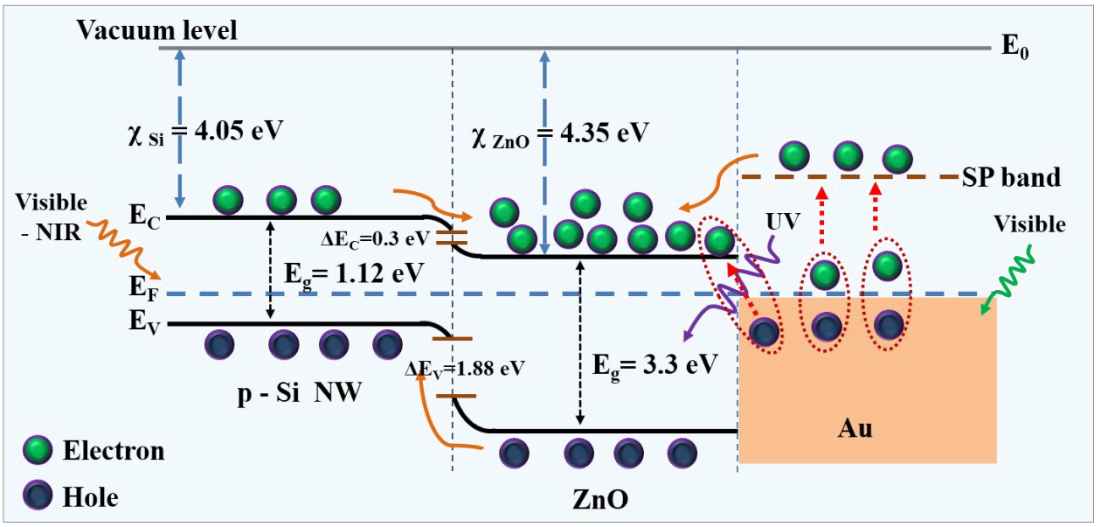

Figure 4.15 Schematic of energy band diagram of ZnO/p-Si NWs decorated with Au NPs.

The electron-hole pairs are generated with the UV and visible-NIR absorption of ZnO and Si NWs respectively. The band bending at the interface leads to an effective carrier separation mechanism and leads to accumulation of electrons in the conduction band on ZnO. This leads to enhancement of photoconduction of ZnO. Additional carriers (electrons) in the conduction band of ZnO that is needed for the enhanced photoresponse in the visible range come from the plasmonic Au NPs. The enhancement of the absorption due to the Au NPs arises from two mechanisms: (i) the surface plasmon resonance in the visible centered around $\lambda \approx 510 - 530nm$ depending on NPs particle size and shape and (ii) the inter-band transition in Au (d band $\rightarrow$ sp band) that starts in the visible at $\lambda \approx 650$ nm and extends to shorter wavelength. These two absorption mechanisms have over lapping wavelength regime leading to strong absorption in the visible starting from 650 nm peaking at the SPR wavelength and extending to UV region as shown in inset of Figure 4.11 (a). Due to both the mechanisms the conduction band of Au NP gets populated when illuminated. Since the conduction band (CB) minimum in ZnO has lower energy than the excited electrons in the sp-band of Au (in the conduction band) these excited electrons get transferred to conduction band of Au without any applied bias. This charge generation process needs no intermediary chemical bonds for charge transfer

of electron to semiconductor from Au NPs and which can work without any functionalization of semiconductor. There are recent suggestions [38] that due to plasmonic excitation one can have direct transfer of electrons to conduction band of ZnO leaving a hole in Au NP. Both the charge transfer mechanisms lead to large photocurrent in ZnO particularly in the visible range.

4.5 Conclusion

To summarize, a high the performance photodetector based on n-ZnO/p-Si NWs core-shell array decorated with ligand-free plasmonic Au NPs has been developed. The ligand-free decoration of Au NPs was done by using pulsed laser ablation in liquid (water) PLAL method. The photodetector works at low bias of 1V and consumes very low power; < 3 μm. The device uses n-ZnO as the active photoconductive channel that is sensitive in UV region. However, using photo-gating as well as favourable band alignments, the photo generated carriers are infused in the conduction band of ZnO using a tandem effect of Si NWs in Visible and NIR region and Au NPs in Visible as well as UV region leading to the enhancement of photoresponse of ZnO not only in visible range but also in UV to NIR broadband region. The filling of the charged defect states on illumination reduced scattering and increased the photocurrent significantly and the transfer of electrons from the Au NPs to ZnO facilitates the process of charge neutralization of defects states leading to faster relaxation of the photocurrent for Au NPs decorated ZnO/p-Si NWs core-shell device. The optical detector combines the visible and NIR detectability of Si NW with the UV detectivity of ZnO through the core- shell structure and broadband detectivity to bridge the gap in the visible was achieved by decorating with ligand-free Au NPs that contributes enhanced absorption and carrier generation at wavelength range < 650 nm. We observed significant enhancement of responsivity R not only in visible range but also in UV and NIR region. The responsivity of the detector ~ 1A/W from 700 nm to longer wavelength (at bias of 1V) and in the visible region the responsivity of the photodetector with Au NPs is > 0.5 A/W and increases to > 1 A/W at UV region.

Bibliography

1. D. Nunes, A. Pimentel, A. Goncalves, S. Pereira, R. Branquinho, P. Barquinha, E. Fortunato, and R. Martins, *Semicond. Sci. Technol*., **34**, 043001 (2019).
2. W. Tian, H. Zhou, and L. Li, *Small*, **13**, 1702107 (2017).
3. C. Ling, T. Guo, W. Lu, Y. Xiong, L. Zhu, and Q. Xue, *Nanoscale*, **9**, 8848 (2017).
4. Z. Zheng, L. Gan, J. Zhang, F. Zhuge, and T. Zhai, *Adv. Sci.*, **4**, 1600316 (2017).
5. Q. Hong, Y. Cao, J. Xu, H. Lu, J. He, and J. L. Sun, *ACS Appl. Mater. Interfaces*, **6**, 20887 (2014).
6. W. Tian, H. Sun, L.Chen, P. Wangyang, X. Chen, J. Xiong, and L. Li, *InfoMat*. **1**, 140 (2019).
7. S. H. Kim, D. M. Geum, M. S. Park, H. Kim, J. D. Song, and W. J. Choi, *Appl. Phys. Lett*., **110**, 153505 (2017).
8. L. Menon, H. Yang, S. J. Cho, S. Mikael, Z. Ma, C. R. Hedlund, M. Hammar, W. Zhou, *IEEE Photonics J*., **8**, 1 (2016).
9. B. D. Boruah, *Nanoscale Adv.*, **1**, 2059 (2019).
10. W. Jin and L. Hu, *Nanomaterials*, **9**, 1359 (2019).
11. P. Giraud, B. Hou, S. Pak, J. I. Sohn, S. Morris, S. N. Cha, and J. M. Kim, *Nanotechnology*, **29**, 075202 (2018).
12. L. Zeng, S. Lin, Z. Lou, H. Yuan, H. Long, Y. Li, W. Lu, S. P. Lau, D. Wu, and Y. H. Tsang, *NPG Asia Materials* **10**, 352 (2018).
13. D. Periyanagounder, P. Gnanasekar, P. Varadhan, J. H. He, and J. Kulandaivel, *J. Mater. Chem. C*, **6**, 9545 (2018).
14. H. Kang, J. Park, T. Choi, H. Jung, K. H. Lee, S. Im, and H. Kim, *Appl. Phys. Lett*., **100**, 041117 (2012).
15. D. Liu, X. Shen, T. Song, J. Hu, and B. Sun, *Phys. Chem. Chem. Phys*., **15**, 4970 (2013).
16. S. Mondal, R. R. Ghimire, and A. K. Raychaudhuri, *Appl. Phys. Lett*., **106**, 041102 (2015).
17. S. Sett, A. Ghatak, D. K. Sharma, G. V. P. Kumar, and A. K. Raychaudhuri, *J. Phys. Chem. C*, **122**, 8564 (2018).
18. S. Sett, R. S. Bisht, A. Ghatak, and A. K. Raychaudhuri, *Appl. Surf. Sci*., **497**, 143754 (2019).
19. K. Das, S. Mukherjee, S. Manna, S. K. Ray, and A. K. Raychaudhuri, *Nanoscale*, 6, 11232 (2014).
20. S. Sett, V. K. Aggarwal, A. Singha, S. Bysakh, and A. K. Raychaudhuri, *Semicond. Sci. Technol*., **35**, 025020 (2020).
21. S. Sett, S. Sengupta, N. Ganesh, K. S. Narayan, and A. K. Raychaudhuri, *Nanotechnology*, **29**, 445202 (2018).
22. J. Lu, C. Xu, J. Dai, J. Li, Y. Wang, Y. Lin, and P. Li, *Nanoscale*, **7**, 3396 (2015).
23. P. Biswas, S. R. Cho, J. W. Kim, S. D. Baek, and J. M. Myoung, *Nanotechnology*, **28**, 225502 (2017).
24. G. Jayalakshmi, and K. Saravanan, *J. Mater. Sci.: Mater. Electron*., **31**, 5710 (2020).
25. Z. Guo, D. Jiang, M. Zhao, F. Guo, J. Pei, R. Liu, L. Sun, N. Hu, and G. Zhang, *Solid-State Electron*., **124**, 24 (2016).

26. R. R. Ghimire, R. Nath, R. K. Neogy, and A. K. Raychaudhuri, *Nanotechnology*, **28**, 295703 (2017).
27. C. L. Hsu, L. F. Changa, and T. J. Hsueh, *RSC Adv*., **6**, 74201 (2016).
28. C. Samanta, A. Ghatak, A. K. Raychaudhuri, and B. Ghosh, *Nanotechnology*, **30**, 305501 (2019).
29. A. Rose, Concepts in Photoconductivity and Allied Problems, *Krieger Publishing Company*, New York **1978.**
30. Z. Liu, T. Luo, B. Liang, G. Chen, G. Yu, X. Xie, D. Chen, and G. Shen, *Nano Research*, **6**, 775 (2013).
31. Ozgur, U.; Alivov, Y. I.; Liu, C.; Teke, A.; Reshchikov, M.A.; Dogan, S.; Avrutin, V.; Cho, S. J.; Morkocd, H. comprehensive review of ZnO materials and devices. *J. Appl. Phys.* **2005,** 98, 041301.
32. Hu, L.; Chen, G. Analysis of Optical Absorption in Silicon Nanowire Arrays for Photovoltaic Applications.*Nano Lett.***2007,** 7, 3249.
33. Sze, S.M.; Ng, K.K. Physics of Semiconductor devices, 3rd Edition, *Wiley Interscience*, New Jersey **2006**.
34. Christensen, O. Quantum efficiency of the internal photoelectric effect in silicon and germanium. *J. Appl. Phys.* **1976,** 47, 689.
35. C. Samanta, S. Bhattacharya, A. K. Raychaudhuri, and B. Ghosh, *J. Phys. Chem. C*, **40**, 22235 (2020).
36. P. M. Wojcik, L. D. Bastatas, N. Rajabi, P. V. Bakharev, and D. N. McIlroy, *Nanotechnology*, **32** 035202 (2021).
37. S. T. Tan, X. W. Sun, J. L. Zhao, S. Iwan, Z. H. Cen, T. P. Chen, J. D. Ye, G. Q. Lo, D. L. Kwong, and K. L. Teo, *Appl. Phys. Lett*., **93**, 013506 (2008),
38. K. Wu, J. Chen, J. R. McBride, and T. Lian, *Science*, **349**, 6248 (2015).

Chapter 5

ZnO/Si NWs arrays based nitric oxide (NO) ultra-high sensitive gas sensor with noise limited detectivity ~ 10 ppb through injection of charge carrier by gas in heterojunction

In this chapter, we have demonstrated the gas sensing properties of ZnO/silicon nanowires (ZnO/Si NWs) heterojunction arrays and the injection of charge carrier by gas through the interface of ZnO and Si NWs leading to ultra-high sensitive (~ 500 ppb) detection of nitric oxide (NO) gas even at room temperature. In the previous chapter 4, we have discussed how photo-gating effects tuned the charge carriers in broadband photoconduction of Au NPs decorated ZnO/p-Si NWs arrays. In this chapter, we would like to explore that charge carriers can also be induced by gas injection innovatively in ZnO/Si NWs heterojunction devices. These heterostructures devices go beyond the conventional chemiresistors based gas sensor. Here the heterostructure builds a synergy that leads to much enhanced sensitivity with noise limited response ~ 10 ppb and the enhanced sensitivity of heterojunction comes from enhancement of charge carrier density through the interface of ZnO and p-Si NWs on gas exposure. A mechanism has been proposed for operation of the sensor and been validated by numerical simulation with COMSOL Multiphysics. The simulation shows the essentiality of the heterojunction in the enhancement of sensitivity over that expected from chemiresistor mechanism.

5.1 Introduction

It has been known that absorption or desorption of a gas on the surface of a metal oxide changes the conductivity and this phenomenon being first investigated in ZnO thin film layers [1]. The metal oxide semiconductor gas sensors have been utilised in a variety of different roles and industries [2]. They are extensively used to measure and monitor the trace amount of environmentally hazardous gases such as carbon monoxide (CO), nitrogen dioxide (NO_2), nitric oxide (NO) etc [3-7]. Gas sensors particularly those based on solid-state devices are commercially available and are widely used [8]. In recent years, in addition to hazardous gas monitoring, new vistas for application are opening up for solid-state gas sensors for use in healthcare such as exhaled breath analysis [9-10]. Use in exhaled breath analysis has challenging requirement that it in most cases the sensor would need detection capability below 1 ppm. Among all the gas sensing semiconductor metal oxides, ZnO has gained great attention due to its high electron mobility, high sensitivity, chemical and physical stability, nontoxic and abundance in raw material. It has been also found that the gas sensing performances of ZnO nanostructure sensor go down due to the reduction of chemisorbed oxygen ions on the surface above optimum operating temperature [11]. Generally, metal oxide required a high working temperature in the range of 200-500 ^oC for better gas response. Thus, the necessity for the improvement in gas response, rise and recovery time, stability, selectivity, and reproducibility at low operating temperature has paved advanced route for the modification of ZnO nanostructures. The sensing performances can be enhanced via tunning of surface morphology of ZnO, doping with metal into ZnO, functionalization of ZnO surface by noble metal nanoparticles and UV/visible light activation [12-19]. The most studies of ZnO based sensors focused on the influence of surface morphology on gas detection, opening new strategies which could boosted the performances of gas sensor due to large surface area of the nanostructures renders them high sensitivity and their small dimensional, cost-effective nature provides better prospects for various trace gas sensing applications [20]. The key role for high performances devices mainly depends on how much carrier is contributed to the charge conduction from sensor to target gases. Although the morphology tuning and surface functionalization can improve the gas sensitivity of ZnO based devices. However, combining ZnO with other materials is also a common strategy. Different materials are integrated to form the heterojunction, homojunction and Schottky junction, which are beneficial to reduce the grain boundary barrier and make electrons easily migrate inside the material which can further improve the gas sensing properties of the composite system [21-24]. However, the choice of

integrated materials with ZnO for further enhancement of gas sensing performance needs to be addressed. While chemiresistors based on oxides still form the main stay of solid-state gas sensors, they have limitations of detection capability below 10 ppm and also selectivity limitations. In such sensors, more often than not, there is need of heated operation thus requiring additional heater arrangements as well as enhanced power consumption. For sensors working on tight power budget (i.e., portable hand-held detectors, space applications etc.) heated operation is indeed a bottle-neck. Recently, different nanostructured materials are being used and they hold promises of better performance and even unheated operation [25-26]. Enhanced surface to volume ratio, higher gas diffusion rate and enhanced reactivity are some of the factors that make nanostructured materials an improved device material for gas sensing. Interesting device concepts based on nanostructured materials such as heterostructure and core-shell structure have been proposed recently that go beyond conventional chemiresistors [27-28]. These devices are expected to be compact, have low power consumption and also enhanced detection capability.

In parallel with metal oxide-based gas sensors, Si nanowires (NWs) arrays and porous silicon have attracted much current attention as new generation of enabling sensor materials that can be integrated with other active materials to make heterostructures or FET type device structures that can be used for gas sensing with enhanced capability [29-31]. Si NWs have relatively high carrier mobility~ 200-350 cm^2/Vs and can be tuned to have a desired conductivity by suitable doping. Si NW can also be easily integrated into heterojunction with different materials like gas sensitive oxides. In this context we specially refer to the very recent work [32] where Silicon Nanowires/TiO_2 core-shell heterojunctions based CH_4 gas senor with low power consumption has been reported that can be utilized as unheated sensor and has a gas detection capability down to 10 ppm. Another report of hybrid structures of ZnO nanorod/porous silicon nanowire n-n heterojunctions showed gas sensing performance for various NO_2 concentration at room temperature with a gas detection capability down to 5 ppm [33].

The novelty of our work is, we have fabricated a ZnO/silicon nanowires (ZnO/Si NWs) heterojunction arrays based nitric oxide (NO) gas sensor that can show a calibrated detection capability at least down to 0.5ppm (with dry N_2 as the ambience gas) with a noise limited resolution down to 10 ppb workable at room temperature. It can be noted that this hetero structure builds a synergy that leads to much enhanced sensitivity compare to either of the constituent material (like only ZnO or only Si NW). The sensor shows excellent selectivity and can be operated in unheated operation with reasonable response time. The nanostructure

devices have been tested both as a p-n junction with p-type NWs array and as n-n junction with n-type NWs array. Better performance has been obtained with the p-n junction array (reason has been explained in gas sensing mechanism section). ZnO has been selected as the active gas sensitive material because ease of synthesis, high carrier mobility and stability. The ease of fabrication of the sensor from Si wafers and ZnO by simple chemical processing and need of around few μW powers for its operation makes it viable for large scale use and cloud compatibility. Generally, the semiconductor gas sensors are based on single layered nano-structured films, whereas the present system provides a concept of a specific bilayer heterostructure. In this context, it is noted that both ZnO and Si-NWs array can act as NO sensors albeit with much less sensitivity but the hetero-structure builds a synergy that leads to much enhanced sensitivity that can be obtained from either of the materials. The highly sensitive detection of NO gas can be ascribed to enhance of charge carrier transport through the interface of ZnO and Si NW. A mechanism has been proposed for operation of the sensor and been validated by numerical simulation. The simulation shows the essentiality of the hetero-junction in the enhancement of sensitivity over that expected from chemiresistor mechanism.

Nitric oxide (NO) gas is one of the gases emitted from combustion of fossil fuels and takes part in the formation of various other nitrogen oxides which are harmful and hazardous environmental pollutants and cause acid rain. NO gas is also responsible for ozone depletion by converting ozone to nitrogen dioxide and oxygen. NO is extremely hazardous gas when inhaled [34]. Various safety standards suggest that inhaling NO at 100 ppm level can cause immediate danger. Inhaling NO below 25ppm has a safety limit of 8 hours. Thus, it is important to monitor NO closely in places where human/animal can get exposed to the gas.

NO is also a biologically significant molecule and can be utilized as a primary signalling molecule (present in exhaled breath) for non-invasive diagnosis of certain pulmonary diseases such as asthma, bronchitis, airflow limitation leading and chronic obstructive pulmonary disease (COPD). However, detection of NO in exhaled breath for diagnosis would need detection capability well below one ppm. Conventional metal oxide based chemiresistor sensors do not meet this requirement. Thus, a portable NO unheated gas sensor that can reach sub-ppm capability of detection and can be fabricated without use of costly fabrication facilities will be of high utility. The sensor reported here meets these criteria. Noise limited sensing resolution down to tens of ppb, reported in this work, is indeed a major advancement towards utilization of the sensor in exhaled breath analysis for diagnostic. The innovation of room

temperature sensing device may push forward the integration of gas sensing element with wireless device and that can be connected to the Internet of Things (IOT) platforms. This proof of concept has been patented (Patent reference no: *201731038036*) and activities related to packaging of prototype/product are in the final stage of processing [35].

5.2 Experimental details

The gas sensor devices have been fabricated from heterojunction of ZnO/Si NWs arrays by deposition of ZnO on Si NWs (both p-type and n-type) arrays to make p-n and n-n junction devices by using chemical solution deposition (CSD) method. The details of fabrication processes have been given in chapter 2. The characterization of ZnO/Si NWs nanostructure was done by X-ray diffraction (XRD). The nanostructured complete device was also studied using scanning electron microscopy (SEM) (Quanta FEG 250) and cross-sectional transmission electron microscopy (TEM) (Tecnai G2, TF-20, FEI Make) as well as energy dispersive X-ray spectroscopy (EDS). The lamellar for the cross-sectional electron microscopy was made from the actual device using a focused ion beam (FIB) set-up discussed in chapter 3. The imaging of the cross-section of the device enables us to make a proper physical model that we utilized to make a numerical model-based simulation with COMSOL Multiphysics. The gas sensing properties were measured at room temperature (25 ^{o}C) in a high vacuum (HV) custom-made chamber (Figure 5.1) discussed in chapter 3. In this section we recapitulate some of the important issues and point out the parameters. For electrical measurements Cr/Au contacts pad are deposited on the top ZnO layer of the ZnO/Si NWs heterostructure device by thermal evaporation through hard mask. A schematic diagram of ZnO/Si NWs heterojunction arrays-based gas sensing device along with real image of the sensor is also shown in Figure 5.1. The length and width of the channel is 2mm x 2 mm. The sensor is biased with 0.5 V and the current and resistance of the sensor are recorded over time till it is stable. The $I-V$ curve is also measured. After getting stable values of device current at a given bias a known concentration (ppm) of nitric oxide (NO) gas was injected into the chamber (Figure 5.1) and the changed device current was measured. The $I-V$ curves after gas exposure were also measured. The measurements were done using a source- meter. By repeating the measurements for several times, the changes of current/resistance with time under different concentrations of NO were recorded. Data were taken in controlled NO concentration range of 0.5 – 200 ppm (in dry N_2 ambience). We have tested a number gas sensing devices made in similar fashion to establish the reproducibility of the sensors. The sensor is also stable under dry air. NO gas is known to react with oxygen to form NO_2. Due to this instability of NO in air, we did all the measurements

in dry N_2. From the device current I (at a given bias V), the device resistance was obtained. The performance of gas sensor device is quantified by the normalized response Ř defined as:

$$\check{R}(\%) = \frac{R_g - R_0}{R_0} \times 100\% \qquad (5.1)$$

Where R_0 and R_g are the measured electrical resistances of gas sensing devices in dry nitrogen environment and on exposure to nitric oxide (NO) respectively. In this definition when the device resistance increases (decreases) on gas exposure Ř is positive (negative).

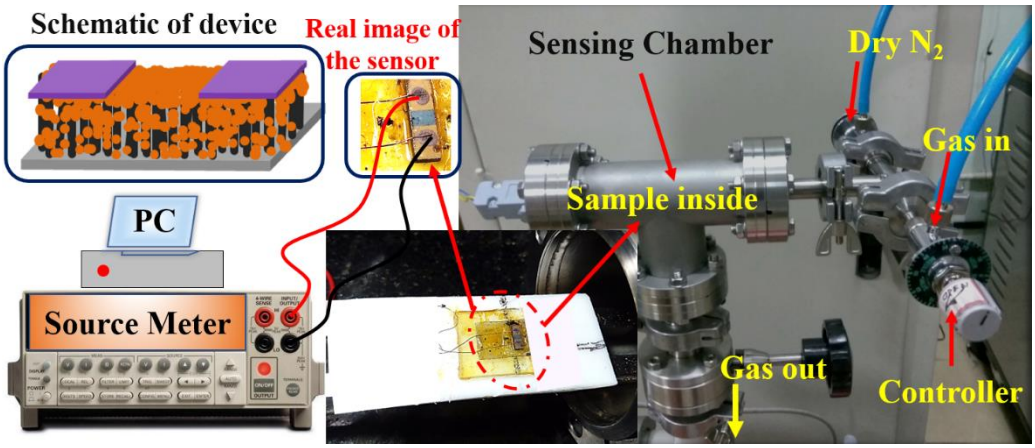

Figure 5.1 Gas sensing measurement process in a custom-made chamber along with a schematic of ZnO/Si NWs nanostructure based gas sensor and real image of the sensor.

5.3 Experimental results

5.3.1 Cross-sectional TEM and SEM of the device

In order to establish the physical structure of the ZnO/Si NWs based gas sensing devices, we have done cross-sectional SEM and TEM along with elemental analysis (EDS).

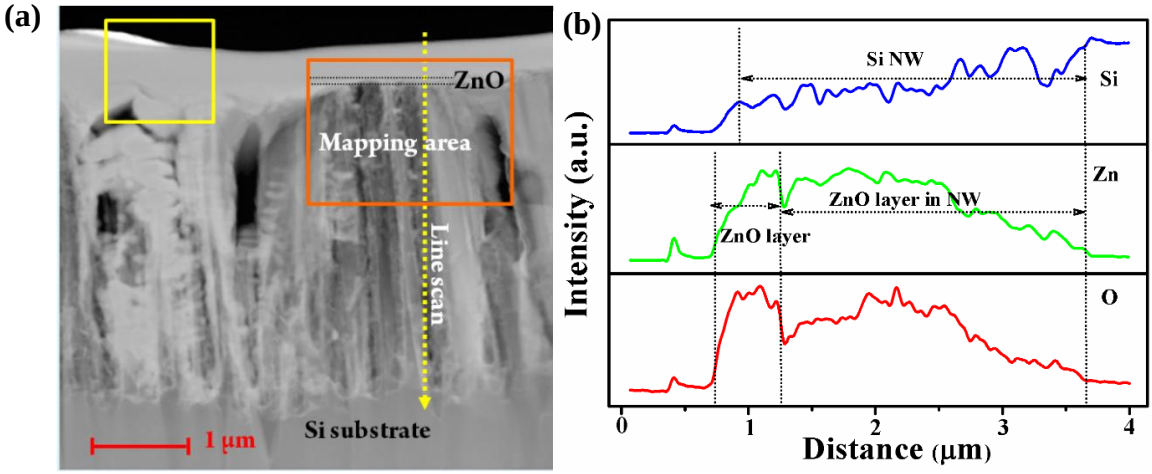

Figure 5.2 (a) STEM-HAADF image taken on the cross-sectional lamella of the device. (b) Elemental composition of ZnO coated Si NWs taken by EDS line scan.

Figure 5.2 (a) shows a scanning tunnelling electron microscopy high angle annular dark-field (STEM HAADF) imaging of the cross-section lamellar of ZnO/Si NWs arrays. A composition profile of the device is obtained by line EDS and the data are shown in Figure 5.2 (b). The line scan of the ZnO/Si NW shows the contents of Si, Zn and O. There is a clear top ZnO layer (thickness ≈ 350 nm) on the NWs array, which is followed by the array of ZnO nanoparticles /nanostructured film coated Si NWs and the un-etched substrate [36]. Figure 5.3 (a), (b) and (c) shows the STEM-EDS mapping for Silicon K shell, Zinc L shell and Oxygen K shell of ZnO coated Si NW respectively. The STEM EDS mapping on a portion of ZnO coated Si NW (marked by orange box in Figure 5.2 (a)) shows presence of Zn and O throughout the length Si NW. This establishes that there is a layer of ZnO all around the Si NWs. Zinc L shell mapping (Figure 5.3 (b) as well as Oxygen K shell mapping (Figure 5.3 (c)) show that concentrations of Zinc and Oxygen are highest on the top of the Si NWs due to the thick ZnO film.

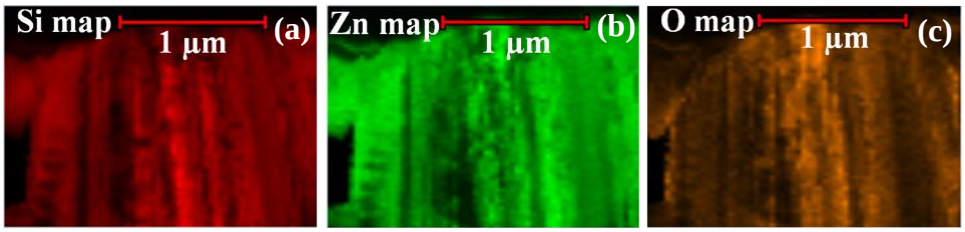

Figure 5.3 STEM EDS mapping of (a) Silicon (K shell) (b) Zinc (L shell) (c) Oxygen (K shell) of the ZnO coated Si NWs.

From a detailed analysis of cross-sectional microscopy and the compositional analysis, a physical model is proposed below (Figure 5.4).

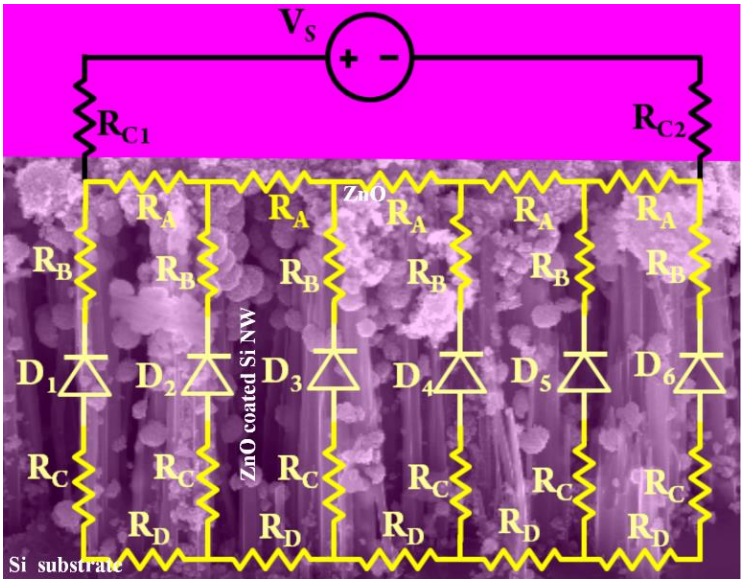

Figure 5.4 A physical model of the sensor with schematic of the electrical model embedded on SEM with it.

The device has a layer of ZnO making heterostructure with Si NWs. The top layer of ZnO takes part in electrical current conduction. The Si NWs also has an all-round layer of ZnO that also acts as "chemical sensing gate" to modulate the depletion layer on the surface of the NW. The all-around layer does not take part in current conduction. In the same figure we show a schematic electrical model that we will use for simulation and will be discussed later on.

5.3.2 Gas sensing performances

5.3.2.1 Essentiality of the ZnO/Si NWs heterostructure

To understand the importance of the ZnO/Si NWs heterostructures for sensing of NO gas, we have measured the gas response of both ZnO/p-Si NWs (p-n) and ZnO/n-Si NWs (n-n) heterojunctions arrays for different concentration of NO gas at room temperature. We have measured the conductive gas response for only ZnO nanostructured films as well as p-Si NWs and n-Si NWs at room temperature separately to give an insight into the role of heterojunction (p-n and n-n junction of ZnO/Si NWs heterostructures) for enhanced gas response. Both the parts have been reported to show NO response [37-38]. Figure 5.5 (a) and (b) shows the gas response and recovery curve of only ZnO nanostructured films and only Si NWs (p and n type) arrays to the concentration of 10 ppm NO gas at room temperature respectively. The data show the response as a function of time when the gas is turned ON (gas injected into chamber) and OFF (when chamber flashed of NO and dry N_2 admitted). Data show that both ZnO nanostructured film and Si NWs exhibit very small response (< 5 %) at room temperature, which is in accordance with the widely accepted fact that both ZnO and Si NWs act as chemiresistors based gas sensor operated at a temperature higher than 100 ^{o}C. Whereas, the heterostructure of ZnO and Si NWs (both p-n and n-n junction) offered the better the gas response towards NO gas detection even at room temperature shown in Figure 5.6 (a) and (b).

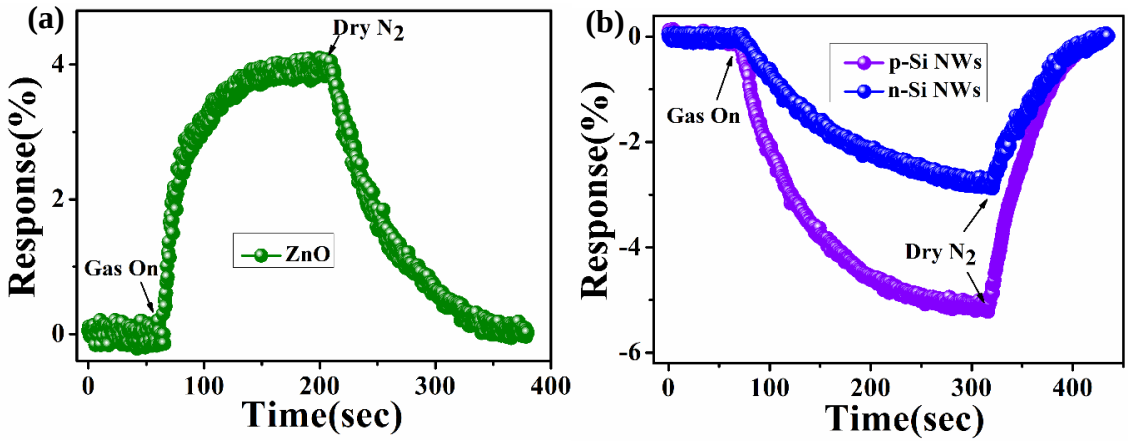

Figure 5.5 Room temperature gas response of (a) ZnO nanostructured film. (b) p-Si NWs and n-Si NWs arrays to the concentration of 10 ppm NO gas.

Data in the Figure 5.6 (a) show the response of the device ZnO/p-Si NW on exposure to NO gas in the low concentration range 2ppm -10ppm. The data show the response as a function of time when the gas is turned ON (gas injected into chamber) and OFF (when chamber flashed of NO and dry N_2 admitted). In the same graph we also show the data on the ZnO/n-Si NW arrays. For the device on p-Si NWs, the device current increases leading to decrease of the device resistance on exposure to NO gas. This makes Ř negative.

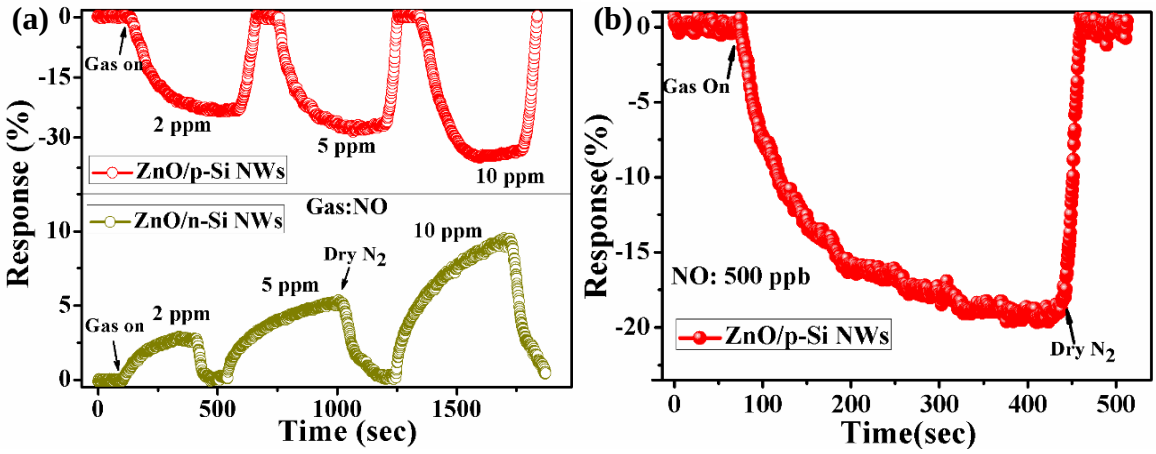

Figure 5.6 (a) Gas response of the ZnO/Si NWs arrays in low concentration range (≤10 ppm). The upper panel shows the response of the device made from p-Si and the lower one that made from n-Si. (b) Variation of response Ř of ZnO/p-Si NWs device with time when exposed to 0.5 ppm concentration of NO.

As shown in the Figure 5.6 (a) an opposite behaviour is seen in the ZnO/n-Si NWs device on gas exposure where the device current decreases (and device resistance increases) Ř is positive. The response Ř on the n-Si NWs device is sufficiently muted (explained later on). The response and recovery curve of the ZnO/p-Si NWs sensor on exposure to only 500 ppb of NO gas is shown in Figure 5.6 (b). This shows that even in unheated operation the sensor can respond to an exposure as small as 0.5 ppm in around 100-120 sec (90% of full value). From the response we can also estimate the noise limited response. We find that the sensors are ultra-high sensitive (limited by device current noise) and can detect a concentration as low as 10 ppb. This clearly establishes the efficacy of the present sensor in determining low concentration of NO in sub-ppm regime. The sensor performance observed is much better than that of metal oxide based chemiresistor sensor reported till date [35]. So, the prominent enhancement in gas sensing performance has been achieved by combining ZnO nanostructures with Si NWs arrays into heterojunction. The absolute values of the response data |Ř| for p-n heterojunction and individual parts (ZnO and p-Si NWs arrays) are shown in Figure 5.7 (a) for exposure of 10 ppm of NO and Figure 5.7 (b) shows the absolute values of |Ř| for n-n heterostructure and individual parts (ZnO and n-Si NWs arrays). The data are given in Figure 5.7 (a) and (b). The

ZnO/p-Si NWs p-n heterojunction structure shows a large response of ~ 35% in comparison with the ZnO/n-Si NWs n-n heterojunction of gas response ~ 9.5 %, the other individual parts (ZnO, p-Si NWs and n-Si NWs arrays) show the very small response limited to within 5%. This clearly indicates the essentiality of the ZnO/p-Si NWs heterostructure in giving rise to such a high response. The junction thus has a "synergetic" effect that the junction device has response that is not only larger than the individual parts (ZnO and p-Si NW array) but it is even larger than the sum total of individual response.

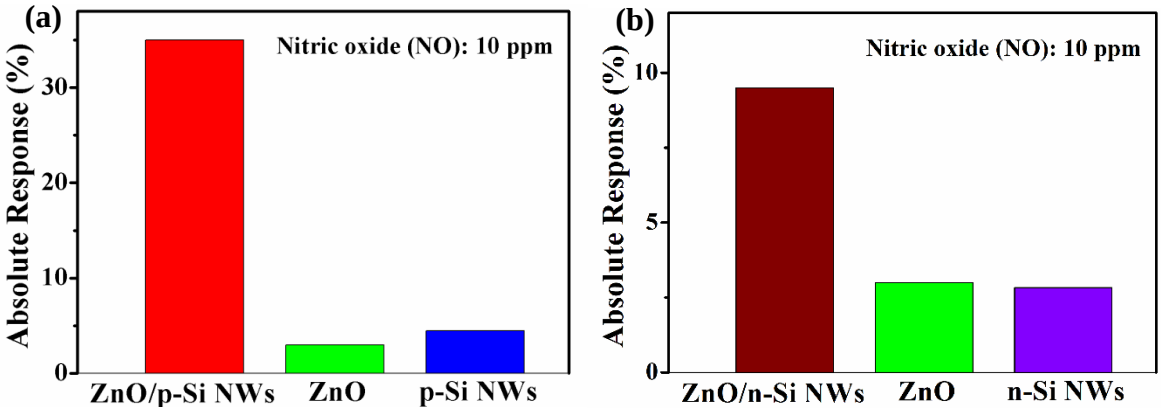

Figure 5.7 Comparison of absolute gas sensing response |Ř| of (a) ZnO/p-Si NWs, ZnO and p-Si NWs arrays, (b) ZnO/n-Si NWs, ZnO and n-Si NWs arrays to 10 ppm of NO gas at room temperature.

In view of the superior performance of the device made on p-Si NWs arrays, we investigated this device thoroughly in remaining part of the chapter.

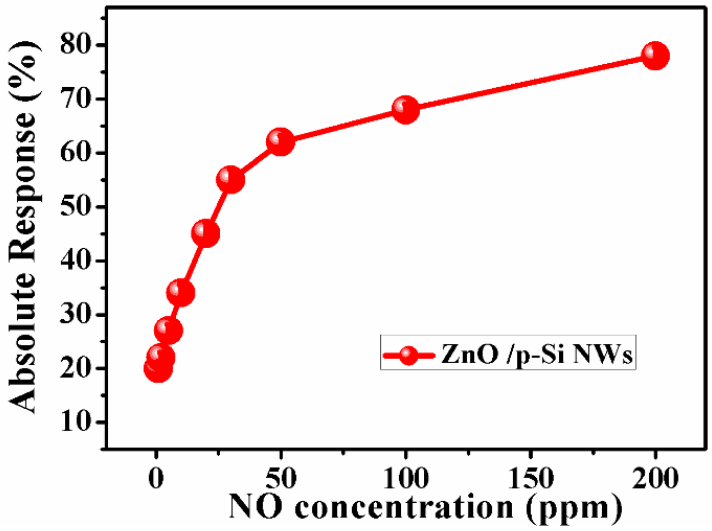

Figure 5.8 Room temperature absolute gas response |Ř| for exposure to different NO concentration ranging from 0.5 ppm to 200 ppm.

Figure 5.8 shows the room temperature absolute gas response |Ř|, when data in the device are taken successively for exposure to different NO concentration ranging from 0.5 ppm to

200ppm. Before each exposure the chamber has been pumped out, flashed and a fresh ambience of dry N_2 was created. At low concentration of NO (< 30 ppm) the response has a linear dependence on concentration and it tends to saturation beyond that. At 200 ppm |Ř| approaches a substantial value ~80%.

5.3.2.2 Figures of merit of the sensor

To estimate the performance of gas sensors for use in any application field, the following characteristics value of the sensors such as selectivity, sensitivity, response/recovery time and effect of humidity should be considered. In this section, we have discussed few important parameters of gas sensors.

(a) Response and Recovery time

Figure 5.9 shows the variation of sensor response time as a function of gas concentration at room temperature. The response rise time τ_{rise} is defined as time from start of gas flow to 90% of full value. The recovery time $\tau_{recovery}$ is defined as time to recover from full value to 90% of final no-exposure value. The rise time τ_{rise} is ≈ 130-140 s for concentration ≤ 10 ppm and it reduces to about 60 sec for concentration reaching 30 ppm and then gradually reduces to about 40 sec at highest concentration measured.

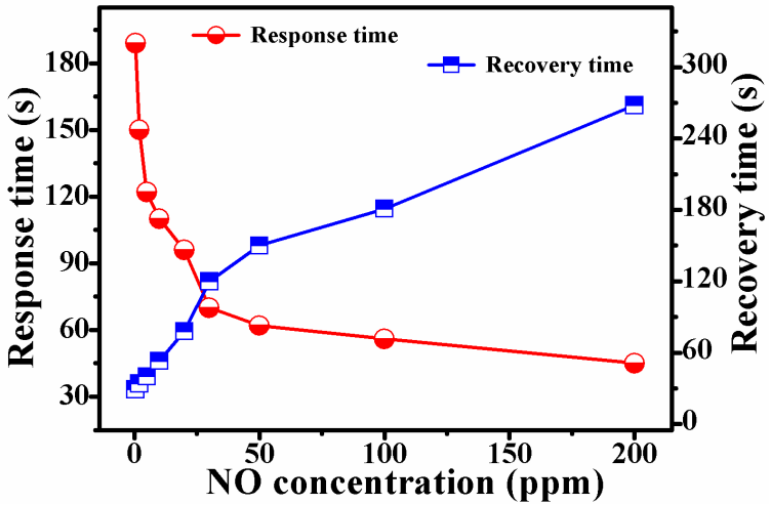

Figure 5.9 Variation of unheated sensor response time and recovery time with different concentration of NO gas.

The recovery time has an opposite dependence on concentration. $T_{recovery}$ is smallest for lowest concentration and highest for largest concentration. This may be understood form the fact that at larger concentration there are more molecules to react at a given time leading to smaller τ_{rise}. However, in the recovery period the gas absorbed in the sensor has to diffuse out. Larger is the concentration more is the depth of penetration and more is the out diffusion time leading to

larger $\tau_{recovery}$. Though one report of NO sensor [36] by using ZnO nanorod thin film has response rise time (τ_{rise}) of about 8 minutes at a concentration of 70 ppm and operated at 200 ^{o}C temperature whereas, our present sensor is operated at room temperature and rise time is much faster ≈ 130-140 s for concentration ≤ 10 ppm and it reduces to about 60 sec for concentration reaching 30 ppm.

(b) Stability and Selectivity of the sensor

We have prepared a number of devices and tested them for exposure to 10 ppm. This establishes that the fabrication process makes sensors that can be used with calibration transferability from one device to other. The data are given in Figure 5.10 (a). Figure 5.10 (b) shows the variation of gas response with different values of relative humidity (RH) at concentration of 10 ppm NO gas. From data it is seen that response decreases somewhat with increasing humidity. The performance of device (response) is not so much degraded with the moisture in the environment. In particular at 10 ppm of NO the absolute gas response is about 35 % at a humidity of 10 % RH while absolute response decreases to 24 % at a humidity of 90 % RH.

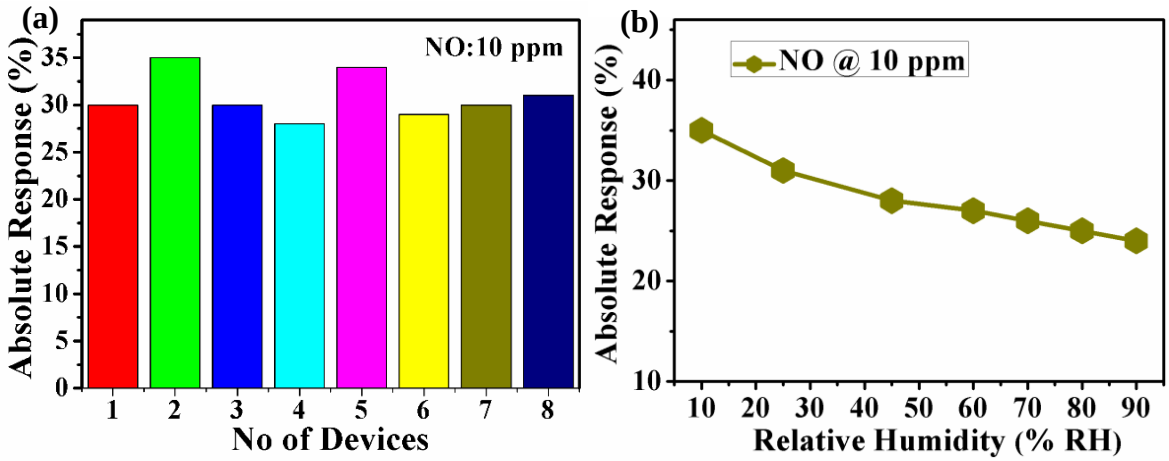

Figure 5.10 (a) Variation of absolute gas response for 8 numbers of ZnO/p-Si NWs gas sensor devices. (b) The humidity dependence of absolute gas response of ZnO/p-Si NWs device to 10 ppm of NO gas concentration.

Selectivity for a specific gas is an important property of any gas sensor. To check selectivity towards NO gas of ZnO/p-Si NWs sensor, the sensor has been tested by exposure to different types of gases. Figure 5.11 shows the selective gas sensor response when exposed to different types of gases like, NH_3, CH_4, H_2S and water vapour (H_2O). The gas response of the device is also tested with other oxidizing gas like NO_2. From data it can be seen that ZnO/p-Si NWs heterostructure sensor showed maximum response of about – 80 % and – 6 % to 200 ppm of NO and NO_2 respectively, while the response to 200 ppm NH_3, H_2S and CH_4 are 10 %, 6% and 1 % respectively and response is 2.5 % for water vapour (RH> 95%). It can be concluded that

the ZnO/p-Si NWs sensor has very high selectivity for response towards NO gas compare to other gases.

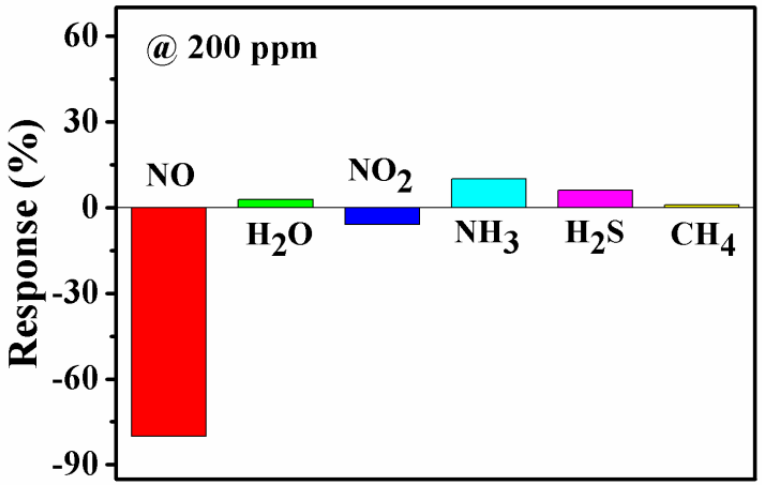

Figure 5.11 Gas sensing response of ZnO/p-Si NWs sensor to various gases to check the selectivity of the sensor.

5.4 Discussions

5.4.1 Simulation of gas sensing devices with COMSOL Multiphysics

The data presented above clearly establish that the ZnO/p-Si NWs heterojunction array, that forms an array of nano sized (p-n) junctions leads to a very sensitive gas detector as demonstrated for the gas NO. In this section we make an electrical model of the both p-n and n-n junction gas sensor devices and then make an analysis of the device model by simulation of the devices electrical characteristics using COMSOL® Multiphysics software.

5.4.1.1 Simulation of p-n junction

The physical model proposed is given in Figure 5.4 that has been obtained from detailed cross-sectional microscopy. The electrical model is embedded on the same figure, which is an array of p-n junctions and resistor arrays. The figure shows the p-n junction (marked by symbol of p-n junction) where the p-part is the p-Si NW and n-part is the ZnO film that is n-type. The top ZnO layer whose resistance is lumped into resistance R_A. Similarly, the p-Si substrate (with resistivity of 1-10 Ω-cm) on which the nanowires (NWs) arrays stands has a lumped resistance R_D. The series resistances R_B and R_C are associated with the ZnO layers close to the junction and the p-Si NW respectively. The resistance R_C is that part of the p-Si NW that has an all-around ZnO around it. In the circuit, R_{C1} and R_{C2} are two contact resistances coming from contacting interface between metal and semiconductor which gives asymmetry in the conductivity curve.

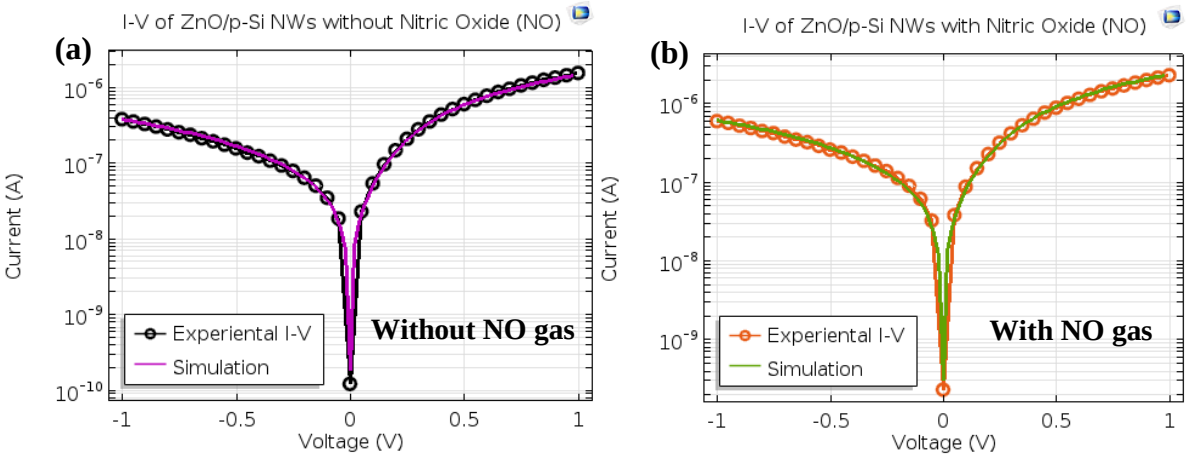

Figure 5.12 (a) Simulation $I-V$ data fitted with experimental data before NO gas exposure. (b) Simulation $I-V$ data fitted with experimental data after NO gas exposure of ZnO/p-Si NWs p-n junction sensor.

Table 5.1 Characteristics value of ZnO/p-Si NWs p-n heterojunction before and after nitric oxide (NO) gas exposure of 5 ppm.

Characteristics of ZnO/p-Si NWs p-n junction	Before gas expose	After gas expose
Reverse saturation current (I_0)	5.35x 10^{-9} Amp	1.05 x 10^{-8} Amp
Ideality factor (η)	1.13	1.36
Resistance of ZnO (R_A)	645 kΩ	395 kΩ
Series resistance of p-n junction (R_B)	130 kΩ	75 kΩ
Series resistance of p-n junction (R_C)	105 kΩ	50 kΩ
Resistance of p-Si NWs arrays (R_D)	25 kΩ	20 kΩ

The measured I-V curves of the ZnO/p-Si NWs p-n junction devices without NO and with 5 ppm of NO exposure are shown in Figure 5.12 (a) and (b) respectively. Figure 5.12 (a) and (b) show the simulated $I-V$ curves agree well with the experimental data both before and after exposure to NO gas for ZnO/p-Si NWs p-n junction sensor. The comparison of the simulation results with the experiment identifies the materials parameters that enhance the device response. The characteristics values of the parameters for the best fits obtained from the simulation are given in Table 5.1 for ZnO/p-Si NWs p-n junction. The values of p-n junction reverse saturation current (I_0) increases from 5.35 x 10^{-9} A to nearly 10^{-8} A with an enhancement of about 49%. The resistance of the ZnO top layer film (R_A) also reduces by 39% for p-n junction device. However, the largest enhancement in the device current for p-n junction are

contributed by drops in resistances R_B and R_C (42% and 52% respectively) which comes from ZnO coating around the p-Si NWs.

5.4.1.2 Simulation of n-n junction

In a similar concept, in case of ZnO/n-Si NWs n-n heterojunction, the electrical model is based on an array of n-n junctions and resistor arrays. The top ZnO layer of ZnO/n-Si NWs n-n junction whose resistance is lumped into resistance $R_A^{\dagger}$. Similarly, the n-Si substrate (with resistivity of > 1000 Ω-cm) on which the nanowire arrays stand has a lumped resistance $R_D^{\dagger}$ and the series resistances $R_B^{\dagger}$ and $R_C^{\dagger}$ are associated with the ZnO layers close to the junction and the n-Si NW respectively. The resistance $R_C^{\dagger}$ is that part of the n-Si NW that has an all-around ZnO around it.

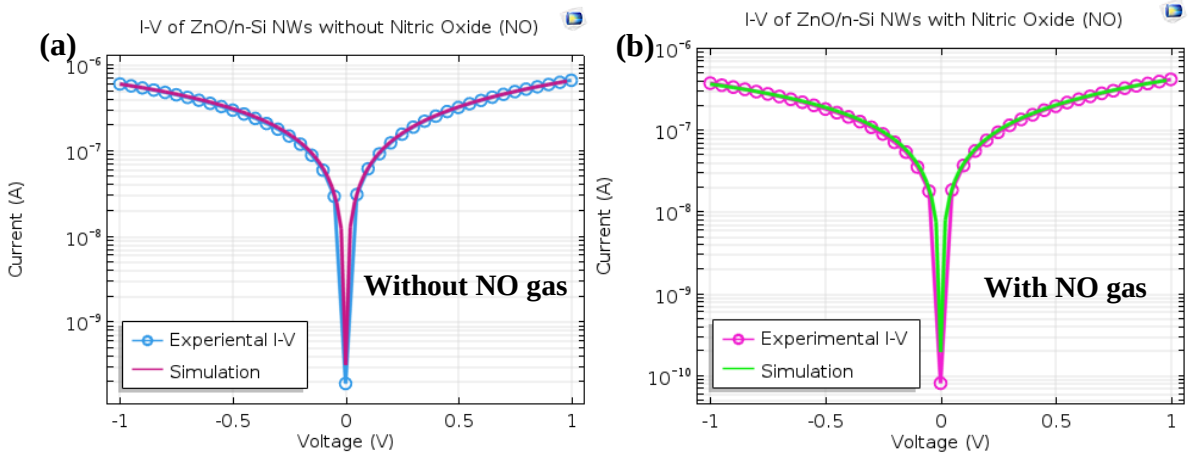

Figure 5.13 (a) Simulation $I-V$ data fitted with experimental data before NO gas exposure. (b) Simulation $I-V$ data fitted with experimental data after NO gas exposure of ZnO/n-Si NWs n-n junction sensor.

The measured $I-V$ curves of the ZnO/n-Si NWs n-n junction device without NO and with 5 ppm of NO exposure are shown in Figure 5.13 (a) and (b) respectively. We have fitted the experimental I-V data before and after exposure to NO gas for ZnO/n-Si NWs n-n junction device in Figure 5.13 (a) and (b). The characteristics values of the parameters for the best fits obtained from the simulation are given in Table 5.2 for ZnO/n-Si NWs n-n junction sensor. The value of n-n junction reverse saturation current ($I_0^{\dagger}$) is decreased by ~ 33% on gas exposure. Whereas, the series resistances $R_B^{\dagger}$ and $R_C^{\dagger}$ are increased by 22% and 24 % respectively on gas exposure for ZnO/n-Si NWs device. However, the reduction of device current on gas exposure is contributed with an enormous enhancement of about 92% the resistance $R_A^{\dagger}$ of top layer ZnO in ZnO/n-Si NWs n-n junction.

Table 5.2 Characteristics value of ZnO/n-Si NW n-n heterojunction before and after nitric oxide (NO) gas exposure of 5 ppm.

Characteristics of ZnO/n-Si NWs n-n junction	Before gas expose	After gas expose
Reverse saturation current ($I_0^{\dagger}$)	6x 10^{-9} Amp	4 x 10^{-9} Amp
Ideality factor (η)	4	4.5
Resistance of ZnO ($R_A^{\dagger}$)	305 kΩ	585 kΩ
Series resistance of n-n junction ($R_B^{\dagger}$)	330 kΩ	405 kΩ
Series resistance of n-n junction ($R_C^{\dagger}$)	310 kΩ	385 kΩ
Resistance of n-Si NWs arrays ($R_D^{\dagger}$)	3060 kΩ	2950 kΩ

From Table 5.1 and 5.2, it can be seen that all the parameters undergo change in the electrical model and this leads to enhancement of current in case of p-n junction sensor whereas there is a lowering of the device current on gas exposure in case of n-n junction device. It is noted that the electrical model analysis is based on finite number of resistors and p-n junctions which are meant to capture the essential physical process. In real device there are larger number of resistors and p-n junctions. Thus, the quantification of parameters from the model that we obtained from finite number of circuit elements will be treated as suggestive than rigorous. The main inference from the simulation is that the observed high performances of the sensor device depend on change in resistances of the constituents as well change in the reverse saturation current at the ZnO/p-Si NW p-n junction. The reverse saturation current mainly arises from the drift current which comes from the minority carriers and is $\propto n_i^2$, where n_i is the intrinsic carrier concentration. The sensing mechanism proposed below proposes that these changes come from enhancement of carrier density in the sensor on gas exposure.

5.4.2 Proposed sensing mechanism

5.4.2.1 Sensing mechanism for p-n junction

In order to explain the gas sensing performances of the devices the following gas sensing mechanism is proposed. A p-n heterojunction is formed at the interface between the p-Si NW and ZnO. Due to strong oxidizing nature of NO gas molecule, chemical reaction can take place between ZnO and silicon with nitric oxide (NO) gas molecules. When strong oxidizing gas like NO is exposed to p- Si NWs samples, the concentration of minority charge carriers electrons decreases and the majority carriers holes increases according to the following reactions [17]:

$$NO_{gas} + e^- \rightarrow NO^-_{ads} \quad (5.2)$$

$$2NO^-_{ads} \rightarrow 2O^-_{ads} + N_{2\,gas} \quad (5.3)$$

$$2NO^-_{ads} + e^- \rightarrow O^-_{ads} + N_2O \quad (5.4)$$

As a result, conductance of p-Si NWs assembly increases as a result the device current increases leading to decrease of the device resistance on exposure to NO gas. This makes gas response negative for p-Si NWs in Figure 5.5 (b). But when NO is exposed to ZnO, the concentration of electron is decreases due to charge transfer from ZnO to NO as result the conductance of ZnO is decreases as a result the device current decreases leading to increase in the device resistance on exposure to NO gas. This makes Ř positive for ZnO nanostructured film in Figure 5.5 (a). As Fermi level of ZnO is lower than that of p-Si NWs electrons will flow from conduction band of p-Si NW to conduction band of n-ZnO which favours charge transfer from nanowire to gas molecule. As the electron affinity of ZnO is higher than that of silicon, this leads to increase of the majority charge carrier concentration in silicon. Also due to higher electron affinity of NO gas, charge transfer is stimulated that leads to enhancement of the hole accumulation layer which decreases the electrical resistance upon exposure to NO gas in ZnO/p-Si NWs p-n junction device. From the upper panel in Figure 5.6 (a), it is seen that for the device made on p-Si NW, the response Ř is negative because hole is transferred from ZnO to p-Si NW through ZnO/p-Si NW interface, as a result resistance of the constituent components (given in Table 5.1) decrease upon exposure to NO gas and junction builds a synergy that leads to much enhanced sensitivity.

5.4.2.2 Sensing mechanism for n-n junction

A n-n junction is constructed at the interface between the n-type Si NW and ZnO. Unlike p-Si NWs, when NO is exposed to n-Si NWs arrays, the conductance of n-Si NWs assembly also enhances by increasing carrier density (electrons) and upon NO adsorption because of strong electron donating power of NO molecules and the charge transfers from NO to n-Si NW. This makes also gas response negative for n-Si NWs assembly in Figure 5.5 (b). So, the electron affinity of silicon can be modulated by nitric oxide (NO) attachment because NO has an unpaired electron and an electron withdrawing/donating tendency. In the device made on n-Si NW, the gas response Ř is positive (lower panel in Figure 5.6 (a)) because electron is transferred through ZnO/n-Si NW interface from ZnO to n-Si NWs. This decreases the carrier concentration of ZnO top layer leading to resistance increment of resistance of constituent component except the n-Si NWs (given in Table 5.2).

So, from the gas response behaviour of ZnO/p-Si NWs p-n junction device it is clear that the dominant conductive path should be p-Si NWs due to lower resistive path of p-Si substrate (< 10 Ω-cm) compared with ZnO (~ 10^2 Ω-cm). Whereas in case of ZnO/n-Si NWs n-n junction device the main conductive path should be ZnO due to higher resistive path of n-Si substrate (> 10^3 Ω-cm).

So, in case p-n heterojunction device, the junction between ZnO and p- Si NWs plays the key role that leads to high detectivity **(**~500 ppb) of NO gas whereas the role of n-n junction between ZnO and n-Si NWs is sufficiently suppressed leads to lower value of gas response in comparison with p-n junction.

5.5 Conclusion

In summary, we showed that a functional oxide (ZnO) and semiconductor (Si) NWs based heterojunction array based NO gas sensor can lead to extremely high sensitivity even in room temperature operation with high selectivity for gas detection without interference of humidity and no extra power is needed for heating arrangement which avoids the complexity in the designed sensor electronics. The sensor has a calibrated response of at least 0.5 ppm and a noise limited resolution of ~10 ppb. This makes it suitable for use in disease diagnosis based on exhaled breath analysis along with conventional applications in monitoring of environment for hazardous gas alert. The sensor has been fabricated by using cost effective chemical processing that is compatible with wafer level processing. Based on model analysis by simulation of the $I - V$ data before and after exposure to gas we could identify the changes in electrical parameter that leads to sensing. We proposed a simple gas sensing mechanism stated above. We observe that the ZnO/p-Si NWs p-n heterostructure leads to a synergetic enhancement of the gas sensing which is more than the sum total of responses of the individual components, namely the ZnO and the p-Si NWs.

5.6 Technological aspect

In this thesis work, we have fabricated innovatively a ZnO/Silicon nanowires (ZnO/Si NWs) heterojunction arrays based nitric oxide (NO) gas sensor that can show a calibrated detection capability at least down to 500 ppb (with a noise limited resolution down to 10 ppb) workable at room temperature. NO is also a biologically significant molecule and can be utilized as a primary signalling molecule (present in exhaled breath). However, detection of NO in exhaled breath for diagnosis would need detection capability well below 1 ppm. Thus, a portable NO unheated gas sensor that can reach sub-ppm capability of detection and can be fabricated

without use of costly fabrication facilities will be of high utility. The sensor reported here meets these criteria. This experimental observation/understanding as well as ingenious use of ZnO/p-Si NWs heterojunction is indeed a major advancement towards utilization of the sensor in exhaled breath analysis for non-invasive diagnosis of certain pulmonary diseases such as asthma, bronchitis, airflow limitation leading and chronic obstructive pulmonary disease (COPD). The innovation of room temperature sensing device may push forward the integration of gas sensing element with wireless device and that can be connected to others Internet of Things (IOT) platforms. This proof of concept has been patented (Patent reference no: *201731038036*) and activities related to packaging of prototype/product are in the final stage of processing. This work has been done under DST sponsored Project; TRC (Technical Research Centre).

5.6.1 Name of the Product/Prototype/Activity

A gas sensing system for selective detection of nitric oxide (NO) gas at room temperature.

Name of prototype: "**NOsense"**

5.6.2 Objectives

The present invention discloses a room-temperature operable, hand-held ZnO/p-Si NWs nitric oxide (NO) gas sensing system and a method for ingenious use of ZnO/p-Si NWs heterojunction. The present invention relates a quick and cheap methods for detection of hazardous gases in work places. The present invention is particularly adapted to exhibit long-lasting reusability, stability and perform the NO gas detection at room temperature and even in an open environment with extremely high sensitivity at least down to 500 ppb. Noise limited sensing resolution down to tens of ppb, in this invention, is indeed a major advancement towards utilization of the sensor in exhaled breath analysis for non-invasive diagnosis of certain pulmonary diseases such as asthma, bronchitis, airflow limitation leading and chronic obstructive pulmonary disease (COPD). The cost-effective fabrication of the sensor from Si wafers and ZnO by simple chemical processing and need of around few µW powers for its operation makes it viable for large scale use and cloud compatibility. The innovation of room temperature sensing materials may push forward the integration of gas sensing element with wireless device and can be connected to others Internet of Things (IOT) platforms.

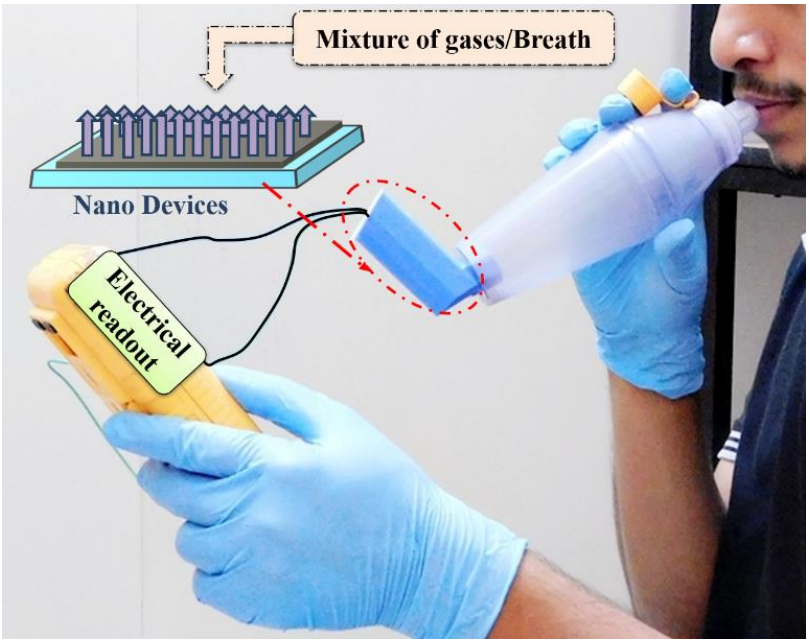

Figure 5.P A pictorial representation of the "**NOsense"** prototype use in exhaled breath analysis.

5.6.3 Salient features

- ✓ Low projected cost and easy read out with remote access through WiFi and wireless technology.
- ✓ Uses easily available materials and innovative use of new nano-materials.
- ✓ Portable readout devices.
- ✓ Room temperature operation and low power consumption.
- ✓ Good selectivity and high sensitivity (< 1ppm).
- ✓ Easy production method and does not need costly capital investment.

- **Present status (Name of the company, in case of transfer of technology)**

Finalizing the packaging of the prototype and cost calculation for transferring the technology is under process.

Patent*:** S. Maithani, **C. Samanta**, A. Maity, K. Das, M. Pradhan, B. Ghosh, and A. K. Raychaudhuri, "A gas-sensing system for selective detection of (nitric oxide) NO gas and a method for fabricating the same." **(*Indian Patent Filed No. *201731038036A* dated: 10/11/2017).

Publication: Chandan Samanta, Ankita Ghatak, A K Raychaudhuri and Barnali Ghosh, "ZnO/Si nanowires heterojunction array based nitric Oxide (NO) gas sensor with noise limited detectivity approaching 10 ppb." *Nanotechnology*, **30**, 305501 (2019).

Bibliography

1. T. Seiyama, A. Kato, K. Fujiishi, and M. Nagatani, *Anal. Chem.*, **34**, 1502 (1962).
2. G. F. Fine, L. M. Cavanagh, A. Afonja, and R. Binions, *Sensors*, **10**, 5469 (2010).
3. I. Elmi, S. Zampolli, E. Cozzani, F. Mancarella, and G. C. Cardinali, *Sens. Actuat. B*, **135**, 342 (2008).
4. Y. Guo, X. W. Zhang, and G. R. Han, *Mater. Sci. Eng.: B*, **135**, 83 (2006).
5. A. Gurlo, N. Barsan, M. Ivanovskaya, U. Weimar, and W. Gopel, *Sens. Actuat. B*, **47**, 92 (1998).
6. T. Kida, A. Nishiyama, M. Yuasa, K. Shimanoe, and N. Yamazoe, *Sens. Actuat. B*, **135**, 568 (2009).
7. D. E. Williams, *Sens. Actuat. B*, **57**, 1 (1999).
8. M. M. Arafat, B. Dinan, S. A. Akbar, and A. S. M. A. Haseeb, *Sensors*, **12**, 7207 (2012).
9. M. Righettoni, A. Tricoli, and S. E. Pratsinis, *Anal. Chem.*, **82**, 3581 (2010).
10. A. Rydosz, *Sensors*, **18**, 2298 (2018).
11. Z. Jing and J. Zhan, *Adv. Mater*., **20**, 4547 (2008).
12. S. Agarwal, P. Rai, E. N. Gatell, E. Llobet, F. Guell, M. Kumar, and K. Awasthi, *Sens. Actuators B*, **292**, 24 (2019).
13. V. Postica et. al., *Adv. Funct. Mater*., **27**, 1604676 (2017).
14. M. Navaneethan, V. L. Patil, S. Ponnusamy, C. Muthamizhchelvan, S. Kawasaki, P. S. Patil, and Y Hayakawa, *Sens. Actuators B*, **255**, 672 (2018).
15. K. Shingange, Z. P. Tshabalala, O. M. Ntwaeaborwa, D. E. Motaung, and G. H. Mhlongo, *J. Colloid Interface Sci*., **479**, 127 (2016).
16. S. W. Fan, A. K. Srivastava, and V. P. Dravid, *Appl. Phys. Lett*., **95**, 142106 (2009).
17. L. D. Bastatas, P. Wagle, E. Echeverria, A. J. Austin, D. N. McIlroy, *Materials*, **12**, 302 (2019).
18. Q. Zhang, G. Xie, M. Xu, Y. Su, H. Tai, H. Du, and Y. Jiang, *Sens. Actuators B*, **259**, 269 (2018).
19. J. Wang, S. Fan, Y. Xia, C. Yang, and S. Komarneni, *J. Hazard. Mater*., **381**, 120919 (2019).
20. Y. Kang, F. Yu, L. Zhang, W. Wang, L. Chen, and Y. Li, *Solid State Ionics*, **360**, 115544 (2021).
21. H. Naderi, S. Hajati, M. Ghaedi, J. P. Espinos, *Sens. Actuators B*, **297**, 126774 (2019).
22. S. Tata, L. Chabane, N. Zebbar, M. Trari, M. Kechouane, and A. Rahal, *Mater. Sci. Semicond. Process*., **109**, 104926 (2020).
23. P. Srinivasan and B. G. Jeyaprakash, *J. Alloys Compd*., **768**, 1016 (2018).
24. N. Han, G. Pan, J. Zheng, R. Wang, and Y. Wang, Mater. Res., **22**, 1 (2019).
25. S. Ozturk, N. Kılınç, N. Taşaltin, and Z. Z. Ozturk, *Thin Solid Films*, **520**, 932 (2011).
26. H. H. Lu, C. Y. Lin, T. C. Hsiao, Y. Y. Fange, K. C. Ho, D. Yang, C. K. Lee, S. M. Hsu, and C. W. Lin, *Analytica. Chimica. Acta.*, **640**, 68 (2009).
27. F. L. Meng, Z. Guo, and X. J. Huang, *Trends Anal. Chem*., **68**, 37 (2015).
28. A. Shimizu, M. T. Tsubasa, T. Yamaguchi, and K. Hara, *Sensors and Materials*, **30**, 1123 (2018).

29. L. Boarino, C. Baratto, F. Geobaldo, G. Amato, E. Comini, A.M. Rossi, G. Faglia, G. Lerondel, and G. Sberveglieri, *Mater. Sci. Eng. B*, **69**, 210 (2010).
30. M. Cuscunà, A. Convertino, E. Zampetti, A. Macagnano, A. Pecora, G. Fortunato, L. Felisari, G. Nicotra, C. Spinella, and F. Martelli, *Appl. Phys. Lett.*, **101**, 103101 (2012).
31. H. H. Li, C. E. Yang, C. C. Kei, C. Y. Su, W. S. Dai, J. K. Tseng, P. O. Yang, J. C. Chou, and H. C. Cheng, *Thin Solid Films*, **529**, 173 (2013).
32. D. Liu, L. Lin, Q. Chen, H. Zhou, and J. Wu, *ACS Sens*. **2**, 1491 (2017).
33. J, Liao, Z. Li, G. Wang, C. Chen, S. Lv, and M. Li, *Phys.Chem.Chem.Phys.*, **18**, 4835 (2016).
34. F. L. M. Ricciardolo, P. J. Sterk, B. Gaston, and G. Folkerts, *Physiol Rev*., **84**, 731 (2004).
35. S. Maithani, C. Samanta, A. Maity, K. Das, M. Pradhan, B. Ghosh, and A. K. Raychaudhuri, Indian Patent Filed No. 201731038036 dated: 10/11/2017.
36. C. Samanta, A. Ghatak, A. K. Raychaudhuri, and B. Ghosh, *Nanotechnology*, **30**, 305501 (2019).
37. B. Yuliarto, M. F. Ramadhani, Wieno H and Nugraha, *Int. J. Mater. Sci. Eng*. **2**, 15 (2014).
38. K. Q. Peng, X. Wang, and S. T. Lee, *Appl. Phys. Lett*., **95**, 243112 (2009).

Chapter 6

Induction of charge carrier by field effect using electric double layer (EDL) gate

In this chapter, we have investigated the electrical characteristics of electric double layer (EDL) thin film transistor with doped ZnO (amorphous indium gallium zinc oxide) channel on flexible substrate. In the previous chapter 4 and 5 we have demonstrated the tuning the charge carriers by the effects of photo-gating in optoelectronic studies and by gas injection in the heterojunction respectively to understand the charge carrier transport phenomena in oxide heterostructures. In this chapter, we would like to explore how one can tune the charge carriers in oxide semiconductor by field effect using electric double layer (EDL) gate. Here, we have shown the charge carrier induction through EDL as a gate dielectric (a solid polymer electrolyte) formed the EDL gate capacitance at oxide/electrolyte interface induces an ultra-high charge carrier density on the surface of the channel. This high carrier density yielded high value of saturation mobility μ_{sat} *~ 42* cm^2/Vs*, good ON/OFF ratio of ~*10^5*, and low threshold voltage of ~ 0.7 V due to influence of high value of EDL gate capacitance of polymer electrolyte. This experimental observation/ understanding as well as invention leads to a very good contribution to flexible electronics with a very good technological application potential. This proof of concept has been patented.*

6.1 Introduction

The hydrogenated amorphous silicon (a-Si:H) is the conventional semiconductor for large area electronics application mainly in thin film transistor (TFT) which is used in backplane of display technology [1]. But its low carrier mobility (0.5-1.0 cm^2/V-s), optical opacity, poor current-carrying capacity and modest mechanical flexibility are present challenges for future electronics technology. Among the state-of-the-art flexible TFT technologies, metal oxide semiconductors (MOSs), especially the amorphous one, are promising candidate, owing to their unique properties such as excellent carrier mobility even in amorphous state, high electrical conductivity, high optical transparency in visible as well as near-infrared region and large area uniform deposition at low temperature [2-4]. Large varieties of semiconductor materials such as indium oxide (In_2O_3), zinc oxide (ZnO), and tin oxide (SnO_2) have been reported in TFTs technology [5-7]. In recent years capability to grow oxide semiconductors at low processing temperature on flexible substrates has given a boost to the general area of oxide electronics [8-9].

An important turning point in oxide TFT including research as well as its application, is the use of amorphous IGZO as a channel material in the class of both in flexible as well as non-flexible display units by using of respectively conventional (HfO_2, SiO_2 etc) and non-conventional dielectric mainly ion gel, polymer electrolyte etc [10-14]. The first flexible TFT with IGZO channel grown on polyethylene terephthalate (PET) with conventional oxide Y_2O_3 as gate dielectric showed a saturation mobility (μ_{sat}) ~ 6 - 9 cm^2/V-s, with current ON/OFF ratio ~ 10^3 and threshold voltage (V_{th}) ~ 1.6 V [10]. The mobility observed is well in excess of that observed in organic semiconductors used in flexible electronics [15]. Another work of IGZO based flexible TFT was made on paper substrate and used conventional SiO_x as gate dielectric. The TFT exhibited μ_{sat} of 1.2 cm^2/Vs, current on-off ratio 10^4 and V_{th} of ~ 1.9 V [16]. While Si based material like hydrogenated amorphous Si (a-Si:H) and silicon carbide (SiC) are used for TFT applications on hard substrates, they don't show much promise in applications in flexible electronics, particularly for poor mobility and high processing temperatures [17-18]. The conventional oxide gate dielectrics used in FET device have low charge accumulation capacity due to their low value of specific gate capacitances in the order of ≈ nF/cm^2 and the value of gate capacitance is limited by their thickness. So, the conventional oxide gate dielectric unable to modulate such high value of charge carriers appropriately which also justify the need of the electric double layer (EDL) gate dielectric in a metal oxide FET

device. The modulation of charge carriers by using electric double layer (EDL) gate dielectric in a field effect transistor (FET) device has recently emerged as a strong tool for electrostatic modulation of electronic states in solids [19-20]. The key feature in electric double-layer transistor is the formation of electric double layers based on electrolytes such as ionic liquids and polymer electrolytes with mobile charges which induces an ultra-high charge carrier density on the surface of the channel. The electric double layer (EDL) interface act as a nanogap capacitor with a huge specific gate capacitance can induce a large charge carrier density at low operation voltage resulting in remarkable progresses in high performance EDL transistors [21]. The choice of gate dielectric and the interface of semiconductor channel and dielectric layer are crucial for device performances. Materials with a high dielectric constant (high- κ) are preferable because this increased capacitance induces high charge carrier density, decreasing the subthreshold swing (SS) and threshold voltage (V_{th}). But most of the high κ dielectrics can degrade the performance and stability of oxide TFTs because of their polycrystalline structure and rough surface, since grain boundaries act as favourable paths for impurities diffusion and leakage current and degraded interface properties. In the present investigation the most important component is the use of electrolyte as gate dielectric on a semiconductor channel at room temperature and there is no need of vacuum, unlike conventional oxide gate dielectrics where deposition of gate dielectric requires a high vacuum and often high temperature [22]. The process of low temperature method to make the gate dielectric has natural compatibility with the flexible substrate and thus obviating the need to have a high temperature process which has fundamental incompatibility to flexible electronics. There are some reports of IGZO based TFT made of non-conventional gate dielectric particularly ionic liquid or ion gel or polymer electrolyte. However, they have all been fabricated on non-flexible quartz substrates [23]. There are reports of IGZO TFT made on flexible polyamide or paper substrate by using conventional gate dielectric i.e., Al_2O_3, SiN_x or SiO_x relatively higher processing temperature comparable to present work. These reports are summarized for comparison in Table 6.2 later. But there is no report of a-IGZO TFT made on flexible substrates by using of polymer electrolyte or ionic liquid as gate. A first report of a flexible TFT using EDL as gate dielectric and PLD grown ZnO on polyimide as channel was done by our group before [24]. In this present work, the metal oxide channel a-IGZO was deposited at a relatively lower temperature of range (100-120) ^oC using pulsed laser deposition (PLD) technique. The condensation of the ablated target species on flexible substrate gives a carbon free amorphous metal oxide channel at low temperature of growth. The high performance of a-IGZO TFTs was achieved using a solid polymer electrolyte as a gate dielectric which induces an ultra-high charge carrier density

on the surface of the channel. This experimental observation/understanding as well as invention leads to a very good contribution to flexible electronics with a very good technological application potential. This proof of concept has been patented (Patent reference no: *201731015268*) and activities related to packaging of prototype/product are in the final stage of processing [25].

6.2 Experimental processes

6.2.1 Fabrication of thin film transistor (TFT)

In the device fabrication process, first amorphous indium gallium zinc oxide (a-IGZO) channel is deposited on flexible polyimide substrate (Kapton ® tape) by pulsed laser deposition (PLD) method. The details of deposition processes have been given in chapter 2. The film has been characterized by X-ray diffraction (XRD), atomic force microscopy (AFM) and Scanning Electron Microscopy (SEM). The thickness of the film used is around 295 nm as determined from ellipsometry as well as cross sectional scanning electron microscopy (SEM). Figure 6.1(a) shows the AFM image taken in Lateral Force Microscopy (LFM) mode, which shows a dense growth pattern of the IGZO film with nanoscopic grains. The rms surface roughness of the film is ≈ 1 nm. The inset of Figure 6.1 (a) shows the cross-sectional SEM images of the IGZO film. Figure 6.1 (b) shows the XRD data that establishes the amorphous nature of the IGZO film grown on the Kapton tape.

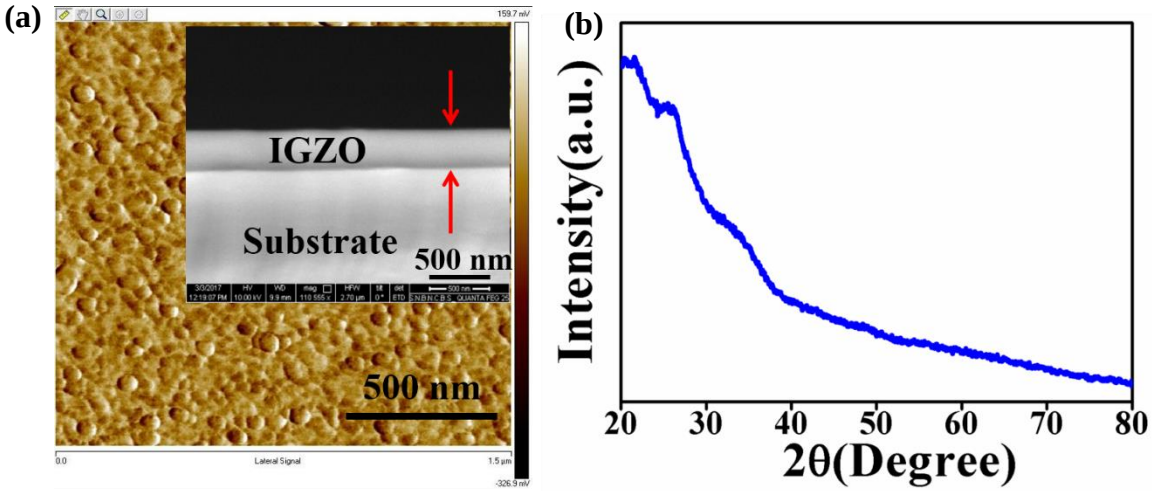

Figure 6.1 (a) Lateral force microscopy (LFM). Inset is the cross-sectional SEM of a-IGZO channel. (b) XRD of a- IGZO channel deposited on Kapton.

After deposition of a-IGZO channel it is patterned and Au/Cr contact pads act as source (S) and drain (D) as well as gate (G) electrodes are deposited by thermal evaporation method through stencil mask. Then the electrolyte is patterned on that by drop casting and spin coating.

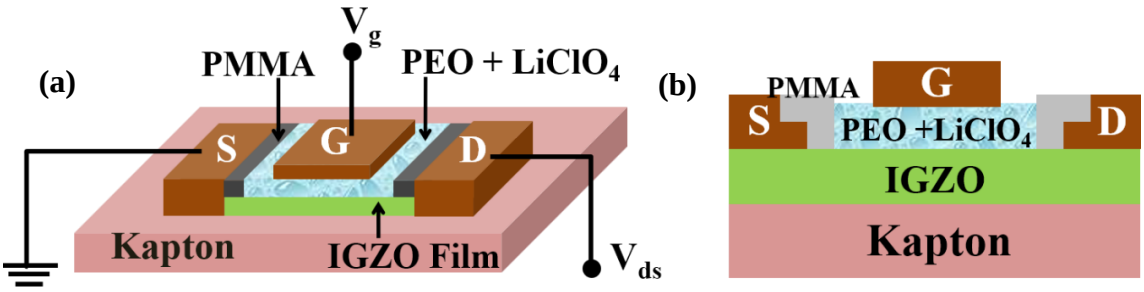

Figure 6.2 (a) A schematic of Flexible TFT composed of a kapton substrate, source, drain and gate Au/Cr electrode patterns, an amorphous IGZO semiconducting channel and polymer electrolyte (PEO + $LiClO_4$) as gate dielectric and PMMA layer for electrical isolation. (b) Schematic diagram of the cross-section of the device.

In the top gate TFT device structure, shown in Figure 6.2 (a), the a-IGZO and the polymer electrolyte (PEO+$LiClO_4$) serve as the channel and gate dielectric layer respectively. The ratio of width and length (W/L) of active channel of IGZO is fixed as 1:3. The gate dielectric was prepared from a gel containing 10:1 weight ratio of polyethylene oxide (PEO) and $LiClO_4$, which was deposited on the a-IGZO channel at room temperature by spin coating / drop casting. The S and D metal electrodes were protected from the electrolytes by a layer of poly(methyl methacrylate) (PMMA). This protection by PMMA reduced the gate leakage current significantly and the ratio of drain to gate current > 10^3. The schematic diagram of the cross section of the device is shown in the Figure 6.2 (b). The electrical measurements were done at room temperature using source-meters (Keithley 2410).

6.3 Experimental results

6.3.1 Electrical characteristics of flexible thin film transistor

Figure 6.3 (a) shows the variation of drain current (I_d) with gate voltage (V_g) transfer characteristic i.e. (I_d vs. V_g) of the a-IGZO TFT with EDL gate dielectric in forward sweep from -2.5 V to 3 V and reverse sweep from 3 V to -2.5 V at constant drain to source voltage (V_{ds} = 1V). Transfer curve observed here showed less hysteresis that favoured a smaller number of charge carrier trapping at the interfaces of the gate dielectric and semiconductor channel [26]. The drain current (I_d) increases with increasing positive gate voltage (V_g), which is expected of a TFT with an n-type channel. I_d starts to saturate nearly to 0.2 mA for $V_g \geq V_{th}$ and at this stage device act as n-type enhancement mode transistor and surface of the semiconductor that had a depleted region gain n-type behaviour because of higher surface electron density than hole density.

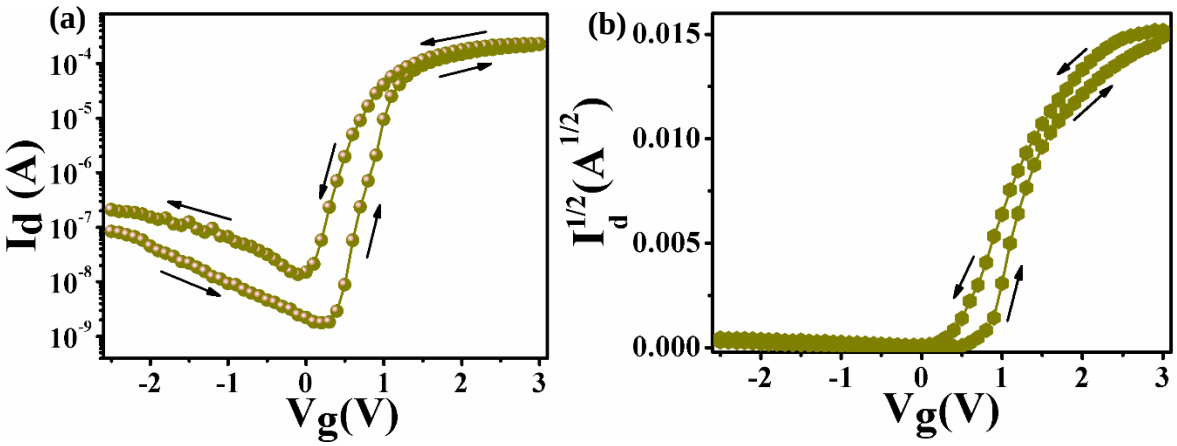

Figure 6.3 (a)Transfer characteristic curve (I_d vs. V_g) at V_{ds} = 1V. (b) Square-root of the channel current with gate voltage (($\sqrt{I_d}$ vs. V_g) for calculation of mobility of the a-IGZO TFT.

Figure 6.3 (b) shows the variation square-root of the channel current with gate voltage ($\sqrt{I_d}$ vs. V_g) for calculation of saturation mobility and threshold voltage of the device. In the data shown in Figure 6.3 (a) and 6.3 (b) the current ON/OFF ratio is 10^5 and the threshold voltage V_{th} = 0.7 V. We have tested a number of devices made in similar fashion and obtained current ON/OFF ratio in the range 10^4-10^5 and V_{th} in the range ≈ 0.7- 0.8 V. Important parameters obtained from the data are given in Table 6.1. Another important performance parameter of the TFT is the subthreshold swing (SS) defined as $SS = [\frac{\mathrm{d}(\log I_d)}{\mathrm{d}V_g}|_{max}]^{-1}$, which has been calculated from the transfer curve for $V \leq V_{th}$ [26]. For the device, the value of SS and current ON/OFF ratio are ≈ 175 mV/dec and ~ 10^5 respectively which is better than other type of oxide semiconductor especially for amorphous oxide semiconductor made on flexible substrates.

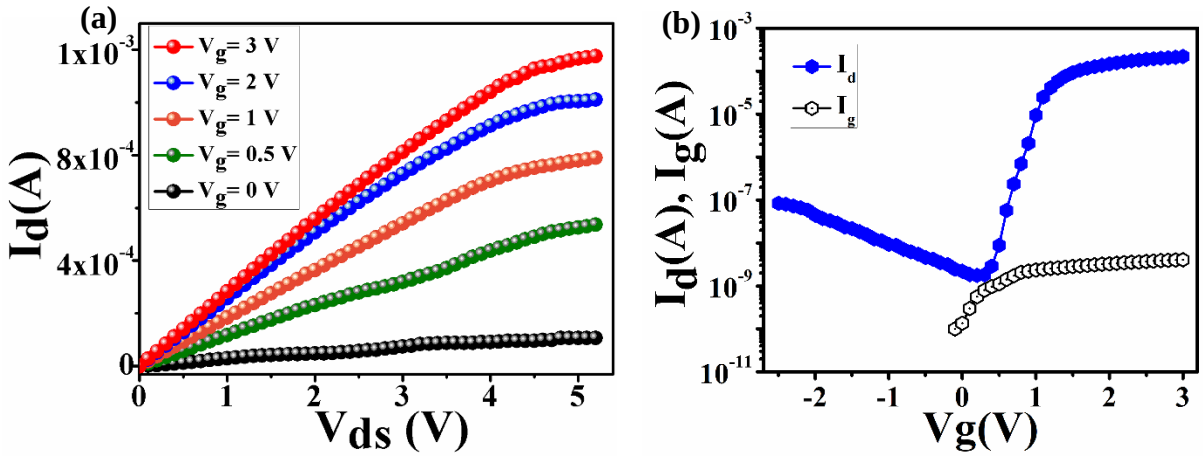

Figure 6.4 (a) Output characteristic (I_d vs. V_{ds}) of the a-IGZO TFT with different gate bias. (b) Variation of drain current (I_d) and gate leakage current (I_g) with the gate voltage.

The output characteristic i.e., the variation of I_d with V_{ds} is shown in Figure 6.4 (a) with fixed different gate bias (V_g) ranging from 0 V to 3 V. The output characteristics show a regular

behaviour expected of a TFT. Another important parameter of transistor is the value of gate current for determination of quality of gate dielectric. The Figure 6.4 (b) shows the variation of drain (I_d) and gate current (I_g) with the gate voltage (V_g) and at lower gate voltage the value of gate current, I_g is order of 10^{-11} A.

Table 6.1 Electrical characteristic of a-IGZO TFT with EDL gate dielectric.

Device	**Capacitance (μF/cm²)**	μ_{sat} **(cm²/Vs)**	μ_{FE} **(cm²/Vs)**	V_{th} **(V)**	SS **(mV/dec)**	**I_{ON}/I_{OFF} ratio**
IGZO TFT	31 ± 3.5	39.3 ± 1.8	17.4 ± 1.6	0.7 ± 0.04	180 ± 5	10^4 ~10^5

6.4 Discussions

6.4.1 Carrier mobility

The performance of a TFT depends on the quality of the channel that it can give rise to high carrier mobilities. The saturation mobility (μ_{sat}) and field effect mobility (μ_{FE}) of the carriers in the channel and the threshold voltage V_{th} of the TFT have been calculated using the following conventional equations [28]:

$$I_d^{1/2} = \left(\frac{C_g W \mu_{sat}}{2L}\right)^{\frac{1}{2}} (V_g - V_{th}) \qquad (6.1)$$

$$\mu_{FE} = \frac{g_m}{C_g \frac{W}{L} V_{ds}} \qquad (6.2)$$

Where L and W are the length and width of the device respectively, C_g is the specific gate capacitance and $g_m = \frac{\partial I_d}{\partial V_g}$, is the mutual conduction or transfer conduction that depends on gate voltage (V_g). Figure 6.5 (a) shows the variation of mutual conduction (g_m) with gate bias. The value of g_m starts to increase at threshold voltage (V_{th}) and then rolls off at larger gate bias when variation of I_d with V_g starts to saturate. There is yet another effective mobility (μ_{eff}) that depends on V_g which can be obtained from output characteristics and defined as:

$$\mu_{eff} = \frac{g_D}{C_g \frac{W}{L} (V_g - V_{th})} \qquad (6.3)$$

Where conduction, $g_D (= \frac{\partial I_d}{\partial V_{ds}})$ obtained from the output characteristics curve with low V_{ds} at a fixed gate voltage (V_g). Figure 6.5 (b) represents the variation of effective mobility (μ_{eff}) of

the device with the gate voltage. At low V_g, the μ_{eff} is large and its value decreases with increasing V_g because of scattering of charge carriers at interface region. The values of carrier mobilities such as saturation (μ_{sat}) and field effect (μ_{FE}) mobility are ≈ 42 cm^2/V-s and 20 cm^2/V-s respectively as obtained from data shown in Figure 6.3 (a) and 6.3 (b). There are few reports of IGZO TFT made on flexible polyamide or paper substrate by using conventional gate dielectric such as Al_2O_3, SiN_x or SiO_x relatively at higher processing temperature. But there is no report of IGZO electric double layer TFT made on flexible substrates by using of polymer electrolyte deposited at room temperature except ours [29]. It can be seen that electrical characteristics i.e., threshold voltage (V_{th}), subthreshold swing (SS) and mobilities are high compared to that seen in many oxide gates [30-34]. A comparison of the devices in our work with other reported flexible IGZO TFTs has been summarized in Table 6.2. As seen in Table 6.2, the performance of the device reported in the present investigation can be seen to be comparable or even better with performance of devices reported that required higher temperature thermal treatment.

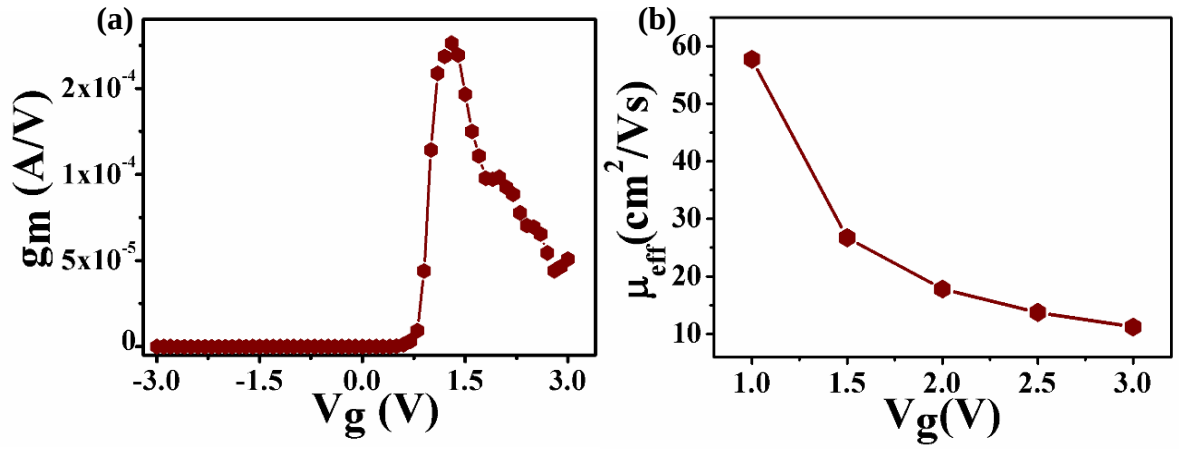

Figure 6.5 (a) Variation of mutual conduction (g_m) with gate voltage (V_g) of the a-IGZO TFT at a fixed V_{ds}. (b) Variation of effective mobility (μ_{eff}) with gate bias.

6.4.2 Charging of EDL gate dielectric

The charging of the polymer electrolyte gate dielectric differs from that in conventional oxide gate dielectrics. The mobile positive Li^+ and negative ClO_4^- charge carriers form electric double layer at the semiconductor/electrolyte interface (shown in Figure 6.6). The concept of electric double layer in electrolyte gated transistor is similar to the electric double layer capacitor. According to Stern model by application of small gate voltage the ions in the electric double layer transistor are aligned near the surface and the charge carriers are accumulated on the surface of the electrodes because of electrostatic potential [35]. As a result, the electric double layer capacitor exhibits very large specific gate capacitance and fast response to the gate

voltage. The electric double layer acts as a nanogap capacitor with a large specific capacitance (~ 30 μF/cm^2) which leads to accumulation of large surface charge density at the interface even at low gate voltage [36]. This leads to large reduction of the threshold voltage (V_{th}) of the device compared to that achievable in TFT's with conventional gate dielectrics.

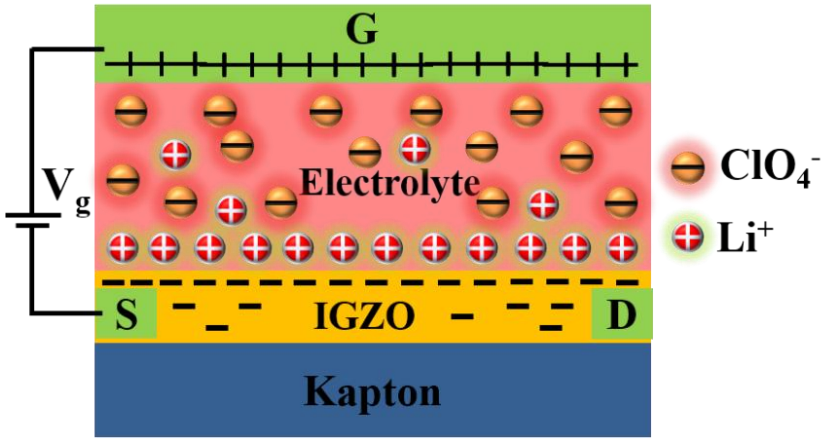

Figure 6.6 Configuration of a-IGZO electric double layer (EDL) transistor.

Table 6.2 Summary of IGZO TFTs prepared on flexible substrates from literature including the device presented in this work.

Channel/ Substrates	Dielectrics	V_{th} (V)	SS (V/dec)	I_{ON}/I_{OFF}	Mobilities (cm^2/V-s)	Maximum processing Temp. (^{o}C)	Ref.
IGZO/ Kapton tape	**Polymer electrolyte**	**0.76**	**0.17**	**10^5**	**μ_{sat} = 42 μ_{FE} = 20**	**120**	**Present work**
IGZO/PET	Y_2O_3	1.6	---	10^3	μ_{sat} = 8	RT	[9]
IGZO/PEN	Al_2O_3	2.5	0.3	10^7	μ_{sat} = 18	RT	[14]
IGZO/Paper	SiO_x	1.9	0.65	10^4	μ_{sat} = 1.2	100	[16]
IGZO/PEN	SiN_x	4.0	0.5	10^7	μ_{FE} = 9.5	150	[30]
IGZO/ PI	PS/PVP	4.0	1.2	10^7	μ_{sat} = 4.5	350	[32]
IGZO/ Parylene	Al_2O_3	- 0.72	0.2	10^6	μ_{FE} = 12.6	150	[33]

Figure 6.7 (a) shows the transient gate current (I_g) when a step change in gate bias of 1V is applied. The gate current is maximum at t = 0 as observed in charging a capacitor and then it

decays with time. The gate resistance R_g has been obtained from the maximum gate I_{gmax} current at t = 0, where maximum gate current is given as $I_{gmax} = V_g/R_g$. Typical R_g ~ 30 MΩ for this device. The charging current decays from the maximum value I_{gmax} and the decay curve can be quantified by two times constants [24]. The dominant components of charging and discharging of transient gate current have a time constant τ_{1g} ~ 30 sec. There is also another component of the transient current that has a relatively smaller time constant of value τ_{2g} = 1~2 sec. The time constant τ_{1g} is associated with dominant component of charging and discharging of the gate capacitance C_g through R_g. From the observed R_g and τ_{1g}, we obtain the value of typical specific gate capacitance ≈ 30 μF/cm^2. An independent measurement of the gate capacitance was obtained as stated. Figure 6.7 (b) shows the variation of specific gate capacitance with applied frequency for metal/electrolyte/metal configuration. The value of the directly measured specific gate capacitance reaches a low frequency limiting value of 25 μF/cm^2, which agrees well with the specific capacitance of 30 μF/cm^2 measured from charging current as mentioned before. The specific capacitance rolls of above few hundred Hz due to ionic nature of the gate dielectric [37].

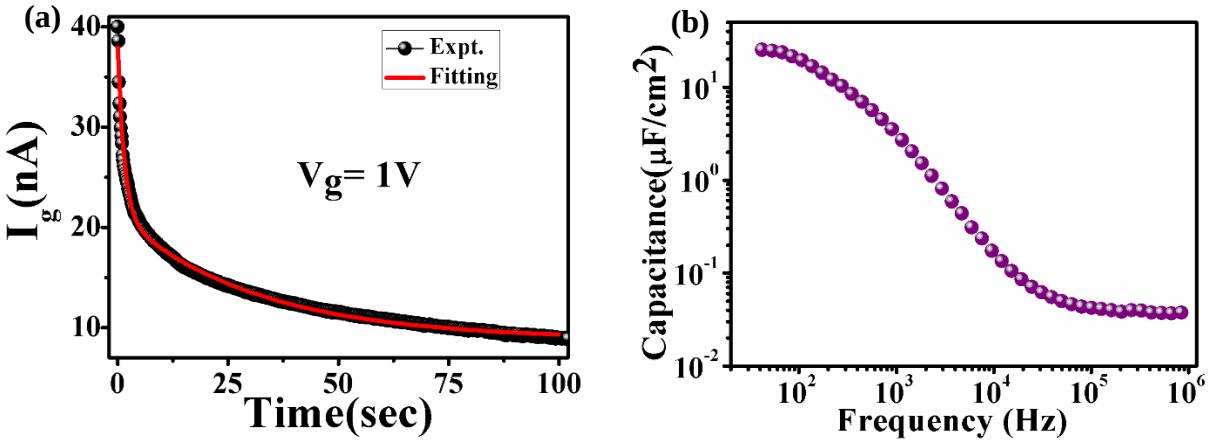

Figure 6.7 (a) Transient response of gate current (I_g vs. t) for the step change in gate bias from 0 V to 1V. Red line is fitted curve. (b) Specific gate capacitance (C_g) as a function of applied frequency.

6.5 TFT device stability and Bending test

Stability of the fabricated TFT is an important issue. We have measured the electrical characteristic of the a-IGZO TFT within period of three to four weeks for device stability. From data in Figure 6.8 (a), no noticeable degradation was noted for threshold voltage (V_{th}), saturation mobility (μ_{sat}) and current ON/OFF ratio within these periods of test. To investigate the flexibility of the IGZO TFT, a set of electrical measurements were carried out under

different bending radius of curvature (see Figure 6.8 (b)). The bending of TFT is such that the channel is under tensile stress.

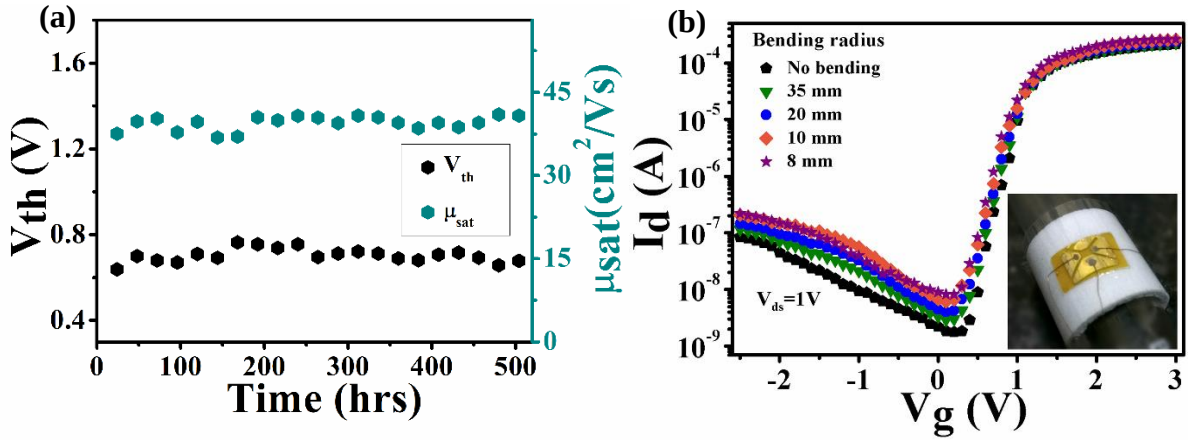

Figure 6.8 (a) Stability testing within period of three weeks. (b) Transfer characteristics of a-IGZO flexible-TFT under different radius of curvature with constant drain bias V_{ds} = 1V. Inset shows the measurement technique under bend condition.

The device was found to show stable and reversible characteristics down to a radius of curvature ~ 15 mm (Table 6.3). For the bending radius down to less than 10 mm the saturation mobility (μ_{sat}) and threshold voltage (V_{th}) does not show noticeable changes in their value but the current on-off ratio of the device is decreased by one order of magnitude because of defects generation in the interface between channel and electrolyte due the strain of the channel.

Table 6.3 Change in device performances with bending radius.

Bending radius (mm)	**μ_{sat} (cm^2/Vs)**	**V_{th} (V)**	**ON/OFF ratio**	***SS* (mV/dec)**
No bending	42	0.72	10^5	176
35 mm	41	0.69	10^5	175
20 mm	40	0.65	10^5	172
10 mm	39	0.67	10^4	180
8 mm	38	0.70	10^4	185

6.6 Conclusion

In summary, we demonstrated fabrication of high performance flexible thin film transistor on flexible Kapton substrate using amorphous IGZO as a channel material and polymer electrolyte (PEO+$LiClO_4$) as gate dielectric. Tis solid polymer electrolyte as a gate dielectric formed the EDL gate capacitance at oxide/electrolyte interface with large specific gate capacitance (≈ μF/cm^2) which induces an ultra-high charge carrier density on the surface of the channel and

this high value of EDL gate capacitance easily modulated the carrier density of oxide semiconductors and device can be operated with low threshold voltage. The electrical characteristics of device exhibit high saturation mobility (μ_{sat}) of ~ 42 cm^2/V-s, good current ON/OFF ratio of 10^5, low threshold voltage (V_{th}) of 0.7 V and low subthreshold swing (SS) of 175 mV/dec. The device has been operated within small voltage (≤ 2 V) because of large specific gate capacitance (≥ 30μF/cm^2) of the EDL gate and leads to large reduction of the threshold voltage (V_{th}) of the device compared to that achievable in TFT's with conventional gate dielectrics. The stable electrical characteristic under different bending stress will make it a useful contribution to flexible electronics.

6.7 Technological aspect

Understanding of charge carrier induction in oxide semiconductor by field effect using electric double layer (EDL) gate has been studied trough several experiments in this thesis work. This experimental observation/ understanding as well as invention leads to a very good contribution to flexible electronics with a very good technological application potential. This proof of concept has been patented (Patent reference no: *201731015268*) and activities related to packaging of prototype/product are in the final stage of processing. This work has been done under DST sponsored Project; TRC (Technical Research Centre).

6.7.1 Name of the Product/Prototype/Activity

A flexible electric double layer thin film transistor for wearable and stretchable electronic devices.

Name of prototype: "**EDLFlex-TFT"**

6.7.2 Objectives

The present invention discloses a high performance flexible thin film transistor (referred as Flex-TFT) based on oxide semiconductors using electric double layer (EDL) as gate dielectric. High performance Flex-TFT is a key component for future electronics technology particularly for wearable and stretchable electronic devices. Flex-TFT can be fabricated on any of commonly available flexible substrate that include polymeric substrates, biodegradable papers and cloths that have cellulose content using functional oxide materials (such as ZnO and IGZO) as a semiconducting material. The functional materials mentioned above are examples and are not exhaustive. The dielectrics such as polymeric electrolytes, ionic gels etc. used as the electric double layer gate in this Flex TFT, enables the transistor performances at low voltage operation but also retains the mechanical flexibility and high optical transparency. The voltage operation

is particularly useful in such platforms like mobiles and wireless usage and in such operation where use of a high voltage for the TFT operation may become detrimental to its use.

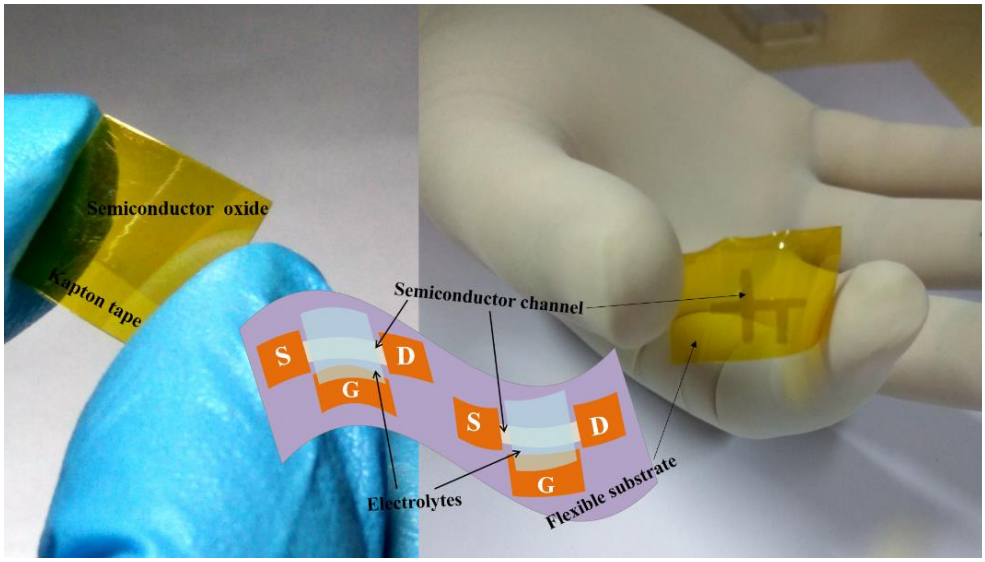

Figure 6.P Digital camera images and schematic diagram of EDL Flexible-TFT under different bending conditions.

6.7.3 Salient Features

- ✓ Innovative use of earth abundant materials.
- ✓ Uses commonly available biodegradable flexible substrates like papers, cloths etc, flexible polymers.
- ✓ Use of Low temperature deposited dielectrics.
- ✓ Very small subthreshold swing (*SS*) that ensures a sharp switching in TFT.
- ✓ Considerable mechanical flexibility and high optical transparency.
- ✓ Easy production method and does not need costly capital investment.

- **Present Status (Name of the company, in case of transfer of technology)**

Prototype is under final stage of processing and transfer of technology is under process through National Research Development Corporation (NRDC).

***Patent*: R. Ghimire, C. Samanta**, B. Ghosh, and A. K. Raychaudhuri, "Flexible thin film transistor using electric double layer as gate dielectric and a method of fabricating thereof." **(*Indian Patent Filed No. 201731015268* dated: 09/06/2017).**

***Publication:* C. Samanta**, R. R. Ghimire, and B. Ghosh, "Fabrication of Amorphous Indium–Gallium–Zinc–Oxide Thin-Film Transistor on Flexible Substrate Using a Polymer Electrolyte as Gate Dielectric." *IEEE Trans. Electron Devices*, **65**, 2827, (2018).

Bibliography

1. W. Spear and P. L. Comber, *Solid State Commun.*, **17,** 1193 (1975).
2. T. Kamiya, K. Nomura, and H. Hosono, *J. Disp. Technol*., **5**, 468 (2009).
3. X. Yu, T. J. Marks, and A. Facchetti, *Nature Mater*, 15, 383 (2016).
4. S. D. Brotherton, "Introduction to Thin Film Transistors: Physics and Technology of TFTs," *Springer international publishing*, 2013.
5. R. Hoffman, B. J. Norris, and J. Wager, *Appl. Phys. Lett.*, **82,** 733 (2003).
6. R. E. Presley, C. L. Munsee, C. H. Park, D. Hong, J. F. Wager, and D. A. Keszler, *J. Phys. D: Appl. Phys.*, **37,** 2810 (2004).
7. L. Wang, M. H. Yoon, G. Lu, Y. Yang, A. Facchetti, and T. J. Marks, *Nat. Mater.*, **5**, 893 (2006).
8. R. Martins, I. Ferreira, and E. Fortunato, *Phys. Status Solidi RRL*, **5**, 332 (2011
9. D. Gaspar, S. N. Fernandes, A. G. Oliveira, J. G. Fernandes, P. Grey, R. V. Pontes, L. Pereira, R. Martins, M. H. Godinho, and E. Fortunato, *Nanotechnology*, **25**, 094008 (2014).
10. K. Nomura, H. Ohta, A. Takagi, T. Kamiya, M. Hirano, and H. Hosono, *Nature*, **432**, 488 (2004).
11. I. Cunha, R. Barras, P. Grey, D. Gaspar, E. Fortunato, R. Martins, and L. Pereira, *Adv. Funct. Mater*., **27**, 1606755 (2017).
12. M. Benwadih, R. Coppard, K. Bonrad, A. Klyszcz, and D. Vuillaume, *ACS Appl. Mater. Interfaces*, **8**, 34513 (2016).
13. W. Lim, J. H. Jang, S. H. Kim, D. P. Norton, V. Craciun, S. J. Pearton, F. Ren, and H. Shen, *Appl. Phys. Lett*., **93**, 082102 (2008).
14. Z. Zheng, Y. Zeng, R. Yao, Z. Fang, H. Zhang, S. Hu, X. Li, H. Ning, J. Peng, W. Xie, and X. Lu, *J. Mater. Chem. C*, **5**, 7043 (2017).
15. Y.Y. Lin, D. J. Gundlach, S. F. Nelson, and T. N. Jackson, *IEEE. Electron. Device. Lett.*, **44**, 1325 (1997).
16. W. Lim, E. A. Douglas, D. P. Norton, S. J. Pearton, F. Ren, Y. W. Heo, S. Y. Son, and J. H. Yuh, *Appl. Phys. Lett.*, **96**, 053510 (2010).
17. C. Y. Chen and J. Kanicki, *IEEE Electron Device Lett.*, **17**, 9 (1996).
18. G. Han, P. Guo, Y. Yang, C. Zhan, Q. Zhou, and Y. Yeo, *Appl. Phys. Lett.*, **98**, 153502 (2011).
19. H. Du, X. Lin, Z. Xu, and D. Chu, *J. Mater. Sci*., **50**, 5641 (2015).
20. R. R. Ghimire, S. Mondal, and A. K. Raychaudhuri, *J. Appl. Phys*., **117**, 105705 (2015).
21. L. L. Zhang and X. S. Zhao, *Chem. Soc. Rev*., **38**, 2520 (2009).
22. G. Han, P. Guo, Y. Yang, C. Zhan, Q. Zhou, and Y. Yeo, *Appl. Phys. Lett*., **98**, 153502 (2011).
23. M. N. Fujii, Y. Ishikawa, K. Miwa, H. Okada, Y. Uraoka, and S. Ono, *Sci. Rep*., **5**, 18168 (2016).
24. R. R. Ghimire and A. K. Raychaudhuri, *Appl. Phys. Lett*., **110**, 052105 (2017).
25. R. Ghimire, C. Samanta, B. Ghosh, and A. K. Raychaudhuri, Indian Patent Filed No. 201731015268 dated: 09/06/2017.
26. Y. S. Chun, S. Chang, and S. Y. Lee, *Microelectron. Eng*., **88**, 1590 (2011).
27. K. Lee, K. H. Lee, S. Lee, and W. J. Cho, *ACS Appl. Mater. Interfaces*, **6**, 22680 (2014).

28. E. Fortunato, P. Barquinha, and R. Martins, *Adv. Mater*., **24**, 2945 (2012).
29. C. Samanta, R. R. Ghimire, and B. Ghosh, IEEE Trans. Electron Devices, **65**, 2827 (2018).
30. M. J. Park , D. Jeong Y. Ryu, J. H. Yang, J. E. Pi, O. Kwon, G. H. Kim, and C. Yoon, *J. Vac. Sci. Technol*., **33**, 051209 (2015).
31. A. Tari and W. S. Wong, *Appl. Phys. Lett*., 107, 193502 (2015). 30
32. K. C. Ok, S.H. K. Park, C. S. Hwang, H. Kim, H. S. Shin, J. Bae, and J. S. Park, *Appl. Phys. Lett*., **104**, 063508 (2014).
33. M. Benwadih, R. Coppard, K. Bonrad, A. Klyszcz, and D. Vuillaume, *ACS Appl. Mater. Interfaces,* **8**, 34513 (2016). 32
34. W. J. Kang, C. H. Ahn, M. G. Yun, S. W. Cho, Y. K. Kim, D. E. Kim, B. Kim, H. K. Cho, and Y. Kim, *RSC Adv*., **6**, 63418 (2016). 33
35. H. Du, X. Lin, Z. Xu, and D. Chu, *J. Mater. Sci*., **50**, 5641 (2015).
36. W. Cai, X. Ma, J. Zhang, and A. Song, *Materials*, **10**, 429 (2017).
37. H. Yuan, H. Shimotani, J. Ye, S. Yoon, H. Aliah, A. Tsukazaki, M. Kawasaki, and Y. Iwasa, *J. Am. Chem. Soc*., **132**, 18402 (2010).

Chapter 7

Defects control photoconduction of oxide nanostructures in broadband region

In this chapter, we have investigated the role of surface/interface defects on photoconduction mechanism of ZnO/p-Si NWs nanostructures arrays grown by different methods using chemical solution deposition (CSD) and pulsed laser deposition (PLD) methods. In chapter 4, we have discussed how photo-gating effects tunned the charge carriers in broadband photoconduction of ZnO/p-Si NWs arrays decorated with plasmonic Au NPs. In this chapter, we would like to explore how the optical response of ZnO/p-Si NWs photodetectors can also be tuned by changing the surface/interface defects and also how the defects can be tailored by different processing conditions. The photo detection characteristics are investigated under different illumination of light in the broad frequency range from UV (300nm) to NIR (1100nm). We have shown that the photoconduction and photoresponse properties of ZnO/p-Si NWs nanostructures are strongly dependent on the functionality of surface/interface state with different synthesis method where existence of undesired recombination sites can hamper the carrier transport as well as photoconduction. This has been investigated by analysis of oxygen vacancy (V_o) using photoluminescence (PL) and X-ray photoelectron spectroscopy (XPS). The as fabricated pulsed laser deposition (PLD) grown photodetector with lower percentage of chemisorbed O_2 and oxygen vacancies ($V_o s$) exhibits better performance in UV to NIR broadband region because of less scattering/capturing of charge carriers in defect centres of heterostructure.

7.1 Introduction

The role intrinsic defects such as vacancies, self-interstitials, and anti-sites have substantial impact on the functionality of semiconducting materials [1-3]. The defect profiles in semiconductors can be regulated by introducing foreign atoms and several physical-mechanical treatments. Defect-induced trap states play an important role in determining the performances of semiconductor photodetectors. On the other hand, the characteristics of trap states would strongly affect the response or decay time of the photoconductor [4-5]. For an example, as a donor source, the oxygen vacancies play an important role to enhance photoexcited carrier life time, resulting a high photoconductive gain in the system. However, the excessive oxygen vacancies become the recombination center by trapping the photoinduced electrons that recombine with holes [6-7]. The transport of photo-generated charge carriers is facilitated by increased majority carrier concentration without serious recombination with a proper level of the oxygen vacancy. So, the excess defects in the semiconductors could increase the trapping and recombination probabilities of photo-generated charge carries on their way towards electrodes, thus leading to weakened photoresponse. To minimize this inadequacy, it is necessary to adopt exquisite and precise growth methods as well as appropriate post-treatments to fabricate the good quality semiconductor with high crystallinity and moderate defects, so as to increase the efficiency of charge-carrier transport and improve the photoelectric performance. As the characteristics of the photo-generated charge carriers play an indispensable role in the photodetector operation, researchers have proposed several strategies, including modification of light absorption, design of novel heterostructures, utilization of defects engineering, and construction of specific geometries to modulate the charge-carrier behaviours which could pave the way of fabricating suitable photodetectors [8-9]. The photo detection properties of ZnO have been widely investigated due to its peculiar morphology, interesting, complex and varied vacancy states [10-12]. Due to its superior surface morphology depended photosensitivity, the ZnO is mostly studied in 1D form with various modifications such as; decorating with plasmonic nanoparticles such as Al, Ag, Au, etc. [13-14], doping with metals [15-16] and making heterostructures [17-20] to enhance multi-spectral absorbance in visible and UV region, all of which include a variety of defect states in the band gap such as oxygen vacancies ($V_o s$), zinc vacancies (V_{Zn}), oxygen and zinc interstitials (O_i and Zn_i). This defect states are characterised through photoluminescence (PL) spectroscopy. The PL is associated with the carrier recombination emission, in particular, if it is associated with impurity or defect states emission then one can interrelate the interdependence between the

defects and photoconduction of ZnO/p-Si NWs nanostructures with different growth methods. These defects can act as preferential sites for physical/chemical adsorption of environmental species that can introduce additional scattering/capturing of the photo-generated charge carriers that could hamper the performances of photodetector. Therefore, control over surface defects is an important task for utilization of ZnO nanostructured in device applications. Additionally, the photoresponse characteristics of ZnO based photodetector are significantly influenced by a number of factors such as the presence of different amounts of defect concentration, grain size, surface morphology and processing conditions such as annealing treatment/ growth methods etc. These factors could be at interplay to influence the photoresponse characteristics of ZnO based photodetectors. Successful control of the defect density in ZnO nanostructures has been obtained through doping [15-16], modifying growth conditions [21], and annealing [22-24]. Understanding and controlling of defect states and how they affect the electrical and optoelectronic properties of ZnO nanostructures is therefore paramount for the optimization of ZnO-based device architectures. The modulation of defect states has mainly focused on surface/interface treatment with different growth techniques. Growth techniques can control the surface defects but according to state-of-the-art review, it has seen that not much work has been done in order to understand the role of growth techniques in controlling the surface defects. A proper control over the surface/interface defect states is indeed mandatory for practical application of ZnO nanostructures in photodetection.

Previously, in the chapter 4, we have described the photoconduction mechanism of Au NPs decorated ZnO/p-Si NWs core-shell arrays in broadband (300-1100 nm) region and how to extend the response of ZnO/p-Si NWs heterostructure based photodetector beyond its fundamental band gap by exploiting the concept of surface "photo-gating" [25]. In this chapter, we also tried to explore how one can improve the photodetection of oxides heterostructures by covering the range from UV to NIR broadband range by combining the visible and NIR detectability of Si NWs with the UV detectivity of ZnO through ZnO/p-Si NWs nanostructures arrays. It has been done by properly engineering of defect-induced trap states through surface-interface treatment with different growth methods. We have investigated the room temperature optoelectronic properties in the broad frequency range from UV (300nm) to NIR (1100nm) of nanostructures n-ZnO/p-Si NWs heterojunction arrays by different processing methods such as chemical method (CSD) and physical method (PLD). In conjunction with the photoconductivity measurement, first we have made a careful analysis of broad visible emission in the photoluminescence (PL) spectra which is associated with different types of defects. The amount of defects concentration is further confirmed by X-ray Photoelectron

Spectroscopy (XPS) measurement. From the reported studies, it is ensured that for an undoped ZnO photodetector, it is only the multiple scattering or defects that enables the visible response. But the effects of surface/interface defects on photoconduction mechanism of ZnO/p-Si NWs heterojunction arrays have not been explored thoroughly and there is no clear interdependence between the defects and photoconduction of ZnO/p-Si NWs based photodetectors to the best of our knowledge. Here, we have mainly put an effort to explain the effects of the incorporation of defects states in the heterojunctions on the photoresponse of the ZnO/p-Si NWs arrays and a schematic of energy band diagram models have been proposed to explain the transient photocurrent of photodetectors especially in visible and NIR region.

7.2 Experimental methods

The devices are fabricated around a base of vertically aligned Si nanowires (Si NWs) arrays fabricated on a p-type silicon wafer. Then a layer of ZnO is deposited on prefabricated Si NWs arrays by chemical solution deposition (CSD) and pulsed laser deposition (PLD) methods to form ZnO/p-Si NWs nanostructures arrays. Though it has been reported that atomic layer deposition is commonly recommended for the conformal deposition of ZnO nanostructures films with precise thickness and composition [25-26]. But in this work, we have concentrated to make a conformal coating using PLD by optimizing the laser parameter i.e., laser fluence, repetition rate and number of laser shots. The details of fabrication processes have been given in chapter 2. The nanostructured complete devices are studied using cross-sectional TEM as well as energy dispersive X-ray spectroscopy (TEM-EDS) which enables us for understanding of physical structure of the devices. We have also used Photoluminescence (PL) spectroscopy and X-ray Photoelectron Spectroscopy (XPS) through depth profiling to quantify the defects and also to probe the vertical compositions of the oxide heterostructures, which is essential for a better understanding of its optoelectronics properties. Photoresponse measurement was carried out by depositing of two Cr/Au contact pads on ZnO layer in the ZnO/p-Si NWs nanostructures arrays in MSM configuration by thermal evaporation with a channel length and width of 1.5 x 1 mm through a hard mask. The details of experimental work have been given in chapter 3. All measurements were taken at room temperature and under ambient atmospheric conditions.

7.3 Experimental results

7.3.1 Physical structure of ZnO/p-Si NWs nanostructures arrays

In order to establish the physical structure of photo detector, we characterised the sample through the cross sectional TEM along with elemental analysis (EDS). Scanning tunnelling electron microscopy high angle annular dark-field (STEM-HAADF) imaging of the cross-section lamellar of CSD and PLD grown ZnO/p-Si NWs nanostructures arrays are shown in Figure 7.1 (a) and (b) respectively. A composition profile of the CSD and PLD grown ZnO/p-Si NWs nanostructures were obtained by EDS line scan marked by white arrow and the data are shown in Figure 7.1 (c) and (d) respectively. The line scan of the ZnO/Si NWs shows the contents of Zn, Si and O. There is a clear top layer of ZnO (≈ 300 nm) on Si NWs arrays, which is followed by the array of ZnO nanostructured film coated Si NWs and the un-etched substrate in case of CSD grown nanostructure (Figure 7.1 (c)). Whereas, there is a top ZnO layer of same thickness and the core-shell structure of the vertically aligned ZnO/p-Si NWs arrays in case of PLD grown nanostructure (Figure 7.1 (d)).

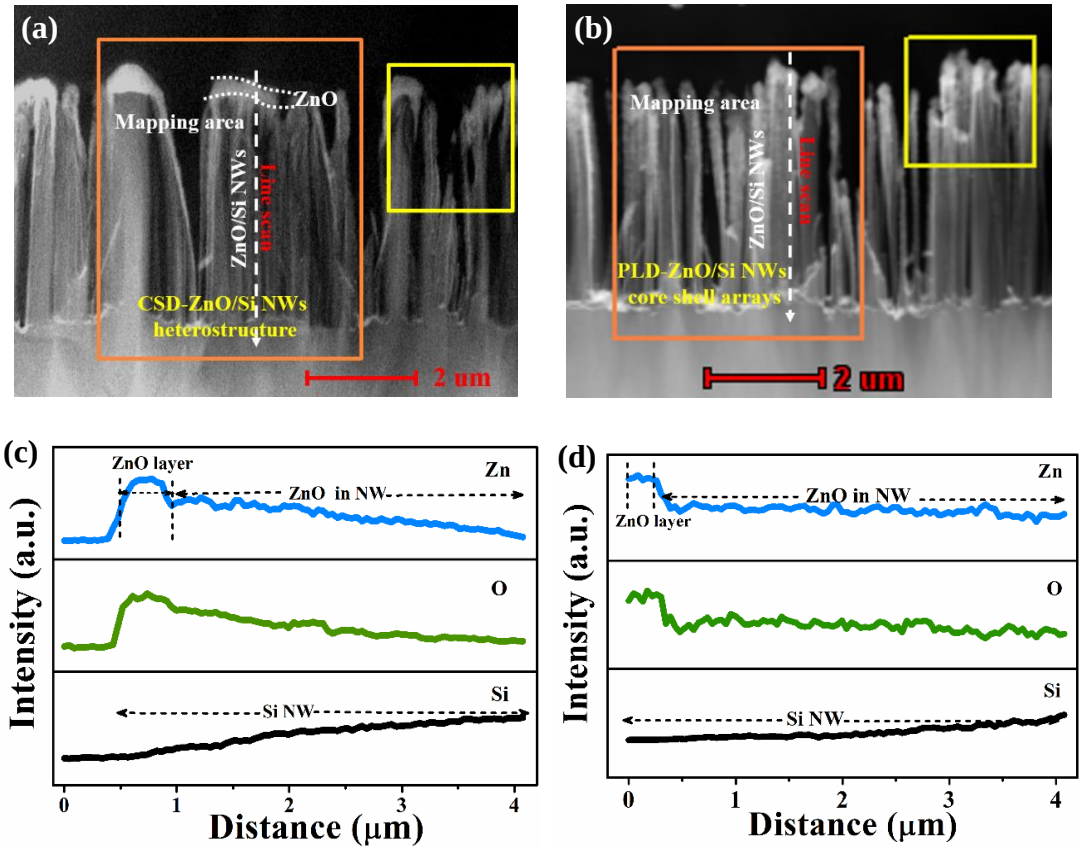

Figure 7.1 (a) Cross-sectional scanning tunnelling electron microscopy high angle annular dark field (STEM-HAADF) images of (a) CSD grown and (b) PLD grown nanostructures arrays. Elemental composition of (c) CSD grown and (d) PLD grown ZnO/p-Si NWs sample taken by EDS line scan showing the chemical composition.

The STEM-EDS mapping for the Zn L shell, O K shell and Si K shell of CSD grown ZnO/p-Si NWs arrays and PLD grown ZnO/p-Si NWs core-shell arrays are shown in Figure 7.2 (a), (b), (c) and (d), (e), (f) respectively. STEM-EDS mapping on a portion of CSD grown ZnO/p-Si NWs nanostructure exhibits a clear top layer of ZnO on Si NWs arrays in Figure 7.2 (a), (b) and (c) for the Zn L shell, O K shell and Si K shell respectively whereas a ZnO layer is fairly uniform and homogeneous throughout the NWs arrays in case of PLD grown ZnO/p-Si NWs core-shell arrays in Figure 7.2 (d), (e) and (f) for the Zn L shell, O K shell and Si K shell respectively.

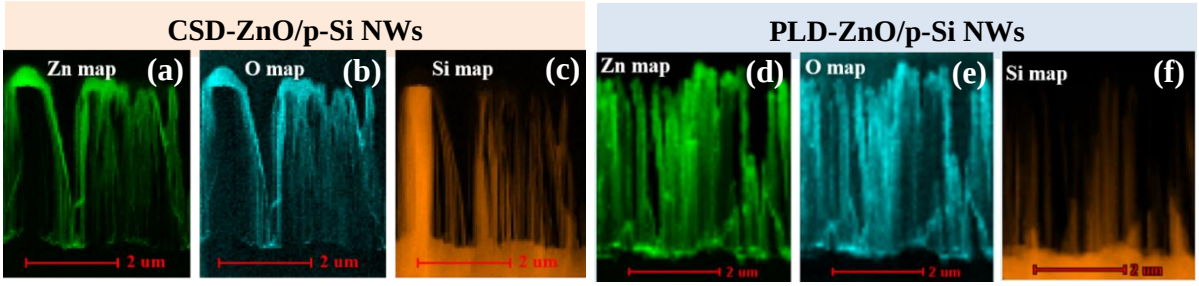

Figure 7.2 STEM-EDS mapping of (a) Zn (L shell), (b) O (K shell), (c) Si (K shell) of CSD grown ZnO/p-Si NWs nanostructure arrays. STEM EDS mapping of (d) Zn (L shell), (e) O (K shell), (f) Si (K shell) of PLD grown ZnO/p-Si NWs core-shell arrays.

7.3.2 Defect study

The electrical conductivity and photosensitivity of oxide semiconductors are strongly dependent upon the concentration of surface/interface defects. The emission/absorption in the UV-visible-NIR region are investigated via analysing of the defects states by studies of photoluminescence (PL) and which is further confirmed by X-ray photoelectron spectroscopy (XPS). To investigate the type of defects and their impact on photoconduction of ZnO/p-Si NWs nanostructures, PL measurements have been carried out. Figure 7.3 (a) shows the room temperature PL spectra of CSD and PLD grown ZnO/p-Si NWs nanostructures arrays for an excitation wavelength of 300 nm. The PL spectra of both the samples exhibit the general feature of ultraviolet (UV) emission centered at ~ 375 nm which is corresponding to the near-band-edge (NBE) transition of wide band gap intrinsic ZnO. In addition to NBE emission there is a broad defects band emission in the range of 430-850 nm. The CSD grown detector demonstrates high intense broad defects band while PLD grown sample exhibits very small defect emission intensity.

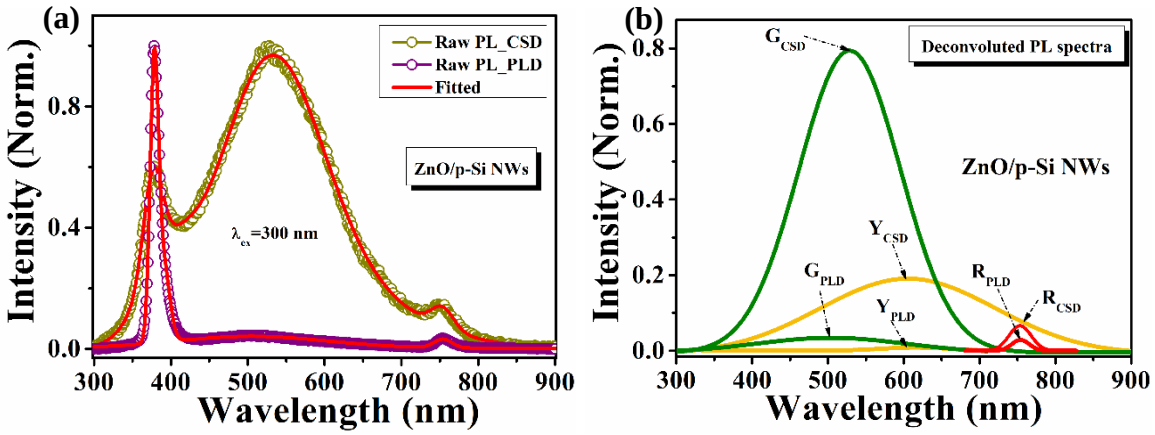

Figure 7.3 (a) Room temperature PL spectra. (b) The broad defects emission resolved in three Gaussian fitting for green defect (G_{CSD} and G_{PLD}), yellow defect (Y_{CSD} and Y_{PLD}) and red defect (R_{CSD} and R_{PLD}) for CSD and PLD grown photodetectors.

The origin of broad defects emission is however controversial and several kinds of defects and vacancies are supposed to be responsible for this emission. The commonly reported defects in ZnO system are oxygen vacancies with different charges (V_o, V_o^+, V_o^{++}), zinc vacancies (V_{Zn}), zinc and oxygen interstitials (Zn_i, O_i), and adsorbed molecules (O_2, H_2O). The broad defects emission in the range of 430-850 nm, which can be readily deconvoluted into different bands named as green defect (G_{CSD} and G_{PLD}), yellow defect (Y_{CSD} and Y_{PLD}) and red defect (R_{CSD} and R_{PLD}) shown in the Figure 7.3 (b). Generally, it is accepted that the origin of green emission is associated with the oxygen related defect states. It is suggested that a non-radiative electron capture from conduction band by a singly charged oxygen vacancy (V_o^+) due to the formation of unstable V_O^+state that recombines with a photoexcited hole in the valance band (V_o→VB), yielding green emission approximately 500-530 nm depending upon the formation energy of V_o states [27-28]. The other possibility of green emission may occur due to transition from conduction band (*CB*) to V_o^+ [29]. All of the transitions have equal possibility to generate the green emissions around 500-530 nm in the PL spectra. The origin of the yellow emission (Y_{CSD} and Y_{PLD}) is commonly attributed to the doubly charged oxygen vacancy (V_O^{++}) and also due to band transition from zinc interstitial (Zn_i) to oxygen interstitial (O_i) [30-31]. The red emissions (R_{CSD} and R_{PLD}) can be attributed to the excess oxygen on the ZnO surface, which depends on annealing, surface modifications and processing conditions [32-33]. A dominant process for this defect emission may be dependent on the concentration of these defects which is further confirmed by XPS analysis.

XPS measurement has also been carried out to investigate the chemical state of O1s in ZnO/p-Si NWs nanostructures to clarify the defects states present in the samples Figure 7.4 (a) and (b) demonstrates high resolution XPS spectra corresponding to O1s core level for CSD and PLD

grown ZnO/p-Si NWs photodetectors respectively. These spectra are fitted with three Gaussian peaks at three binding energy peaks such as lower binding energy peak (LP), middle binding energy peak (MP) and higher binding energy peak (HP). The lower binding energy peak (LP) centered at 530.6 eV is attributed to lattice oxygen (O_L) leads to the hexagonal structure of ZnO lattice and the presence of middle binding energy peak (MP) centered at 530.97 eV for CSD and 530.8 eV for PLD grown ZnO/p-Si NWs photodetectors is ascribed to oxygen vacancies ($V_o s$) in ZnO [34]. The observation of $V_O s$ supports the presence of broad defect emission (mainly green emission) in PL spectra. The higher binding energy peak (HP) centered at 532.2 eV is generally assigned to loosely bound chemisorbed oxygen, such as $-OH$ groups or adsorbed O_2 and H_2O on the surface [29, 35]. Further, the change in the percentage of oxygen content related to each deconvoluted peak is estimated by calculating the change in percentage area of the peaks. From the calculations, we found that the percentage area of oxygen vacancies in CSD grown photodetector is ~32%, whereas in case of PLD grown photodetector it reduces to ~ 15 %. At the same time, the percentage area of the chemisorbed oxygen ~ 47% in CSD decreases to ~ 16 % in PLD grown photodetector. The relative content and peak position of the three kinds of oxygen chemical states are listed in Table 7.1. There is a broadening of MP and HP for CSD grown sample (Figure 7.4 (a)) in comparison with PLD grown sample (Figure 7.4 (b)) due to higher concentration of oxygen vacancies which gives strong defect (green) emission in PL spectra.

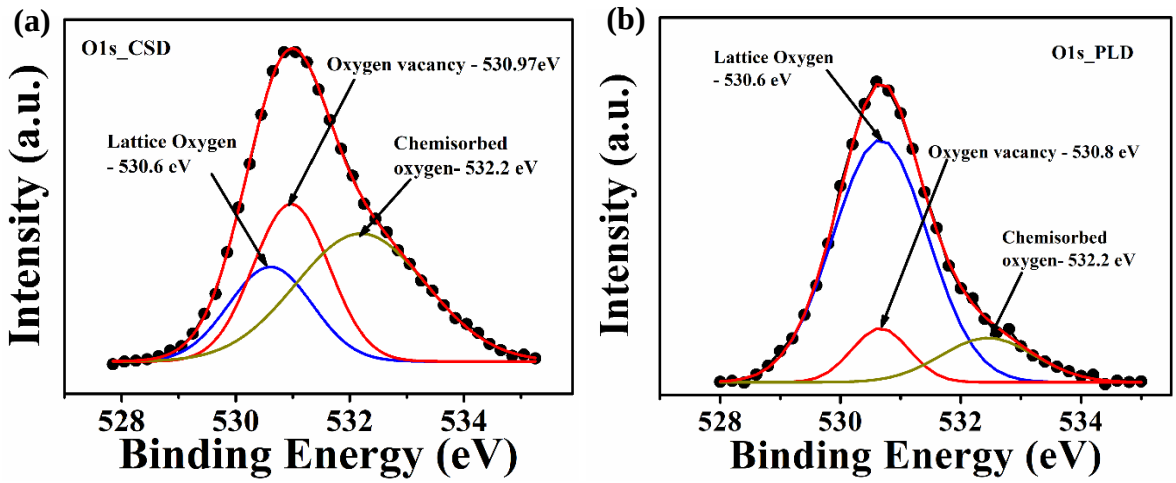

Figure 7.4 Gaussian deconvoluted XPS spectrum for O1s in lattice oxygen, oxygen vacancies and chemisorbed oxygen for (a) CSD and (b) PLD grown ZnO/p-Si NWs photodetectors.

Figure 7.5 (a) and (b) illustrates high resolution XPS spectra corresponding to $Zn2p_{3/2}$ core level for CSD and PLD grown ZnO/p-Si NWs photodetectors respectively. The peak $Zn2p_{3/2}$ is deconvoluted in three satellite peaks at different binding energies such as 1021.8 eV (lower

side), 1022.5 eV (middle) and 1023 eV (higher) in case of CSD grown samples (Figure 7.5 (a)). The lower energy peaks centered at 1021.8 eV is assigned to metallic Zn while the middle peak centred at 1022.5 eV corresponds to the divalent Zn in ZnO and the third peaks centered at higher energies 1023 eV correspond to +2 oxidation state of Zn due to the presence of $Zn(OH)_2$ for CSD grown ZnO/p-Si NWs photodetector. The peaks corresponding to $Zn(OH)_2$ also confirms the chemisorbed oxygen (generally in $-OH$ and/or water molecules) in CSD grown detectors [36].

Table 7.1 Area percentage of deconvoluted O1s peak for CSD and PLD grown ZnO/p-Si NWs nanostructures arrays.

Growth methods	**O type and area percentage (%) of deconvoluted O1*s* peak**		
	Lattice (O_L)	**Vacancy (V_{OS})**	**Chemisorbed O_2**
CSD	21 %	32 %	47 %
PLD	69 %	15 %	16 %

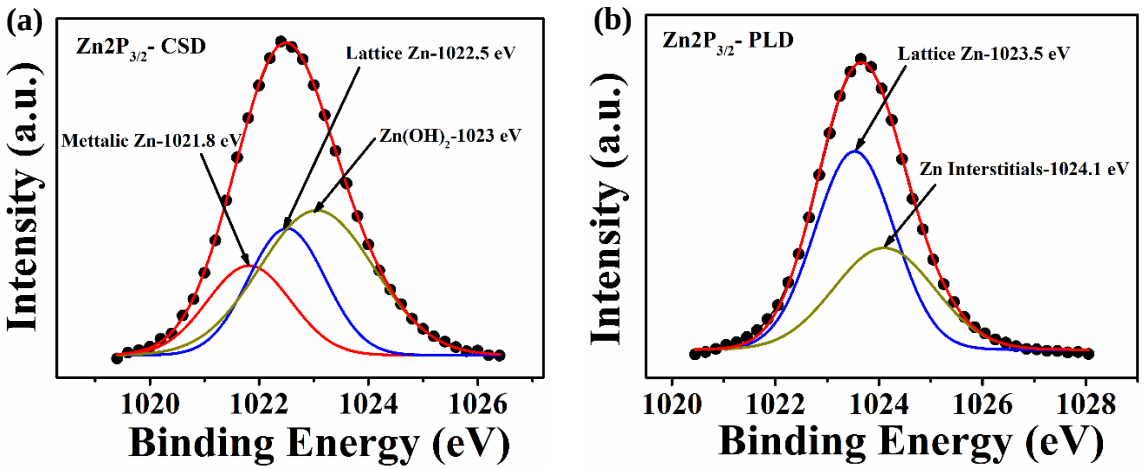

Figure 7.5 Gaussian deconvoluted XPS spectrum of $Zn2p_{3/2}$ peak for (a) CSD and (b) PLD grown ZnO/p-Si NWs photodetectors.

But in case of PLD grown ZnO/p-Si NWs photodetector, the $Zn2p_{3/2}$ is deconvoluted in two peaks at energies 1023.5 eV and 1024.1 eV (Figure 7.5 (b)). The peak centred at binding energies 1023.5 eV corresponds to lattice Zn with +2 valance state in ZnO. However, in this sample the higher energy satellite peak 1024.1 eV located at significantly higher energies. It may be attributed to a possibility that the Zn atom is surrounded by more than one oxygen atoms and is occupied at interstitial positions [37]. These interstitial Zn could be neutral Zn_i, extended states of Zn_i; single and double ionized zinc interstitials ($Zn_i^+$and Zn_i^{++}). This can also be rather confirmed from the silicon peak which shows an extra peak at higher binding energies that arises a possibility of an interface formation in PLD grown samples. This may

happen due to the ion impingement that generally occurs in case of PLD grown samples. Due to high laser fluence the ions of Zn and O may get impinged into a few nm of Si that may give rise to a possible interface of $(Si - O - Zn)$ solid solution [38-39]. This can be later explained in the section of photo response of the PLD photodetector.

7.3.3 Photoconduction of ZnO/p-Si NWs nanostructures arrays

We have fabricated two different geometries of ZnO/p-Si NWs heterojunctions photodetectors where the photoconductive channel ZnO is deposited on p-Si NWs by two different methods such as chemical (CSD) and physical (PLD). A schematic diagram of CSD and PLD grown ZnO/p-Si NWs photodetectors is shown in Figure 7.6 (a) and (b) respectively. The carrier conduction mechanism depends on the quality of metal-semiconductor interface which can be significantly tuned by oxygen vacancies available in the semiconductor.

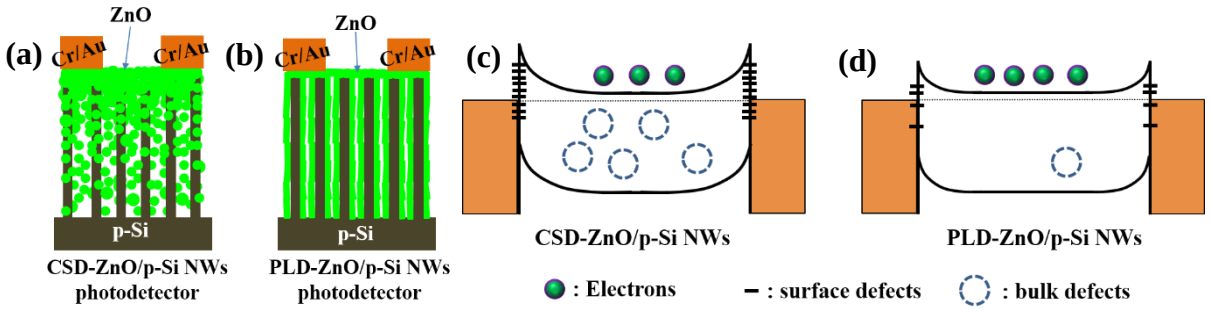

Figure 7.6 Schematic diagram of (a) CSD and (b) PLD grown ZnO/p-Si NWs photodetectors and the corresponding energy band diagram of (c) CSD and (d) PLD grown ZnO/p-Si NWs photodetectors without bias under dark condition.

Figure 7.7 (a) shows the variation of current with voltage $(I - V)$ in dark for CSD and PLD grown ZnO/p-Si NWs nanostructure arrays. The CSD grown ZnO/p-Si NWs nanostructure has lower dark conductance in comparison with PLD grown ZnO/p-Si NWs core-shell arrays. Lesser value of dark conductance of CSD grown ZnO/p-Si NWs arrays might be corresponding to the higher values of surface defects/adsorbates such as amorphous layer $(Zn(OH)_2)$ accompanied by higher concentration of oxygen vacancies. These surface defects act as scattering/capturing centers for conduction charge carriers [22, 40]. This can be explained on the basis of surface adsorbed oxygen molecules (O_2^-) on the ZnO/p-Si NWs nanostructures. It is known that the intrinsic defects such as oxygen vacancies in the surface layer of ZnO readily act as adsorption sites. O_2 molecules absorbed at these sites act as electron acceptors to form (O_2^-) at room temperature [10]. These chemisorbed oxygen (O_2^-) deplete the surface electron states and consequently reduces the channel conductivity in the dark, whereas in case of PLD grown core-shell device, the amorphous layer associated with oxygen defects has been reduced

and shrink the surface barrier leading to an increase in conductivity of the channel as illustrated in Figure 7.6 (c) and (d). Figure 7.7 (b) shows the variation of photocurrent (I_{PC}) with bias voltage (V) of CSD and PLD grown ZnO/p-Si NWs photodetectors with an illumination intensity ($\Im$) ≈ 100 μW/cm^2 at a wavelength of 900 nm. In the right-hand scale in the same graph show the photocurrent gain (G) as obtained from the data. The value of G calculated as 0.4 and 8 for CSD and PLD grown photodetectors respectively at a bias of 1 V.

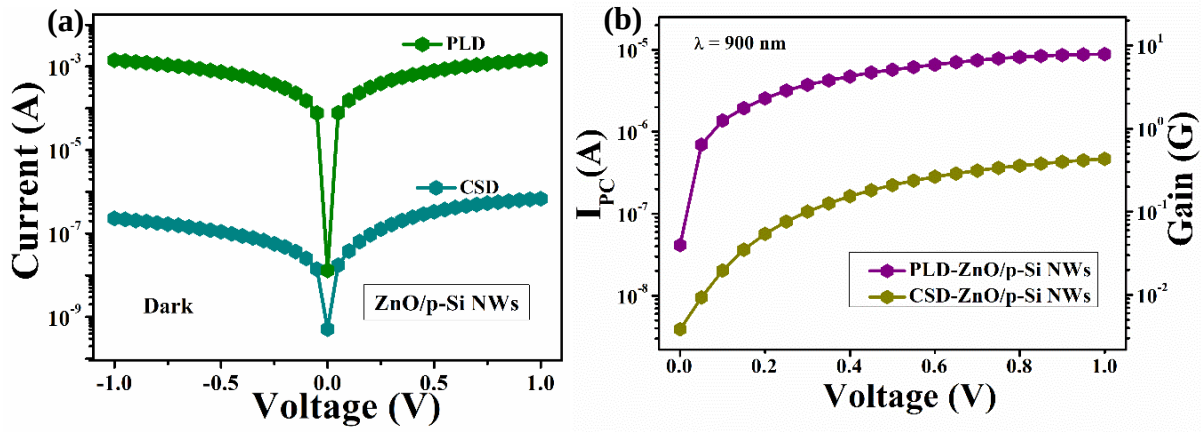

Figure 7.7 (a) Variation of $I-V$ under dark condition. (b) Variation of photocurrent (I_{PC}) and current gain (G) for CSD and PLD grown ZnO/p-Si NWs photodetectors.

Data in Figure 7.7 (b) shows the lower values of I_{PC} and G in CSD grown detector in comparison with the PLD grown core-shell detector that could be understand on the basis of PL and XPS study. As mentioned, the PL intensity reflects some extent of recombination probability of photo induced charge i.e., higher charge recombination probability or lower charge separation probability is associated with the higher defects intensity/density. Therefore, lower values of photocurrent for CSD grown photodetector can be attributed to higher recombination rate of photo-generated electrons and holes by this defects-induced trap centers. In case of PLD grown photodetector, the higher values of photocurrent can be ascribed to lesser values of density of surface states, which reduces the charge carrier recombination and improve the photodetector performances discussed in later section. Moreover, the conduction electron trapping at the interface states between ZnO and Si NWs can partially contribute to the change of the electrical characteristics of the photodetectors in visible and NIR region.

To study the performance of photodetectors, photoresponse of devices are measured with respect to different illumination of light in UV, visible and NIR region. Figure 7.8 (a) and (b) show the time dependent photoresponse of CSD and PLD grown photodetectors respectively at a bias voltage of 1 V in UV region (λ = 300 nm) with an illumination intensity ($\Im$) ≈ 100 μW/cm^2. The shaded area represents the time period when the devices are illuminated with the

respective illumination of light. The rapid raise in photocurrent is followed by a slower component which follows to an exponential relation (discussed in later section). Figure 7.8 (c) and (d) show the time resolve photocurrent (I_{PC} vs. t) at different illumination of wavelength in visible-NIR region at same bias of 1 V and intensity ($\Im$) ≈ 100 μW/cm^2 for CSD and PLD grown detectors respectively. The data were taken with illumination ON and OFF. As shown in Figure 7.8 (c) in CSD grown ZnO/p-Si NWs photodetector, with the light illumination ON and OFF, the current of the devices exhibit two states, a low current state in dark condition and a high current state under illumination of light of different wavelengths. Whereas the PLD grown photodetector shows significantly enhanced persistent photocurrent (PPC) in Figure 7.8 (d), when the light is turned OFF.

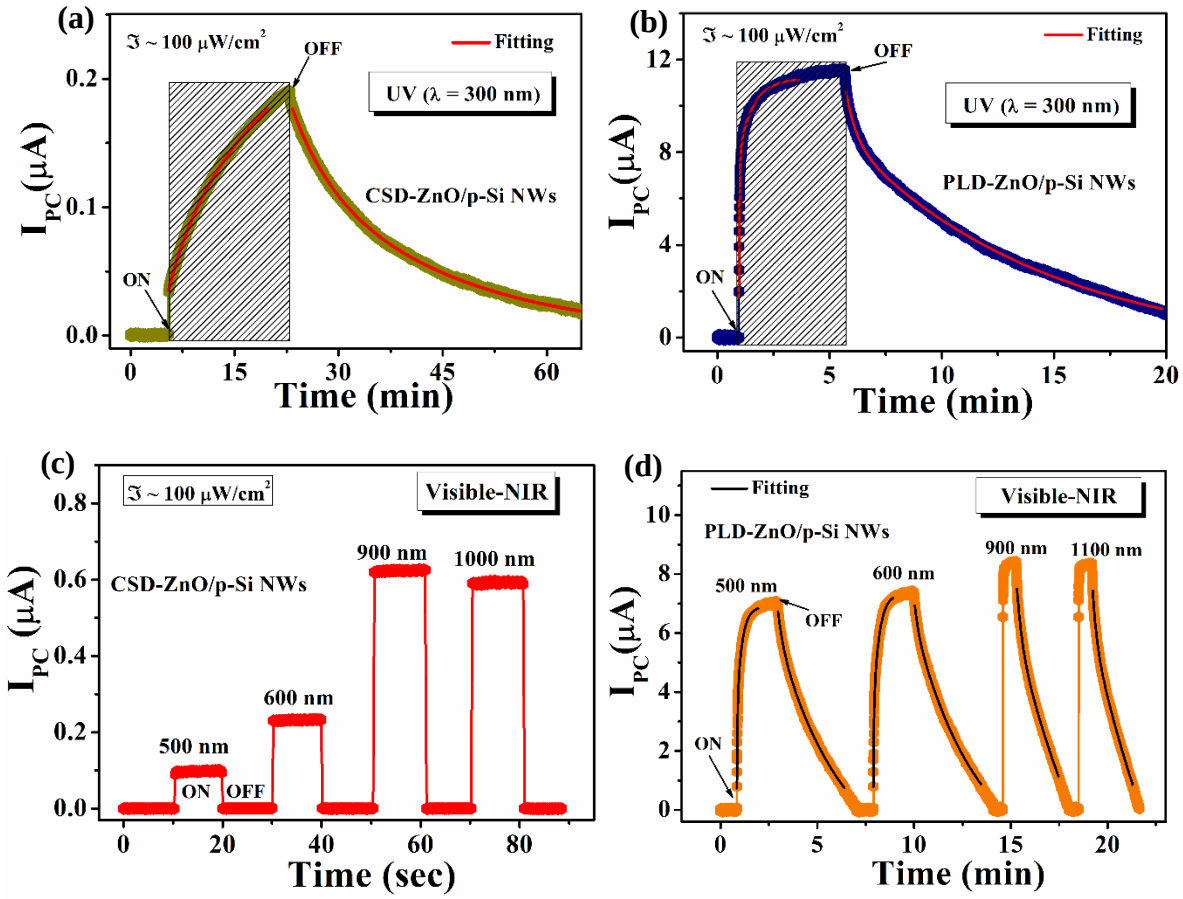

Figure 7.8 Time dependent photoresponse for (a) CSD and (b) PLD grown photodetectors in UV (λ = 300 nm) region. Photocurrent (I_{PC}) at different wavelength (λ) in visible-NIR region for (c) CSD and (d) PLD grown photodetectors at a fixed illumination of 100 μW/cm^2.

From the data it is shown that I_{PC} of PLD grown ZnO/p-Si NWs device is enhanced considerably over the whole spectral range in comparison with CSD grown ZnO/p-Si NWs device. We found a sharp and distinct ON/OFF states in visible and NIR region for CSD grown photodetector with rise and decay time constants of < 0.3 s when the illumination is turned

ON/OFF whereas, the PLD grown photodetector exhibits significantly enhanced persistent photocurrent (PPC) when the light is turned OFF. The saturation photocurrent (I_{PC}) of PLD grown photodetector is ~ 11 μA in UV region (λ = 300 nm), ~ 6.95 μA in visible (λ = 500 nm) and ~ 8.4 μA in NIR region (λ = 900 nm) whereas the CSD grown photodetector shows the smaller value of ON state saturation photocurrents as ~ 0.19 μA in UV (λ = 300 nm), ~ 0.1 μA in visible (λ = 500 nm) and ~ 0.62 μA in NIR (λ = 900 nm) region (Table 7.2). Figure 7.9 shows the spectral responsivity R for CSD and PLD grown n-ZnO/p-Si NWs photodetectors at a bias of 1 V measured at illumination intensity $\Im$ = 100 μW/cm^2. The responsivity of PLD grown core-shell device is enhanced significantly not only in UV region but also in visible and NIR region in comparison with CSD grown photodetector. The average value of R at 1V bias for PLD grown device is ~ 0.7 A/W for the wavelength range 600 nm-1100 nm whereas in UV region (≤ 375 nm) the value of R reached ~ 1.4 A/W. Data in Figure 7.9 shows that the responsivity (R) in PLD grown detector is enhanced ~ 10^2 folds in UV region whereas the average value of R is increased ~ 20 folds in visible-NIR region in comparison with CSD grown ZnO/p-Si NWs detector.

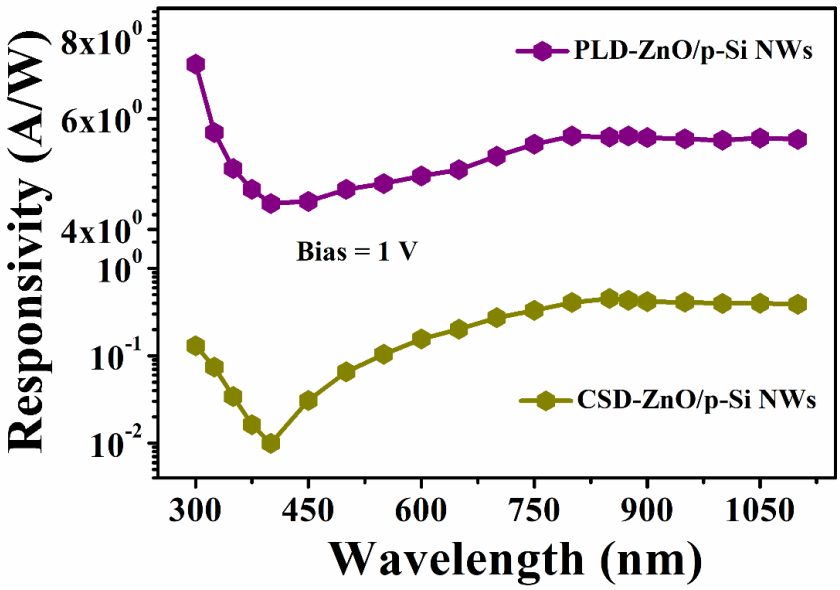

Figure 7.9 Spectral responsivity (R) of CSD and PLD grown ZnO/p-Si NWs photodetectors at a bias of 1 V under illumination intensity $\Im$ = 100 μW/cm^2.

The intensity dependence of photocurrent I_{PC} of CSD and PLD grown photodetector is shown in Figure 7.10 (a) at a bias of 1V for illumination λ = 900 nm. It is seen that intensity dependence of photocurrent follows the power law $I_{PC} \propto P^{\beta}$ with an exponent (β) ≈ 0.79 for CSD and ≈ 0.13 for PLD grown ZnO/p-Si NWs photodetectors. Figure 7.10 (b) shows the power (P) dependence of responsivity R for CSD and PLD grown photodetectors at a bias of

1V for illumination λ = 900 nm. Since the responsivity $R = I_{PC}/P$, variation of R with incident power P is given by the relation $R \propto P^{-(1-\beta)}$. Data in Figure 7.10 (b) shows the value of responsivity R decreases as the incident power P on the device increases due to sublinear dependence on intensity i.e., $\beta < 1$, correspond to trapping, recombination, and electron–hole pair generation within the semiconductor. Since, rate of generation of charge carrier is expected to be linear in intensity, the strong sub-linear dependence of I_{PC} on light intensity could be due to a saturation of traps or a speed up of de-trapping dynamics with increasing carrier density [20]. The value β depends on the existence of localized traps near the band edges that controls the process of recombination and the energy distribution of the localized states near the conduction band edge. The charging of the surface state with the electron trapping by oxygen adsorption changes the distribution of trap states between the conduction band and the Fermi level. In general, β depends on the distribution of trap states around the Fermi Level E_F and band edges. It is expected that traps are distributed non-uniformly within the Si NW. These traps that control this exponent, are likely to lie within Si NW core or at the intermediate state of ZnO and Si NW that affects the transportation of photo-generated charge carrier in the interface of ZnO and Si NW causes the changes of responsivity of the photodetectors in NIR region [41].

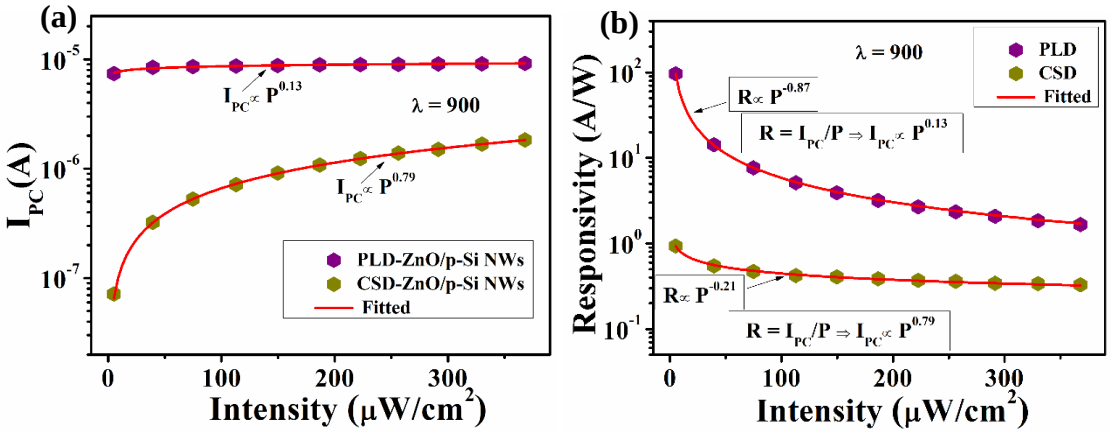

Figure 7.10 (a) Variation of photocurrent (I_{PC}) with illumination intensity. (b) Variation of responsivity R with illumination intensity for λ = 900 nm at a bias of 1 V for CSD and PLD grown ZnO/p-Si NWs photodetectors.

7.4 Discussions

7.4.1 Role of defects on charge carrier transportation

The interaction of light with semiconductor is a complex phenomenon which includes the electron–hole pair generation, trapping, and recombination. In order to understand the photoresponse and photoconductance mechanism for UV illumination in CSD and PLD grown ZnO/p-Si NWs photodetectors in metal-semiconductor-metal (MSM) configuration, a

schematic energy band diagram is shown in Figure 7.11 (a)-(d). The transportation of charge carrier is strongly influenced by surface/interface defect states available in semiconductors. The density of surface/interface defects ($V_o s/O_2^-$) of CSD grown ZnO/p-Si NWs is higher than that of PLD grown ZnO/p-Si NWs nanostructure arrays. Under UV illumination (λ = 300 nm), due to higher abundance of oxygen vacancies in CSD grown photodetector, the photo-generated charge carriers are captured more easily (Figure 7.11 (a)). As result lower value of steady-state photocurrent (I_{PC}) with delayed response time has been observed in CSD grown photodetector. In PLD grown photodetector, the photo-generated holes are trapped in the depletion region which increase the positive charge density in the depletion region (Figure 7.11 (b)). As a result, the depletion layer for PLD grown photodetector is narrowed down to a width λ_{PLD} in contrast to λ_{CSD}, depletion width for CSD grown photodetector, where $\lambda_{PLD} < \lambda_{CSD}$. The narrowing of the depletion region allows the electrons to tunnel in the M-S interface [42]. Due to fewer oxygen vacancies in PLD grown photodetector, the photo-generated electrons and holes undergo a rapid separation and passed on to the corresponding electrodes. Thus, we observed a larger and faster photoresponse for PLD grown photodetector in comparison with CSD grown photodetector.

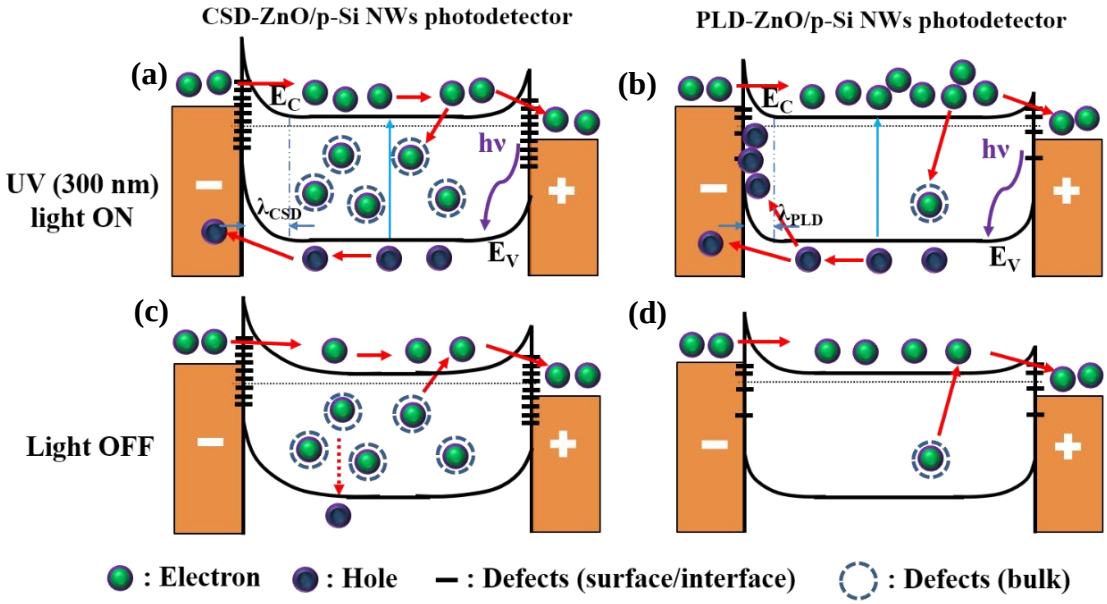

Figure 7.11 Schematic of energy band diagram for (a) CSD and (b) PLD grown photodetectors under UV illumination with bias. Energy band diagram for (c) CSD and (d) PLD grown ZnO/p-Si NWs photodetectors again in dark condition with bias in MSM configuration. Filled (green and dark blue) and empty circles represent intrinsic carriers and bulk defects inside ZnO respectively. Thick dashes represent the surface defects.

When illumination turned OFF in Figure 7.11 (c) and (d) for CSD and PLD grown photodetector respectively, the electrons in the conduction band (CB) are captured at

recombination centers/annihilated by band-to-band transition (fast decay components), or captured by oxygen vacancies are released and recombine with holes slowly (slower recovery components) discussed in next section. The CSD grown photodetector has smaller value of ON state saturation photocurrent than that of PLD grown photodetector with respect to different illumination of light as shown data in Figure 7.8 (a) - (d) and Table 7.2. The difference in the saturation photocurrent (I_{PC}) can be correlated with different concentrations of surface-interface defects centers in the ZnO/p-Si NWs nanostructures arrays. The observed defects intensities in CSD grown photodetector is higher than that of PLD grown photodetector. These intensities/densities are unfavourable to the ON state saturation photocurrent (I_{PC}). It is noted that not all defects densities are contributed to the photocurrent generation upon illumination; rather it indicates the possibility of participation of any/all of defects states in the photocurrent generation mechanism. The observed adverse effect of defect states over the ON state saturation photocurrent indicates that there should be capturing/scattering of photo-generated charge carriers during transportation. In other words, the higher is the defect density, lower is the photo current or vice versa.

7.4.2 Role of defects on transient photoconductivity

When illumination photon energy exceeds the band energy, the photo-generated electron-hole pairs are created. This process is fast and responsible for the rapid rise of photocurrent in the first few seconds. The photo-generated holes are captured by adsorbed oxygen ions then discharge the negatively charged adsorbed oxygen ions. The trapping of photo-generated hole results in an accumulation of photo excited electron that are available for conduction which decreases the width of the depletion layer cause a significant increase in free carrier density resulting in a large change in photocurrent. This process is slow and responsible for the following slower rise of current in the next stage [29]. An important parameter of photodetector is rise time and decay time. In photocurrent measurement, rise time is the time for the photocurrent to rise 90% of its peak value and decay time defined as the time for the photocurrent to decay to 10 % of the peak value. We have estimated the time constants quantitatively by the fitting of the photoresponse rise curve in Figure 7.8 (a) and (b) with a biexponential equation of the following form [20]:

$$I = I_0 - A_1 e^{-t/\tau_{r1}} - A_2 e^{-t/\tau_{r2}} \qquad (7.1)$$

Where I_0 is the steady state photocurrent, t is the time, A_1 and A_2 are positive constant, τ_{r1} and τ_{r2} are the fast and slow time constants respectively. The estimated value of rise time

constants from the double exponential fits are about τ_{r1} ~ 20 s, τ_{r2} ~ 225 s in UV region (λ= 300 nm) for CSD grown photodetector whereas the time constants are τ_{r1} ~ 1 s, τ_{r2} ~ 14 s for PLD grown photodetector (Table 7.2). It is evidently note that the PLD grown core-shell photodetector device shows much faster response corresponding to UV light (λ = 300 nm) than that of the CSD grown ZnO/p-Si NWs photodetector. We found the estimated values of rise time constants τ_r < 0.3 s in visible and NIR region for CSD grown photodetector, whereas, the value of rise time constants are τ_{r1} ~ 0.6 s, τ_{r2} ~ 12 s in visible and τ_r < 1 s in NIR region for PLD grown photodetector.

Table 7.2 Comparison of the performance of CSD and PLD grown ZnO/p-Si NW photodetectors under different spectral illumination.

Photodetectors	**Saturation I_{PC} (μA) for each λ (nm)**			**Rise time (sec) for each λ**	**Decay time (sec) for each λ**
CSD grown ZnO/p-Si NWs	UV	300	~ 0.19	τ_{r1} ~ 20, τ_{r2} ~ 225	τ_{d1} ~ 150, τ_{d2} ~ 1100
	Visible	500	~ 0.1	τ_r < 0.3	τ_d < 0.3
		600	~ 0.23	τ_r < 0.3	τ_d < 0.3
	NIR	900	~ 0.62	τ_r < 0.3	τ_d < 0.3
		1100	~ 0.59	τ_r < 0.3	τ_d < 0.3
PLD grown ZnO/p-Si NWs	UV	300	~ 11.7	τ_{r1} ~ 1, τ_{r2} ~ 14	τ_{d1} ~ 24, τ_{d2} ~ 220
	Visible	500	~ 7.1	τ_{r1} ~ 0.6, τ_{r2} ~ 12	τ_{d1} ~ 15, τ_{d2} ~ 125
		600	~ 7.45	τ_{r1} ~ 0.6, τ_{r2} ~ 10	τ_{d1} ~ 14, τ_{d2} ~ 130
	NIR	900	~ 8.71	τ_r < 1	τ_{d1} ~ 14, τ_{d2} ~ 110
		1100	~ 8.65	τ_r < 1	τ_{d1} ~ 11, τ_{d2} ~ 90

For decay/off state recovery time of photodetectors, it is known that the decay time depends mainly upon three factors; the available defect states ($V_O s$, V_{Zn}/O_i), surface area and adsorbate (O_2 or H_2O). The photocurrent decay curves have been best fitted with a double exponential function with the following form [20]:

$$I = I_0 + B_1 e^{-t/\tau_{d1}} + B_2 e^{-t/\tau_{d2}} \qquad (7.2)$$

Where I_0 is the steady state photocurrent, t is the time, B_1 and B_2 are positive constant, τ_{d1} and τ_{d2} are the fast and slow decay time constants respectively. The estimated values of decay time constants are τ_{d1} ~ 150 s, τ_{d2} ~ 1100 s in UV region (λ = 300 nm) for CSD grown photodetector and τ_{d1} ~ 24 s, τ_{d2} ~ 220 s for PLD grown photodetector (Table 7.2). The observed time-dependent photoconductive decay can be characterized by a fast photoresponse process followed by a slow one. The initial rapid decay after turning OFF the illumination is likely due to quick re-adsorption of oxygen at grain boundaries or near the surface. The second

one is strongly dependent on the existence of chemisorbed oxygen molecules at their surfaces, because holes discharge oxygen species from the surface by indirect electron-hole recombination mechanisms. We found the decay time constants τ_d < 0.3 s in visible-NIR region in Figure 7.8 (c) for CSD grown photodetector. Whereas the value of decay time constants for PLD grown photodetector are τ_{d1}, τ_{d2} ~ 15, 125 s (λ = 500 nm) and τ_{d1}, τ_{d2} ~ 14, 110 s (λ = 900 nm) in visible-NIR region in Figure 7.8 (d) (Table 7.2). As, the PLD grown ZnO/p-Si NWs nanostructure possesses lower amount of surface chemisorbed O_2 and defects (V_o) than CSD grown nanostructure. Hence there is a lesser probabilities of oxygen related hole trap states at the surface which prevent carrier recombination which causes persistent photocurrent. Another possibility can also be explored that the higher energy peak in Si may be due to the interfacial layer (solid solution of ($Si - O - Zn$)) in the junction and that traps the oxygen related hole and prevent the recombination causing a persistent photocurrent. From the XPS analysis of Si peak of PLD grown ZnO/p-Si NWs nanostructure core-shell arrays in Figure 7.12 (b), it has been observed that there is a possibility of ZnO/Si interface formation of as the higher energy peaks indicates a formation interfacial layer of solid solution of ($Si - O - Zn$). But in the case of CSD detectors that solid solution formation has not been observed in Figure 7.12 (a). A Schematics of energy band diagram models have been proposed in the next section to explain the transient photocurrent of CSD and PLD grown photodetector especially in visible and NIR region.

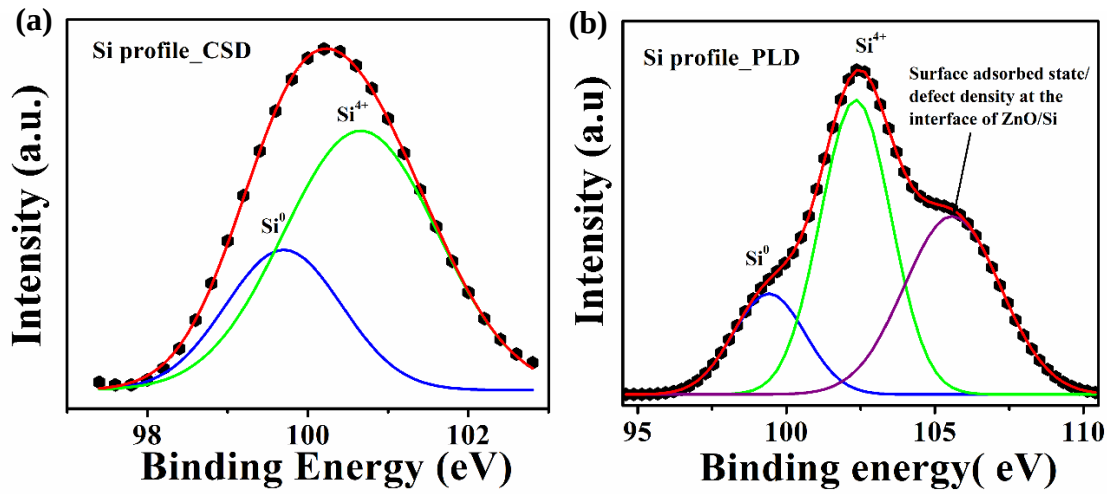

Figure 7.12 XPS spectra for Si peak (dark circles) and simulated plots (lines) of (a) CSD grown (b) PLD grown ZnO/p-Si NWs nanostructures arrays.

7.4.3 Proposed model for charge transfer

The characteristics of photoresponse in visible as well as NIR region is based on the transfer of photo-generated charge carriers from Si NW to the n-ZnO by taking into account the role of

surface/interface defect states on the photo-generated carriers transportation and recombination properties in the p-n junction. The transfers of carriers are proposed to be explained on the basis of models shown schematically in Figure 7.13 (a) and (b) for CSD and PLD grown ZnO/p-Si NWs photodetectors, respectively. The models show the band alignments. The electron affinities of ZnO (χ_{ZnO}) and Si (χ_{Si}) are taken as 4.35 and 4.05 eV, respectively [25]. While the band gaps of ZnO and Si are taken as 3.3 and 1.12 eV, respectively. The band gap discontinuity at conduction band and valence band is therefore equal to ΔE_C = 0.3 eV and ΔE_V = 1.88 eV. At the n-ZnO and p-Si interface, which is an interface of a p-type and an n-type material, the conduction and valence bands in the p-type material bend-down and those in n-type material bend-up. This allows transfer of electrons from the conduction band of p-type Si NW to the conduction band of n-ZnO and transfer of holes from valence band of ZnO to valence band of Si without application of any bias. Upon NIR illumination, the photo-generated electron-hole pairs are mostly generated in Si side due to small absorption of ZnO in NIR range. Whereas, the photo-generated electron-hole pairs are generated both in ZnO and in Si side for visible illumination.

In CSD grown ZnO/p-Si NWs, photoexcited carriers (electrons) are transferred from the Si NW to ZnO layer with a very low efficiency due to a lot of surface/interface states act as the recombination centers within the p-n junction in Figure 7.13 (a) [43]. Lots of interface states in ZnO hinder the transportation of photo-generated electrons from Si through ZnO, as a result, few electrons are collected at external electrode, and a very small the steady-state photocurrent (I_{PC}) has been observed. At the same time, we observed very small values of the decay time constants (τ_d < 0.3 s) in visible-NIR region in Figure 7.8 (c) due to faster recombination at the interface of ZnO and p-Si NW in case of the CSD grown photodetector.

PLD grown ZnO/p-Si NWs core-shell arrays possesses very lower amount of surface/interface defect states in comparison with the CSD grown nanostructure arrays. This reduction of defect states will benefit the transportation of photoexcited carriers from Si NW to ZnO layer with a high efficiency in visible as well as NIR region and the steady state photocurrent (I_{PC}) is thus greatly enhanced. At the same time, the interfacial layer (solid solution of ($Si-O-Zn$), observed from XPS analysis) in Figure 7.12 (b) of PLD grown ZnO/p-Si NWs heterostructure within the p-n junction acts as an energy barrier [44] which slower the electron-hole recombination causing a persistent photocurrent in visible-NIR region in Figure 7.8 (d). These two coupling effects offer a high efficiency transportation of photo-generated electrons from

Si through ZnO and the transient photocurrent of the PLD grown photodetector in visible and NIR region is thus dramatically enhanced in comparison with CSD detector. In UV region (≤ 375 nm) the carrier conduction mechanism of ZnO/p-Si NWs devices are strongly dependent on the surface/interface defect states of ZnO. Whereas, in visible and NIR region, the transportation of photo-generated charge carrier is not only dependent on the surface/interface defects of ZnO but also it is strongly influenced by the interface states of the p-n junction, resulting the changes of responsivity in visible and NIR region of the photodetectors.

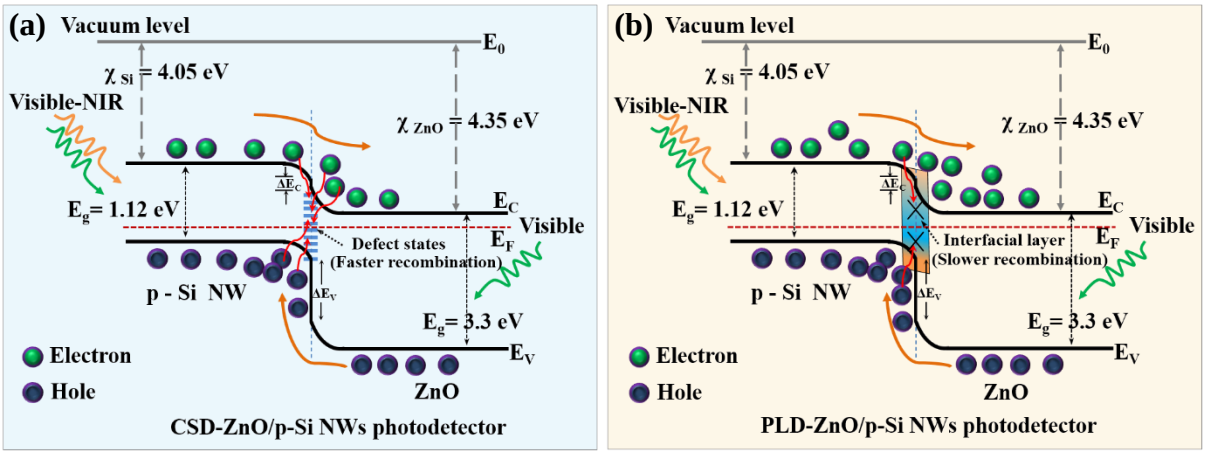

Figure 7.13 Schematic of energy band diagram for photoexcited charge transport by taking into account the role interface defect states within the p-n junction for (a) CSD and (b) PLD grown ZnO/p-Si NWs nanostructures arrays.

7.5 Conclusion

To summarize, optical response of ZnO/p-Si NWs photodetectors can be tuned by changing the surface-interface defects and transport of charge carriers is strongly dependent on the different concentration of defects with processing conditions which is prolific for electronic and optoelectronic properties of heterostructure devices. The value of *R* in PLD grown detector is enhanced ~ 10^2 folds in UV region whereas the average value of R is increased ~ 20 folds in visible-NIR region in comparison with CSD grown ZnO/p-Si NWs detector because of less scattering/capturing of charge carriers in defect centres of ZnO/p-Si NWs arrays. The performances of ZnO/p-Si NWs photodetectors are strongly dependent on the functionality of surface-interface state where existence of undesired recombination sites can hamper the carrier transport as well as photoconduction and transient photoconductivity. The transport of photo-generated charge carrier is facilitated by increasing the majority carrier concentration without recombination with proper level of oxygen vacancy. In case of PLD grown photodetector, the coupling of the lesser values of density of surface states and the interfacial layer (solid solution of $Si-O-Zn$) of p-n junction reduce the charge carrier recombination, resulting a large

enhancement of transient photocurrent in visible and NIR region. However, in case of CSD grown photodetector, the excessive oxygen vacancies become the trap assisted recombination center by trapping of photoinduced charge carriers.

Bibliography

1. H. J. Queisser and E. E. Haller, *Science*, **281**, 945 (1998).
2. A. Rose, Concepts in Photoconductivity and Allied Problems, Interscience Publishers, New York, 1963.
3. S. Baia, N. Zhang, C. Gao, and Y. Xiong, *Nano Energy*, **53**, 296 (2018).
4. S. V. Kalinin and N. A. Spaldin, *Science*, **341**, 857 (2013).
5. B. Liu, J. Li, W. Yang, X. Zhang, X. Jiang, and Y. Bando, *Small*, **13**, 1701998 (2017).
6. S. Shen, J. Jiang, P. Guo, C. X. Kronawitter, S. S. Mao, and L. Guo, *Nano Energy*, **1**, 732 (2012).
7. J. H. Kim, Y. J. Jang, J. H. Kim, J. W. Jang, S. H. Choic, and J. Lee, *Nanoscale*, **7**, 19144 (2015).
8. F. Yang, J. Guo, L. Zhao, W. Shang, Y. Gao, S. Zhang, G. Gu, B. Zhang, P. Cui, and G. Cheng, *Nano Energy*, **67**, 104210 (2020).
9. W. Ouyang, F. Teng, J. H. He, and X. Fang, *Adv. Funct. Mater*., **29**, 1807672 (2019).
10. C. Soci, A. Zhang, B. Xiang, S. A. Dayeh, D. P. R. Aplin, J. Park, X. Y. Bao, Y. H. Lo, and D. Wang, *Nano Lett*., **7**, 1003 (2007).
11. X. Liu, L. Gu, Q. Zhang, J. Wu, Y. Long, and Z. Fan, *Nat. Commun*., **5**, 4007 (2014).
12. B. D. Boruah, *Nanoscale Adv*., **1**, 2059 (2019).
13. X. Wang, K. Liu, X. Chen, B. Li, M. Jiang, Z. Zhang, H. Zhao, and D. Shen, *ACS Appl. Mater. Interfaces*, **9**, 5574 (2017).
14. R. R. Ghimire, R. Nath, R. K. Neogy, and A. K. Raychaudhuri, *Nanotechnology*, **28**, 295703 (2017).
15. K. Mahmood, S. B. Park, and H. J. Sung, *J. Mater. Chem. C*, **1**, 3138 (2013).
16. M. Saini, R. Singh, A. Mitra, and T. Som, *Solar Energy*, **207**, 228 (2020).
17. D. Liu, X. Shen, T. Song, J. Hu, and B. Sun, *Phys. Chem. Chem. Phys*., **15**, 4970 (2013).
18. T. H. Flemban, M. A. Haque, I. Ajia, N. Alwadai, S. Mitra, T. Wu, and I. S. Roqan, *ACS Appl. Mater. Interfaces*, **9**, 37120 (2017).
19. C. L. Hsu, Y. C. Wang, S. P. Chang, and S. J. Chang, *ACS Appl. Nano Mater*., **2**, 6343 (2019).
20. P. M. Wojcik, L. D. Bastatas, N. Rajabi, P. V. Bakharev, and D. N. Mcilroy, *Nanotechnology*, **32**, 035202 (2021).
21. M. R. Alenezi, S. J. Henley, and S. R. P. Silva, *Sci. Rep*., **5**, 8516 (2015).
22. A. Kushwaha and M. Aslam, *J. Appl. Phys*., **112**, 054316 (2012).
23. L. D. Bastatas, P. Wagle, E. Echeverria, J. D. Slinker, and D. N. Mcilroy, *Nanotechnology*, **30**, 234006 (2019).
24. M. K. Kavitha, K. B. Jinesh, R. Philip, P. Gopinath, and H. John, *Phys. Chem. Chem. Phys*., **16**, 25093 (2014).
25. C. Samanta, S. Bhattacharya, A. K. Raychaudhuri, and B. Ghosh, *J. Phys. Chem. C*, **40**, 22235 (2020).
26. H. Kang, J. Park, T. Choi, H. Jung, K. H. Lee, S. Im, and H. Kim, *Appl. Phys. Lett*., **100**, 041117 (2012).
27. K. Vanheusden et al., *J. Appl. Phys.*, **79**, 7983 (1996).
28. M. Ghosh, A. K. Raychaudhuri, *Appl. Phys. Lett*., **93**, 123113 (2008).

29. R. Khokhra, B. Bharti1, H. N. Lee, and R. Kumar, *Sci. Rep*., **7**, 15032 (2017).
30. S. Vempati, J. Mitra, and P. Dawson, *Nanoscale Res. Lett*., **7**, 470 (2012).
31. N. H. Alvi, K. Hasan, O. Nur, and M. Willander, *Nanoscale Res. Lett*., **6**, 130 (2011).
32. T. Chen, G. Z. Xing, Z. Zhang, H. Y. Chen, and T. Wu, *Nanotechnology*, **19**, 435711 (2008).
33. Y. Zuo, S. Ge, Z. Chen, L. Zhang, X. Zhou, S. Yan, *J. Alloys Compd*., **470**, 47 (2009).
34. M. M. Can, S. I. Shah, M. F. Doty, C. R. Haughn, and T. Firat, *J. Phys. D: Appl. Phys.*, **45**, 195104 (2012).
35. M. Kunat, S. G. Girol, U. Burghaus, and C. Wöll, *J. Phys. Chem. B*, **107**, 14350 (2003).
36. N. T. Mai, T. T. Thuy, D. M. Mott, and S. Maenosono, *Cryst. Eng. Comm.*, **15**, 6606 (2013).
37. F. Kayaci, S. Vempati, I. Donmez, N. Biyikli, and T. Uyar, *Nanoscale*, **6**, 10224 (2014).
38. U. Meier and C. Pettenkofer, *Appl. Surf. Sci*., **252**, 1139 (2005).
39. D. K. Kim et. al., *Sci Rep*., **6**, 34945 (2016).
40. W. Park, W. K. Hong, G. Jo, G. Wang, M. Choe, J. Maeng, Y. H. Kahng, and T. Lee, *Nanotechnology*, **20**, 475702 (2009).
41. K. Das, S. Mukherjee, S. Manna, S. K. Ray, and A. K. Raychaudhuri, *Nanoscale*, **6**, 11232 (2014).
42. P. P. Das, S. Samanta, L. Wang, J. Kim, T. Vogt, P. S. Devi, and Y. Lee, *RSC Adv*., **9**, 4303 (2019).
43. Y. Zhang, M. Hu, and Z. Wang, *Nano Energy*, **71**, 104630 (2020).
44. A. Ashok, S. N. Vijayaraghavan, S. V. Nair, and M. Shanmugam, *RSC Adv*., **7**, 48853 (2017).

Chapter 8

Summary and concluding remarks

In this final chapter, we have summarized the important observations of this thesis work and discussed the scope for future works. The main focus of this dissertation is the induction of charge carrier of oxide by field effect using gate in FET type device or effects of photo-gating in optoelectronics studies or injection of charge carrier by gas. In this thesis, we have mainly investigated a selected portion of physical properties such as electrical, optoelectronics and gas sensing properties of oxide semiconductor through the ingenious use of heterojunction of ZnO/Si NWs and thin film of doped ZnO. Other than basic physics, the experimental observation/ understanding leads to a very good contribution to flexible electronics and also in gas sensing application with a very good application potential. The proof of concept has been patented and highlighted in this thesis work also. All the important observations during this thesis work are pointed out below.

8.1 Conclusion

Control of the electrical and optical properties of oxide semiconductors is a key requirement for practical applications in optoelectronic and other sensing devices. The basic physical idea that has been utilized in this thesis is the effect of growth techniques and standardization of growth parameters that can tailor size, shape, morphology and homogeneity of semiconductor oxide nanostructures arrays. This thesis led to definite results because we were able to grow high quality semiconductor oxide hetero structures. In this thesis, the tuning of charge carriers has been done by using photo gating, gas injection or by field effect using electric double layer (EDL) gate and to understand the basic physics underlying the charge carrier transport phenomena in oxide semiconductors. In this thesis, we have concentrated on heterojunction arrays (both p-n and n-n junction) which has been formed using zinc oxide/doped ZnO and vertically aligned 1D silicon nanowires (Si NWs) arrays. The thesis work is mainly focused with the dealing of known challenges on fabrication processes and the electrical, optoelectronics and gas sensing properties of oxides can be tuned by making heterostructures or FET type device structures or by decorating with plasmonic nanoparticles. A summary of the work done in this thesis is presented below:

(a) In chapter 2, we have discussed the synthesis methods on the successful integration of oxide semiconductor with 1D nanostructure into heterojunction (ZnO/Si NWs) and thin film of doped zinc oxide (indium gallium zinc oxide (IGZO)) of very good quality so that one can get definite results by controlled and optimized growth techniques such as chemical solution deposition (CSD), atomic layer deposition (ALD) and pulsed laser deposition (PLD). physical and chemical). In this thesis work, ligand-free plasmonic nanoparticles (such as Au, Pd) have been prepared by custom made pulsed laser ablation in liquid (PLAL) technique. The presence of ligands between ZnO and Au NPs inhibits charge transfer and reduces the inter band transition which degrade the photodetector performances. Since the photoresponse of the device depends on the efficiency of the charge transfer, a ligand-free attachment is preferred as discussed in chapter 4 in this thesis.

(b) In chapter 3, the fabrication processes of different devices such as photodetector, gas sensor and thin film transistors (TFTs) have been demonstrated and also discussed the experimental techniques and development of experimental set-up for electrical, optoelectronics and gas sensing measurements. We have provided the details overview of cross-sectional TEM (XTEM) sample preparation techniques by using spatially resolved

advance tools and techniques for high resolution TEM analysis that enables us to make a proper physical model of the devices.

(c) In chapter 4, we have shown tuning of charge carrier in plasmonic Au nanoparticles decorated ZnO/p-Si NWs core-shell arrays to extend the response of a photodetector beyond its fundamental band gap by exploiting the concept of surface "photo gating". The ligand-free decoration of Au NPs was done by using pulsed laser ablation in liquid (water) PLAL method. The details experimental study and also photo conduction mechanism has been described in this chapter to show how the device engineering makes it very good broadband (300-1100nm) photo detector. However, using photo-gating as well as favourable band alignments, the photo generated carriers are infused in the conduction band of ZnO using a tandem effect of Si NWs in Visible and NIR region and Au NPs in Visible as well as UV region leading to the enhancement of photoresponse of ZnO not only in visible range but also in UV to NIR broadband region. The responsivity *R* of the detector ~ 1 A/W from 700 nm to longer wavelength (at bias of 1V) and in the visible region the responsivity of the photo detector with Au NPs is > 0.5 A/W and increases to > 1 A/W at UV region. The significant enhancement of optical response and photoconductive gain in visible region can also be correlated with enhancement of absorption in visible region due to surface plasmon resonance (SPR) coupling of Au NPs with ZnO.

(d) In chapter 5, we have discussed induction of charge carrier by gas injection in ZnO/Si NWs heterojunction devices. We have shown that functional oxide (ZnO) and semiconductor (Si) NWs based heterojunction arrays based nitric oxide (NO) gas sensor can lead to extremely high sensitivity of ~ 500 ppb **(**noise limited resolution of ~10 ppb**)** even in room temperature operation with high selectivity for gas detection without interference of humidity and no extra power is needed for heating arrangement which avoids the complexity in the designed sensor electronics. In this particular ZnO/p-Si NWs based device, the enhanced sensitivity of heterojunction comes from enhancement of charge carrier density through the interface of ZnO and p-Si NWs on gas exposure. We have proposed a mechanism for operation of the sensor and that have been validated by numerical simulation with COMSOL Multiphysics. The simulation shows the essentiality of the heterojunction in the enhancement of sensitivity over that expected from chemiresistor mechanism. This experimental observation/understanding as well as ingenious use of ZnO/p-Si NWs heterojunction is indeed a major advancement towards utilization of the sensor in exhaled breath analysis for diagnostic. The innovation of room temperature sensing materials may push forward the integration of gas sensing element

with wireless device and that can be connected to others Internet of Things (IOT) platforms. This proof of concept has been patented (Patent reference no: *201731038036*).

(e) In chapter 6, we have demonstrated the induction of charge carriers in oxide semiconductor by field effect using electric double layer (EDL) gate in field effect transistor (FET) devices. We have investigated the electrical characteristics of electric double layer (EDL) thin film transistor with doped ZnO (amorphous indium gallium zinc oxide) channel on flexible Kapton substrate. the charge carrier induction through EDL as a gate dielectric (a solid polymer electrolyte) formed the EDL gate capacitance at oxide/electrolyte interface with large specific gate capacitance ($\approx 31\ \mu F/cm^2$). This induces an ultra-high charge carrier density on the surface of the channel and this high value of EDL gate capacitance easily modulated the carrier density of oxide semiconductors and device can operated with low threshold voltage. This high carrier density yielded high value of saturation mobility μ_{sat} ~ 42 cm^2/Vs, good ON/OFF ratio of ~10^5, and low threshold voltage of ~ 0.7 V due to influence of high value of EDL gate capacitance of polymer electrolyte. The stable electrical characteristic under different bending stress will make it a useful contribution to flexible electronics. The device has been operated within small voltage (≤ 2 V) because of large specific gate capacitance ($\geq 30\mu F/cm^2$) of the EDL gate. This low voltage operation is particularly useful in such platforms like mobiles and wireless usage and in such operation where use of a high voltage for the TFT operation may become detrimental to its use. This experimental observation/ understanding as well as invention leads to a very good contribution to flexible electronics with a very good technological application potential. This proof of concept has been patented (Patent reference no: 201731015268).

(f) In chapter 7, we have investigated the role of surface/interface defects on photoconduction mechanism of ZnO/p-Si NWs nanostructures arrays grown by different methods using chemical solution deposition (CSD) and pulsed laser deposition (PLD) methods. The optical response of ZnO/p-Si NWs photodetectors have been tuned by changing the surface-interface defects and transport of charge carriers is strongly dependent on the different concentration of defects with processing conditions experimentally. We have also shown that the photodetection performances of ZnO/p-Si NWs nanostructures are strongly dependent on the functionality of surface/interface state. This has been investigated by analysis of oxygen vacancy (V_o) using photoluminescence (PL) and X-ray photoelectron spectroscopy (XPS) through depth profiling to quantify the defects and also to probe the vertical compositions of the devices, which is essential for a better understanding of its

optoelectronics properties. Here, we have mainly put an effort to explain the effects of the incorporation of defects states in the heterojunctions on the photoresponse of the ZnO/p-Si NWs arrays and a schematic of energy band diagram models have been given to explain the transient photocurrent of photodetectors especially in visible and NIR region.

8.2 Scope for future works

1. In this thesis, we have mainly focused on the integration of ZnO into heterojunction (both p-n and n-n junction) with Si nanowires arrays. There are several metal oxide semiconductors that can be integrated with 1D nanostructures but the choice of the integrated material is a main focus in the research field for further enhancement in the field of electrical, optoelectronic and gas sensing and that needs to be cultivate in near future.
2. In this thesis work, we have shown tuning of charge carrier in ligand-free plasmonic Au NPs decorated ZnO/p-Si NWs core-shell arrays by photo gating effect to extend the photoresponse up to 1100 nm beyond its fundamental band gap. One can also enhance the photoresponse of ZnO/p-Si NWs core-shell arrays via tunning of surface morphology with controlled defects states.
3. We have shown that functional oxide (ZnO) and semiconductor (Si) NWs based heterojunction arrays based NO gas sensor can lead to extremely high sensitivity (~ 500 ppb) and selectivity even in room temperature operation**.** The gas sensing performances can be enhanced via tunning of surface morphology of ZnO, doping with metal into ZnO, functionalization of ZnO surface by noble metal nanoparticles and UV/visible light activation. In this context, one can decorate ZnO/Si NWs core-shell arrays with the ligand-free palladium nanoparticles (Pd NPs) by using pulsed laser ablation in liquid (PLAL) method which can detect the hydrogen (H_2) gas very efficiently because Pd can absorb H_2 about 900 times of its own volume approximately. This unique property of palladium signifies its use in hydrogen fuel industries, hydrogen sensor technology etc.
4. In this thesis work, we have shown that the photoconduction mechanism of ZnO/p-Si NWs nanostructures are strongly dependent on the functionality of surface/interface state in the p-n junction with different synthesis methods. One can enhance the photoresponse properties of ZnO/p-Si NWs heterostructures by interface passivation layer like ultrathin aluminium trioxide (Al_2O_3) interlayer. The intrinsic built-in electric field can effectively stimulate charge carrier transportation in n-ZnO/Al_2O_3/p-Si NWs core-shell arrays.

Moreover, the inserted ultrathin Al_2O_3 nanolayer not only passivate interfacial defects, but also serve as an antireflection (AR) film to enhance NIR absorption of Si.

5. One of the major challenges of oxide-based photodetectors are the slow response and high persistence due to the surface-related oxygen desorption, recombination, and oxygen re-adsorption process and it depends mainly upon three factors; the available defect states ($V_o s$, V_{Zn}), surface area and adsorbate (O_2 or H_2O). The control of PPC can be done by doping, functionalization of oxides and tuning of surface/interface defects. However, the PPC effect can also be controlled by elevated temperatures which accelerate the carrier capture rate by introducing of thermally activated recombination centers that corresponds to the thermal ionization of free holes from the acceptor level (V_{Zn}) to the valence band.

Appendix A

Wavelength dependent persistence photoconduction of indium gallium zinc oxide (IGZO) thin film

In this appendix, we have studied the behaviour of photoresponse characteristics of indium gallium zinc oxide (IGZO) thin film grown by pulsed laser deposited on quartz. During illumination, photocurrent (I_{PC}) increased gradually in the wavelength range of 500-300 nm (visible to ultraviolet) while, a large increase of photo-current was observed below 325 nm i.e., the band edge wavelength. By removing the illumination, the polycrystalline film of IGZO shows the persistence nature of photocurrent and persistence strongly depends on the wavelength of incident light. By fitting the dynamic response, we observed the raising time (τ_r) and decay time (τ_d) of photo current is 120-205 s and 1000-5500 s respectively. The observed results are consistent with the optical gap of ~ 3.68 eV extracted from the absorption measurement.

A.1 Introduction

Metal oxide semiconductors shows very unique properties from conventional inorganic semiconductor with respect to electronic properties, structure, defect states and optoelectronics properties. Metal oxide semiconductors, especially the amorphous one, are promising candidate in thin film transistor technology owing to their unique properties such as excellent carrier mobility even in amorphous state, high electrical conductivity, high optical transparency in visible as well as near-infrared region and large area uniform deposition at low temperature [1-2]. Among different metal oxides, indium gallium zinc oxide (IGZO) has great advantages in thin film transistor (TFT) and also have the interesting behaviour of photoconduction of charge carrier [3-4]. However, it has been commonly observed that the decay time for transient photocurrent (falling transient) of oxide (ZnO/IGZO) based photodetectors especially in UV region is extremely long (minutes to hours) after removing the optical excitation [5-9]. This phenomenon is commonly known as persistent photoconductivity (PPC). By the desorption of oxygen, free electrons are released into the metal-oxide semiconductor and increase the carrier density and the conductivity. In this chapter, we have studied the wavelength dependent photoresponse of IGZO nanostructured film which shows the maximum response of photo current in UV region. We have analysed the dependence of persistence photocurrent (PPC) with wavelength of expose light.

A.2 Experimental details

For deposition of film by pulsed laser deposition (PLD), the indium gallium zinc oxide (IGZO) target (pellet) is prepared by the solid-state method. The details are given in the main chapter 2 in this thesis. The deposition of the IGZO films are done by PLD on quartz substrate at temperature of 650 ^{o}C. In PLD a KrF excimer laser (λ =248 nm) with energy density of ~ 2.11 J/cm^2 is employed. The films have been deposited under 10 mT O_2 pressure. The structural characterization and surface morphology of the films are done by X-ray diffraction (XRD), scanning electron microscopy (SEM). The optical characterization of IGZO film is done by UV-visible and photoluminescence (PL) spectroscopy. Photo response of IGZO film is measured by making a channel of length and width of 5 mm and 100 μm respectively. A 60-nm-thick Cr/Au layer is deposited through a hard mask by thermal evaporation to form the source and drain contacts. The Keithley 2400 used as current source and illumination with varying wavelengths (λ) connected with a monochromator.

A.3 Results and discussions

Figure A.1 (a) shows the XRD of IGZO film grown on quartz by PLD and inset is the SEM image for analysis of surface morphology. From XRD and SEM image we concluded that the film is polycrystalline in nature. Figure A.1 (b) is variation absorption coefficient with wavelength and inset is the Tauc plot for calculation of band gap. The band gap of IGZO film is around 3.68 eV which is measured from absorption spectra. Figure A.1 (c) is the PL spectrocppy of IGZO film with an exciation wavelength of 300 nm for determination of defect state.

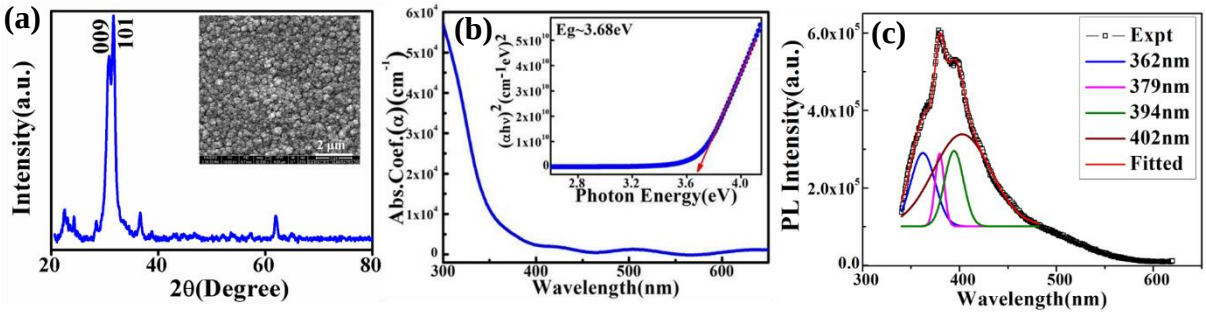

Figure A.1 (a) XRD of IGZO film on quartz. Inset is the SEM image. (b) Optical absorption spectra for determination of band gap. Inset is the variation of $(\alpha hv)^2$ vs. photon energy (hv). (c) PL spectra of polycryatlline IGZO film on quartz.

Figure A.2 (a) shows the variation of $I-V$ data for dark and under illumination of light of λ= 300 nm. The I-V curve is asymmetric and nonlinear [10]. This may arise due to different height of Schottky barrier.

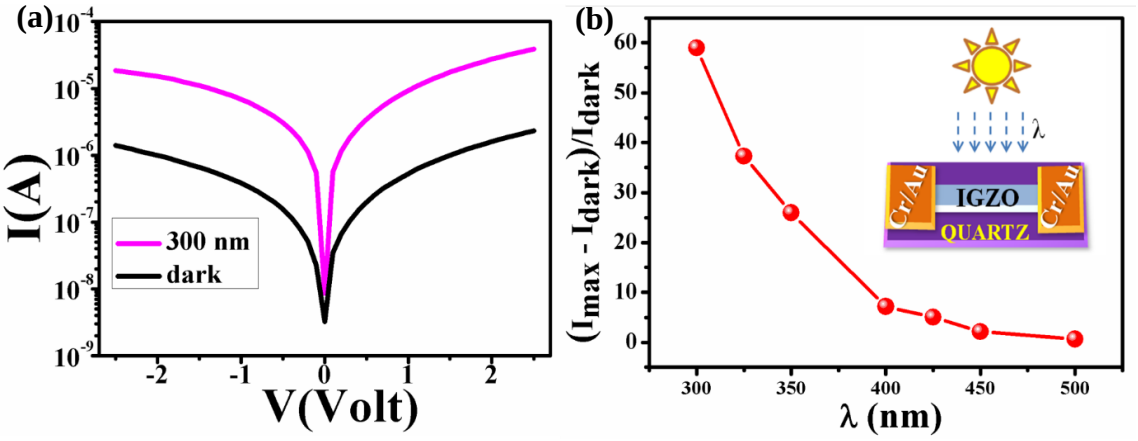

Figure A.2 (a) Variation of $I-V$ data under dark and light (λ = 300 nm). (b) Variation of photocurrent over dark current with λ. Inset is the schematic diagram for photoconductivity measurement set up.

Figure A.2 (b) shows the increase of photocurrent (PC) over dark current as $(I_{max}-I_{dark})/I_{dark}$ with wavelength (λ) of light. The change of PC is maximum about 60 %

at 300 nm wavelength. The inset of Figure A.2 (b) is the schematic diagram of photoconductivity measurement with vertically falling of monochromatic light (λ) on IGZO thin film on quartz.

The dynamic response of photo current was taken under different wavelength of light ranging from 300- 500 nm. Figure A.3 (a) represents the variation of photocurrents with time under different wavelengths of incident light. From data, we see that current is gradually increased under illumination and after off the illumination the photocurrent showed at persistence in nature and some value of current is retained over long period of time. This phenomenon is commonly known as persistent photoconductivity (PPC). The persistence is longer for shorter wavelength [11]. The origin of PPC is coming form surface defects which increases the relaxation time of carriers and as result photocurrent is persistence [12-13]. The quantitative analysis of the dynamic response general stretched exponential model is applied for PC. According to this model, the raising part of the photoresponse curve in presence of illumination follows the equation given below [11]:

$$I = I_{dark} + I_{PC}[1 - e^{-(t/\tau_r)^{\beta^r}}] \qquad (A.1)$$

Where I_{dark} is the dark current, I_{PC} is the photocurrent, τ_r is the raising time constant, and β_r is the stretched exponential for rise curve.

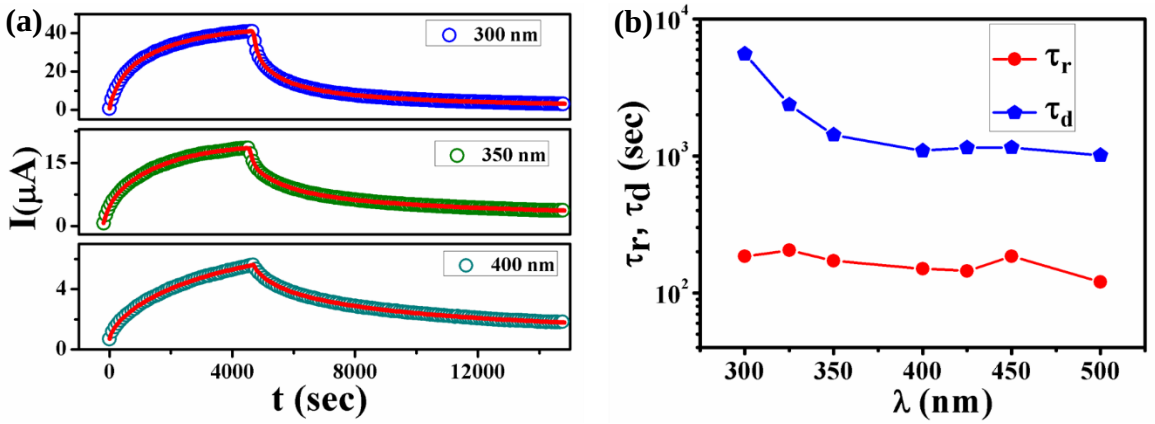

Figure A.3 (a) The time dependent photoresponse of polycrystalline IGZO film for different wavelengths (λ) of light. Experimental data represented by symbols; the continuous line represents the fitting of the curve. (b) Wavelength dependence of raising time constant (τ_r) and decay time constant (τ_d) as obtained from fitting curve.

When the illumination is turned off, the PC decreases following by the other equation given below [11]:

$$I = I_{dark}^{\infty} + (I_{max} - I_{dark})e^{-(t/\tau_d)^{\beta^d}} \qquad (A.2)$$

Where I_{dark}^{∞} is the dark current after a long time after the removal of the illumination and I_{max} is the maximum PC just before removal of illumination, τ_d is the time constant for decay, and β_d is the stretched exponential for decay curve.

By fitting the dynamic response of photocurrent (Figure A.3 (a)) by using equation (1) and (2) we have calculated the rising time constant (τ_r) and decay time constant (τ_d). The value of τ_r ≈ 150- 230 s, τ_d ≈ 1000 – 5000 s, stretched exponential for rise β_r ≈ 0.1 - 0.7 and stretched exponential for decay β_d ≈ 0.4- 0.9 obtained from fitted data depending on λ of the illumination. Figure A.3 (b) shows the variation of spectral dependence of raising time constant (τ_r) and decay time constant (τ_d) as obtained from fitting curve. The characteristics of PPC is dependent on τ_r and τ_d which is related to the surface-related oxygen desorption, recombination, and oxygen re-adsorption process [8, 10] and the decay time depends mainly upon three factors; the available defect states ($V_O s$, V_{Zn}), surface area and adsorbate (O_2 or H_2O).

A.4 Conclusion

In summary, we deposited the polycrystalline IGZO film by pulsed laser and film is characterized by different technique. During illumination, photocurrent (I_{PC}) increased gradually in the wavelength range of 500-300 nm (visible to ultraviolet) while, a large increase of photo-current was observed below 325 nm i.e., the band edge wavelength. We study the photoresponse behavior of IGZO film and the origin of persistence photocurrent which is strongly depends on the surface and defects structure of the film. The film shows the maximum photo current at UV region and this can be valuable for UV photo detector and sensor.

Bibliography

1. T. Kamiya, K. Nomura, and H. Hosono, *J. Disp. Technol*., **5**, 468 (2009).
2. X. Yu, T. J. Marks, and A. Facchetti, *Nature Mater*, 15, 383 (2016).
3. K. Nomura, H. Ohta, A. Takagi, T. Kamiya, M. Hirano, and H. Hosono, *Nature*, **432**, 488 (2004).
4. I. Cunha, R. Barras, P. Grey, D. Gaspar, E. Fortunato, R. Martins, and L. Pereira, *Adv. Funct. Mater*., **27**, 1606755 (2017).
5. B. Jiming, S. Ilan, S. Zhihua, G. Ron, C. Federico, W. Xiaowei, and R. Zhifeng, *Nanoscale Res. Lett*., **6**, 404 (2011).
6. Z. G. Yin, X. W. Zhang, Z. Fu, X. L. Yang, J. L. Wu, G. S. Wu, L. Gong, and K. Paul, *Phys. Status Solid RRL*, **6**, 117 (2012).
7. H. K. Li, T. P. Chen, S. G. Hu, X. D. Li, Y. Liu, P. S. Lee, X. P. Wang, H. Y. Li, and G. Q. Lo, *Optics Express*, **23**, 27683 (2015).
8. D. L. Jiang, L. Li, H. Y. Chen, H. Gao, Q. Qiao, Z. K. Xu, and S. J. Jiao, *Appl. Phys. Lett*., **106**, 171103 (2015).
9. M. Lee, K. T. Kim, M. Lee, S. K. Park, Y. H. Kim, *Thin Solid Films*, **660**, 749 (2018).
10. C. Samanta and B. Ghosh, *AIP Conference proceedings*, **2115**, 030332 (2019).
11. S. R. Moulik, S. Samanta, and B. Ghosh, *Appl. Phys. Lett*., **104**, 232107 (2014).
12. M. S. Ulmann and J. Augustynski, *J. Appl. Phys*., **54**, 6061 (1983).
13. S. Mondal and A. K. Raychaudhuri, *Appl. Phys. Lett*., **98**, 023501 (2011).